



HAL
open science

Transmission electron microscopy study of low-temperature silicon epitaxy by plasma enhanced chemical vapor deposition

Farah Haddad

► **To cite this version:**

Farah Haddad. Transmission electron microscopy study of low-temperature silicon epitaxy by plasma enhanced chemical vapor deposition. Materials Science [cond-mat.mtrl-sci]. Université Paris Saclay (COmUE), 2016. English. NNT: 2016SACLX107 . tel-01508918

HAL Id: tel-01508918

<https://pastel.hal.science/tel-01508918>

Submitted on 15 Apr 2017

HAL is a multi-disciplinary open access archive for the deposit and dissemination of scientific research documents, whether they are published or not. The documents may come from teaching and research institutions in France or abroad, or from public or private research centers.

L'archive ouverte pluridisciplinaire **HAL**, est destinée au dépôt et à la diffusion de documents scientifiques de niveau recherche, publiés ou non, émanant des établissements d'enseignement et de recherche français ou étrangers, des laboratoires publics ou privés.

NNT : 2016SACLX107

THESE DE DOCTORAT
DE
L'UNIVERSITE PARIS-SACLAY
PREPAREE A
"L'ÉCOLE POLYTECHNIQUE"

ÉCOLE DOCTORALE N° 573

Interfaces : approches interdisciplinaires / fondements, applications et innovation

Spécialité de doctorat : Physique

Par

Mme Farah Haddad

Transmission electron microscopy study of low-temperature silicon epitaxy by
plasma enhanced chemical vapor deposition

Thèse présentée et soutenue à « Palaiseau », le « 14 décembre 2016 » :

Composition du Jury :

M. Gilles Patriarche	DR CNRS, C2N	Président
Mme Sabine Lay-Dietrich	DR CNRS, INPG-PHELMA	Rapporteur
M. Pierre Ruterana	DR CNRS, ENSICAEN	Rapporteur
Mme Agnès Granier	DR CNRS, IMN	Examinatrice
M. Jean-Luc Maurice	DR CNRS, Ecole Polytechnique	Directeur de thèse
M. Pere Roca i Cabarrocas	DR CNRS, Ecole Polytechnique	Co-directeur de thèse

Acknowledgment

First and foremost, I thank God for providing me this opportunity and granting me the capability to proceed successfully. The present manuscript would not have been possible without the help, encouragement and support of many persons. I thank all of them and I present them all my gratitude.

I am deeply grateful to all members of the jury for agreeing to read the manuscript and to participate in the defense of this thesis. Very special thanks go to Jean-Luc Maurice, my supervisor, for his kind guide, support, help, encouragement and... much more. I appreciate the freedom and confidence he provided me. He was always there to answer my questions and discuss whenever I needed. I express my gratitude to Pere Roca i Cabarrocas, my co-supervisor and the head of LPICM, for his constant encouragement and relevant advices, despite his very busy agenda; I admire his passion during scientific discussions.

I would like to thank my colleague Prabal Goyal who made the growth experiments for me, he gave me a lot of samples to study and characterize and was always ready to make new ones with pleasure. I appreciate his honesty and care in our collaboration. I would like to thank Ronan Léal for his collaboration and for the growth experiments. I cannot forget Jean-Christophe Dornstetter who was ready to discuss about microcrystalline and epitaxial silicon at anytime. Thanks to him, I made a background on this topic during the beginning of my thesis. I confess he was my inspiration to do some studies.

I would like to acknowledge Erik Johnson, Holger Vach and François Siva for their valuable discussions on some results. I would like to thank Martin Foldyna for his advices and coffee breaks. I express my gratitude to the CIMEX team, especially Ileana Florea, Pierre-Eugène Coulon, Eric Larquet and Mathias Kobylko for helping me working on the TEM when it had problems. I extend my sincere thanks to all members of LPICM, especially Huda Haddad, Paul Narchi, Mariam Ezzedine, Fatima Jardali, Fatima Bouaniss, Warda Hadouchi, Mutaz Al-Ghzaiwat, Angelo Grimaldi, Xin Yang Wang, Wanghua Chen, Loic Loisel, Bastien Bruneau and Romain Cariou for making LPICM a nice place to work.

A special thank goes to Pierre Legrain (for his confidence and support), Michel Rosso, François Ozanam and Fouad Maroun, I will never forget their support during my first year of PhD.

Without the support of my mother, my father, my brothers, and my parents-in-law, their prayer for me was what sustained me so far. I acknowledge their confidence and love. Finally, I would like to extend my warmest thanks to my lovely husband who is always supporting and encouraging me especially in the most difficult situations. Caring and tender, he is illuminating my life.

Résumé

Cette thèse s'intéresse à la croissance épitaxiale à basse température ($\sim 200^\circ\text{C}$) des couches minces de silicium par dépôt chimique en phase vapeur assisté par plasma (PECVD), pour des applications aux cellules solaires. L'objectif de départ était de mieux comprendre cette croissance épitaxiale, en utilisant la microscopie électronique en transmission (MET) comme principal outil expérimental. Afin de réussir les observations MET en coupe, une étape d'amincissement est indispensable pour avoir un échantillon transparent aux électrons.

D'abord, nous avons étudié les premiers stades de cette croissance épitaxiale en chimie tétrafluorure de silicium, hydrogène et argon ($\text{SiF}_4/\text{H}_2/\text{Ar}$) ou en chimie silane et hydrogène (SiH_4/H_2), en menant une série de dépôts courts – quelques dizaines jusqu'à quelques centaines de secondes – sur différents types de substrats. Nous avons utilisé comme substrats des wafers de Si (100), des wafers de Si (111), des wafers d'arséniure de gallium GaAs (100), des grilles MET de Si (100), ou des grilles MET de cuivre avec membrane de carbone amorphe). Nous avons établi une corrélation entre les images MET de coupes et de vues planes et les mesures d'ellipsométrie in-situ. Nous avons discuté les mécanismes de croissance en nous basant sur l'hypothèse de la croissance traditionnelle à base de radicaux et ions et l'hypothèse (relativement nouvelle) reposant sur la fonte des particules générées par le plasma au moment de l'impact avec le substrat.

De plus, pour comprendre comment l'épitaxie par PECVD à basse température se maintient, nous avons étudié comment elle se brise ou se perd. Pour cela, des expériences de perte d'épitaxie ont été visées en augmentant soit la puissance de la source radiofréquence (RF), soit le flux d'hydrogène, pour une chimie $\text{SiF}_4/\text{H}_2/\text{Ar}$. Dans les deux cas, le mécanisme de brisure d'épitaxie fait intervenir des macles et des fautes d'empilement qui interrompent la configuration épitaxiale. Après avoir comparé nos résultats avec ceux de la littérature, nous proposons que la brisure d'épitaxie du silicium passe par une rugosification de surface (mise en évidence par le signal de l'ellipsométrie in-situ pour tous les échantillons ayant subi une brisure d'épitaxie) qui introduit les macles et les fautes d'empilement. Grâce à cette nouvelle compréhension de la brisure d'épitaxie, nous proposons quelques moyens pour maintenir l'épitaxie pour de plus grandes épaisseurs.

En outre, nous avons observé une fascinante quasi-symétrie cinq dans les diagrammes de diffraction pour ces couches et aussi pour d'autres élaborées par un plasma de chimie $\text{SiH}_4/\text{H}_2/\text{HMDSO}/\text{B}_2\text{H}_6/\text{Ar}$. Nous avons attribué une telle symétrie à une brisure d'épitaxie par l'intermédiaire d'un maillage multiple. Nous avons développé une méthode d'analyse quantitative qui permet de : (1) discriminer les positions de maillage de celles du microcristal aléatoire dans les diagrammes de diffraction, (2) estimer

le nombre des opérations de maclage et (3) évaluer la contribution de chaque ordre de maclage. Nous avons aussi discuté quelques raisons probables pour l'incidence du maclage et du maclage multiple sous forme de symétrie cinq. La tendance du système à aligner les plans {111} presque parallèlement à l'axe de croissance nous semble un facteur majeur pour l'apparition d'une telle symétrie.

Finalement, une importante réalisation pour le monde de la MET, durant ce travail doctoral, est l'optimisation de la préparation traditionnelle d'échantillon ou polissage par la méthode du tripode. Nous l'avons transformée d'une méthode longue et ennuyeuse en une méthode rapide qui devient compétitive par rapport à la technique du FIB relativement chère. Un des secrets de cette réalisation est la superposition de plusieurs échantillons dans un même sandwich (voire 4 échantillons au lieu de 2). Un autre secret est le polissage de la première face de plusieurs sandwiches (voire 4 sandwiches ou 16 échantillons) simultanément, alors que le polissage de la deuxième face de chaque sandwich est fait séparément (étape très critique et sensible) ; Ceci réduit énormément le temps d'amincissement d'échantillons.

Contents

Acknowledgment	iv
Résumé.....	v
Contents	vii
List of figures.....	x
List of tables.....	xviii
List of acronyms	xix
Chapter 1. General introduction.....	1
1.1. Solar energy.....	2
1.2. Silicon photovoltaic technology	4
1.3. Low-temperature Si epitaxy by plasma enhanced chemical vapor deposition.....	5
1.3.1. Motivation.....	5
1.3.2. History	6
1.3.3. Some challenges.....	7
1.4. SiF ₄ /H ₂ /Ar plasma chemistry	9
1.5. SiH ₄ /H ₂ /HMDSO/B ₂ H ₆ /Ar plasma chemistry.....	10
1.6. Framework of this thesis	11
1.6.1. Focus on understanding epitaxial growth of Si thin films by LT-PECVD.....	11
1.6.2. Aim and outline of this PhD thesis	14
Chapter 2: Growth and characterization methods	16
2.1. Plasma enhanced chemical vapor deposition (PECVD).....	17
2.1.1. Fundamentals of PECVD.....	17
2.1.2. Brief description of the reactors	18
2.2. Characterization methods.....	20
2.2.1. Transmission electron microscopy.....	20
2.2.2. Ellipsometry.....	31
Chapter 3. Initial stages of epitaxial growth.....	34

3.1. Introduction.....	35
3.2. SiF ₄ /H ₂ /Ar plasma (CLUSTER reactor).....	37
3.2.1. Evidence for the presence of a transient regime- long deposition.....	37
3.2.2. Short deposition on Si (100) wafers.....	41
3.2.3. Short deposition on TEM copper grids with carbon membrane.....	43
3.3. SiH ₄ /H ₂ plasma (ARCAM reactor).....	46
3.3.1. Growth morphology on Si (100), GaAs (100) and Si (111) wafers - short depositions.....	47
3.3.2. Short deposition on Si (100) TEM grids.....	49
3.4. Discussion.....	51
3.4.1. Hypothesis of growth mediated by atoms, radicals or ions.....	52
3.4.2. Hypothesis of growth mediated by plasma generated particles.....	56
3.4.3. Growth mechanisms: an open discussion.....	62
3.4.4. Effect of the substrate.....	64
3.5. Summary and perspectives.....	65
Chapter 4. Epitaxy breakdown using SiF₄/H₂/Ar plasma.....	66
4.1. Introduction.....	67
4.2. Intentional epitaxy breakdown with increasing the RF power.....	69
4.2.1. RF power of 20 W on Si (100) substrate.....	69
4.2.2. RF Power of 25 W on Si (100) and Si (111) substrates.....	76
4.2.3. Summary of the results – epitaxy and breakdown by increasing the RF power.....	82
4.3. Intentional epitaxy breakdown with increasing the H ₂ flow rate.....	84
4.3.1. Hydrogen flow rate of 2 sccm on Si (100) wafers.....	84
4.3.2. Hydrogen flux of 3 sccm on Si (100) wafers.....	90
4.3.3. Summary of results - epitaxy and breakdown by increasing the H ₂ flow rate.....	93
4.4. Discussion.....	95
4.4.1. Breakdown by power.....	96
4.4.2. Breakdown by hydrogen.....	100
4.5. Summary and perspectives.....	105
Chapter 5. Twinning in epitaxial films and fivefold symmetric diffraction patterns.....	106

5.1. Introduction.....	107
5.1.1. Overview of twinning and fivefold symmetry in literature.....	107
5.1.2. Fivefold symmetric diffraction patterns in Si thin films.....	108
5.2. Twinning in Si films promoted by epitaxy breakdown from SiF ₄ /H ₂ /Ar plasma.....	111
5.2.1. Epitaxy breakdown by increasing the RF power.....	112
5.2.2. Epitaxy breakdown caused by increasing the H ₂ flow rate.....	121
5.3. Twinning in Si films promoted by epitaxy breakdown from SiH ₄ /H ₂ /HMDSO/B ₂ H ₆ /Ar plasma.....	126
5.3.1. Effect of the substrate.....	127
5.3.2. Effect of HMDSO flow rate.....	131
5.3.3. Number of twin operations.....	133
5.3.4. MT and microcrystalline contributions.....	133
5.3.5. Chemical analysis.....	136
5.4. Discussion.....	138
5.4.1. Growth twins and fivefold symmetry.....	138
5.4.2. Origin of twinning and multiple twinning.....	139
5.4.3. Twinning and epitaxy breakdown.....	143
5.4.4. Effect of the seed orientation on twinning - Si (100) vs Si (111).....	148
5.5. Summary and perspectives.....	150
Chapter 6. Conclusion and perspectives.....	151
6.1. Contribution to the research field.....	152
6.2. Perspectives for future work.....	153
References.....	155
List of publications.....	164

List of figures

Figure 1. Estimated renewable energy share of global final energy consumption, 2014 [2].....	2
Figure 2. Average annual growth rates of renewable energy capacity and biofuels production from end 2010 to end 2015 [2] (*CSP for concentrating solar power).	3
Figure 3. Solar PV global capacity, by country/region, from 2005 to 2015 [2].	3
Figure 4. Market share of different PV technologies from 1980 to 2015 [3]	4
Figure 5. Transmission electron microscopy image showing crystalline parts embedded in an amorphous matrix: this is polymorphous Si [29]	8
Figure 6. Structure of hexamethyldisiloxane (HMDSO)	11
Figure 7. Diamond cubic crystal structure of Si.....	12
Figure 8. Silicon crystal seen along the <110> direction	13
Figure 9. ABC stacking in a face centered cubic crystal.....	14
Figure 10. Schematic view of the potential distribution in a capacitively coupled plasma in a RF discharge. The substrate is grounded and the RF voltage is applied to the RF electrode, for most of the cases.	18
Figure 11. Photos of CLUSTER [51], PHILIX [31] and ARCAM [51] reactors located at PICM laboratory.	19
Figure 12. The transmission electron microscope compared with a slide projector	21
Figure 13. Schematic ray diagram showing a comparison of the lens conditions between diffraction and image modes.	23
Figure 14. Bragg diffraction: two beams approach a crystalline solid and are scattered off two different atoms within it. Constructive interference occurs when the path difference between the two beams ($2d \cdot \sin \theta$) is equal to an integer multiple of the radiation wavelength. Note that, in the case of TEM, θ is of the order of a few mrad (≈ 1 degree).....	23
Figure 15. (a) Thickness map and (b) its profile for an epitaxial sample prepared by polishing and ion milling. The thickness of the sample is around 45 nm	24
Figure 16. The JEOL 2010F microscope used in this doctoral work in the CIMEX.....	25
Figure 17. Procedure before polishing: (a) cutting the sample with a diamond tip into slices and glue them face to face, (b) cutting them into thinner slices (the dashed lines indicate further slicing) and (c) gluing one slice on the glass of the tripod polisher.....	26
Figure 18. Wire saw system for a high precision cutting of a sample into small slices.....	26
Figure 19. (a) Different abrasive disc, each one corresponds to a granulation size: 30, 15, 6, 3, 1 and 0.5 μm from left to right. (b) Polishing system	27
Figure 20. Each color corresponds to an abrasive disc characterized by its granulation size. Transitional thicknesses to move from one abrasive disc to another are: 125, 70, 35, 6, 3, 1 and 0.5 μm	27
Figure 21. Precision ion polishing system	29

Figure 22. TEM image showing an amorphized region in the thinnest part as indicated by the arrow. The dark regions correspond to twinned monocrystalline domains.	29
Figure 23. Copper grid covered by a carbon membrane.....	30
Figure 24. (a) Plan view and (b) cross-section view of the Si (100) TEM grid.....	31
Figure 25. Schematic of ellipsometry principle [57].....	31
Figure 26. Photo of the ex-situ experimental setup at LPICM	33
Figure 27. Cross-section TEM image of sample C1 (long deposition) showing defects at the interface and island shapes on top of the epitaxial film.	37
Figure 28. HRTEM image of sample C1 showing the high quality epitaxy.	38
Figure 29. In-situ ellipsometry for deposition times $t=0, 90$ and 450 s. A minimum intensity at 4.2 eV is reached at 90 s, and then a stabilization occurs for $t \geq 1000$ s.....	38
Figure 30. Time evolution of the imaginary part of the pseudo-dielectric function measured at 4.2 eV (in blue) and 3.4 eV (in red). The stars indicate where the growth was stopped for the TEM samples discussed in section 3.2.2.....	39
Figure 31. Evolution of the plasma potential with deposition time.....	40
Figure 32. Cross-section TEM images of (100) c-Si wafers exposed to an epitaxial plasma for (a) 12 s, (b) 90 s and (c) 240 s.....	42
Figure 33. Cross-section HRTEM images of a (100) c-Si wafers exposed to an epitaxial plasma for (a) 12 s, (b) 90 s and (c) 240 s.	42
Figure 34. (a) and (b) Low resolution TEM images of the deposition on the carbon membrane (for 90 s). (c) Diffraction pattern recorded on a zone of (b) including the large islands.....	44
Figure 35. (a) Carbon map, (b) silicon map and (c) image combining silicon in red and carbon in green for the deposition on TEM copper grid for a deposition time of 90 s.	44
Figure 36. TEM images of the deposition on the carbon membrane corresponding to 12 s (a), 90 s (b) and 240 s (c). (a) shows dendritic aggregation of particles (with particle size of $12-25$ nm), (b) shows spherical aggregation (~ 50 nm) and particles (~ 25 nm) aggregating in defective dendritic shapes and (c) shows big aggregates ($110 - 200$ nm).	45
Figure 37. TEM image showing the growth on a Si (100) wafer for deposition time of 8 s.	47
Figure 38. TEM image showing the growth on a GaAs (100) wafer for a deposition time of for 8 s.	48
Figure 39. TEM image illustrating the growth for 8 s on Si (111) wafer, it shows an amorphous film having a thickness around 5 nm.....	48
Figure 40. TEM images recorded on the Si (100) grids near the edges of the windows showing contamination on the membrane before any deposition.....	49
Figure 41. A series of TEM images of the Si membrane showing a smooth surface for (a) focused image, (b) underfocused image and (c) overfocused image ($\Delta f = \pm 56$ nm).....	49
Figure 42. A series of TEM images (focused, underfocused and overfocused, $\Delta f = \pm 35$ nm) corresponding to deposition for 8 s on Si (100) grids.	50

Figure 43. TEM images showing crystalline islands found on Si (100) grids, they have size in the range of 10-20 nm	50
Figure 44. TEM images of the deposition on the Si grids. Few islands up to 80 nm in width are found, they are not uniformly distributed on the grids.	51
Figure 45. Growth modes at low temperature [78]	53
Figure 46. Evolution of the deposition rate, $\langle \epsilon_i \rangle$ 3.4 and 4.2 eV and the Raman full width at half maximum as a function of the plasma potential and power [65].	55
Figure 47. Map of stress component σ_{yy} as simulated by Moras et al. [69]; tensile stress is represented in red and compressive stress in blue.	56
Figure 48. Time evolution of the pressure, the DC bias between the electrodes and the real (ϵ_1) and imaginary (ϵ_2) parts of the pseudo-dielectric function spectra measured at 3.4 eV, in the work of Schmidt et al. [84]. An initial transient stage is detected at a power of 10 W due to particle formation, this is not the case at 3 W where no particles are formed.....	59
Figure 49. TEM images recorded on carbon membrane showing crystalline particles having a diameter of 5 to 10 nm, these images are taken from the study of (a) Dornstetter [31] and (b) Johnson et al. [96].	63
Figure 50. The growth conditions for the films presented in this chapter: two series of depositions were carried out starting from the reference film, by increasing either the RF power or the H ₂ flow rate.....	68
Figure 51. (a) Low magnification and (b) high resolution TEM images of the reference film obtained at a RF power of 15 W and a H ₂ flow rate of 1 sccm. The microstructure reveals a thickness of 750 nm of high quality epitaxy that is almost free of defects.	69
Figure 52. TEM image of the film deposited using a RF power of 20 W and a H ₂ flow rate of 1 sccm. The black dotted circles indicate the areas selected for the EDPs shown in Figure 53. Numbers are attributed to each area.....	70
Figure 53. (a), (b) and (c) TEM images showing the areas selected for the EDPs shown in (d), (e) and (f), respectively. (d) shows a perfect monocrystalline structure in region #1, (e) shows the monocrystalline orientation of the wafer (circled in red), twin orientations (indicated by yellow arrows), random microcrystalline orientations and amorphous contribution, in region #2. (f) is somehow similar to (e) but with a larger contribution of random microcrystalline, in region #3.	71
Figure 54. Profile of the blue rectangle in Figure 53(e) showing a small peak related to amorphous contribution in the film. It corresponds to the diffused part between 220 and 311 rings.....	71
Figure 55. HRTEM image confirming epitaxial growth in the beginning of the film: {111} planes are continuous from the wafer to the film across the interface.	72
Figure 56. TEM image showing a high defect density after a certain thickness of epitaxial growth	73
Figure 57. Time evolution of the imaginary part of the pseudo-dielectric function $\langle \epsilon_i \rangle$ measured at 4.2 eV, for the sample deposited using a RF power of 20 W and a H ₂ flow rate of 1 sccm.	74
Figure 58. Decomposition of the film deposited at 20 W and 1 sccm of H ₂ flow rate, into four parts in the light of the ellipsometry measurements of Figure 57.	75

Figure 59. Plasma potential as a function of the deposition time for the film grown using a RF power of 20 W and a H ₂ flow rate of 1 sccm.	75
Figure 60. TEM image of the film deposited using a RF power of 25 W and a H ₂ flow rate of 1 sccm.	76
Figure 61. HRTEM image revealing epitaxy in the beginning of the film deposited using a RF power of 25 W and a H ₂ flow rate of 1 sccm.	77
Figure 62. HRTEM image showing a V-shaped defect formed within the monocrystalline matrix in the film. (b) and (c) are FFTs performed on the matrix and on the defective region, respectively.	78
Figure 63. (a) HRTEM image taken from the top of the film, (b) EDP recorded on the top of the film including an area of 210 nm in diameter and dominated by monocrystalline and twin orientations (c) FFT corresponding to the red square showing microcrystalline and amorphous contributions.	78
Figure 64. In-situ ellipsometry measurements monitoring the evolution of the film growth.	79
Figure 65. Plasma potential as a function of the deposition time for the film deposited using a RF power of 25 W and a H ₂ flow rate of 1 sccm.	79
Figure 66. (a) TEM image of the sample deposited on Si (111) wafer using a RF power of 25 W and a H ₂ flow rate of 1 sccm. The region of the film near the interface is enlarged in (b), it shows an epitaxial growth for the first 25 nm of the film growth.	81
Figure 67. (a) EDP taken from the white dotted circle in Figure 66(a), it shows the presence of the monocrystalline wafer orientation (111 spots in red circles), twin orientations (indicated by arrows), random microcrystalline orientations and amorphous contribution. (c) EDP taken from the top of the film, it shows the presence of microcrystalline and amorphous phases.	81
Figure 68. FFTs performed inside the flame and outside it. The dark region corresponds to monocrystalline and twin orientations, whereas the brighter is composed of amorphous and microcrystalline phases.	82
Figure 69. Summary of images corresponding to epitaxy (a) and epitaxy breakdown (b) and (c) for samples deposited on Si (100) using a H ₂ flow rate of 1 sccm and different RF powers (15 W in (a), 20 W in (b) and 25 W in (c)).	83
Figure 70. Description of epitaxy breakdown and <i>epitaxy comeback</i> mechanisms, on the basis of the TEM observations in this chapter. Epitaxy breakdown occurs by (i) twinning followed by (ii) formation of a microcrystalline and amorphous phase. Twinning can be reversible and so <i>epitaxy comeback</i> is sometimes possible.	83
Figure 71. TEM images of the sample deposited on Si (100) using a RF power of 15 W and a H ₂ flow rate of 2 sccm; (b) corresponds to a thinner region of the foil. White dotted circles in (b) indicate the areas selected for the EDPs shown in Figure 72. Numbers refer to defects discussed in the text.	85
Figure 72. Diffraction patterns recorded on a region including (a) the wafer and the film and (b) the top of the film, as indicated by the white dotted circles of Figure 71.	85
Figure 73. Defects numbered 1 in Figure 71(b) exhibiting Moiré fringes (due to stacking faults and twins). The inset corresponds to the FFT of this image, it shows monocrystalline and twin spots.	86

Figure 74. Defects numbered 2 are platelets following {111} planes and having a size of the order of 10 nm. In the inset, arrows indicate the presence of a lot of platelets within the film.....87

Figure 75. Defects numbered 3 are indicated by arrows, these are stacking faults following {111} plane and displaying a strange contrast. They could correspond to dislocations decorated with hydrogen.87

Figure 76. HRTEM image (a) and its associated diffractogram (b) where we selected (using masks of 0.7nm^{-1} in diameter) two 111 spots to obtain the filtered images in (c), (d), (e) and (f). Yellow arrows point at lattice distortions and the red ones at dislocations.....88

Figure 77. Selection of two 200 spots in the diffractogram (a) to form the filtered image (b).89

Figure 78. In-situ ellipsometry measurements monitoring the evolution of the film deposited using a RF power of 15 W and a H_2 flow rate of 2 sccm.....90

Figure 79. TEM image of the sample deposited on Si (100) using a RF power of 15 W and a H_2 flow rate of 3 sccm.91

Figure 80. HRTEM image of the interface exhibiting some defects which are most likely hydrogen platelets.91

Figure 81. (a) TEM image showing the same crystalline structure in the first 20 nm of the film and in the wafer, then V-shaped defects appear initiating a highly defective region. (b) TEM image recorded on a thinner region of the TEM foil allowing us to better visualize the defects.92

Figure 82. TEM image of the defective region, it corresponds to a highly twinned structure as shown by the EDP in the inset.92

Figure 83. In-situ ellipsometry monitoring the evolution of the film structure deposited using a RF power of 15 W and a H_2 flow rate of 3 sccm.....93

Figure 84. Summary of images corresponding to (a) epitaxy, (b) defective epitaxy and (c) epitaxy breakdown for films deposited using a RF power of 15 W and different H_2 flow rate: 1, 2 and 3 sccm respectively.94

Figure 85. TEM images showing epitaxy breakdown for germanium Ge (100) layers deposited by LT-MBE for substrate temperatures of 95°C (a) and 135°C and (b) from the work of Bratland et al. [103]. They both show critical thicknesses h_1 and h_2 , where h_1 defines the onset of epitaxial breakdown and h_2 defines the entire film transformation from epitaxial to amorphous. (c) Schematic illustration revealing the evolution of the microstructure and surface morphology.97

Figure 86. Time evolution of the pseudo-dielectric function at 4.2 eV and the plasma potential while increasing the RF power from 15 W to 21 W [80]. $\langle \epsilon_i \rangle$ is stable when the plasma potential is below 61 V but decreases abruptly above 61 V.....100

Figure 87. Schematic illustration of the hydrogen platelet generation and evolution according to Hochbauer [118].....102

Figure 88. TEM images of Si films showing stacking faults appearing after a certain thickness of epitaxial growth, obtained in the work of Rosenblad et al. [21]. Such defects, also observed in our samples (Figure

81), were attributed to a buildup of roughness caused by the adsorbed hydrogen through reducing surface diffusion.	103
Figure 89. Electron diffraction pattern along the [0-11] zone axis displaying a fivefold symmetry (sample prepared with 0.45 sccm of HMDSO, see section 5.3)	108
Figure 90. (a) HRTEM image, recorded in the [0-11] zone axis, of the same layer as that imaged in Figure 89(b) FFT of (a), (c) selection of five grain orientations and (d) colored image constructed from the IFFTs of orientations 1, 3 and 5.	110
Figure 91. The growth conditions for the films presented in this chapter: two series of depositions were carried out starting from the reference film, by increasing either the RF power or the H ₂ flow rate. The substrates used are Si (100) and Si (111), they are indicated for each film.	112
Figure 92. Schematic representation of the monocrystalline orientation of the substrate in black circles and the allowed twin positions in red (anticlockwise) and blue (clockwise) spots for 111 ring. The zone axis is [0-11] and the growth axis is vertical. The order of twinning is indicated for each spot. Orders marked by * refer to twinning of the plane family associated with the spots at 70.53° and 250.53°, the others refer to that associated with spots at 0 and 180°. Only three orders of twinning are illustrated for visibility.	114
Figure 93. (a) EDP recorded on the MT part for the film deposited on Si (100) at 20 W, (b) azimuthal projection of (a), the black shape is caused by the beam-stopper used while recording the EDP. (c) Profile of 111 reflections deduced from (b). M and M' refer to spots of the monocrystalline grain (angles at 0 and 250.53° in Figure 92) and t refers to twin positions. The horizontal lines indicate the angles formed by the peak M and peaks attributed to a certain order of twinning about M situated at 0.	115
Figure 94. TEM images of the film deposited at 20 W: (a) shows the epitaxial and twinned parts of the film displaying different contrasts. A “zigzag” intermediate line separating these two parts is shown in (b) where V-shaped defects are noticeable.	116
Figure 95. TEM images showing the twinned part (or MT part) around the zigzag line for the Si films deposited using a RF power of 25 W on (a) Si (100) and (b) Si (111) substrates. For both cases, V-shaped defects initiate the MT part.	117
Figure 96. TEM images for the sample deposited on Si (100) at 20 W and a series of FFTs (1-7) performed on the squares drawn on the TEM images. These FFTs show the evolution of the MT phase crystallinity with thickness. The yellow arrows in the FFTs indicate the apparition of twin spots, the orange arrows in the TEM images indicate the growth direction of the darker phase	118
Figure 97. TEM image for the sample deposited on Si (100) at 20 W and a series of FFTs (1-5) performed on the squares drawn on the TEM images. These FFTs show the evolution of the crystalline structure of the bright phase with thickness. The blue arrows indicate spots associated with microcrystalline growth.	119

Figure 98. EDPs recorded on the films deposited from SiF ₄ /H ₂ /Ar at 25 W on (a) Si (100) substrate and (b) Si (111) substrate. They are taken on regions associated with the beginning of twin formation, as shown in the insets.....	120
Figure 99. (a) Electron diffraction pattern for the sample deposited at 2 sccm of H ₂ flow rate (10 W), showing a monocrystalline structure. (b) TEM image showing few regions (like the red rectangle) presenting a twinned region, which is confirmed in the FFT shown in (c).	122
Figure 100. Electron diffraction pattern recorded on the sample deposited at a H ₂ flow rate of 3 sccm. It exhibits twin spots associated with twinning.	122
Figure 101. (a) EDP recorded on the sample deposited at a H ₂ flow rate of 3 sccm. The profile of 220 ring is shown in (b) and its azimuthal projection in (d). (c) Schematic representation of the monocrystalline orientation of the substrate in black circles and the allowed twin positions in red (anticlockwise) and blue (clockwise) spots. M refers to one spot of the monocrystalline grain. The growth axis is vertical. The order of twinning is indicated for each spot.....	124
Figure 102. TEM images of the sample deposited at a H ₂ flow rate of 3 sccm. (a) Thin part displaying columnar structures growing perpendicularly to the interface. (b) HRTEM image of the film revealing a high density of twins.	125
Figure 103. HRTEM image showing local epitaxy at the film/substrate interface and some amorphous regions	128
Figure 104. Electron diffraction patterns recorded on (a) the wafer, film and glue and (b) just the film and the glue.	128
Figure 105. TEM image showing a layer deposited with an HMDSO flow rate of 0.24 sccm on Si (100) without epitaxial interface. The inset shows the EDP recorded on the film exhibiting no fivefold symmetry...	129
Figure 106. (a) Stack of films with different HMDSO flow rates and (b) EDP recorded on the stack without the first film.....	130
Figure 107. Electron diffraction patterns recorded on samples deposited with different HMDSO flow rates: (a) 0.05, (b) 0.45, (c) 0.62 and (d) 2.4 sccm, all except last showing multiple twinning.	132
Figure 108. Electron diffraction pattern along the [0-11] zone axis recorded on the selected area shown in the inset including the film and the glue.	132
Figure 109. HRTEM image of the film deposited on Si (100) with 0.05 sccm of HMDSO.....	132
Figure 110. (a) Azimuthal projection of the EDP of Figure 107(a). (b) and (c) Profiles of 111 reflections deduced from (a) after background subtraction. M, t and u refer to the monocrystalline grain, allowed twin positions and unauthorized twin positions, respectively.	134
Figure 111. Elemental maps of silicon (a), oxygen (b) and carbon (c). (d) and (e) represent the profiles of oxygen and carbon, respectively.	137
Figure 112. (a) TEM image showing epitaxy breakdown, on Si (100) wafer, mediated by twin formation for a sample deposited in the same growth conditions as our samples deposited in SiF ₄ /H ₂ /Ar plasma except for the flow rate of H ₂ and the power that corresponded to 2 sccm and 20 W respectively. (b) EDP	

corresponding to region 3, (c) EDP corresponding to region 1 and 2 (the arrow indicate a twin spot) and (d) TEM image showing the twinned structure of region 2.....	146
Figure 113. (a) TEM image showing epitaxy breakdown, on Si (111) wafer, occurring by the means of twin formation for another sample deposited in the same growth conditions as our samples deposited in SiF ₄ /H ₂ /Ar plasma except for the flow rate of H ₂ and the power that corresponded to 1.5 sccm and 15 W respectively. (b) EDP recorded on the circled region of (a) exhibiting spots characteristic of repeated twinning	146
Figure 114. Onset of epitaxy breakdown occurring with the formation of defects oriented along {111} planes and identified as twins (V-shaped defects). This sample was deposited on a Si (100) wafer in CLUSTER reactor [165].	147
Figure 115. (a) Film deposited on Si (100) wafer, using SiH ₄ /H ₂ plasma chemistry. The epitaxy breakdown occurs by the means of primary and secondary twin formation as shown by (b) the FFT performed on the rectangular area in (a).	148

List of tables

Table 1. Interplanar distances (d_{hkl}) corresponding to low index families of planes {hkl}	13
Table 2. Process conditions for the deposition of Si thin films leading to epitaxial growth in CLUSTER and ARCAM reactors.....	36
Table 3. Table summarizing the results of reference [95] for different impact energies of $Si_{29}H_{24}$ clusters (the biggest clusters in their study) and the impact modes (bounce-back, soft landing and shattering).....	60
Table 4. Contribution of the MT part and the microcrystalline part among the crystalline reflections present in the EDPs for the three different states of the substrate mentioned in section 5.3.1: c-Si substrate with epitaxy where individual films and stacking of films were deposited and c-Si with the presence of the native oxide.....	135
Table 5. Contribution of the MT part and the microcrystalline part among the crystalline reflections present in the EDPs for the three crystalline samples deposited under different HMDSO flow rates (section 5.3.2) in epitaxial relation with the substrate.....	136
Table 6. Potential reasons for the occurrence of twinning for three cases categorized by the order of their twins: twinning in HMDSO layers, twinning in samples deposited using $SiF_4/H_2/Ar$ at 20 and 25 W of RF power (1 sccm), and twinning in samples deposited at 3 sccm of H_2 flow rate (15 W).	142

List of acronyms

Acronym	Definition
TEM	Transmission electron microscopy
HRTEM	High resolution transmission electron microscopy
EFTEM	Energy filtered transmission electron microscopy
EDP	Electron diffraction pattern
MT	Multiple twinned
PECVD	Plasma-enhanced chemical vapor deposition
LT	Low temperature
Si	Silicon
c-Si	Monocrystalline silicon
SiF ₄	Silicon tetrafluoride
SiH ₄	Silane
H ₂	Hydrogen
HMDSO	Hexamethyldisiloxane
Ar	Argon
B ₂ H ₆	Diborane
HF	Hydrofluoric acid
$\langle \epsilon_i \rangle$	Imaginary part of the pseudo-dielectric function
V _{pl}	Plasma potential

Chapter 1. General introduction

1.1. Solar energy.....	2
1.2. Silicon photovoltaic technology.....	4
1.3. Low-temperature Si epitaxy by plasma enhanced chemical vapor deposition.....	5
1.3.1. Motivation.....	5
1.3.2. History.....	6
1.3.3. Some challenges.....	7
1.4. Context of SiF ₄ /H ₂ /Ar plasma chemistry.....	9
1.5. SiH ₄ /H ₂ /HMDSO/B ₂ H ₆ /Ar plasma chemistry.....	10
1.6. Framework of this thesis.....	11
1.6.1. Focus on understanding epitaxial growth of Si thin films by LT-PECVD.....	11
1.6.2. Aim and outline of this PhD thesis.....	14

1.1. Solar energy

“We are like tenant farmers chopping down the fence around our house for fuel when we should be using Nature’s inexhaustible sources of energy--sun, wind and tide. I’d put my money on the sun and solar energy. What a source of power! I hope we don’t have to wait until oil and coal run out before we tackle that.” — A fascinatingly sensed remark by the inventor Thomas A. Edison [1] in 1931.

Renewable energy, green energy, clean energy... all of these terms are becoming one of the most trending topics discussed nowadays, particularly after the Paris conference of parties COP21 in December 2015. Most renewable energies (solar, wind, hydro, biomass) are a direct or indirect product of the energy provided by the sun. They account only for ~19 % of the global energy consumption, as shown in Figure 1.

Presently, there is a strong international consensus for a transition toward renewable energy sources, away from fossil fuels (coal, oil and gas) that are till now the primary sources of energy consumption (78%). Environmental concerns are one of the most important drivers for this transition. Moreover, the incessant increase of the world population and the continual growth of energy demand highlight the problem of rarefaction of the non-renewable energy (fossil resources). All these factors motivated researches paving the way for photovoltaics (PV), in particular, to play a significant role in the future energy mix.

Figure 2 shows that the direct conversion of solar radiation into electricity with photovoltaic devices occupies the highest growth rate of renewable energy capacity in 2015 (28 %). Over the past ten years, the installed capacity of solar cells (PV) over the world is continually increasing: it has reached 177 GW in 2014 and 227 GW in 2015 as shown in Figure 3.

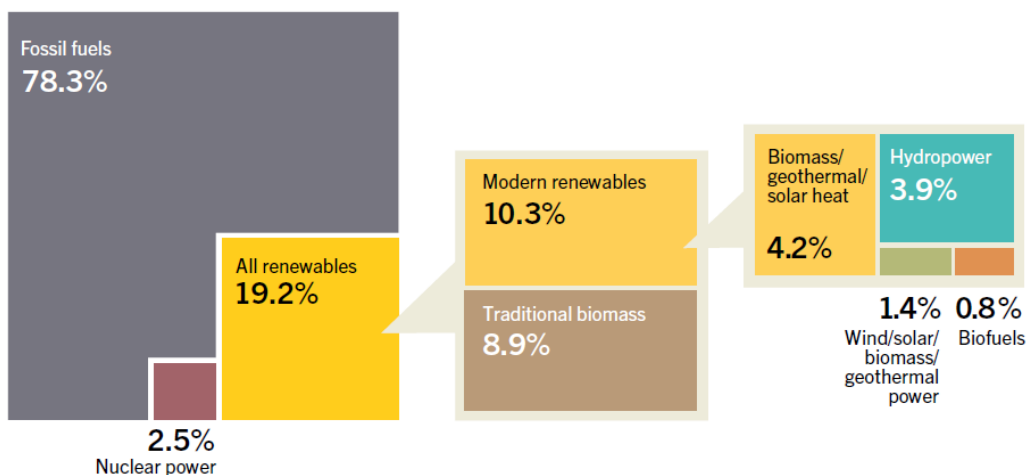


Figure 1. Estimated renewable energy share of global final energy consumption, 2014 [2]

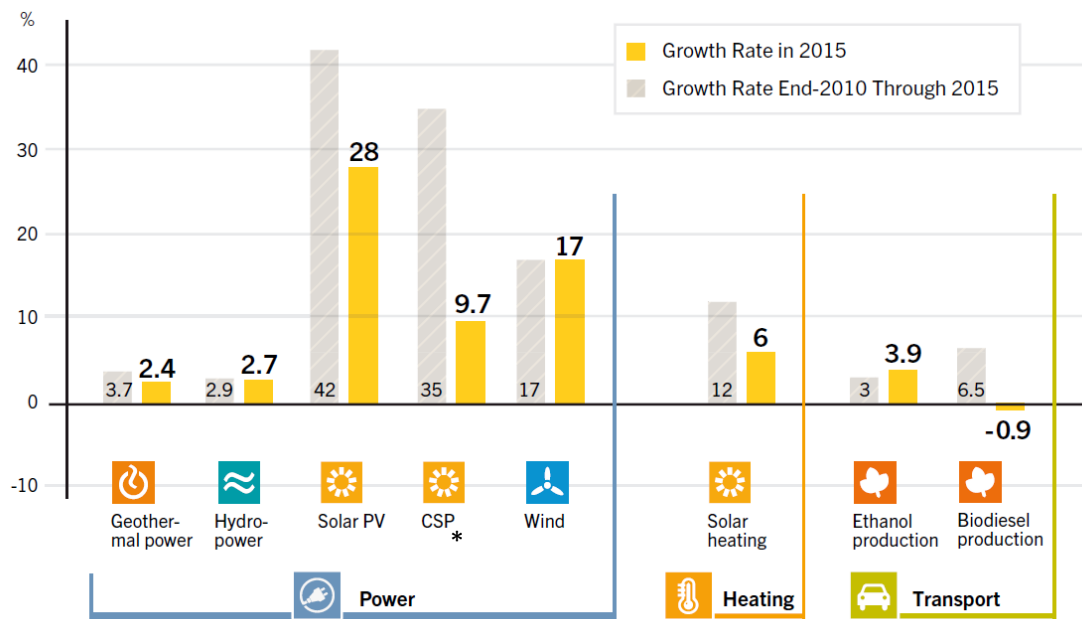


Figure 2. Average annual growth rates of renewable energy capacity and biofuels production from end 2010 to end 2015 [2] (*CSP for concentrating solar power).

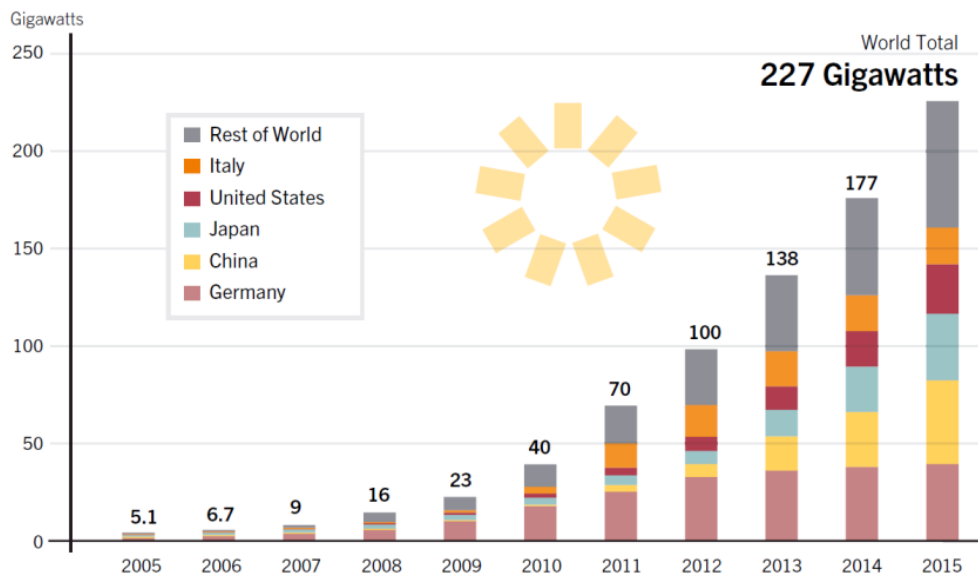


Figure 3. Solar PV global capacity, by country/region, from 2005 to 2015 [2].

The PV effect refers to photons of light (solar radiation) exciting electrons in a material into a higher state of energy and creating electron-hole pairs; the freed electrons are induced to travel through an electrical circuit thus powering electrical devices.

1.2. Silicon photovoltaic technology

The research on solar cells is vast; PV technologies can be separated into four categories:

- Silicon (Si) wafer, like monocrystalline and multicrystalline Si
- Thin films, like hydrogenated amorphous or microcrystalline Si, cadmium telluride (CdTe), copper indium gallium selenide (CIGS)
- III-V materials combining elements of columns III and V, like Ga and As, In and P
- Emerging PV materials, like organic solar cells, perovskites

The reader is invited to look at the famous NREL chart¹ time evolution for more information on the record cell efficiencies associated with each category.

Among all these technologies, the PV production is dominated by standard crystalline Si, as shown by the annual production share of different PV technologies in Figure 4. This fact is based on the abundance and non-toxicity of Si material besides the low cost of Si technology.

Solar cells based on Si material are split into two parts: crystalline Si and Si thin films. Crystalline Si (also called bulk crystalline) solar cells are based on monocrystalline or multicrystalline, 100-300 µm thick, wafers obtained by Czochralski or float-zone processes. They are cut from ingots which have been obtained by crystallization from the melt.

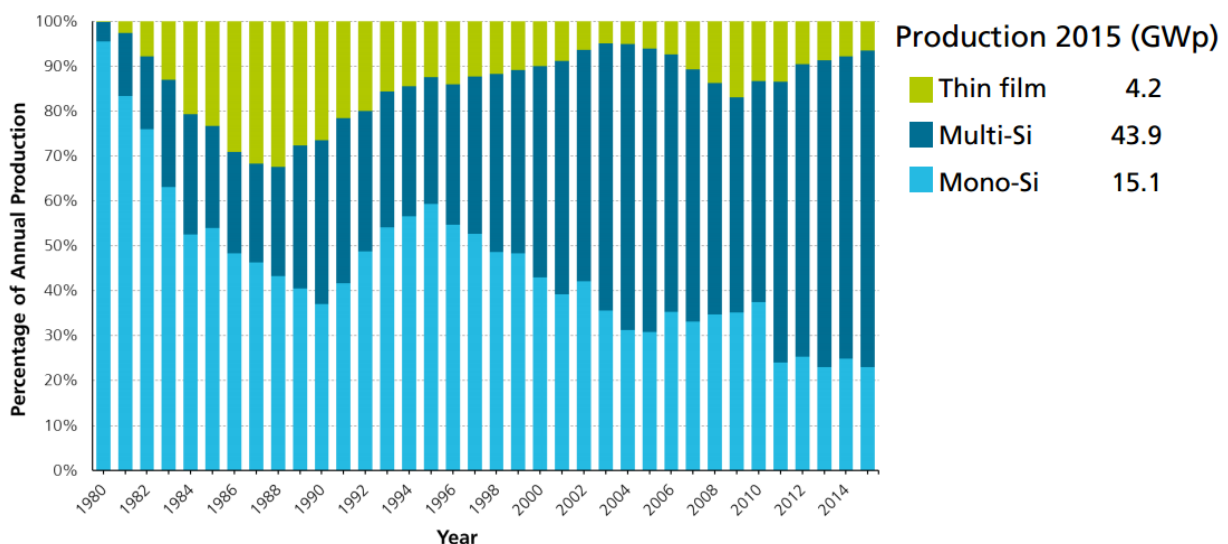


Figure 4. Market share of different PV technologies from 1980 to 2015 [3]

¹ Available on: http://www.nrel.gov/ncpv/images/efficiency_chart.jpg

Si thin films, typically from 300 nm to 1 μm thick, are directly deposited on substrates without a melting step. Silicon based thin film solar cells are low cost but less efficient than the Si wafer based solar cells [4]. Silicon photovoltaics industry is constantly trying to improve solar cells efficiency ensuring at the same time some cost reduction in order to stay competitive. Using thinner and thinner wafers is the general trend in crystalline Si industry [5]. A promising way for making very thin monocrystalline wafers is that provided by applying thin film techniques to crystalline Si growth through “epitaxy growth”. The epitaxial film can then be removed by “smart-cut” techniques and the substrate re-used for another epitaxy [6, 7].

Epitaxy refers to the process of growing a thin layer of material on a crystalline substrate in such a way that it continues the underlying crystalline structure. The word *epitaxy* derives from the Greek prefix *epi* meaning placed upon and *taxis* meaning arrangement or order. This word was first introduced by the mineralogist L. Royer [8]. There are two types of epitaxy: homoepitaxy where the film and the substrate are of the same material (like Si growth on Si) and heteroepitaxy where the film and the substrates are of different materials (like Si growth on GaAs). By extending the crystalline substrate with homoepitaxial growth, it is possible to have a superior crystalline quality and purity than that of the substrate, and an independent doping of the film; this is another reason why homoepitaxy is interesting. In the framework of this thesis, we aim at studying the growth mechanisms of homoepitaxy of Si thin films.

1.3. Low-temperature Si epitaxy by plasma enhanced chemical vapor deposition

1.3.1. Motivation

The commonly used processes for epitaxial growth are chemical vapor deposition (CVD) and molecular beam epitaxy (MBE), they either require high temperatures or ultra-high vacuum. For MBE deposition, which is one of the physical vapor deposition PVD techniques, an ultra-pure polycrystalline material is evaporated by an electron beam to produce a thin film. CVD is a method to grow solids from the decomposition of gaseous sources through chemical reactions; this is achieved, in the simplest and standard form, by the thermal energy of the substrate. Standard CVD processes result in high quality films with acceptable high growth rates (few $\mu\text{m}/\text{min}$ [9]) when high temperatures (between 800 to 1200°C) are applied.

When decreasing the substrate temperature, the growth rate decreases considerably, this is why, at low temperature, a diversity of excitation techniques is used for dissociating the gases, such as plasma enhanced CVD (PECVD), electron cyclotron resonance CVD (ECR-CVD) and hot wire CVD (HWCVD). Only the first technique is regarded in this manuscript as it was used for the deposition of our thin Si films in

epitaxial conditions. The specific PECVD epitaxial growth presented here does not involve high temperatures, neither ultra-high vacuum (in contrast to standard CVD and MBE) but operates at low substrate temperature (LT). The use of a plasma, produced by a RF power source in our case, is the key for LT-epitaxial growth to occur by dissociation of the gaseous sources or in other words by increasing the energy for chemical reactions.

Our motivation behind the use of PECVD at low substrate temperature has industrial origins. The p-type doped layers in Si thin film solar cells, necessary to separate electron-hole pairs in the absorber layer, are suggested to be grown directly from a low temperature process ($\sim 200^\circ\text{C}$) [10-12] instead of being produced by p-dopant² diffusion employing a high-temperature thermal annealing step (at $\sim 1000^\circ\text{C}$). The need to develop low temperature processes is driven by a strong interest in minimizing the thermal budget, not only to reduce the costs, but also to avoid some factors reducing the PV efficiency, such as the diffusion of impurities, precipitation of oxygen and crack formation.

In some cases and before finding the process conditions for the growth of the epitaxial doped layers, the growth of intrinsic layers is studied and optimized, in order to well separate intrinsic causes of epitaxy loss from those due to dopant. In the following section, we give a broad overview of epitaxy by LT-PECVD from publications in the literature.

1.3.2. History

Low-temperature epitaxial growth by PECVD was first studied by Japanese groups in 1987 [13, 14], using a substrate temperature as low as 250°C , in contrast to the previously used PECVD processes in the range of 750 to 800°C [15, 16]. While changing the difluorosilane (SiH_2F_2) flow rate from a plasma mixture composed of hydrogen, silane and SiH_2F_2 ($\text{H}_2/\text{SiH}_4/\text{SiH}_2\text{F}_2$ plasma), these groups observed a microcrystalline-to-amorphous growth transition and an epitaxial growth occurring in between. This change in the growth mode was linked to a competition between hydrogen and fluorine effects: H enhances the surface migration of precursors whereas fluorine extracts the excess bonded H through the formation of hydrogen fluoride (HF). It was found that epitaxy could be achieved thanks to a balance between these two effects. It was also reported that a high radio-frequency (RF) power plays a significant role in hindering epitaxial growth.

Later in 1989, epitaxial growth by LT-PECVD was achieved using a SiH_4/H_2 plasma chemistry, without fluorine, for temperatures between 150 and 300°C [17, 18]. It was attributed to a balance between deposition by SiH_x radicals and etching by atomic hydrogen. The authors explained that etching occurs through reactions generating volatile species and that it is more effective on unfavorable configurations

² Like boron

(more effective on amorphous Si than on microcrystalline Si). In their study, 10-nm sized and {111} oriented platelets were formed as a result of H incorporation in the epitaxial films, mostly through the dissociation of SiH₄. The ion bombardment energy was reported, in 1991 by another group [19], to play an important role in sustaining epitaxial growth at low substrate temperature. It was concluded experimentally that by optimizing the ion bombardment energy (about 25 eV), a compensation of the low adatom mobility—that normally prevents epitaxial growth at low substrate temperature—is possible and explains the establishment of epitaxy at such low temperatures (300°C).

The effect of the H₂ flow rate on epitaxial growth was studied in 1995 by Chen et al. [20] for a SiH₄/H₂ plasma chemistry. A high H₂ flow rate resulted in a microcrystalline growth, whereas a low one resulted in an amorphous growth, but optimizing this flow rate allowed an epitaxy to take place. Later in 1998, Rosenblad et al. [21] also stated that ion bombardment energy had a good effect on epitaxy by enhancing adatoms mobility (for an optimized energy), but a negative effect as well by inducing bulk damage and defects (for a too high energy). They evidenced the presence of an ion energy threshold (15 eV at a plasma pressure of ~ 10 mTorr) above which structural defects started to form in the epitaxial films.

The majority of the researches, published in the first decade of this century and investigating epitaxy by LT-PECVD, were carried out in the context of photovoltaic applications. Epitaxial growth was viewed as a negative event during the deposition of microcrystalline or amorphous Si thin films on clean (100) oriented Si substrates. Epitaxy was observed only at the very beginning of the growth, at the interface, and then disappeared with the formation of an amorphous or microcrystalline phase. A reduction of the passivation quality and a consequent decrease of PV efficiency were the results of such an accidental epitaxy [22]. PECVD epitaxy has also been studied by some groups such as Gohary et al [23], Mosleh et al. [24] and Shahrjerdi [25]. During the past ten years, LT-PECVD has been and is still a hot topic studied in LPICM in terms of deposition, characterization of amorphous, microcrystalline and epitaxial Si thin films devices and understanding [11, 26-28].

1.3.3. Some challenges

Low temperature epitaxy in PECVD environment is not yet clearly understood. Generally, the standard approach to explain Si thin film deposition is to consider the contribution of SiH_x or SiF_yH_z radicals formed in the plasma. However, there are many more species than radicals which can interact with the substrate and be the building blocks of the film deposition. There are positively charged ions that can reach the substrate and contribute to the deposition. More importantly, there are plasma synthesized particles, for some growth conditions, that can participate in the growth of the thin films. These particles were evidenced with the famous polymorphous Si [29] where crystalline particles embedded in an amorphous

matrix were obtained on glass substrates, as shown in Figure 5. All these species present in the PECVD environment make complicated the understanding of the growth conditions. The role of these species is discussed in this PhD work.

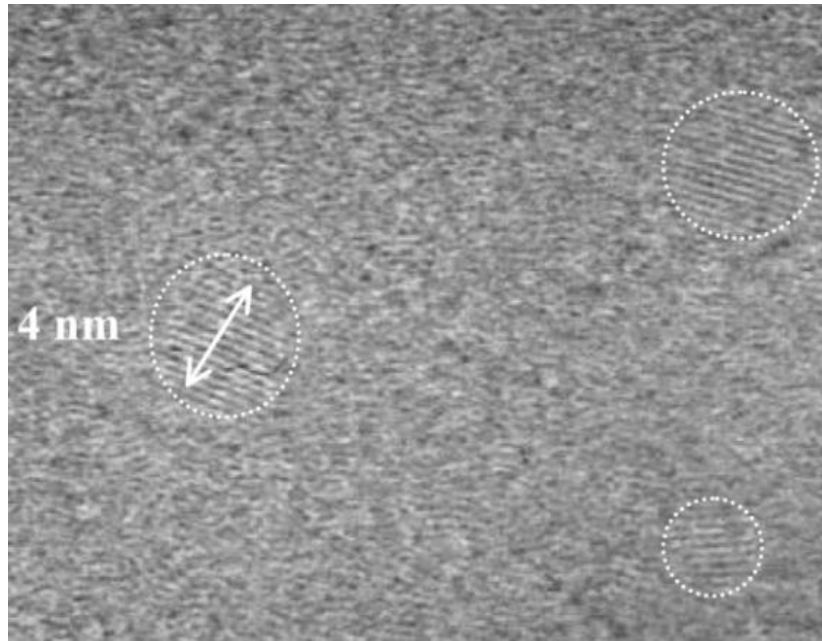


Figure 5. Transmission electron microscopy image showing crystalline parts embedded in an amorphous matrix:
this is polymorphous Si [29]

Several studies are ongoing at LPICM to face some challenges related to epitaxy by LT-PECVD growth in the framework of IPVF (Ile-de-France Photovoltaic Institute), such as the development of thin crystalline Si films (c-Si) with a high quality and high growth rates ($> 10 \text{ \AA/s}$), the development of p-type and n-type c-Si and the transfer of the epitaxial films to foreign substrates.

In order to increase the deposition rate, performing growth in the nanoparticles regime (regime where the nanoparticles are the main building blocks of the deposition) is suggested, as it was proved to lead to a radial growth rate of nanoparticles in the range from 75 \AA/s to 750 \AA/s using a pulsed discharge [30]. Such regime can be accessed by using special experimental growth parameters like a high pressure, a high power source and a high inter-electrode distance³. A product of pressure \times inter-electrode distance equal to 6 Torr.cm at a power density of 0.27 W/cm^2 is found to provide the highest growth rate associated with the nanoparticle regime [31]. Therefore, optimizing the growth parameters is

³ Distance between the RF electrode and the substrate holder electrode.

indeed a key to face these challenges and understanding the growth mechanisms seems to be essential for such optimization.

That said, the present study aims at investigating epitaxy by LT-PECVD in order to provide a better understanding of the growth mechanisms, this is done by correlating the growth parameters with the microstructure of the films. Transmission electron microscopy (TEM) is the main experimental tool of characterization in this thesis. Two plasma chemistries are studied and explored in this context.

1.4. SiF₄/H₂/Ar plasma chemistry

The SiH₄/H₂ plasma chemistry is commonly used for the deposition of hydrogenated amorphous or microcrystalline Si thin films by PECVD. Replacing SiH₄ with silicon tetrafluoride (SiF₄) mixed with H₂ and argon (Ar) has been suggested as an alternative chemistry to deposit such films. Some reasons are briefly given: firstly, epitaxy obtained using SiF₄ instead of SiH₄ resulted in higher crystallinity and lower defect density [32, 33]; secondly, a lower amount of oxygen was incorporated into the layers, thus facilitating the achievement of epitaxial growth [34].

SiF₄/H₂/Ar plasma was first introduced in LPICM to grow microcrystalline layers for thin film transistors (TFT) applications [35]. Several theses concentrated on this plasma chemistry: R. Brenot [36] made the first test using SiF₄, S. Kasouit [37] studied the growth of fluorinated microcrystalline Si and the transport mechanisms in it, and Y. Djeridane [33] investigated nanoparticles generation and their impact on the deposition of fluorinated microcrystalline Si. Then the study in LPICM of such plasmas turned towards photovoltaic applications and Si epitaxial growth on different substrates: crystalline Si and gallium arsenide (GaAs) (M. Moreno [26]) and FeNi₄₂ (A. Torres Rios [38]). Later on, J.-C Dornstetter [39] proposed a simple phenomenological model for the growth under such a complex plasma chemistry and studied the fabrication of solar cells using conditions corresponding to a transition between amorphous and microcrystalline Si. In his model, HF molecules formation was a key parameter that determined the structure of the films. It originates from the dissociation of SiF₄ and H₂ followed by the recombination of the F atoms with H atoms. This is the main difference that distinguishes SiF₄/H₂/Ar plasmas from SiH₄/H₂ plasmas where no F is present. Regarding Ar, it has been shown that it helps the decomposition of SiF₄ species. Motivated by the high quality microcrystalline thin film solar cells obtained by J.-C Dornstetter with SiF₄/H₂/Ar, M. Moreno [26] explored Si epitaxial growth using this plasma chemistry from an industrial photovoltaic perspective as well as for a fundamental knowledge. In this thesis, we characterize epitaxial films grown using this specific gas mixture, from a microstructural point of view using transmission electron microscopy (TEM). Epitaxial growth was achieved by R. Léal (PhD student at LPICM and Total) by tuning the plasma conditions to the same settings as for obtaining amorphous deposition on glass substrates.

In addition, we were interested in investigating the microstructure of Si thin films deposited by LT-PECVD using another plasma chemistry; the details of this plasma are given in the next section.

1.5. SiH₄/H₂/HMDSO/B₂H₆/Ar plasma chemistry

The window layer to a p-i-n solar cell device is generally a p-type layer that fulfils some basic requirements such as optical transparency (so a wide bandgap) to maximize the absorption of light in the intrinsic layer and at the same time, high electrical conductivity in order to form a high built-in voltage across the p-i-n junction. Among several p-type layers, p-type hydrogenated microcrystalline silicon oxide (p- μ c-SiO_x:H) [40] and p-type hydrogenated silicon carbide (p- μ c-SiC_x:H) [41] appear as promising materials in thin film Si solar cells since they could enhance absorption of light in the active material by providing reduced optical absorption and good electrical conductivity when used in optimized deposition conditions. Our group is exploring p-type hydrogenated microcrystalline silicon oxy-carbide (p- μ c-SiO_xC_y:H), a mixture of the two previous materials using a liquid precursor, the hexamethyldisiloxane (HMDSO, C₆H₁₈OSi₂), as an alternative to the conventional gaseous sources of oxygen and carbon. The structure of an HMDSO molecule is shown in Figure 6: it consists of two atoms of Si, one atom of oxygen and six methyl groups. In a process where both liquid and gaseous precursors could be equivalently used, the former were proved to be six-times safer to handle than the latter [42]. From a practical point of view, HMDSO is a liquid precursor at room temperature that can be more easily stored and handled in canisters, compared to the gaseous precursors stored in metallic cylinders at high pressure around 100 atm. Moreover, HMDSO is non-toxic and non-corrosive. That is why it is very beneficial to encourage its use as a precursor instead of toxic gaseous ones for photovoltaic applications [43]. HMDSO was used to grow SiO₂ thin films [44] and dielectric barriers [45] in the semi-conductor and packaging industry.

In previous studies between PICM and Air Liquide [46], it has been shown that HMDSO is an easy-to-handle precursor that enables to control the crystalline fraction, the refractive index and dark conductivities of the films in a certain range, simply by changing the flux of this molecule. The detailed investigation on the optical and electrical characterization of p- type layers grown from HMDSO on glass substrates showed that these layers are comparable with those deposited with CO₂ in terms of solar cell properties. The growth experiments in these studies (performed by Prabal Goyal during his PhD thesis) used a plasma chemistry composed of SiH₄/H₂/HMDSO/B₂H₆/Ar (B₂H₆ for diborane) and used glass substrates. In this manuscript, we explore the microstructure of films deposited using the same plasma chemistry but on crystalline Si substrates. Prior to deposition, the native oxide of the substrate was partially removed (in-situ) by a plasma treatment. The latter left a sufficiently clean surface that allows quasi-epitaxial growth to take place. In this particular case where epitaxial or defective epitaxial growth was unintentionally obtained, fascinating quasi-fivefold symmetric diffraction patterns were observed

all over several samples. In this manuscript, we deepened our study and focused on this quasi-fivefold symmetry observed for the first time in the case of this plasma mixture. We insist on the quasi fivefold symmetry because it is by seeing the fivefold symmetric diffraction patterns that we were attracted to discuss the twinning in this system. In fact, such symmetry was often observed on decahedral particles[47], but very seldom in bulk materials. It seems to us that this originality is worth mentioning. By the way, other growth conditions using other precursors lead to other form of epitaxy breakdown by twinning, with no quasi-fivefold symmetry. Later, we realized that some films deposited under epitaxial conditions using SiF₄/H₂/Ar plasma chemistry reveal quasi-fivefold symmetric electron diffraction patterns (EDPs) too, but after a certain deposited thickness of monocrystalline growth.

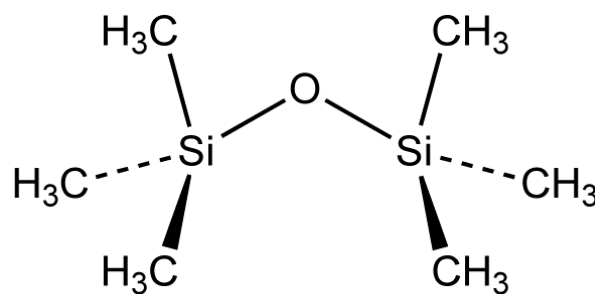


Figure 6. Structure of hexamethyldisiloxane (HMDSO)

1.6. Framework of this thesis

1.6.1. Focus on understanding epitaxial growth of Si thin films by LT-PECVD

The goal of this thesis is to deepen the understanding of the establishment of epitaxial Si growth by PECVD at low substrate temperature. We will try to give answers to some questions as:

- How can we describe the initial stages of epitaxial growth? Do nanoparticles play a role in the establishment of epitaxy?
- Which factors cause the loss of epitaxy by LT-PECVD? What are the paths used by the system to break epitaxial growth, when changing the H₂ flow rate or the RF power? What type of defects mostly characterizes epitaxy breakdown? Is there a general mechanism for the breakdown of epitaxy by LT-PECVD?
- How can we explain the observation of unusual quasi-fivefold symmetric EDPs? What are the probable reasons for multiple twinning in epitaxial samples? How can we estimate the number and the weight of twin operations from EDPs?

- What is the effect of changing the HMDSO flow rate on the microstructure of the films?

Before going into the details of this study, it seems important to remind some important definitions, keywords or basics.

The crystalline Si is a semi-conductor having a lattice constant of 0.357 nm and crystallizing in the diamond cubic crystal structure $Fd-3m$. The corresponding unit cell is shown in Figure 7: there are eight atoms on the cube corners (shared by eight cubes) and six on the faces (shared by two cubes) and four atoms inside: this makes eight atoms per cell. Each atom has four neighbors at the corners of a tetrahedron around it. Figure 8 displays the Si crystal viewed along the $\langle 110 \rangle$ direction. The Si interplanar distances of (d_{hkl}) corresponding to each family of planes characterized by Miller indices $\{hkl\}$ are displayed in Table 1.

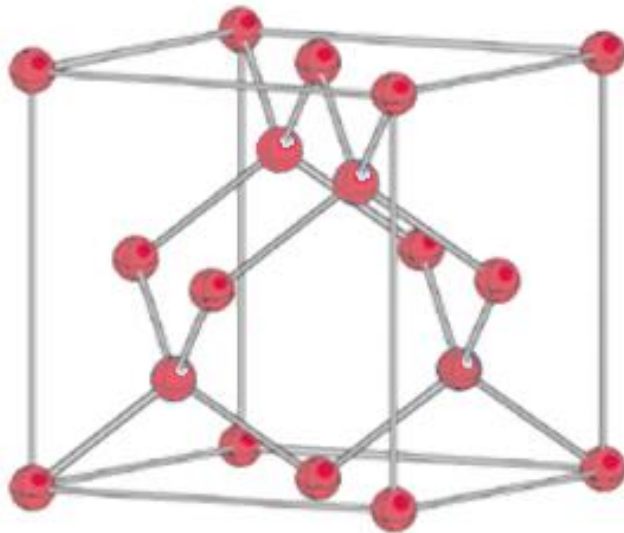
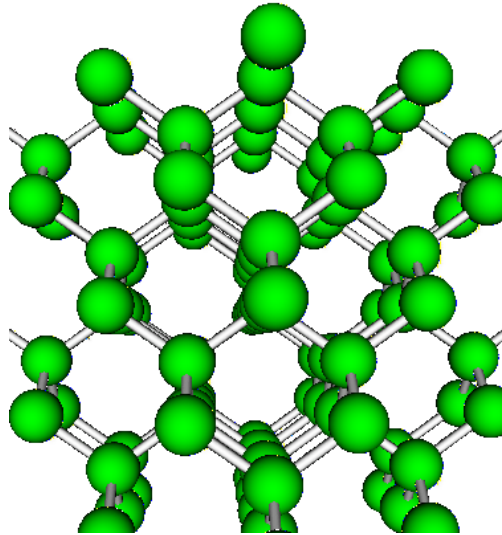


Figure 7. Diamond cubic crystal structure of Si.

Figure 8. Silicon crystal seen along the $\langle 110 \rangle$ directionTable 1. Interplanar distances (d_{hkl}) corresponding to low index families of planes $\{hkl\}$

d_{hkl} (Å)	hkl
3.138	111
1.920	220
1.638	311
1.357	400

In the case of diamond crystal structure (which is one type of face centered cubic crystal), the structure in a $\langle 111 \rangle$ direction is made up of an alternating regular ABCABC arrangement; where A, B and C correspond to $\{111\}$ planes (Figure 9). If a layer A is followed by a layer of misplaced atoms in the wrong position C, upon which a regular stacking appears again, the sequence ABCACB will form. In this case, the layer A is a mirror plane or a twin plane. In this way, twin defects may appear in a face centered cubic crystal. In other words, twins may form as a result of erroneously attaching atoms to a growing crystal such that two crystals then grow with a mirror symmetry about the $\{111\}$ (twin) plane which makes the boundary between them. Mirror symmetry in the cubic system has 23 equivalent by the symmetry operations including rotations of 70.53° about three $\langle 110 \rangle$ axis. This kind of defect is highlighted in this manuscript and some interesting effects of twinning are discussed. We present a type of crystal twinning that occurred naturally during crystal growth, therefore called “growth twinning”.

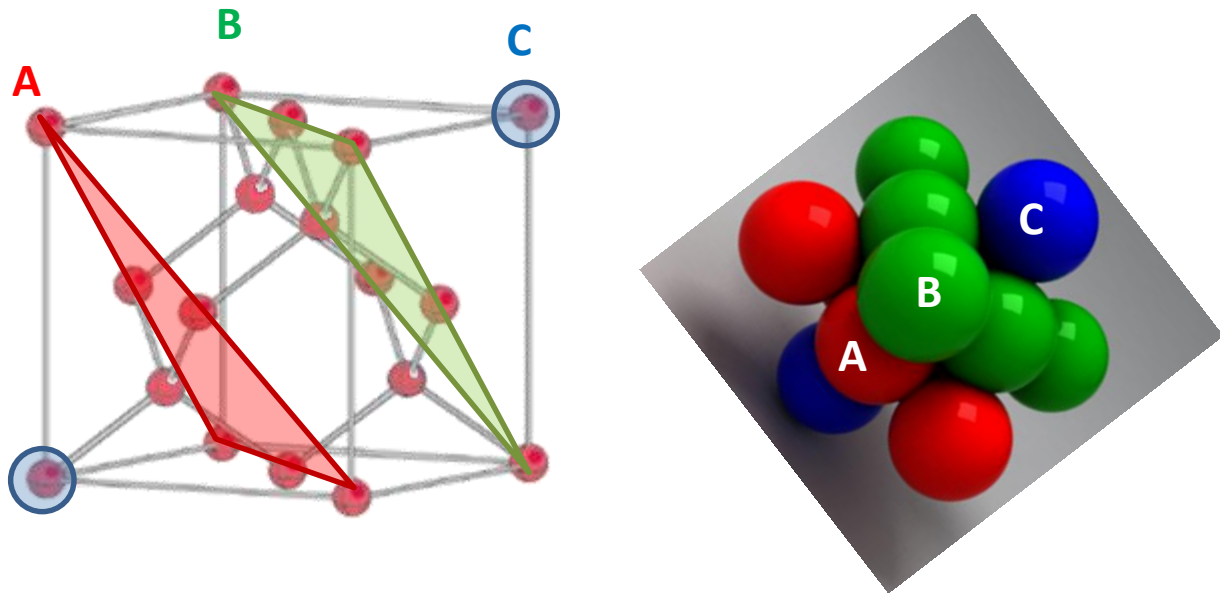


Figure 9. ABC stacking in a face centered cubic crystal

1.6.2. Aim and outline of this PhD thesis

After the general introduction and context of this PhD thesis presented in this chapter (**chapter 1**), we are going to focus on the topic of this work. **Chapter 2** describes the PECVD deposition technique and the reactors used for the growth experiments. It also introduces the characterization methods, in particular transmission electron microscopy, and gives highlights on our method for sample thinning using a fast polishing process.

In **chapter 3**, we give insight into the first stages of epitaxial growth by low temperature PECVD using $\text{SiF}_4/\text{H}_2/\text{Ar}$ and SiH_4/H_2 plasma chemistries with different reactors. On the basis of depositions performed on different types of substrates, we discuss the growth mechanisms behind the epitaxy. A transient regime is noticed from in-situ ellipsometry and from TEM imaging.

Chapter 4 gives answers to the path used by Si films to break epitaxial growth by LT-PECVD using $\text{SiF}_4/\text{H}_2/\text{Ar}$ plasma mixtures. By increasing the H_2 flow rate or the RF power source, we induced intentional epitaxy breakdown and investigated the evolution of the microstructure within a parametric study. Furthermore, by comparing our results with those of literature, we discuss the probable causes of epitaxy breakdown.

In **chapter 5**, we highlight on quasi-fivefold symmetric EDPs observed on samples deposited under epitaxy breakdown conditions using $\text{SiF}_4/\text{H}_2/\text{Ar}$ and $\text{SiH}_4/\text{H}_2/\text{HMDDSO}/\text{B}_2\text{H}_6/\text{Ar}$ plasma chemistries. We explained and attributed such unusual EDPs to a multiple twinning effect. We developed a simple

quantitative method to evaluate the number of twin operation from one hand and to estimate the weight of each twin order from another hand. Moreover, we discussed the probable reasons that drove the system to twinning. In addition, we suggested a model to explain the multiple twinning and so the formation of quasi-fivefold symmetric EDPs.

Finally, this doctoral work is summarized in the conclusion section, and perspectives are suggested for future work.

Chapter 2: Growth and characterization methods

2.1. Plasma enhanced chemical vapor deposition (PECVD).....	17
2.1.1. Fundamentals of PECVD.....	17
2.1.2. Brief description of the reactors.....	18
2.2. Characterization methods.....	20
2.2.1. Transmission electron microscopy.....	20
2.2.1.1. Introduction.....	20
2.2.1.2. Operation modes: image and diffraction modes.....	22
2.2.1.3. TEM techniques used in this thesis.....	24
2.2.1.4. Microscope specifications.....	25
2.2.1.5. TEM sample preparation method.....	25
2.2.1.6. Carbon-coated copper TEM grids and Si TEM grids used as substrates.....	30
2.2.2. Ellipsometry.....	31

2.1. Plasma enhanced chemical vapor deposition (PECVD)

2.1.1. Fundamentals of PECVD

In this section, we briefly describe some general basics of plasma enhanced chemical vapor deposition (PECVD), the growth technique used in this work.

PECVD allows one to deposit a variety of thin films at temperatures lower than those utilized in standard CVD reactors. It uses electrical energy, a radio frequency (RF) power supply at 13.56 MHz in our case, to generate a glow discharge or a plasma in which the energy is transferred into a gas mixture. In this mixture, electrons and ions are continually generated and lost by collisions and recombination. The RF power is applied to two parallel electrodes separated by a distance of a few centimeters. One of the electrodes is connected to the RF power through a matching box (to minimize the reflected power), and the other one is grounded, the latter is for most of the cases the substrate holder (Figure 10). The electrical energy dissociates the gas mixture and transforms it into reactive species: radicals, ions, neutral atoms and molecules, other highly excited species and even nanoparticles under some growth conditions. The ionization of the neutral species occurs via collisions with the electrons accelerated in the oscillating electric field. Since the formation of the reactive and energetic species in the gas phase occurs by collisions in the gas phase, we understand why PECVD does not require high temperature processes when using such a plasma (called capacitively coupled plasma) (Figure 10).

Electrons, being much lighter than ions, can be more easily accelerated; they reach the electrodes at each RF oscillation, which is not the case for the ions that have a too low mobility to follow the oscillating electric field. To compensate the electron loss and so to maintain the neutrality of the plasma, a static electric field appears in the sheaths (Figure 10), which tends to accelerate positive ions towards the substrate. The material deposition occurs via complex plasma-surface interactions, but only neutral and positive species can contribute to the deposition whereas negative species are trapped in the bulk of the plasma due to the repulsive forces of the sheaths.

If the area of the grounded electrode (A_{GR}) is larger than the one of the RF (A_{RF}), the discharge becomes asymmetric and makes the RF electrode negatively charged. This behavior is called self-bias or DC bias (V_{DC}) (the blocking capacitor in the matching box will allow a self-bias on the RF electrode). This will result in a potential distribution as represented in Figure 10.

A relationship has been established [48] between the electrode areas and their voltage drops as: $(V_{pl}+V_{DC})/V_{pl}=(A_{GR}/A_{RF})^q$ with q being close to 5/2. Thus, the reactors with symmetric electrodes have a self-bias that is roughly zero.

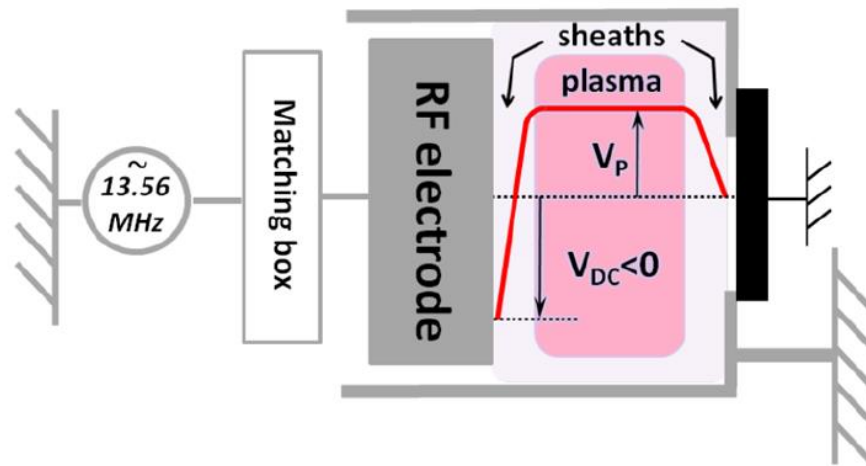


Figure 10. Schematic view of the potential distribution in a capacitively coupled plasma in a RF discharge. The substrate is grounded and the RF voltage is applied to the RF electrode, for most of the cases.

It is important to note that for the films deposited from $\text{SiF}_4/\text{H}_2/\text{Ar}$, the substrates were cleaned prior to loading into the growth reactors using an HF dip. This treatment was efficient to remove the native oxide. Whereas for the films deposited from SiH_4/H_2 or $\text{SiH}_4/\text{H}_2/\text{HMDSO}/\text{B}_2\text{H}_6/\text{Ar}$, the substrates were cleaned in-situ by a plasma treatment using SiF_4 or SiH_4/H_2 , respectively.

2.1.2. Brief description of the reactors

In the following, we briefly describe the PECVD reactors used for the growth of the samples presented in this manuscript. The growth experiments were carried out at LPICM by Prof. Pere Roca i Cabarrocas in ARCAM, Ronan Léal (PhD student) in CLUSTER and PHILIX and at Air Liquide by Prabal Goyal (PhD student) in PLASSYS CVD 300.

2.1.2.1. CLUSTER reactor

This is an industrial, symmetrical reactor with no plasma box and a relatively new system with six PECVD chambers (each one has an area of 225 cm^2) from MVSystems. One chamber is dedicated to $\text{SiF}_4/\text{H}_2/\text{Ar}$ plasmas and the other chambers are generally used to deposit the doped layers for solar cells. This reactor was used in this thesis for the very short depositions (12, 90 and 240 s) while investigating the initial film growth using $\text{SiF}_4/\text{H}_2/\text{Ar}$ plasma. A photo of this reactor is shown in Figure 11.

2.1.2.2. ARCAM reactor

This reactor is a laboratory-made PECVD reactor (see Figure 11). It was designed and built in the early 80's. A lot of details regarding the design of this reactor can be found in reference [49]. Additional

information as well as experimental results dealing with materials and devices produced can be found in reference [50]. This reactor can be described as a multiplasma monochamber reactor (each electrode has an area of 175 cm^2). The samples are located on a rotating plate which allows us to start the plasma on a first substrate or a blank sample and then continue the plasma on another substrate. In this doctoral work, this reactor was used for the study of the initial epitaxial growth: very short epitaxial depositions (few seconds) were performed for a plasma composed of SiH_4 and H_2 .

2.1.2.3. PHILIX reactor

This reactor is a laboratory reactor that was built for research. It consists of a monochamber RF capacitive reactor. A picture of the reactor is given in Figure 11. This is a geometrically asymmetric reactor (the smaller RF electrode has an area of 75 cm^2). It has a small cylindrical confinement box (10 cm in diameter) which is grounded and has several holes to allow for *in-situ* spectroscopic ellipsometry (SE). This reactor was used in this thesis for the investigation of epitaxial growth of Si thin films for a $\text{SiF}_4/\text{H}_2/\text{Ar}$ plasma, as well as conditions leading to a breakdown of this epitaxy.

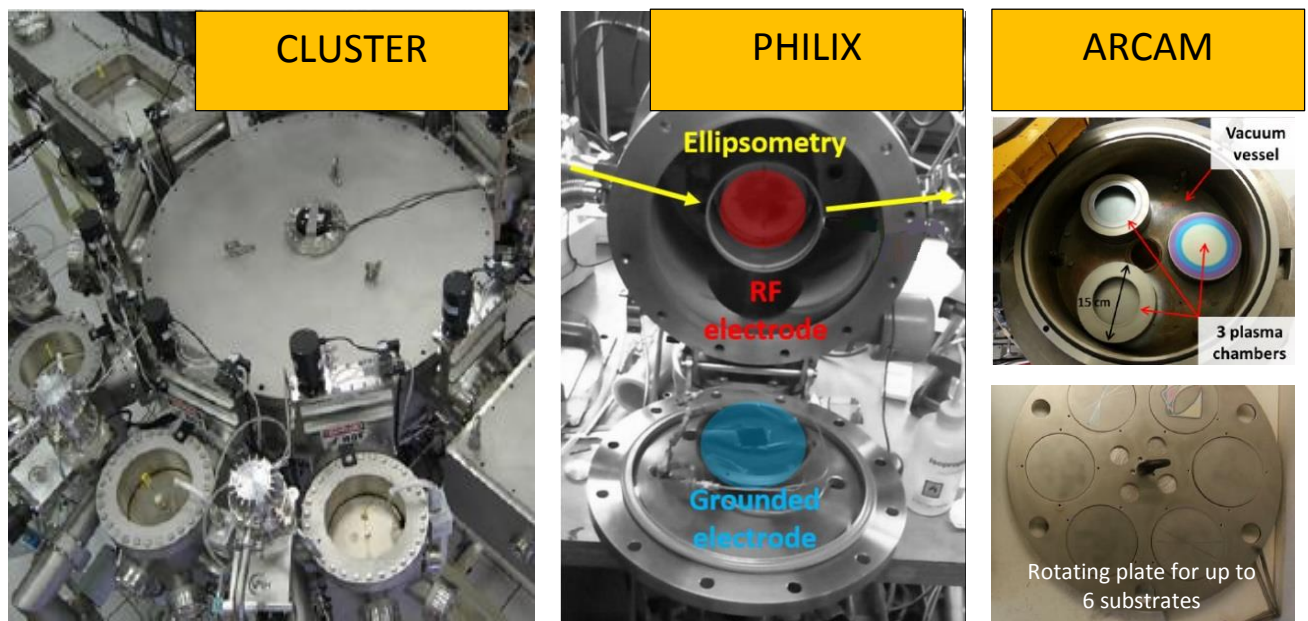


Figure 11. Photos of CLUSTER [51], PHILIX [31] and ARCAM [51] reactors located at PICM laboratory.

2.1.2.4. PLASSYS CVD 300 reactor

This reactor is a single chamber RF-PECVD system located at Air Liquide. It has a area of 176 cm^2 . This reactor was used for the deposition of "HMDSO layers" obtained by a plasma chemistry composed of: SiH_4 , H_2 , B_2H_6 , HMDSO, Ar. On these layers, we first found quasi-fivefold symmetric EDPs that were attributed later to a breakdown of epitaxy. More details on this reactor can be found in reference [52].

2.2. Characterization methods

2.2.1. Transmission electron microscopy

2.2.1.1. Introduction

Transmission electron microscopy is the main experimental tool of this thesis. It is a comprehensive technique that has an extraordinary ability to provide almost all of the structural, phase and crystallographic data of materials down to atomic levels. The basics of TEM are briefly presented in this section; the reader is invited to look at references [53-55] for more detailed information.

The TEM operates on the same basic principles as the light microscope but uses electrons instead of light. However, the electron microscope is much more advantageous from the point of view of spatial resolution. In fact, based on wave-particle duality, we know that electrons have wave-like properties and so can be characterized by a wavelength given by:

$$\lambda = \frac{h}{p}$$

where h is the Planck constant and p represents the momentum. If an electron is accelerated by an electrostatic potential drop U , the electron wavelength can be described as:

$$\lambda = \frac{h}{\sqrt{2m_0 eU(1 + \frac{eU}{2m_0c^2})}}$$

m_0 being the rest mass of the electron, e its charge and c the celerity of light. For a potential of 200 keV, the wavelength is 0.0025 nm. This means that the optimal resolution attainable for TEM images is many orders of magnitude better than that from a light microscope because the wavelength of electrons is much smaller than that of light. We remind that the resolution of a microscope is given by the Rayleigh criterion:

$$\delta = \frac{0.61 \lambda}{\mu \sin \beta}$$

where μ is the refractive index of the view medium and β is the semi-angle of collection of the magnifying lens. In the case of light, current collection angles give resolutions that are about one half of the wavelength. If similar angles were available with TEM, the resolution would be 1.25 pm for 200 keV electrons. However, collection angles are actually much lower in TEM, essentially due to the fact that the spherical aberration (which delivers a focus that depends on beam tilt) of magnetic lenses limits them to a few mrad. Thus a standard TEM, like the Jeol 2010 F used in this work, has a resolution of 0.23

nm. In a microscope with a corrector of the spherical aberration, the spatial resolution is limited by the chromatic and reaches 0.1 nm.

Even with these limitations due to aberrations, TEM can reveal atomic-scale details of internal structure and consequently it has emerged as the perfect tool to find out exactly what material we have made by a certain growth technique, and to know how perfect it is (and so to improve its synthesis). The TEM experiments performed in this thesis aimed at investigating the crystalline quality of layers deposited under epitaxy conditions, their structural defects, the interface sharpness, the chemical composition, the size of particles,...

Despite the advantages of TEM, it has some limitations:

- It provides very local measurements and only small area of the specimen can be examined
- Sometimes, the structural features can be modified by electron illumination
- TEM images represent 2D projections of a 3D specimen, and so misinterpretation of structural features is possible.

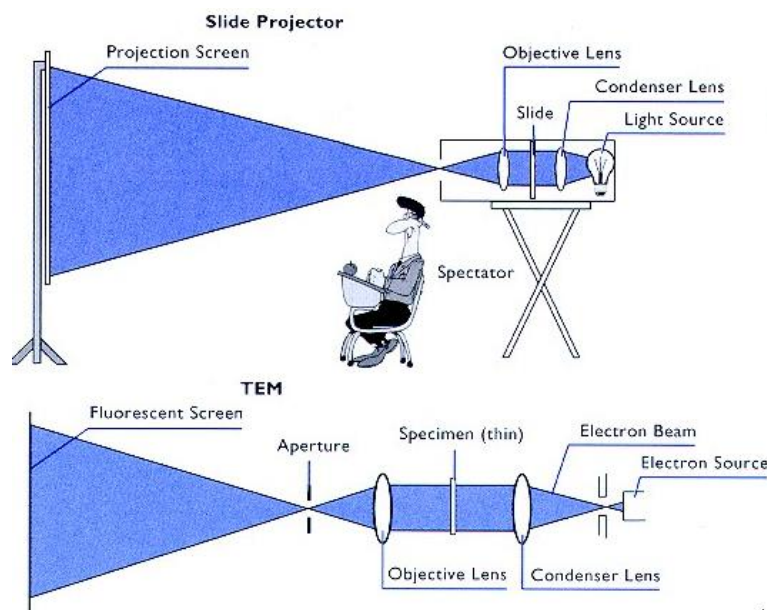


Figure 12. The transmission electron microscope compared with a slide projector

The transmission electron microscope can be regarded as a slide projector (see Figure 12). In a slide projector, light emitted from a light source is condensed into a parallel beam by the condenser lens; this passes through the slide (object) and is then focused as an enlarged image onto the screen by the objective lens. In the TEM, the light source is replaced by an electron gun, the glass lenses by electromagnetic lenses, the projection screen by a fluorescent screen and a digital camera and the slide by a thin specimen (less than 100 nm thick).

The optics in TEM consists of a more complicated system of lenses and apertures aligned along the optic axis. In fact, electrons emitted from the electron gun illuminate the specimen through a two or three stage condenser lens system. The electron intensity distribution behind the specimen is magnified with a three or four stage lens system (intermediate and projector lenses) and viewed on a fluorescent screen. The setting of those intermediate lenses provides the formation of either the image or the EDP of the specimen. The system is in a chamber under ultra-high vacuum. More details on the operating modes are given in the next paragraph.

2.2.1.2. Operation modes: image and diffraction modes

Transmission electron microscopy has two basic modes of operation that are illustrated in Figure 13 and distinguished by the strength of the intermediate lens:

(1) TEM image observation mode (also called projecting the image): in which a TEM image that is a magnified image of a specimen is observed on the screen. We can use low magnification or very high magnification, the latter provides high resolution images or even atomic-resolution images of a material. In this mode, we take the image plane of the objective lens as the object plane of the intermediate and projector lenses.

(2) Diffraction image observation mode (also called projecting the diffraction pattern): in which a diffracted electron beam image focused at the back focal plane of the objective lens is projected onto the screen and observed. So here, we take the back focal plane as the object plane of the intermediate and projector lenses.

The diffraction pattern of an amorphous sample shows diffuse rings, whereas a crystalline sample produces diffraction spots. These spots are formed due to the constructive interference between the diffracted beams according to the Bragg condition:

$$2 d_{hkl} \sin \theta_{hkl} = n \lambda$$

where d_{hkl} is the interplanar distance of a family of planes $\{hkl\}$, n is an integer representing the order of the diffraction, θ_{hkl} is the scattering angle and λ is the wavelength of incident wave (see Figure 14).

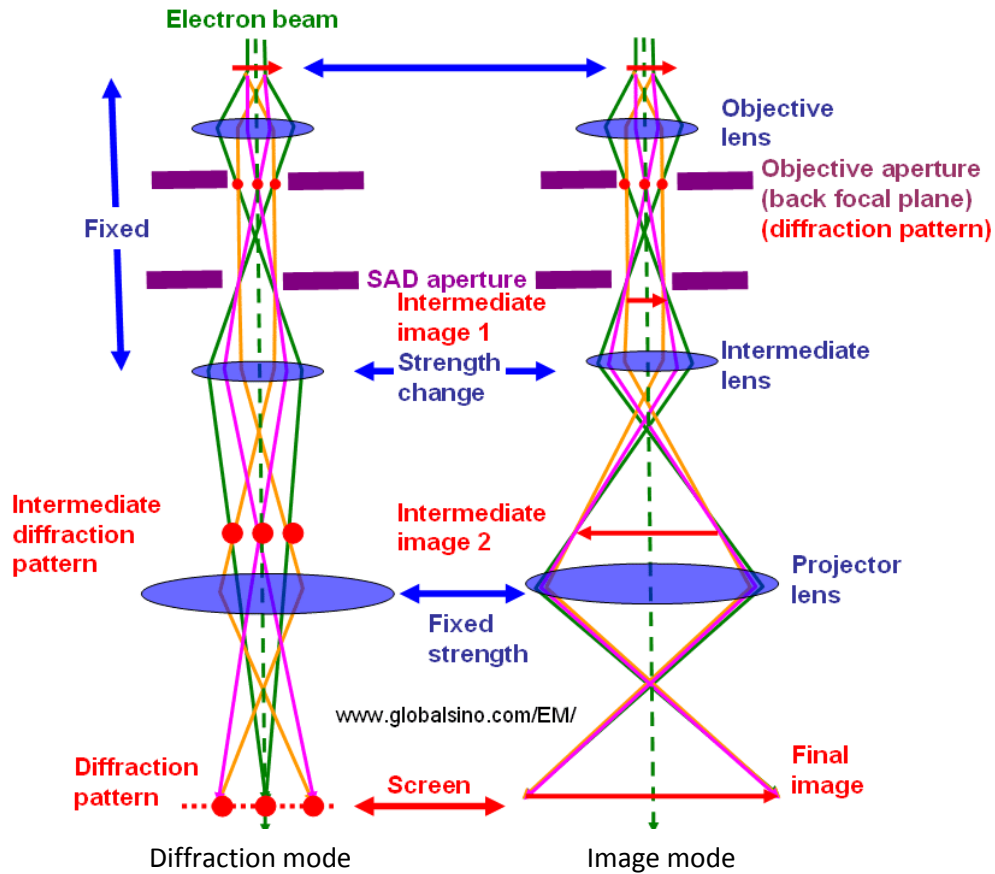


Figure 13. Schematic ray diagram showing a comparison of the lens conditions between diffraction and image modes.

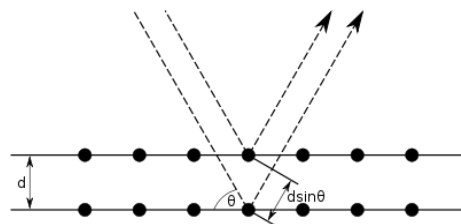


Figure 14. Bragg diffraction: two beams approach a crystalline solid and are scattered off two different atoms within it. Constructive interference occurs when the path difference between the two beams ($2d \cdot \sin \theta$) is equal to an integer multiple of the radiation wavelength. Note that, in the case of TEM, θ is of the order of a few mrad (≈ 1 degree)

The specimens under study have to be thin enough to allow electron transparency and so to transmit electrons such that enough intensity falls on the screen to give an image. In section 2.2.1.5, we present the details of the main thinning procedure we used in this thesis. The typical thickness of our cross-

section samples is around 45 nm (see an example in Figure 15) and sometimes smaller, down to 30 nm, as obtained from thickness map measurements (given by EFTEM imaging).

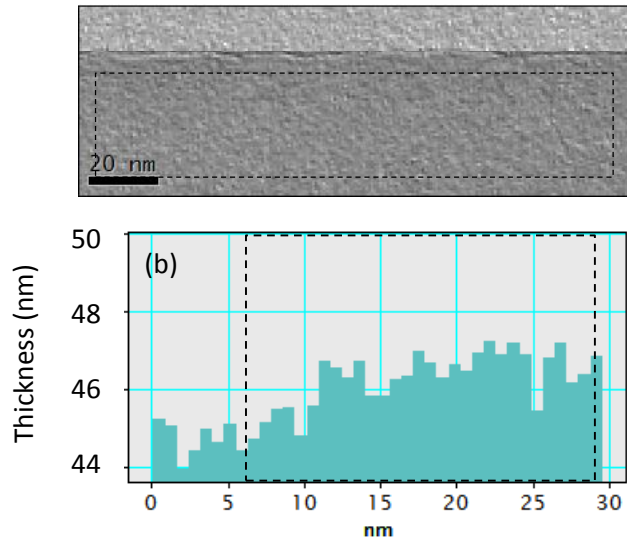


Figure 15. (a) Thickness map and (b) its profile for an epitaxial sample prepared by polishing and ion milling. The thickness of the sample is around 45 nm

2.2.1.3. TEM techniques used in this thesis

In this doctoral work, we used the TEM to characterize the structural details, with mainly:

- High resolution imaging (HRTEM)
- Selected area electron diffraction (SAED) (diffraction mode)
- Energy Filtered TEM (EFTEM): we used this method to perform chemical analysis by producing spatially resolved compositional or elemental maps of the area of interest. This TEM-based elemental analysis technique uses inelastically scattered electrons (or the electrons that have lost energy) to filter an image. The idea is to select or filter electrons of a specific energy coming through the spectrometer and form either an image or a diffraction pattern with them. The filters use a magnetic prism or magnetic sector where electrons with different energies are dispersed when passing through them. This delivers a spectrum where electrons are counted as a function of the energy they have lost. To maintain or reconstruct an image or a diffraction pattern, the filter also contains several magnetic lenses and multipoles. Moreover, using EFTEM, we evaluated the thickness map of the film, deduced from the ratio of the total beam intensity over that of elastically scattered electrons.

2.2.1.4. Microscope specifications

The microstructural characteristics of the layers were studied in the framework of the CIMEX (centre interdisciplinaire de microscopie électronique de l'Ecole Polytechnique) using a JEOL 2010F TEM (Figure 16), which has a Schottky field emission gun and a high resolution pole piece with a spherical aberration of 1.0 mm, and a direct maximum resolution dot to dot of 0.23 nm. The samples were analyzed at an operating voltage of 200 kV; the images were recorded with an Orius SC 200 or US 4000 camera from Gatan. This microscope is equipped with a Gatan Imaging Filter for electron energy loss spectroscopy (EELS) and energy-filtered TEM (EFTEM).



Figure 16. The JEOL 2010F microscope used in this doctoral work in the CIMEX.

2.2.1.5. TEM sample preparation method

2.2.1.5.1. Tripod polishing

The cross-section samples to be analyzed with TEM should be transparent to electrons – the region of interest must be less than 100 nm in thickness - and mechanically robust at the same time for handling. This makes TEM sample preparation a long procedure requiring time, caution, and extreme care to avoid any sample breaking. The following paragraph gives the details of the method we applied in this thesis for TEM sample preparation. This method is called the tripod polisher (based on reference [56]) where the specimen is mechanically thinned with a given wedge angle on a polishing wheel.

Before starting to polish, we first cut the sample, with a diamond tip, into slices ($\sim 3 \times 5 \text{ mm}^2$) and glue them face to face using epoxy (Figure 17). We put them in the furnace at 100°C for about 20 min to allow

the polymerization of epoxy. The next step is cutting them into thinner slices ($\sim 1.5 \times 1.5 \text{ mm}^2$) using a diamond wire saw (Figure 18). We then chose one free-of-damage slice - which will be called hereafter the sandwich - and glue it on the glass foot of the tripod polisher, using transparent wax. This preparation step before polishing is summarized in Figure 17.

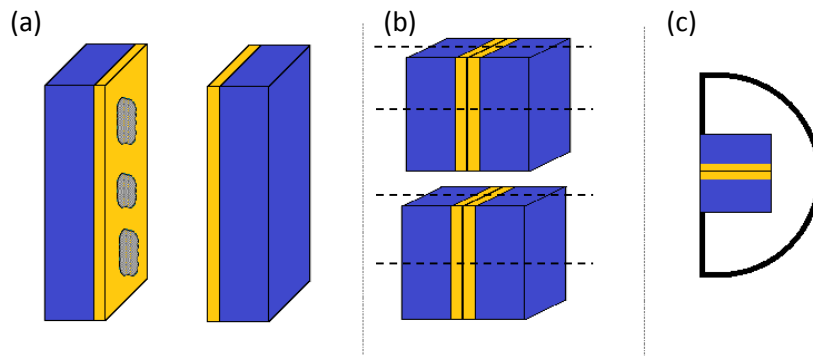


Figure 17. Procedure before polishing: (a) cutting the sample with a diamond tip into slices and glue them face to face, (b) cutting them into thinner slices (the dashed lines indicate further slicing) and (c) gluing one slice on the glass of the tripod polisher.

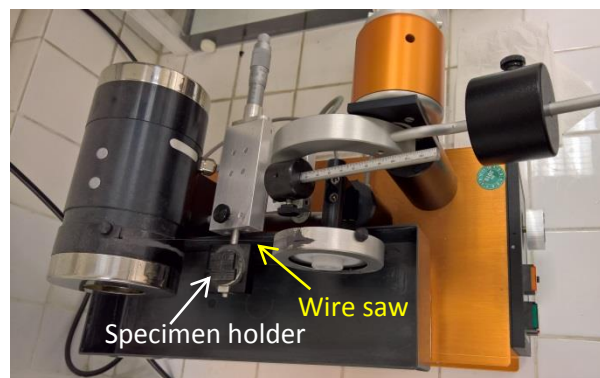


Figure 18. Wire saw system for a high precision cutting of a sample into small slices.

The main preparation step is the mechanical polishing, performed on both sides of the sandwich. Before polishing the first side, we adjust the feet of the tripod to guarantee the flatness of the sandwich with respect to the tripod, in order to limit inhomogeneity effects during the thinning. We start polishing using successive abrasive discs, carefully placed on the polishing wheel after verifying the absence of any bubble between the disc and the wheel. We first use the disc having a granulation size of $30 \mu\text{m}$, then 15, 6, 3, 1 and finally $0.5 \mu\text{m}$ (see Figure 19): we progressively move to smaller grain size after checking the homogeneity of the polishing and the absence of any scratch, using an optical microscope. We also use a high rotation speed for the biggest disc grain sizes ($\sim 30 \text{ rpm}$), in opposition to a small speed for the smallest ones ($\sim 10 \text{ rpm}$) to avoid the formation of cracks at the final steps of polishing where a special care must be taken.

Once the first side of the sandwich is polished, we reverse the sandwich upside-down in order to polish the second side. We repeat the same procedure, except that we tilt the tripod (and so the sandwich) of few degrees so that thinning occurs most importantly at one edge of the sandwich whereas the second edge stays relatively thick to ensure or facilitate the handling of the sandwich without breaking it. For this, we increase the height of the two feet micrometers opposite to the specimen. As long as we are polishing the second side of the sandwich, we periodically examine its thickness using optical microscope in order to change the abrasive disc into a smaller granulation size disc; we follow the instructions relating the sample thickness in the thinnest part with the grain size of the disc (see instructions in Figure 20). In general, we stop the second side polishing when a practical thickness less than 15-10 μm (by taking into account the thickness of the wax between the sandwich and the tripod) is reached or when interference fringes appear on the thinner edge of the sandwich. For this range of thickness, Si starts to transmit light in a progression of colors or even exhibits transmitted and reflected fringes.

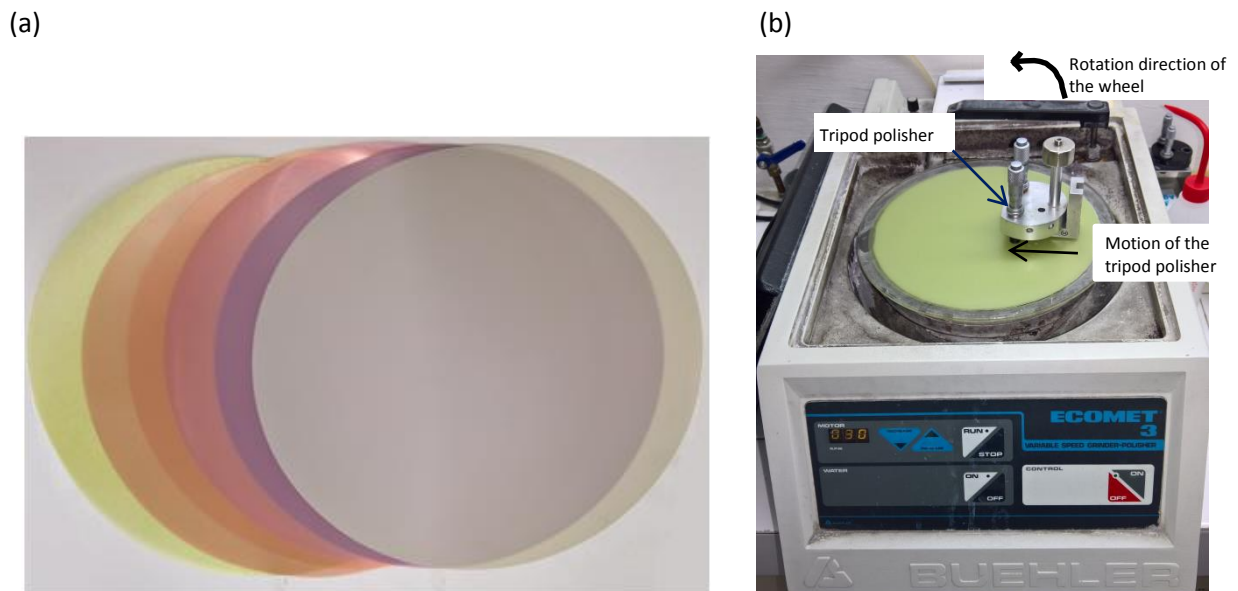


Figure 19. (a) Different abrasive disc, each one corresponds to a granulation size: 30, 15, 6, 3, 1 and 0.5 μm from left to right. (b) Polishing system



Figure 20. Each color corresponds to an abrasive disc characterized by its granulation size. Transitional thicknesses to move from one abrasive disc to another are: 125, 70, 35, 6, 3, 1 and 0.5 μm .

For a successful polishing, there are several secrets in using the tripod polisher:

- The abrasive discs must be very flat with no rays or scratches. In fact, we use the discs as long as they are clean, otherwise, a replacement should be done, especially for the second side polishing which is vulnerable.
- Before starting to polish each side of the sample, we put a puddle of water on the disc. In order to limit damage effects of the sample, we never go back to the same track on the disc (Figure 19), especially for smaller than 3 μm granulation size.
- We keep the glue line oriented perpendicularly to the polishing direction (see Figure 19(b)) to protect the thinnest part. Any deviation from perpendicularity can generate scratch lines which can spread from the interface and deteriorate the film, this should be avoided.
- If the thinnest part of the sandwich is not linear or presents important scratches forming a zigzag shape, we increase the tilt angle of the tripod in order to reshape the thinner edge. At this moment, the thinning is strongly concentrated on the bad edge which is quickly removed and instead a linear edge (desirable) is formed. Then we decrease the tilt angle as it was previously.

2.2.1.5.2. Ion milling using PIPS

Once polishing is done, we detach the sandwich from the tripod using acetone and we fix it on a copper slot grid (specimen support) for a subsequent thinning using argon ion milling in the PIPS (precision ion polishing system) machine (Figure 21).

Ion milling consists of bombarding the thin part of the sandwich with argon ions, and sputtering material from it until it reaches a thickness suitable for electron transparency. We used an energy ranging from 3.2 to 4.5 KeV with an almost grazing incidence (from 3 to 9°) and a rotation speed of 3.5 rpm. We did not use high voltages to minimize damage and preferential thinning and to limit phase transition (amorphization or crystallization). We positioned the two guns to deliver the beam on opposite sides of the sample (top and bottom).

In general, by applying these conditions, we were quite satisfied by the efficiency of this final thinning method since it required around 10 min for most of the samples prepared in this thesis. Apart from being a fast technique, one advantage of the PIPS stems from the ease it provides if we need further thinning: it just requires the insertion of the sample in the PIPS machine again. However, artifacts inherent to this preparation method exist: sometimes, some implantation occurred (or redeposition) so that the chemistry of the near-surface region is changed and the material is physically damaged; nevertheless, in such a case, we record TEM images far away from these damaged zones. For instance, a change concerning the structure in the near-surface region of the sample is shown in Figure 22. The crystalline

quality for all the images presented in this manuscript is conserved after sample preparation as proved by ellipsometry performed before and after specimen preparation.

TEM specimen preparation can be done using another method: instead of the polishing technique followed by ion milling, focused ion beam (FIB) can be used. Its advantages are the high position accuracy of the ion beam, and the low time consuming for one sample (about 4 hours). Its disadvantage is the radiation damages that make this method not applicable for certain samples and its high cost.



Figure 21. Precision ion polishing system

Amorphized region

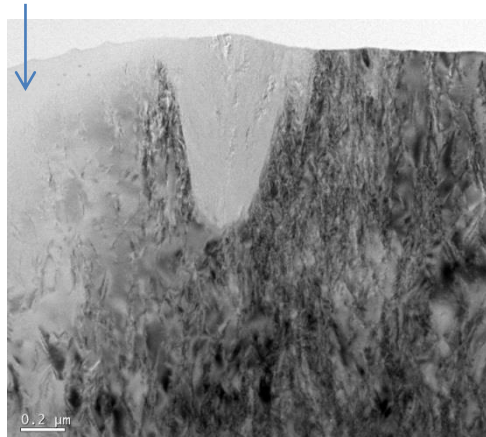


Figure 22. TEM image showing an amorphized region in the thinnest part as indicated by the arrow. The dark regions correspond to twinned monocrystalline domains.

2.2.1.5.3. Tripod polishing and ion milling as a fast and competitive preparation technique

During this doctoral thesis, we mainly used the polishing method followed by ion milling, but we developed an interesting method to limit the time required for specimen TEM preparation. For instance, to prepare six samples, a total maximum time of two working days (16 hours) is enough, and consequently, our technique (polishing and ion milling) becomes less time consuming than the FIB technique. Our method is based on creating a sandwich formed of three different samples or even four, depending on the total thickness of the films and the substrates (we are limited by the dimensions of the TEM copper slot grid). To reduce furthermore the time consumption during specimen preparation, we used to polish the first side of three or even four sandwiches at the same time, but we polished the second side of each sandwich individually because it is the most critical step of polishing. By doing so, the polishing technique becomes more advantageous than FIB from the point of view of productivity. In other words, we optimized the traditional mechanical polishing for TEM sample preparation, in such a way to transform it into a fast preparation method. Thanks to this achievement, the cheap tripod polishing method becomes competitive with the relatively expensive focus ion beam (FIB) technique.

2.2.1.6. Carbon-coated copper TEM grids and Si TEM grids used as substrates

Besides the use of (100) and (111) oriented Si wafers (and sometimes GaAs), TEM copper grids as well as single crystal Si TEM grids (Si (100)) were used as substrates. The advantage of these grids is that they do not require any sample preparation between growth experiments and TEM analysis (like polishing steps or FIB for film cross-section studies). These grids allow global plan-view imaging (averaged information can be extracted), but do not provide information on depth profile as cross-section samples.

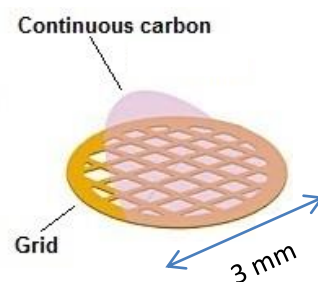


Figure 23. Copper grid covered by a carbon membrane

The carbon-coated copper grids are composed of a copper mesh with a holey amorphous carbon film on top of it as presented in Figure 23. The mesh defines a matrix, each element being a square of $40 \times 40 \mu\text{m}^2$. Within this square, TEM analysis can be performed. The amorphous carbon film is thin enough (15-

30 nm) to be transparent to the electron beam, the carbon contribution can be simply distinguished from the Si deposition by performing EFTEM or SAED.

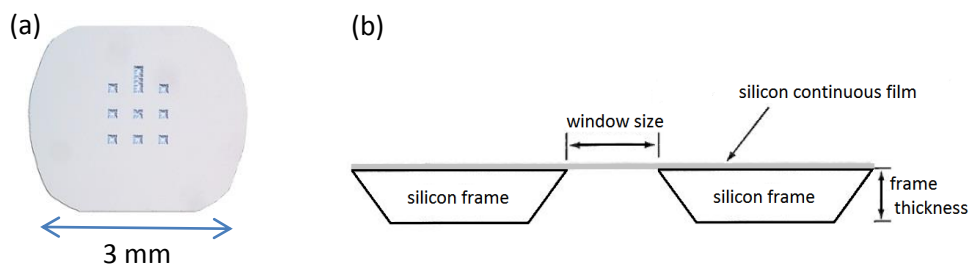


Figure 24. (a) Plan view and (b) cross-section view of the Si (100) TEM grid.

We also used Si (100) grids, which are a new type of TEM grids. To our best knowledge, no one has yet reported on the use of this type of grids. A Si (100) grid has a 100 μm thick frame and a 35 nm thick membrane in each of the nine TEM windows (see Figure 24). Eight windows have dimensions of 100 \times 100 μm^2 , and one has 100 \times 350 μm^2 . During the manipulation of this type of grids, we took a special care as the suspended membrane side of the window should never be placed onto another surface in the opposite “face-down” orientation.

2.2.2. Ellipsometry

Ellipsometry is a characterization technique based on the measurement of the state of polarization of light after reflection on a specimen. This is a non-destructive method which can be used for *ex-situ* and *in-situ* characterization as well.

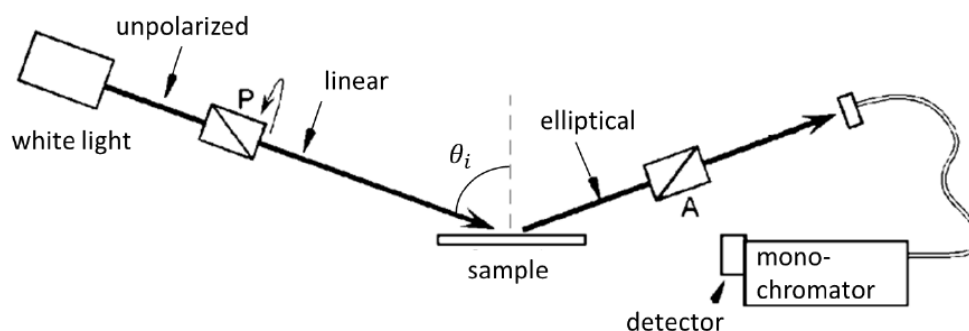


Figure 25. Schematic of ellipsometry principle [57]

Figure 25 shows a schematic explaining the basic principles of ellipsometry. An electromagnetic radiation is emitted by a light source, linearly polarized by a polarizer and is directed towards a specimen. After reflection, the radiation passes through a second polarizer (the analyzer), and finally reaches the detector. The incident and the reflected light can be separated into a component parallel (or p-polarized)

and perpendicular (or s-polarized) to the plane of incidence (the incident and the reflected beams span the plane of incidence). Consequently, two complex reflection coefficients can be defined:

$$r_p = |r_p| e^{i\delta_p} \text{ and } r_s = |r_s| e^{i\delta_s}$$

where $|r_p|$ and $|r_s|$ are the modulus of the complex reflection coefficient and represent the attenuation of the respective polarization ($r_p = \frac{E_p^r}{E_p^i}$ and $r_s = \frac{E_s^r}{E_s^i}$) and δ_p and δ_s represent the phase change of the respective polarization due to the reflection ($\delta_p = \varphi_p^r - \varphi_p^i$ and $\delta_s = \varphi_s^r - \varphi_s^i$).

The change in polarization is characterized by the ratio of the complex reflection coefficient

$$\rho = \frac{r_p}{r_s}, \text{ also written as: } \rho = \tan\psi e^{i\Delta} \text{ where}$$

$$\tan\psi = \frac{|r_p|}{|r_s|} \text{ and } \Delta = \delta_p - \delta_s.$$

The pseudo-dielectric function of the material can be obtained as:

$$\langle \varepsilon \rangle = \sin^2 \theta_i \left[1 + \tan^2 \theta_i \left(\frac{1 - \rho}{1 + \rho} \right)^2 \right]$$

where θ_i is the incident angle and ρ is deduced from the ellipsometric angles ψ and Δ . The pseudo-dielectric function is therefore a complex quantity, expressed as a function of its real and imaginary parts:

$$\langle \varepsilon \rangle = \langle \varepsilon_r \rangle + i \langle \varepsilon_i \rangle.$$

It is important to mention that it corresponds to the dielectric function of an infinitely thick material. More information on spectroscopic ellipsometry can be found in references [57-59].

In this thesis, we show the time evolution of the $\langle \varepsilon_i \rangle$ while studying the initial film epitaxial growth and while monitoring epitaxy before its breakdown (in-situ). The $\langle \varepsilon_i \rangle$ give us valuable information on the quality of the deposited film and particularly that measured at 4.2 eV provides information on the surface roughness. The epitaxial quality was proved by comparing the $\langle \varepsilon_i \rangle$ signal of a wafer after native oxide removal (generally by HF etching) with that of the deposited film. This was done by performing *in situ* and *ex situ* spectroscopy ellipsometry using "UVISEL" equipment from Horiba Jobin Yvon (Figure 26) or *in-situ* Woollam setup. In-situ ellipsometers could be mounted on PHILIX and CLUSTER reactors only.

Furthermore, measurements of thickness of thin films, roughness, and composition of materials can be extracted from modelling using the Bruggeman Effective Medium approximation (BEMA) [60]. The

approximation is based on the fact that the pseudo-dielectric function of a new material can be obtained from the dielectric function of the materials composing this new material.



Figure 26. Photo of the ex-situ experimental setup at LPICM

Chapter 3. Initial stages of epitaxial growth

3.1. Introduction.....	35
3.2. SiF ₄ /H ₂ /Ar plasma (CLUSTER reactor)	37
3.2.1. Evidence for the presence of a transient regime- long deposition.....	37
3.2.2. Short deposition on Si (100) wafers.....	41
3.2.3. Short deposition on TEM copper grids with carbon membrane.....	43
3.3. SiH ₄ /H ₂ plasma (ARCAM reactor)	46
3.3.1. Growth morphology on Si (100), GaAs (100) and Si (111) wafers - short depositions..	47
3.3.2. Short deposition on Si (100) TEM grids.....	49
3.4. Discussion.....	51
3.4.1. Hypothesis of growth mediated by atoms, radicals or ions.....	52
3.4.2. Hypothesis of growth mediated by plasma generated particles.....	56
3.4.3. Growth mechanisms: an open discussion.....	62
3.4.4. Effect of the substrate.....	64
3.5. Summary and perspectives	65

3.1. Introduction

At high substrate temperatures ($> 600^{\circ}\text{C}$), high quality epitaxy can be easily achieved thanks to the thermal energy of the substrate which is the main source of the adatoms mobility. However with PECVD, epitaxial growth has been reported at low substrate temperature ($\leq 300^{\circ}\text{C}$) [12, 24, 61], raising the question of how this epitaxy could be achieved in such growth conditions. In fact, for this range of temperatures, some additional energy besides the low thermal energy of the substrate has to be supplied in order to provide the adatoms with a sufficient amount of energy to overcome surface diffusion barriers, so that they are enabled to finally locate themselves at epitaxial sites. This additional energy can be provided by atomic hydrogen on the surface [24, 62-64] or by the ions bombarding the surface [19, 65]. From another point of view, several researchers highlighted on the role of the plasma generated particles and stated that they are the building blocks of the films. They explained the epitaxial growth by the melt of these particles upon the impact with the substrate and their recrystallization by occupying epitaxial sites. These studies were carried out in theoretical [66, 67] and experimental contexts [68]. Actually, an international consensus is absent on the epitaxial growth mechanisms of Si thin films grown by PECVD at low temperature and a number of investigations is being conducted to elucidate these mechanisms. In other words, there is still a *debate* whether the building blocks for such growth are atoms, radicals and ions from one hand, or plasma generated particles from another hand.

In an attempt to better understand how low temperature epitaxy (LTE) works, we suggest in this chapter to study the early stages of growth for Si films deposited by PECVD at $175\text{-}250^{\circ}\text{C}$. In fact, understanding the epitaxial growth of these films by PECVD requires, obviously, an investigation on the very beginning of growth. The best way for characterizing this stage is to follow instantly this growth. In this chapter, several series of short deposits were carried out, with deposition periods ranging between by few tens and few hundreds of seconds, in an attempt to build, in the absence of in-situ TEM, the TEM movie of the beginning of the growth. These experiments were made on different types of substrates: Si (100), Si (111) and GaAs wafers, TEM copper grids with carbon membranes and a new type of TEM grids composed of Si (100) electron-transparent membranes. The depositions on these grids allowed plan-view TEM investigations (no sample preparation was needed for these grids); whereas the depositions on the wafers were studied by cross-section imaging after TEM sample preparation.

Long depositions were done as well to investigate the structure and to check that epitaxy takes place for the applied growth conditions. Different reactors were used to carry these depositions in order to give a broad image of what is happening during the beginning of a PECVD growth, without being limited

by one reactor; for this, we used the CLUSTER and ARCAM reactors (see the details of these reactors and particularly the advantage of using ARCAM in chapter 2). In the CLUSTER reactor, SiF₄/H₂/Ar plasma chemistry was applied whereas in ARCAM, SiH₄/H₂ was applied. The reason for choosing two different plasma chemistries is to draw a general view on the early stages of epitaxial Si thin films at low temperature. Some depositions were characterized by in-situ ellipsometry measurements. The growth conditions for all the samples presented in this chapter are summarized in Table 2. In the following, the results using SiF₄/H₂/Ar plasma in CLUSTER will be presented firstly, and those using SiH₄/H₂ in ARCAM secondly.

By correlating TEM observations and ellipsometry measurements, we give evidence for the presence of a transient regime in the first stages of epitaxial growth. Furthermore, a discussion on the growth mechanisms is presented, based on two hypotheses: growth by nanoparticles and growth by radicals. We checked if the detection of nanoparticles on the substrates could be confirmed from our results, an affirmative answer would be a sign of the significant role of plasma generated particles in the growth mechanisms.

Table 2. Process conditions for the deposition of Si thin films leading to epitaxial growth in CLUSTER and ARCAM reactors.

Sample/ reactor	SiF ₄ /H ₂ /Ar or SiH ₄ /H ₂	Pressure (Torr)	Power density (W/cm ²)	Substrate tp / RF tp (°C)	Inter-elect distance (mm)	Deposit ion time (s)	Growth rate (Å/s)	Substrates
C1 CLUSTER	20/3/300	2.5	0.17	250/200	20	1800	0.24	Si (100)
C2 CLUSTER	20/3/300	2.5	0.17	250/200	20	12		Si (100)- Cu grid
C3 CLUSTER	20/3/300	2.5	0.17	250/200	20	90		Si (100)- Cu grid
C4 CLUSTER	20/3/300	2.5	0.17	250/200	20	240		Si (100)- Cu grid
A1 ARCAM	350/5	2.04	0.056	175/175	17	8	1.00	Si (100)- Si (111) GaAs (100)- Si grid
A3 ARCAM	350/5	2.04	0.056	175/175	17	20		Si (100), Si (111) GaAs (100), Si grid

3.2. SiF₄/H₂/Ar plasma (CLUSTER reactor)

TEM observations were made on cross-section and plan-view samples for long and short depositions. (100) oriented Si wafers and TEM copper grids were used as substrates after an HF dip. These grids were placed on the wafer by using Kapton tape; we assume that side effects related to the use of Kapton (desorption of Kapton) are negligible in the CLUSTER reactor because a good quality epitaxy is achieved. The depositions were done in the following conditions: SiF₄/H₂/Ar= 20/3/300, variable deposition time from 12 s to 30 min, a pressure of 2.5 Torr, a power density of 0.17 W/cm² (or 40 W), a ratio substrate to RF electrode temperature of 300/200°C and an inter-electrode distance of 20 mm (see Table 2). The growth was monitored by in-situ ellipsometry measurements in this case.

3.2.1. Evidence for the presence of a transient regime- long deposition

A relatively long deposition was performed in epitaxial conditions for 30 min (sample C1). A TEM image of this sample is presented in Figure 27, it shows a film thickness of 43 ± 9 nm with a defective interface and a rough surface. The island-shapes visible at the top of the film suggest that the growth has started in a 3D mode that did not hinder epitaxy over the first ~ 43 nm.

The high quality epitaxy is illustrated by the HRTEM image of Figure 28 which shows that the crystalline structure of the film is the same as that of the substrate (except for some defects at the interface). Moreover, it is clear from this figure that the nucleation in some parts of the interface is so perfect that a line has to be drawn to mark the interface. We can notice some defects at the film/substrate interface but also sometimes up to 7 nm underneath this interface, i.e. in the wafer. One of the defects seems to be a hydrogen-platelet defect [51, 69] which displays a leopard contrast (see the arrow in Figure 28). However, these defects are quickly healed, and then no stacking faults or dislocations are found in the film.

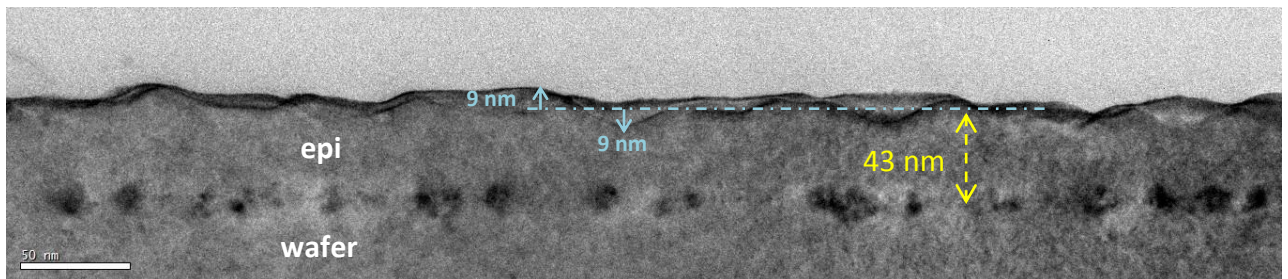


Figure 27. Cross-section TEM image of sample C1 (long deposition) showing defects at the interface and island shapes on top of the epitaxial film.

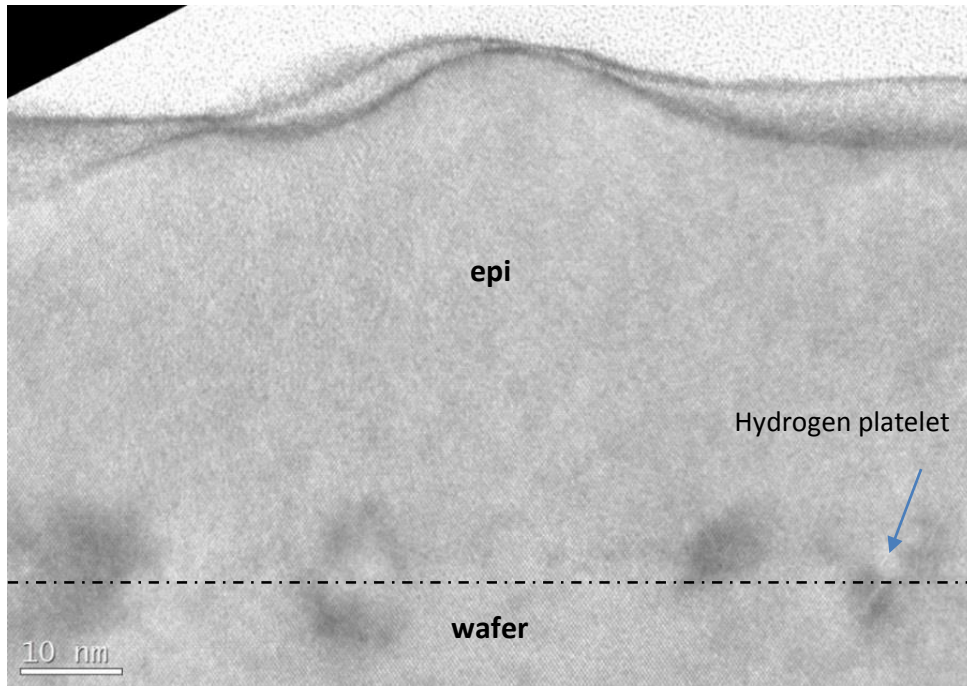


Figure 28. HRTEM image of sample C1 showing the high quality epitaxy.

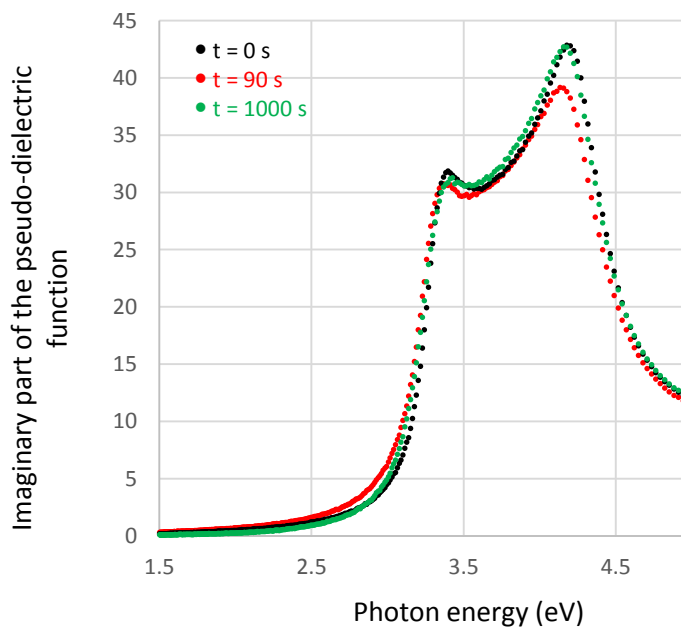


Figure 29. In-situ ellipsometry for deposition times $t=0$, 90 and 450 s. A minimum intensity at 4.2 eV is reached at 90 s, and then a stabilization occurs for $t \geq 1000$ s.

During the growth of this samples, in-situ ellipsometry was used to monitor the evolution of the imaginary part of the pseudo-dielectric function $\langle \epsilon_i \rangle$ versus time. Figure 29 shows the ellipsometry signal for deposition time $t = 0$ and for two critical deposition times where the maximum intensity of $\langle \epsilon_i \rangle$ at 4.2 eV has particular values. These critical times are 90 s where $\langle \epsilon_i \rangle$ reaches a minimum value of ~ 38 , and 450 s where $\langle \epsilon_i \rangle$ restores to its initial value where it stabilizes (~ 42) as shown in Figure

29. It is important to note that the peak at 3.4 eV undergoes smaller intensity modifications compared to the peak at 4.2 eV. Since the latter peak is the most sensitive peak to the surface state (the absorption depth at this specific energy is $\sim 4\text{-}5$ nm), its significant variation with time reveals a modification of the surface roughness happening in the early stages of the growth.

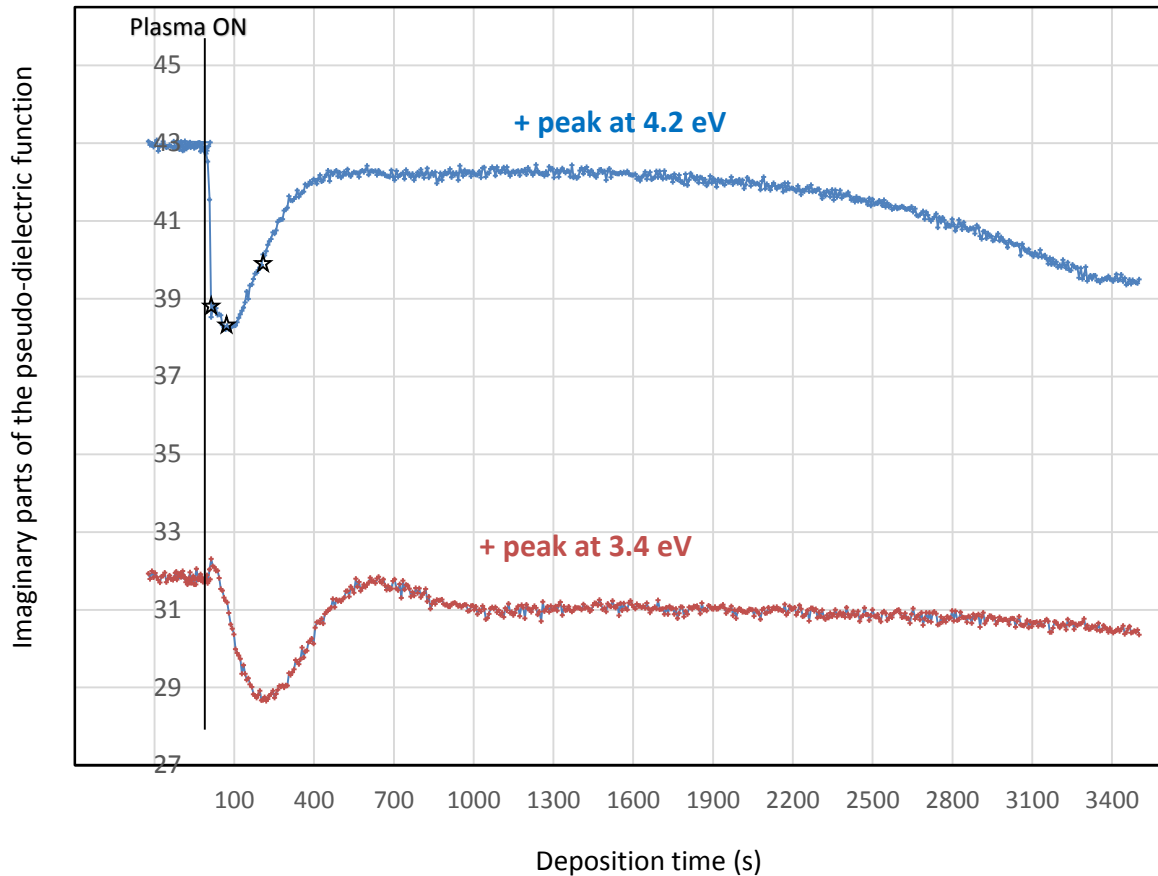


Figure 30. Time evolution of the imaginary part of the pseudo-dielectric function measured at 4.2 eV (in blue) and 3.4 eV (in red). The stars indicate where the growth was stopped for the TEM samples discussed in section 3.2.2.

Let us consider the peaks at 4.2 eV and 3.4 eV and study their evolution with time for a thicker sample deposited for 1 hour, as shown in Figure 30 (the acquisition time between two measurements is 6s). Interestingly, both signals reveal a transient regime before reaching the steady state regime where epitaxy is stable.

From this figure, one can notice that the peak at 4.2 eV decreases abruptly from 42.9 to 38.3 in the first 90 s of the growth, then increases and finally keeps a constant value around 42.2 between 450 s and 1700 s. Beyond the latter value, the signal shows a slow decrease indicating a progressive degradation of the surface quality (that becomes rougher most probably). The modification of $\langle \epsilon_i \rangle$ signal measured at 4.2 eV in the transient regime could be explained by a variation of the state of the surface, and more

precisely by a maximum roughness value reached at 90 s which decreases with deposition time in the transient regime. It is important to point out that $\langle \epsilon_i \rangle$ stabilizes for $450 \text{ s} < t < 1700 \text{ s}$ at 42.2, slightly lower than the value measured on the wafer at $t = 0$ (42.9), indicating that the surface of the film is rougher than that of the wafer after the HF cleaning.

On the other hand, the peak at 3.4 eV (which is more sensitive to the bulk properties of the wafer, given that its penetration depth is about 10 nm) exhibits an intensity decrease from 31.7 to 28.7 in the first 220 s of the growth, probably coming from a crystalline quality degradation in the bulk of the epitaxial layer or in the wafer, due to the formation of some defects (see Figure 28). A compensation for this decrease is observed till 680 s and the signal goes back to its initial value (31.7) before deposition. Next, the signal decreases slowly and stabilizes at 30.9 ($1000 \text{ s} < t < 1700 \text{ s}$). Further slow decrease is noticed beyond 1700 s, as for the peak at 4.2 eV.

An investigation on the transient regime will be carried on in the next section and an interpretation of the evolution of these signals will be presented in the discussion section.

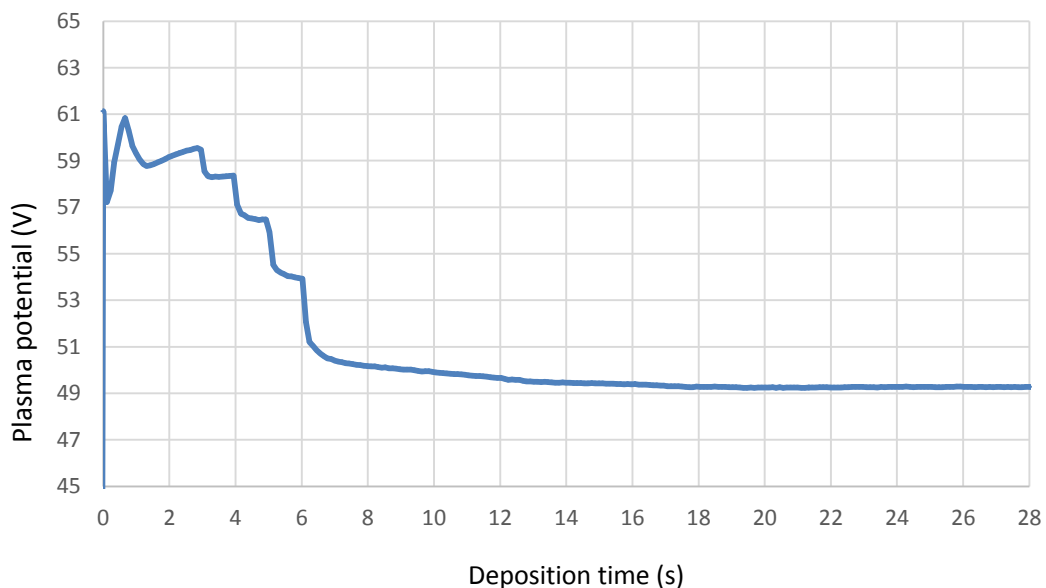


Figure 31. Evolution of the plasma potential with deposition time.

The presence of a transient regime was also detected in the evolution of the plasma potential with time, which is presented in Figure 31. The plasma potential shows variations then a drop in the first 15 s of the growth, followed by a stabilization at 49 V for $t \geq 18 \text{ s}$. This seems to be related to the plasma ignition. It is important to note that a problem in the matching box appeared while performing

depositions in the CLUSTER reactor, only for the initial film growth; this is responsible for the high plasma potential up to 61 V and so might generate some defects near the interface (this will be discussed in section 3.4). Let us remind that the $e.V_{pl}$ represents the maximal kinetic energy a positive ion can acquire when escaping from the plasma and impinging on the growing surface. It is important to note that the signal of Figure 31 was reproducible for all the studied samples.

3.2.2. Short deposition on Si (100) wafers

We are interested here in understanding the factors responsible for the variation of the ellipsometry signal in the transient regime. For this, HRTEM measurements were done on cross-section samples obtained at the deposition times of 12, 90 and 240 s (see the stars in Figure 30). We prepared these samples by focused ion beam (FIB) after protecting them with carbon and platinum layers deposited by evaporation. Figure 32 presents the TEM images corresponding to these three deposition times. We can make the following observations:

- The film grown at 12 s shows a rough surface presenting some islands that are associated with the start of film growth
- The film grown at 90 s shows a rougher surface and a higher density of islands. The islands (or hillocks) here are closer to each other than those at 12 s.
- The film grown at 240 s shows that the surface is getting smoother, this could be understood by the coalescence of islands.

Further investigations are done by performing HRTEM imaging to better illustrate the islands on top of the wafer during the first stages of the growth.

The HRTEM image of the deposit at 12 s (Figure 33 (a)) shows crystalline Si islands of 2 - 4 nm height on top of the wafer, making a rough surface. The already mentioned observations are obviously valid here and become more clear and visible. It seems therefore that at 12 s, these islands (or hillocks) occupy a small fraction of the surface that increases with time until full coverage at the end. Thus, TEM measurements are found to be in agreement with in-situ ellipsometry measurements, confirming the presence of a transient regime where the surface of the film presents a certain roughness.

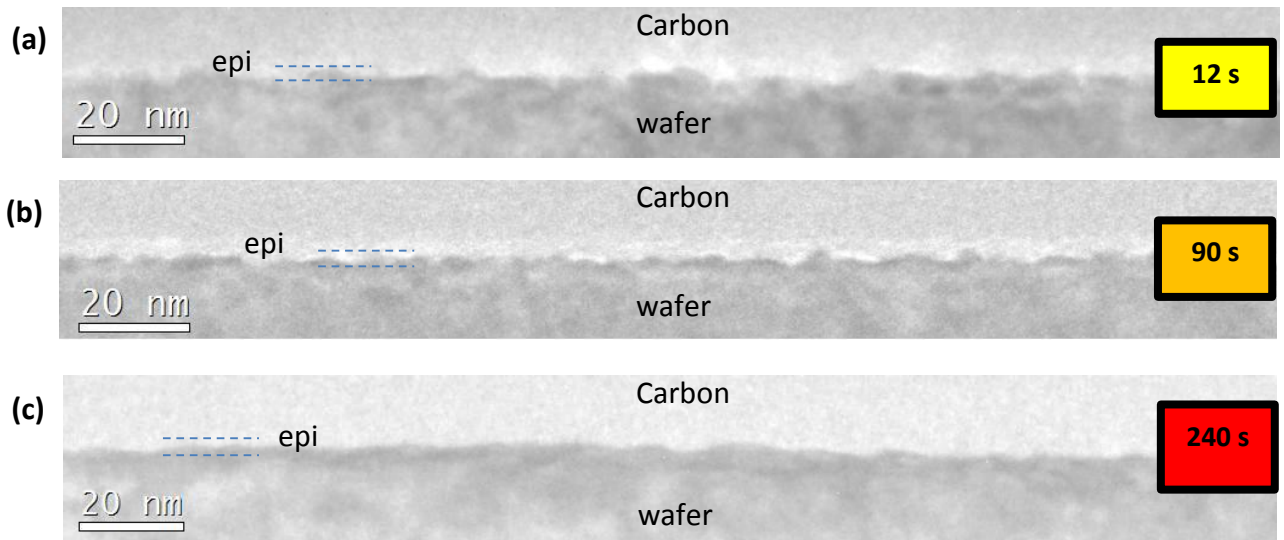


Figure 32. Cross-section TEM images of (100) c-Si wafers exposed to an epitaxial plasma for (a) 12 s, (b) 90 s and (c) 240 s.

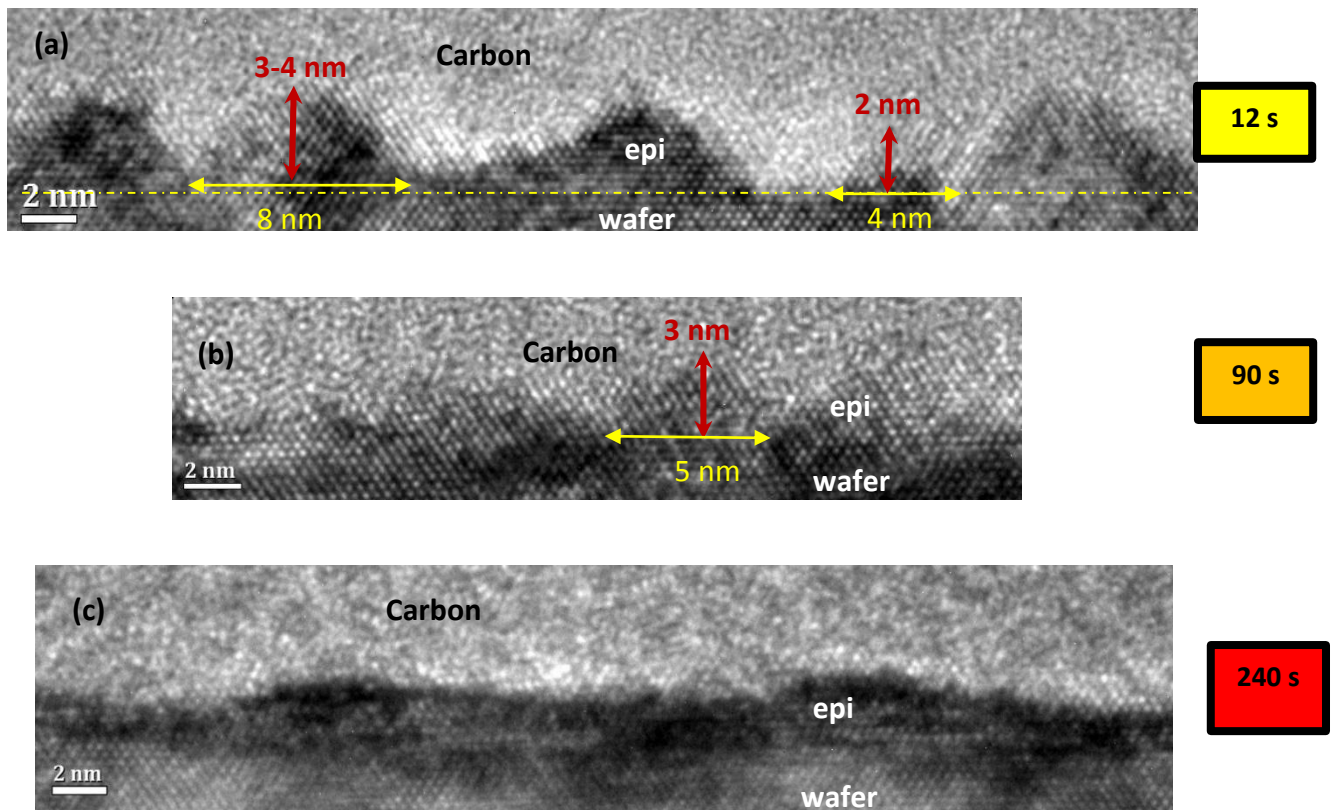


Figure 33. Cross-section HRTEM images of a (100) c-Si wafers exposed to an epitaxial plasma for (a) 12 s, (b) 90 s and (c) 240 s.

It is important to mention that the islands may have greater values of height just after deposition as some oxidation of the surface must have been taken place during air exposure, although the samples were kept in a nitrogen chamber before TEM sample preparation. Since the film/ substrate interface is hardly noticeable for these epitaxial films, we decided, for our next growth experiment in ARCAM

reactor, to make a co-deposition on a GaAs wafer which could enable us to distinguish easily the epitaxial layer from the wafer.

Briefly, we proved in this section that the first stages of the growth present a transient regime where the surface exhibits roughening in the beginning followed by a smoothing process. The TEM observations show that the islands on top of the wafer multiply until they coalesce, which is consistent with in-situ ellipsometry measurements.

3.2.3. Short deposition on TEM copper grids with carbon membrane

During the growth experiments, besides the use of Si wafers, TEM copper grids with carbon membrane were also used as substrates. Deposition on these grids enables plan-view TEM observations without the need of any sample thinning. In the following, we present the results of these observations.

3.2.3.1. General view of the deposition on the grids - continuous film

To provide an overview of the depositions on copper grids, we show TEM observations corresponding to the deposition for 90 s as an example.

At first sight, the carbon membrane seems to be covered by only few dark particles as shown in Figure 34(a) and Figure 34(b). However, by performing a chemical analysis using EFTEM imaging, we realize that an almost continuous but not homogeneous Si film covers the carbon membrane and especially the edges of the holes as shown in Figure 35(a) and Figure 35(b) representing the carbon and the Si maps respectively. These maps were combined in Figure 35(c) such that Si is illustrated in red and carbon in green. We remind that in such type of imaging (EFTEM), the white color means a high concentration of a specific element and the black means a low concentration or the absence of an element.

Concerning the crystalline quality of the deposition, a diffraction pattern was recorded on a zone of Figure 34(b) including particles, it exhibits diffused rings characteristic of amorphous Si and amorphous carbon, as indicated by Figure 34(c). In fact, we were expecting an amorphous Si deposition since the applied growth conditions correspond to epitaxial growth on a monocrystalline wafer (after native oxide removal) and to an amorphous growth on glass or on an amorphous substrate (here the amorphous membrane).

All this ensures that an almost continuous Si thin film grows on the carbon membrane, and that the principal feature of these experiments stems in this film and not in the particles that are visible in Figure 34(a) and Figure 34(b).

Now a question is raised concerning these particles: are they Si particles that escaped from the plasma and contributed to the growth? An answer is presented in the discussion section based on the comparison of our observations with literature. More investigation on these particles is presented in the next section to determine what information they can provide for a better understanding of the growth by PECVD.

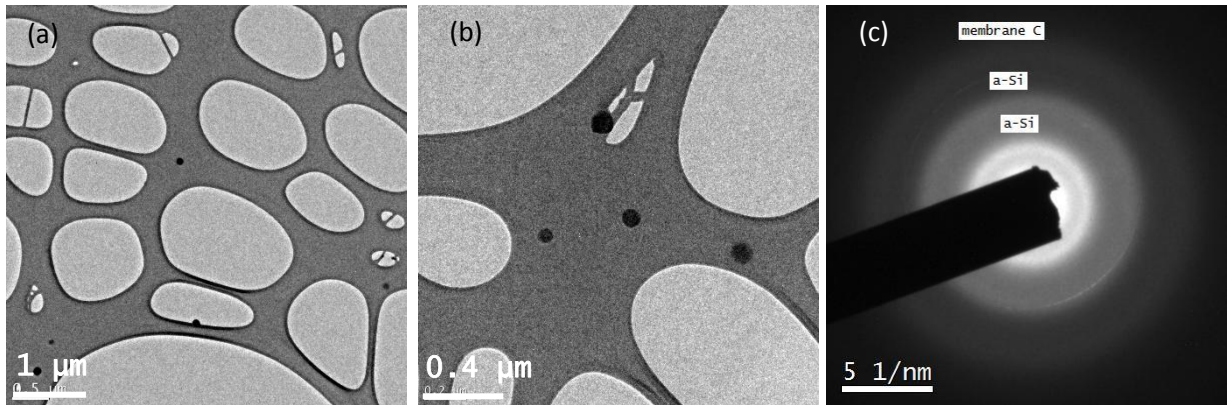


Figure 34. (a) and (b) Low resolution TEM images of the deposition on the carbon membrane (for 90 s). (c) Diffraction pattern recorded on a zone of (b) including the large islands.

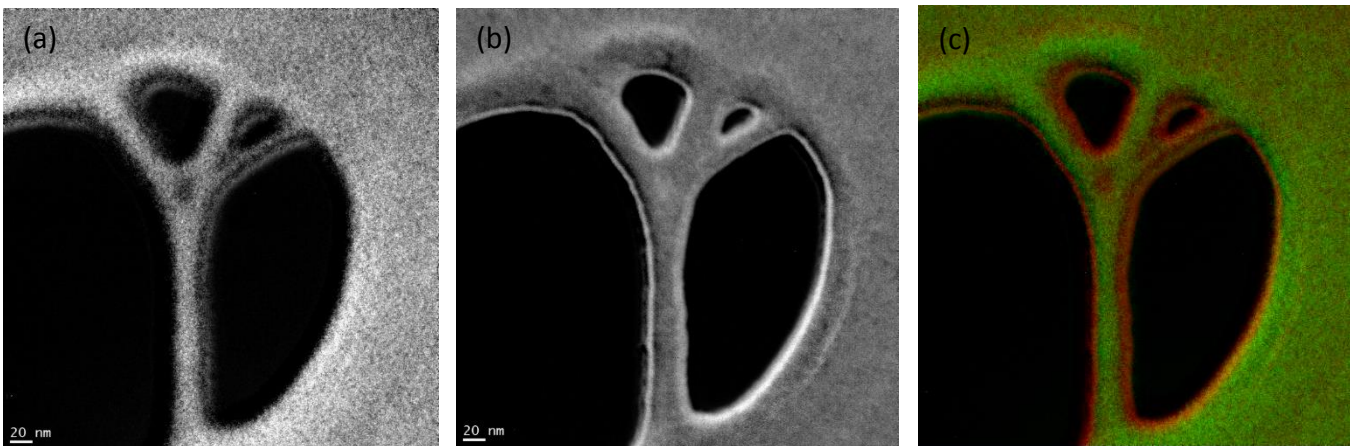


Figure 35. (a) Carbon map, (b) silicon map and (c) image combining silicon in red and carbon in green for the deposition on TEM copper grid for a deposition time of 90 s.

3.2.3.2. Aggregation of particles

TEM observations revealed the presence of aggregations of particles characterized by dendritic and quasi-dendritic shapes for $t = 12$ s (Figure 36 (a)) and 90 s (Figure 36(b)) respectively. The particles have dimensions of 15- 25 nm for 12 s and 25- 50 nm for 90 s. These dendrites are most likely formed

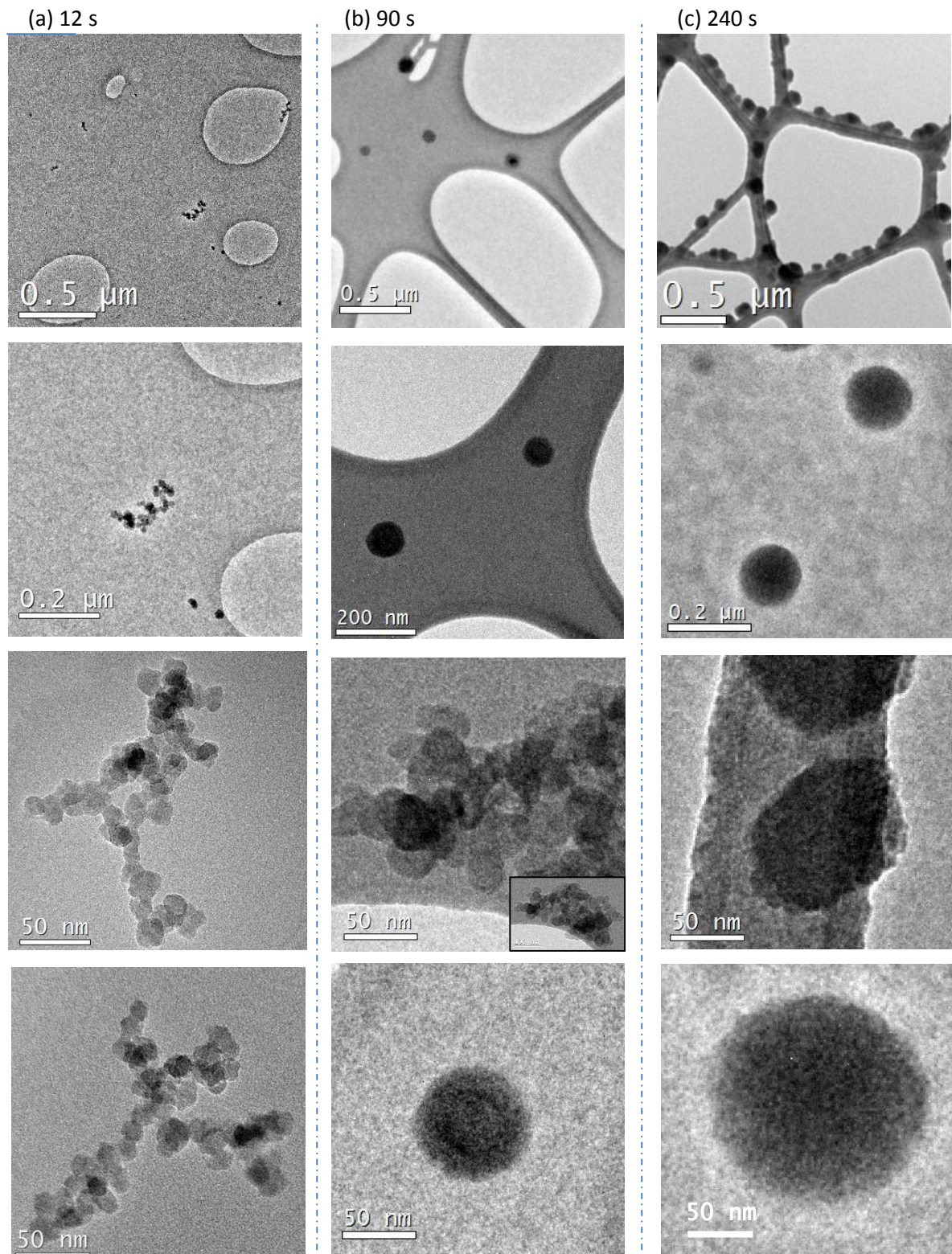


Figure 36. TEM images of the deposition on the carbon membrane corresponding to 12 s (a), 90 s (b) and 240 s (c). (a) shows dendritic aggregation of particles (with particle size of 12-25 nm), (b) shows spherical aggregation (~ 50 nm) and particles (~ 25 nm) aggregating in defective dendritic shapes and (c) shows big aggregates (110 - 200 nm).

as a result of a diffusion-limited aggregation (DLA) phenomenon [70] where the limiting step in aggregation is the diffusion of the particles on the substrate surface. In such conditions, the particles are considered to be in low concentrations so that they do not come in contact with each other until they reach a formed cluster, and the structure grows one particle at a time rather than by chunks of particles. Consequently, the dendritic shapes (or string of pearls) observed at 12 s indicate a low concentration of particles and suggest that the aggregation of particles took place at the surface of the membrane (or the continuous Si film) and not in the plasma. The whole picture suggests that the particles themselves are formed by the aggregation of atoms in the plasma, but remain there until the plasma is switched off. In other words, the two-dimensional formation of some aggregation (dendritic shapes) on the surface indicates that particles have arrived individually at the surface and assembled, rather than agglomerating in the plasma, which would result in a three-dimensional assembly of particles. We discuss later (section 3.4.2.2) why they would land on the substrate only at that time and diffuse on the film just grown. Dendritic shapes are absent for $t = 240$ s (particles size between 110 and 200 nm) where, instead quasi-spherical aggregates of particles are dominant, suggesting that larger aggregates were formed in the gas phase.

Due to the fact that the particles are not distributed in a homogeneous way on the carbon membrane (or on the Si film), estimating quantitatively the concentration of the particles in each case is complicated and not fair. It is important to point out that some of the dendrites were moving/vibrating under the electron beam during TEM experiments, suggesting their weak bonding with the continuous Si film (substrate). Let us note also that the islands visible on the top of the wafer in Figure 33 have a width in the order of few nm and should thus be hidden in the continuous film in Figure 36.

3.3. SiH₄/H₂ plasma (ARCAM reactor)

In order to study the very beginning of Si epitaxial growth, and check if a rough Si deposition is a general characteristic of such growth, our plan was to make short epitaxial depositions in SiH₄/H₂ plasma, other than the previous plasma chemistry. In LPICM, we have already found good process conditions of epitaxy using a SiH₄/H₂ chemistry in the ARCAM reactor. We wanted to check also if plasma generated particles could be detected and would thus be the building blocks for epitaxy.

TEM observations were made on cross-section and plan-view samples for short depositions on different types of substrates: Si (100), Si (111) and GaAs wafers, and Si (100) TEM grids. The use of GaAs wafers would facilitate the determination of the deposited thickness by distinguishing the wafer and the film. These grids were placed on wafers using special masks instead of using the Kapton tape. Prior

to deposition, the removal of the native oxide of the substrates was done in-situ by a SiF_4 plasma (with a flow rate of 30 sccm), at a power of 35 W and a pressure of 90 mTorr for 7 min.

The depositions were done in the following conditions: $\text{SiH}_4/\text{H}_2 = 350/5$, for deposition time of 8 s, a pressure of 2.04 Torr, a power density of 0.056 W/cm^2 (or 10 W), a ratio substrate to RF electrode temperature of 175/175°C and an inter-electrode distance of 17 mm (see Table 2). In-situ ellipsometry measurements were not made in this case because the reactor is not adapted for that; we chose growth times based on our previous experiments using the CLUSTER reactor and the known deposition rate for the conditions in the ARCAM.

3.3.1. Growth morphology on Si (100), GaAs (100) and Si (111) wafers - short depositions

The films deposited using a SiH_4/H_2 plasma exposure of 8 s in the ARCAM reactor are shown in Figure 37, Figure 38 and Figure 39 for Si (100) wafer, GaAs (100) wafer and Si (111) respectively.

The TEM observations on Si (100) wafer (Figure 37) do not allow us to decide whether a deposition has taken place on Si (100) substrates or not, there is no visible interface that could distinguish the film from the substrate. In fact, we were aware of this problem; that is why we performed, in parallel to deposition on Si wafers, heteroepitaxial growth on (100) oriented GaAs wafers which would offer a visible difference of contrast between the film (Si) and the wafer (GaAs). Epitaxy is possible in the latter case due the reasonable lattice mismatch between GaAs and Si (~4 %).

According to Figure 38, the films grown on GaAs exhibited a three-dimensional growth mode (3D) characterized by islands of 3-5 nm in height. It is thus reasonable to state that the deposition on Si (100) has a quasi-two-dimensional growth mode (2D) or an almost smooth surface. In this case,

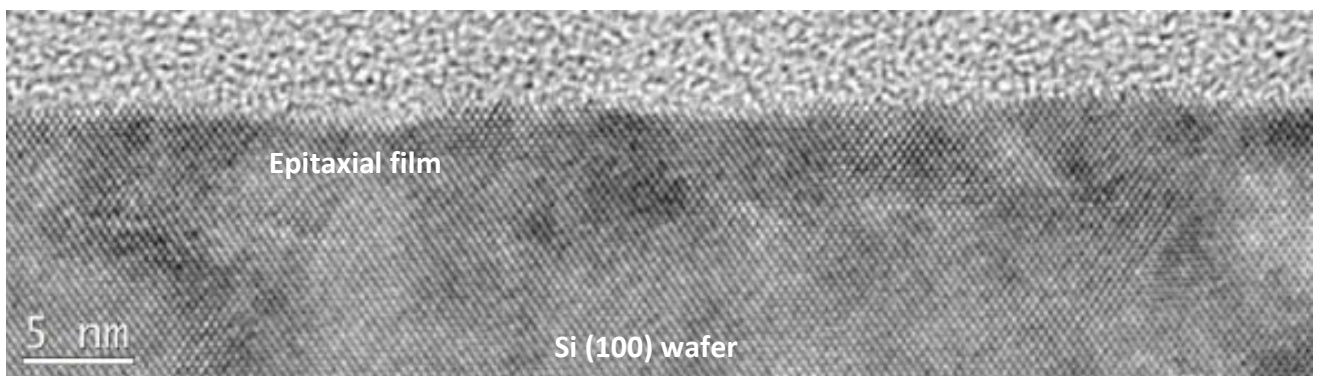


Figure 37. TEM image showing the growth on a Si (100) wafer for deposition time of 8 s.

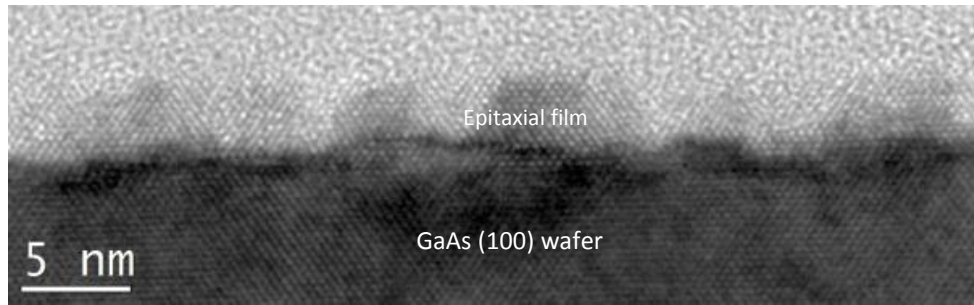


Figure 38. TEM image showing the growth on a GaAs (100) wafer for a deposition time of for 8 s.

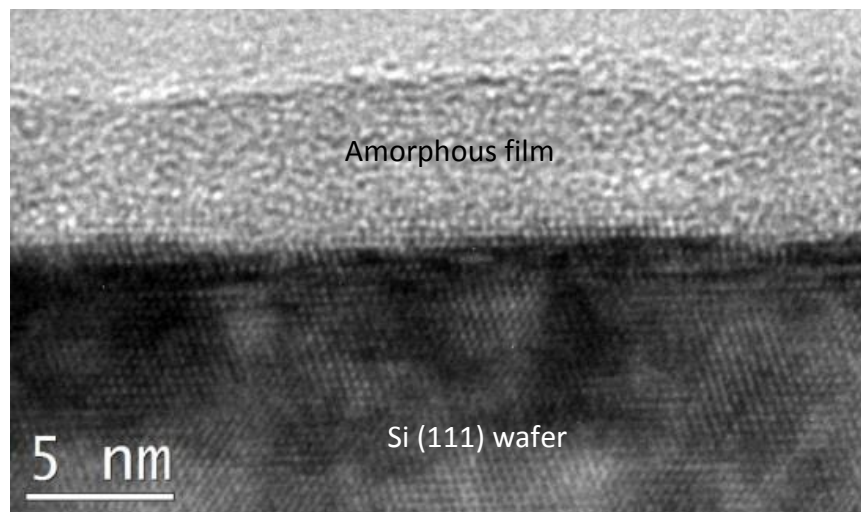


Figure 39. TEM image illustrating the growth for 8 s on Si (111) wafer, it shows an amorphous film having a thickness around 5 nm.

epitaxial growth is confirmed by the continuity of the atomic planes across the interface. The images on GaAs revealed a non-smooth or damaged film/substrate interface that is likely due to an etching effect of the cleaning plasma (SiF_4). Some dark regions in the islands suggest the presence of defects that could be related to strain. Briefly, the epitaxial growth on Si and GaAs wafers is characterized by 2D and 3D growth modes respectively, leading to a continuous film on Si and an islanded film on GaAs.

Concerning the growth on (111) oriented Si wafers, the deposited film is amorphous as shown by the bright contrast in Figure 39 and by the diffraction pattern recorded on this zone. This TEM image also confirms that a deposition on Si (100) had taken place and had a quasi-perfect epitaxial structure.

Let us note at this stage that the films deposited on the same substrates for a longer deposition time of 20 s (not shown here) revealed the same TEM images compared to Figure 37, Figure 38 and Figure 39. They also exhibited a quasi-2D growth mode, but were thicker than the films deposited for 8 s.

3.3.2. Short deposition on Si (100) TEM grids

Deposition on single crystal Si grids were also performed simultaneously with the growth of the films shown in the previous section. To avoid the use of Kapton tape, the grids were fixed on the wafer, after an HF dip, by the means of masks specially designed for this reactor.

Before presenting the results on the grids, a characterization of these grids before any deposition is given in Figure 40. The latter shows that the Si membrane is contaminated by defects of 50-90 nm (see arrows) in some parts, especially near the edges of the windows, most likely due to some contamination problem during the fabrication of the grids.

The TEM images shown from now on correspond to the central regions of the windows far away from the edges (to avoid contaminated regions). A series of images was recorded on such regions: focused, overfocused and underfocused images ($\Delta f = \pm 56$ nm) to better visualize the presence of hillocks. This series shows a smooth membrane surface as well as the absence of any contaminant, as presented in Figure 41.



Figure 40. TEM images recorded on the Si (100) grids near the edges of the windows showing contamination on the membrane before any deposition.

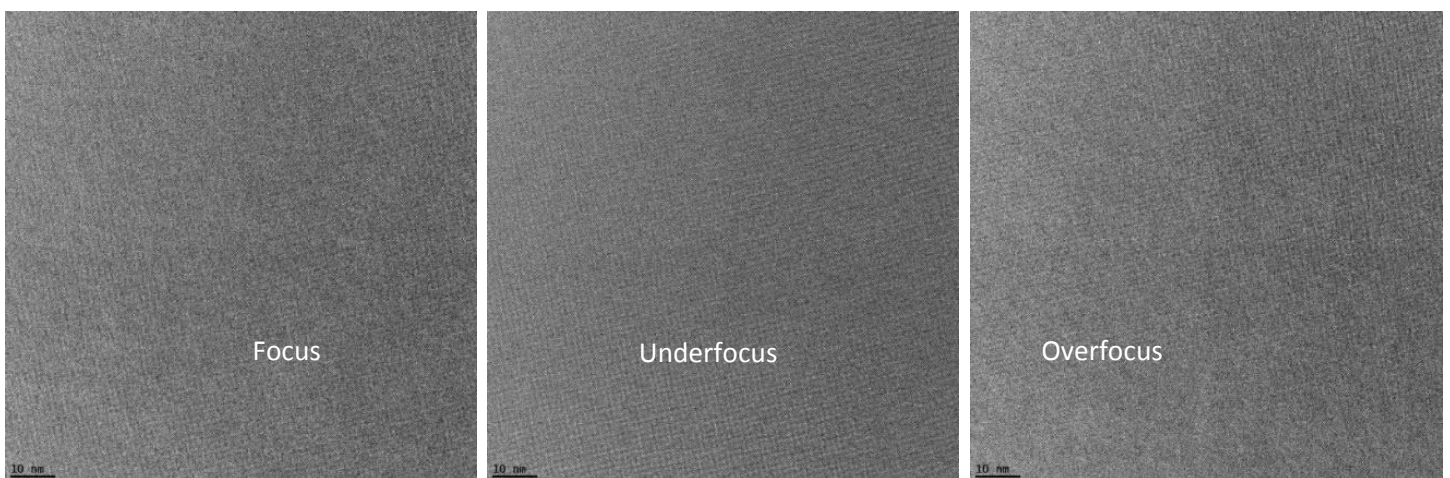


Figure 41. A series of TEM images of the Si membrane showing a smooth surface for (a) focused image, (b) underfocused image and (c) overfocused image ($\Delta f = \pm 56$ nm).

Performing similar series of images with variable focus reveals the presence of islands having a width in the range of few nm (3-7 nm), as presented in Figure 42.

Figure 43 illustrates TEM images for some islands found on Si (100) grids for a deposition time of 8 s. They display larger islands in the range of few tens of nm (10-20 nm). We also found large islands up to 80 nm in width, as shown in Figure 44. We are sure that such islands are not the building blocks of the deposition, since they were not found on the whole Si membrane of the TEM grids (non-uniform distribution). It seems that they arrived on the grids, when the plasma was turned off.

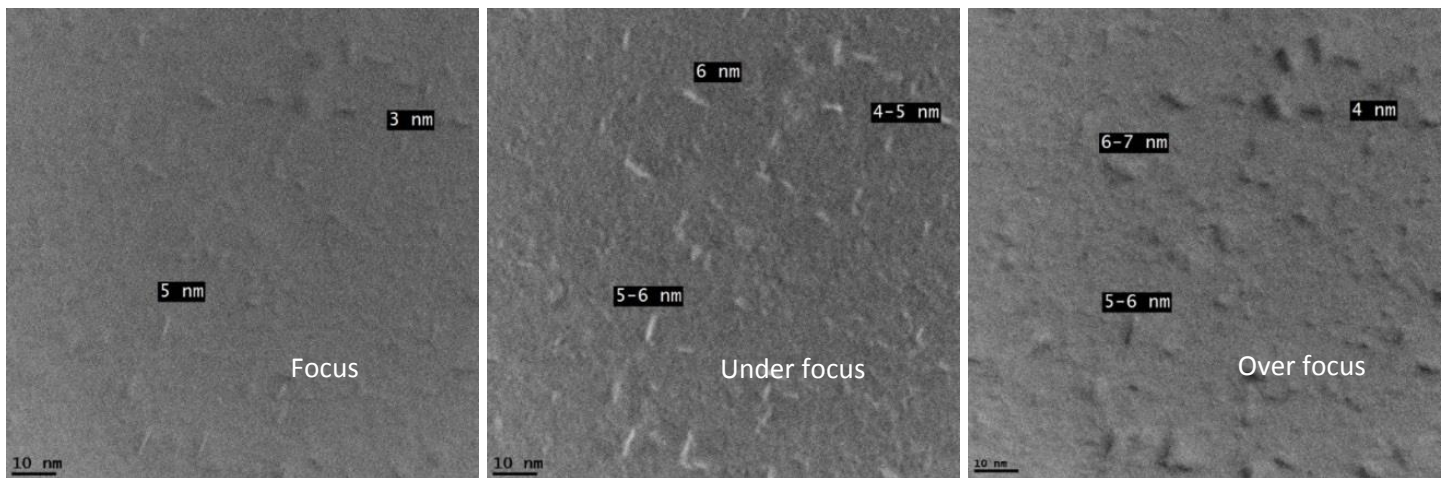


Figure 42. A series of TEM images (focused, underfocused and overfocused, $\Delta f = \pm 35$ nm) corresponding to deposition for 8 s on Si (100) grids.

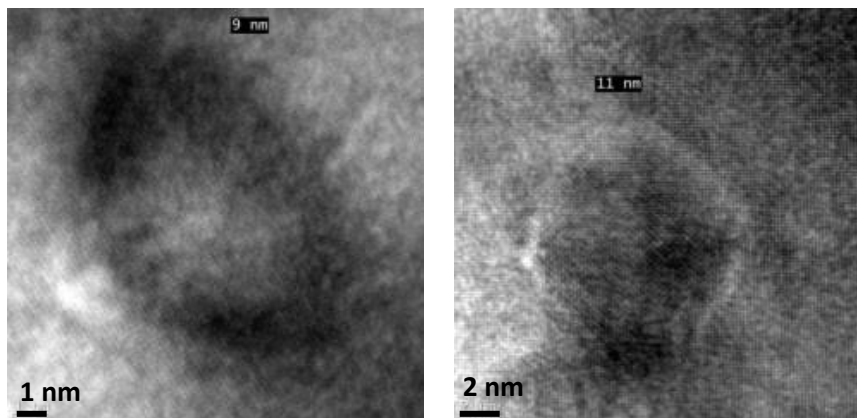


Figure 43. TEM images showing crystalline islands found on Si (100) grids, they have size in the range of 10-20 nm

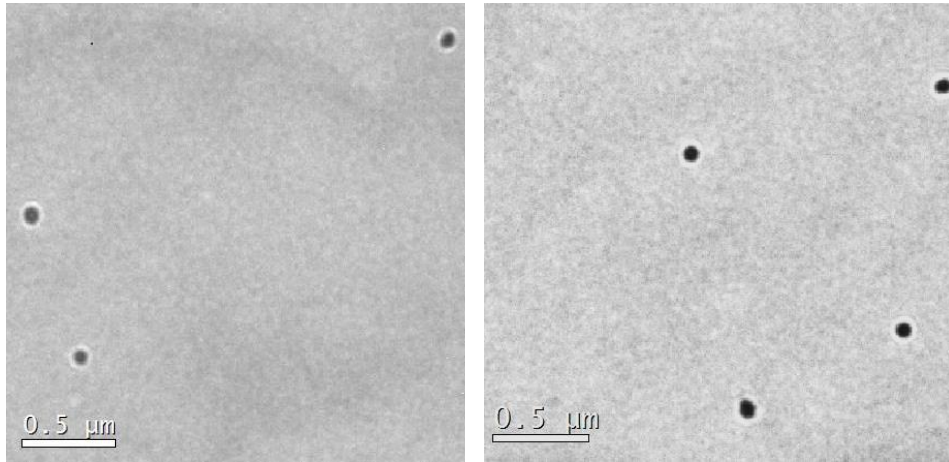


Figure 44. TEM images of the deposition on the Si grids. Few islands up to 80 nm in width are found, they are not uniformly distributed on the grids.

3.4. Discussion

In the light of the results presented above, we will examine in this section what information they can provide for a better understanding of epitaxial growth by LT-PECVD. In such an environment, there are a lot of species that may contribute to the growth: radicals, positive ions, neutral particles and positively charged particles.

Usually, the traditional growth mechanisms for Si thin films are explained by the contribution of radicals like SiF_xH_y [71] or SiF_2 reacting with an impinging H at the surface [72] or ionized Si atoms [73]. However, the use of a plasma at high pressure and high power was proved to be responsible for particle generation; some of these particles are trapped within the plasma but a non-negligible fraction of them (mostly the positively charged ones) are expelled out of the plasma by the electric field present at the sheath. There is no reason why the latter would not reach the substrate and so contribute to the deposition. All this is to say, simply, that the building blocks of the growth could be: atoms, radicals and ions from one side, and plasma generated particles from another side, or all together where the ratio of atoms/cluster may change. In the following, we discuss the tendency of each case, based on our observations and the available literature. Using TEM as the main experimental tool, we check if the detection of nanoparticles is possible on the substrates; a positive answer would confirm the growth mediated (at least partly) by particles, but a negative answer is not a proof of their absence.

3.4.1. Hypothesis of growth mediated by atoms, radicals or ions

3.4.1.1. A standard approach

In the standard approach to Si thin film deposition, one considers the contribution of SiF_yH_z radicals [71, 72]. However, there are many more species than radicals which can interact with the substrate and contribute to thin film deposition. For example, the bombardment of the surface by positive ions (SiH_x^+) has been largely explored and recognized as a source of defect creation in a-Si:H and amorphization in the case of microcrystalline deposition [68], or as a beneficial source enhancing epitaxial growth [19]. It was reported that the effect of atomic hydrogen or energetic ions can compensate the low thermal energy of the substrate, thanks to a chemical annealing phenomenon [74] or a transfer of the kinetic energy to the film [75], respectively, making epitaxy possible even at low temperature. The effects of atomic hydrogen and ion bombardment energy on the epitaxial growth will be studied in details in chapter 4. Besides these effects, another basic requirement for epitaxial growth mediated by radicals is a low deposition rate such that an atom has enough time to occupy an epitaxial site before being hit by another atom.

The standard model to describe the process leading to low defect density epitaxial films is based on the surface diffusion of Si radicals. Three different growth modes are distinguished in homoepitaxial growth (Figure 45), strongly dependent on the substrate temperature (which gives the thermal energy available for visiting metastable and stable surface atomic sites). These modes are determined by kinetic criteria and not macroscopic thermodynamic criteria since there is no difference between bulk and interface energies for the homoepitaxial growth (Si on Si).

(1) *Step flow growth* corresponds to high temperatures above 450°C, and so to high surface mobility. Here, the atoms impinging on the substrate surface are adsorbed (adatoms) and have enough mobility to migrate on the surface. They can occupy sites of least energy (the most neighbors satisfying dangling bonds) at kinks or step edges, such that one monolayer is filled up before the next terrace is formed. However, surface roughening due to kinetically limited growth conditions can be observed for temperatures between 450 and 625°C for deposition on Si (100) wafers [76].

(2) *Layer by layer growth* corresponds to intermediate temperatures between 150 and 450°C. Here, the adatom mobility is slightly lower than the previous case so that they mostly incorporate at step edges. However, new terraces may nucleate by collision of adatoms if the mean free path of the adatoms is significantly lower than the terrace width or the step distance. One factor that can enhance the surface roughness is the presence of a Schwoebel barrier [77] at the surface step, where an adatom on an upper terrace is hindered to move to lower atomic layers if its kinetic energy is lower than the barrier height. (1) and (2) can be considered as 2D growth mode or Frank-van der Merwe mode (FvdM).

(3) *Island growth* corresponds to low temperatures up to 150°C and therefore to low adatom mobility. In this case, the propensity of islanding or clustering of adatoms is considerably higher than for the incorporation at a step edge. Therefore, islands appear on the surface with a high density, and coalesce with the evolution of the growth. Surface roughening and generation of point defects occur when new islands are formed on top while coalescence of the lower layer is incomplete. This 3D mode is the Vollmer-Weber (VW) mode.

It is important to mention that the Stranski-Krastanov (SK) mode which corresponds to a layer-by-layer mode followed by island growth, does not apply to homoepitaxy, since it is often due to strain in the growing layer, typically due to a mismatch in lattice constants between the substrate and the deposited layer. However, it could be effective in our deposits of Si on GaAs. The above-mentioned temperatures may vary with the type of the growth technique, the deposition rate and the materials system.

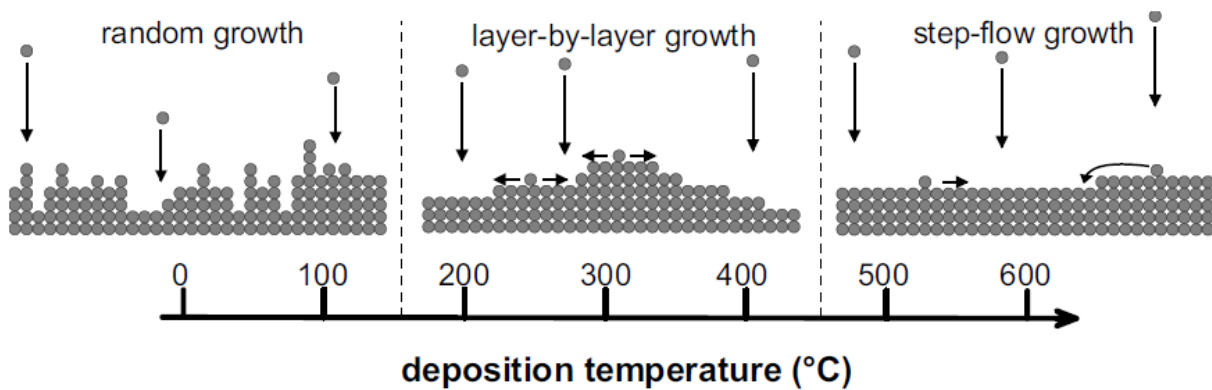


Figure 45. Growth modes at low temperature [78]

3.4.1.2. Deposition in the CLUSTER reactor with SiF₄ precursor

If the deposition of the CLUSTER sample is mediated by radicals or ions, it should have been started by an island growth mode for $t \leq 90$ s because of the following observations:

- A rough surface displaying islands on top of the wafer, with a height of 3-4 nm (Figure 33).
- A high density of defects formed at the interface (Figure 28).

Roughening can be regarded as island formation on top of a terrace while the coalescence of the lower islands has not yet been fully completed. This is accommodated with the formation of a high density of point defects like interstitial Si atoms at or beneath the growing surface (Figure 28); the possible reasons for the formation of defects are discussed later on in this section. However, the specific aspect ratio of those islands (8×4 or 4×2 nm²) does not seem to correspond to the Vollmer-Weber mode

which should normally reveal random growth on the surface of the substrate. In the present case indeed, given the growth rate of 0.2 \AA/s , the typical time for one layer to be covered by another one is more than 1 s. Thus, radicals and adatoms would have more than 1 s to move from the top of a hillock to the nearest valley, which they should do to minimize surface energy. The fact that they do not do it, while they have plenty of time for diffusing (if we extrapolate to 250°C the surface self-diffusion coefficients, given by Acosta-Alba et al. [79]) indicates that a scenario of growth by individual radicals or adatoms can be excluded. Thus, if individual species (radicals, atoms or ions) would play a role in the making of the hillocks, it would be more likely by etching the areas in between those features than by adding matter to them.

Starting from 450 s of the growth, our results showed that the surface became smooth, indicating that a transition from the pronounced 3D to a quasi-2D growth mode occurred. In the latter, we eliminate the probability of a step flow mode for the reasons that the roughness shown by the TEM images is larger than one atomic layer and that the film has a rougher surface than the wafer after the HF treatment, as shown by the ellipsometry signal ($\langle \epsilon_i \rangle$ measured at $4.2 \text{ eV} \sim 43$ in the wafer and 42 in the film).

By analyzing the time evolution of the plasma potential (Figure 31), one can notice that it reaches a maximum value of 61 V in the first few seconds (6 s) of the growth and then stabilizes at 49 V in the steady state regime. This means that the highest energy a positive ion may acquire occurs during the first 6 s and is equal to 61 V. This latter potential is slightly higher than the threshold value for Si atomic displacement at surface $\sim 60 \text{ V}$ [80], but does not hinder epitaxial growth. This is in agreement with the results of Bruneau et al. [65] (Figure 46) where for the high pressure regime (2.3 Torr) and particularly when the plasma potential is about 61 V, the $\langle \epsilon_i \rangle$ is equal to 39.5, a signature of a good epitaxial quality.

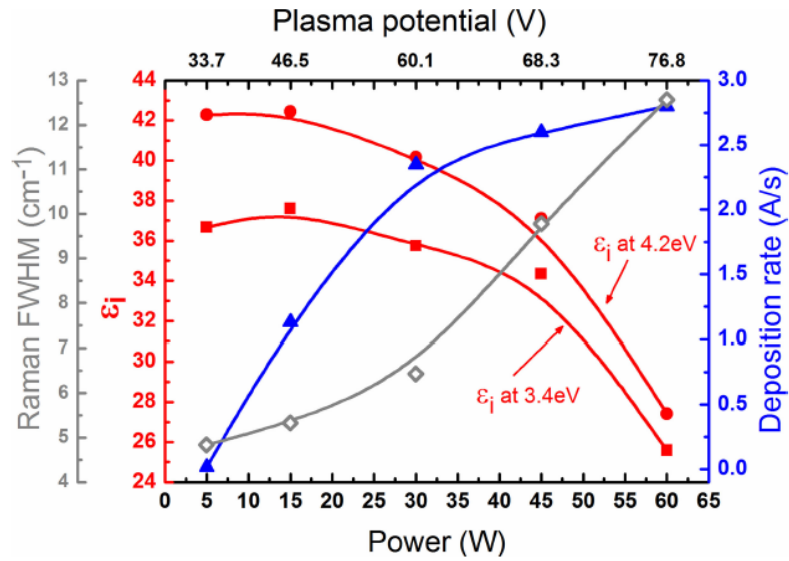


Figure 46. Evolution of the deposition rate, $\epsilon_i > 3.4$ and 4.2 eV and the Raman full width at half maximum as a function of the plasma potential and power [65].

In the following, we discuss the origin of the defects at the interface (Figure 28). These defects are very likely the remnants of the hillocks discussed above. The creation of the latter, in turn, may have been promoted by several factors like sputtering by high energy impinging ions and chemical etching. Those defects, in turn would help the nucleation of hydrogen platelets. Let us consider sputtering by high energy ions. Argon ions with an energy of 100 eV can induce defects at a depth of 1 nm at maximum [81]. In the present case, we found defects (Figure 28) that span over 7 nm on either sides of the interface. Such a size will hardly be the result of this mechanism, given that the highest ion bombardment energy here is 61 eV. Thus these defects would be due to the chemical etching by atomic hydrogen or atomic fluorine.

Some {111} platelets are visible at the interface and even underneath it (Figure 28); they exhibit a contrast similar to the simulated map of stress component around a (100) hydrogen platelet by Moras et al.[69] (Figure 47). These platelets are elongated defects consisting of one or more missing planes forming a cavity in the crystal. H-terminated Si bonds are delimiting this type of defect, and they may contain some molecular hydrogen. Such type of defects was observed in the study of Cariou [51] especially at the interface epitaxial film/ substrate. We expect that the contrast at the interface is related to {100} hydrogen platelets but which are not very clear in Figure 28.

The most probable explanation for the defects near the interface is that hydrogen diffuses within the film and sets ideally in the defective regions [82, 83] making some strained regions. Nevertheless, whatever is the reason for the formation of these defects, they are healed within ~ 500 s corresponding to a deposited thickness of 10 nm, and then perfect epitaxy is achieved as if no defects were formed.

Therefore, the transition from the pronounced 3D mode to a quasi 2D mode in the transient regime could be interpreted, with the hypothesis of growth mediated by radicals, atoms and ions, as the healing of the defects (or the damage) formed at the interface with the deposition time.

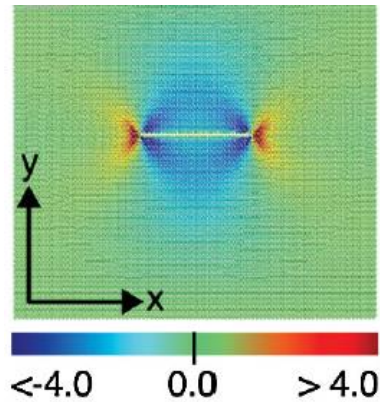


Figure 47. Map of stress component σ_{yy} as simulated by Moras et al. [69]; tensile stress is represented in red and compressive stress in blue.

3.4.1.3. Deposition in the ARCAM reactor with SiH_4 precursor

For the depositions performed with the ARCAM- SiH_4 system, the cross-sectional TEM images on Si (100) (Figure 37) revealed a continuous epitaxial Si film for 8 s with little specificities. This result can be regarded as 2D growth mode, a quasi the layer-by-layer growth mode.

For the plan-view images (Figure 42), the white elongated shapes about 5 nm can be interpreted as hydrogen platelets rather than small Si islands. These platelets are lying in the $\{100\}$ planes, and are known in the literature [69]; they can follow $\{111\}$ and (100) planes and are accompanied with tensile and compressive stress. These platelets are not visible in the images of Figure 37 probably because of their low density compared to the field of view.

3.4.2. Hypothesis of growth mediated by plasma generated particles

3.4.2.1. A relatively new approach

For many years, there was a general agreement that high-quality Si thin films (amorphous, epitaxial or polycrystalline) obtained from plasma deposition should be grown from radicals, and that particle formation must be avoided [84]. Nevertheless, several references showed that under some conditions of particle generation, namely high power or high pressure, high quality films were obtained at a high growth rate thanks to growth by particles [33]. This means that particle formation can be beneficial [85, 86] for the growth in opposition to what was believed before. Such results were experimentally obtained by Roca et al. [87] who found that in these conditions, particles were generated in the plasma,

and more interestingly, they contributed to a considerable fraction of deposition (50-70%). One key parameter in their study was the energy per atom, not the acceleration voltage. Moreover, the achievement of high deposition rates by plasma CVD processes, cannot explain the unexpected results based on the traditional view of film growth by radicals (which imposes low growth rate to achieve epitaxy), and opens the discussion toward growth mediated by clusters.

In fact, the charge state fluctuations on the smallest nanoparticles results in them occasionally adopting neutral or positive charge states, allowing them to escape from the plasma region [88-90] and to be incorporated into the deposited film. From a theoretical point of view and according to ab-initio molecular dynamics, LT-epitaxy happens as follows [67]: Si clusters generated in the plasma escape from it and arrive at the substrate with a high kinetic energy. They penetrate into its lattice and form a disordered structure. The impact energy causes their melt and the rearrangement of Si atoms on the surface of the substrate, finally they settle down in epitaxial positions. Nevertheless, there is no consensus on the size of clusters that contribute to the growth. Most studies deal with smaller than 5 nm-sized clusters but some authors have suggested that 10 nm-sized clusters can also escape from the plasma and constitute the building blocks of the film [91].

Some basic requirements for an epitaxial growth mediated by nanoparticles is a narrow distribution of nanoparticle size, in order to have the same impact energy per atom, to prevent any damage to the film.

3.4.2.2. Deposition in the CLUSTER reactor with SiF₄ precursor

The presence of particles on the grids confirms their formation in the plasma and this is consistent with the high value of the product pressure × inter-electrode distance (5 Torr.cm) and the high power density applied (0.17 W/cm² or 40 W). The size of the observed particles ranges from about 10-12 nm to 1 μm. If a very low power was applied, no nanoparticles could be found [84, 92]. Particle formation is a hot topic discussed in plasma physics over the past years and is still under investigation. It is the first phase of powder formation which in turn is undesired for numerous industrial applications [93]. A schematic description of plasma phases leading to powder formation has been given [94] as: (1) formation, nucleation and accumulation of particles, (2) their coagulation and agglomeration in the gas phase and (3) powder regime and surface growth; the reader is advised to look into some review papers, like [91], for more information. Here, the term “powder” refers to particles larger than 100 nm and “particles” is associated with a particle size less than 100 nm. Silicon-based particles can be generated in the plasma as follows: the negative ions are effectively trapped in the central regions of plasma discharges; this allows the negative ions to grow in size with time, by reacting with radicals and

cations. Particle formation is considered as an unavoidable consequence of the deposition character of the plasma conditions and the relatively large electron affinity of Si.

According to several theoretical investigations on the contribution of nanoparticles in the growth of thin films [67, 95], the particles that contribute to epitaxy by melting and recrystallizing at epitaxial sites, are less than 2 nm in size.

In our case, some of the particles shown in Figure 36 for the CLUSTER reactor have a larger size (> 10 nm), and so could not be considered as the building blocks of the epitaxial growth. We assume that the particles forming aggregation were confined in the plasma and grew with time (negatively charged particles) until the plasma is turned off; at this moment, they could reach the walls of the growth chamber or the surface of the membrane (or the Si continuous film). Not being accelerated by the plasma potential (afterglow), they arrive on the membrane with low kinetic energy, which can loosely explain their low sticking with the membrane, as they are moving under the electron beam (Figure 36). Some of them could diffuse on the surface to reach other particles forming dendritic aggregation (undergoing the diffusion limited aggregation (DLA) [70]). The presence of the large aggregations, like the ones displayed in Figure 36(c), is mostly due to particles nucleation and coagulation in the gas phase (which, in general, precede the powder formation phase). Such agglomerations reveal a compact structure (Figure 36(c)). Briefly, the observed particles were attached to the Si thin films after their formation and growth in the plasma. They do not give information on the deposition itself, but give partial information on what is happening in the plasma, namely the formation of particles for our growth conditions. In other words, if we can detect large particles, smaller one may be present.

Particle formation in the plasma was regarded and shown in the work of Schmidt et al. [84] to be responsible for a transient regime, called initial transient stage (ITS), in a silane discharge after ignition. The ITS was characterized by a transient regime in the measurements of the discharge parameters, namely pressure and DC voltage, as well as the film growth parameters, namely the real and imaginary parts of the pseudo-dielectric function (measured at 3.4 eV); this was observed only when applying a high power of 10 W and not 3 W (Figure 48). Particle formation was considered to be responsible not only for this ITS but also for the reduced density of the deposited amorphous hydrogenated Si (a-Si:H) thin films. The formation of particles was thus a key parameter of the transient regime. Those authors used in-situ laser light scattering to detect particles during the plasma process. Thanks to their optical method, they were able to determine the particle size and number densities with spatial and temporal resolution [92].

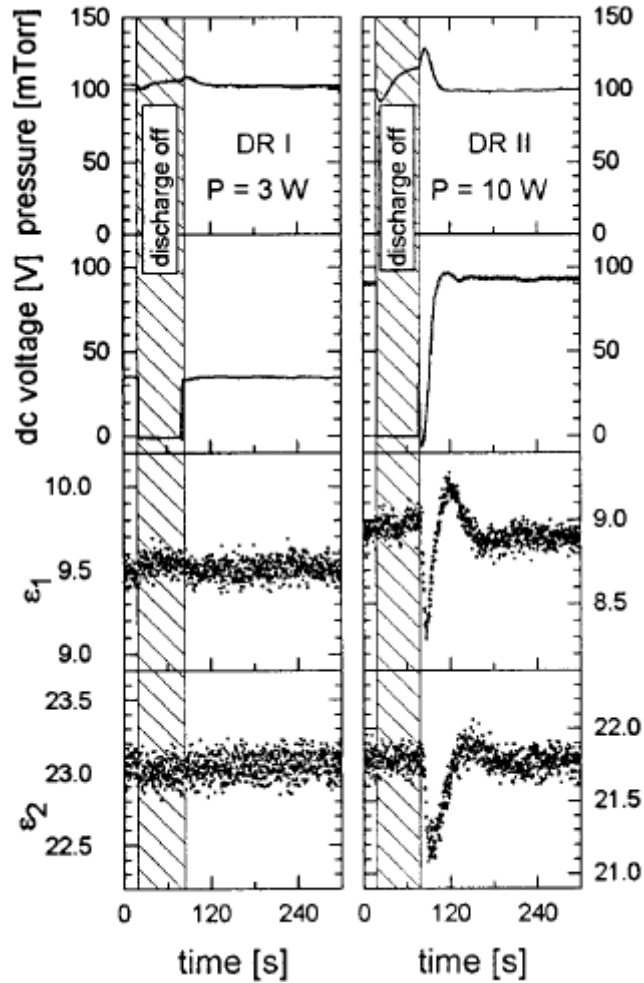


Figure 48. Time evolution of the pressure, the DC bias between the electrodes and the real (ϵ_1) and imaginary (ϵ_2) parts of the pseudo-dielectric function spectra measured at 3.4 eV, in the work of Schmidt et al. [84]. An initial transient stage is detected at a power of 10 W due to particle formation, this is not the case at 3 W where no particles are formed.

Our results are consistent with the study of Schmidt et al.: we also showed the presence of a transient regime in the behavior of the imaginary part of the pseudo-dielectric function $\langle \epsilon_i \rangle$ (growth parameter, Figure 30).

The hypothesis of the growth mediated by particles is based on their melting upon collision with the surface. A simplified calculation is presented below to estimate which particle size could allow such an epitaxial growth.

The key parameter, here again, is the kinetic energy that transforms into thermal energy upon impact; if the latter exceeds the thermal energy needed to cause Si melting (heat of fusion of Si = 50.21 kJ/mol \sim 0.53 eV/at), the particle melts and may contribute to epitaxy. For the sake of clarity, we can neglect the contribution of the thermal energy of the substrate. Since the plasma potential reaches a maximum value of 61 V, the maximum kinetic energy a singly positively charged particle may acquire is 61 eV. A

particle with a diameter of 2 nm (containing ~ 209 atoms, the density of Si being 5.10^{22} at/cm³), for example, has an energy around $61/209 = 0.29$ eV/at. Therefore, if a positively charged 2 nm- sized particle escapes from the plasma, it needs additional 0.24 eV/at to enable its melting upon impact at the surface of the wafer, in order to make possible epitaxy at low substrate temperature. Now, for a 1.5 nm-sized particle, by assuming that its kinetic energy is transformed into heat (0.69 eV/at), we realize that it is higher than the heat of fusion of Si; therefore, the melting could be possible for such small particle, and so epitaxy seems possible in this case.

The real situation is much more complicated, it depends on the deposition conditions. Thus, we expect that very small particles (having a size ≤ 1.5 nm, just to have an idea of the order of magnitude) allow melting, and that larger particles could not contribute to epitaxy. However, the detection of such small particles is far away from our observations. The same analysis applies for a kinetic energy of 49 eV corresponding to the steady-state regime and thus only smaller than 1.5 nm-sized particles (positively charged) could explain the growth by clusters; again such particle size was not detected in our experiments.

In these estimations, we take into account the impact energy per atom in the aggregate (and not the total energy of the whole aggregate), as used in the simulation works for particles containing more than 30 Si atoms (the largest particles) [67]. According to the theoretical studies made by Le [67], the epitaxial growth of Si can be mediated by nanoparticles if the impact energy per atom is sufficiently high to enable a phase transition to the liquid state. The author found epitaxial growth when a high impact energy is involved, it should be high (5.3 eV at a substrate temperature of 100°C (373 K) for Si₁₅H₁₀) to allow the dissociation of the cluster and its rearrangement into epitaxial configurations, but not extremely high (6.21 to 9.38 eV/atom) to avoid serious damage of both the substrate and the growing film. According to Ning et al. [95], the impact energies are quantitatively categorized: (i) low impact energies are around 0.3 eV/at, they correspond to an interaction cluster/ substrate called bounce-back , (ii) intermediate impact energies are around 2 eV/at, they lead to soft landing or partial dissociation of the clusters and (iii) high impact energies are around 5 eV/at leading to shattering or complete cluster dissociation. In this case, the substrate temperature was 27°C (300 K) and Si₁₂H₁₂ clusters were considered. The results of those authors are summarized in Table 3. Similarly, those authors observed epitaxial growth only for clusters with an impact energy of 4.8 eV/atom, they argued that epitaxy may take place at high impact energies that enable the dissociation of the impinging clusters.

Table 3. Table summarizing the results of reference [95] for different impact energies of Si₂₉H₂₄ clusters (the biggest clusters in their study) and the impact modes (bounce-back, soft landing and shattering).

	<i>Bounce-back (low impact energies)</i>	<i>Soft landing (intermediate impact energies)</i>	<i>Shattering (high impact energies)</i>
Substrate temperature (°C)	27	27	27
Impact energy (eV/at)	0.3	~ 2	~ 5

Briefly, ab-initio molecular dynamics studies have shown that high impact energies (4.8 eV/at [95] and 5.3 eV/at [67] from aggregates smaller than 1 nm) are needed for epitaxy. Whereas our study shows that such high impact energies are far away from our experimental conditions: the smallest particles we detected in plan-view images had a size around 12 nm (Figure 36); even more, if we consider the islands on the cross-section images as particles, they have a size of 4-5 nm in height and 4-8 nm in width. Both types of particles would have very small impact energies that do not allow a transition to the liquid phase.

Therefore, what we have detected was very large in size and it can hardly explain epitaxial growth mediated by particles. The detection of the particles that might contribute to the growth does not seem to be an easy task for epitaxy. Thus, a need to a more powerful method emerges to enable the detection of smaller than 2 nm-sized particles.

3.4.2.3. Deposition in the ARCAM reactor with SiH₄ precursor

The images of the deposits performed with the ARCAM-SiH₄ system show little specificities. The white shapes appearing in the plan-view images of Figure 42 are the only remarkable features. They could be the remnants of particles having melted upon impact with the surface and so having contributed to growth. But such particles should normally form quasi-spherical shapes which in Figure 42 would give isotropic rounded shapes rather than elongated shapes. So, this consideration is not really convenient.

TEM images of the deposition on the TEM grids (Figure 36) showed some particles larger than 10 nm. They could hardly be considered as the building blocks of the epitaxial growth, for the same considerations as those mentioned in section 3.4.2.2. Even more, the plasma potential in these experiments was around 37 V (smaller than that in the CLUSTER reactor ~ 49 V) and so the size of the particles that would contribute to epitaxy should be less than 1.5 nm. However, even if we did not detect such small particles, we cannot exclude the possibility of their presence. Consequently, the cross-section and plan view TEM images do not allow us to determine whether particles have participated or not in the making of the 5-nm continuous film.

The major information which comes out of these experiments is that during the first stages of growth, the Si film is continuous and its thickness is homogeneous. We believe that shorter depositions (4 s, for

example) are interesting for future studies. They would help us to determine the morphology of the film in the very beginning of growth, and to determine if hillocks on top of the wafer exist as the case of deposition in the CLUSTER reactor.

3.4.3. Growth mechanisms: an open discussion

A lot of theoretical investigations, e.g. molecular dynamics [67] were conducted to clarify how epitaxy works and much more investigations correlated with experimental work are still needed. In this chapter, in an attempt to have a better understanding, we monitored experimentally the first stages of the growth using TEM and in-situ ellipsometry for interrupted depositions of few seconds; the results allowed us to discuss a possible interpretation scheme under the light of the available literature. Our work does not pretend to bring evidence of the physical process explaining LTE, partly due to experimental limitations that hinder a complete understanding of the process. These limitations can be summarized by the inadaptability of some equipment to monitor the growth in the range of seconds or less (picoseconds), this is the case of the optical emission spectroscopy (OES) normally used to monitor the evolution of the gases in the plasma. We were also limited by the unavailability – during the period of this PhD – of a highly precise time-resolved in-situ set-up.

We cannot exclude that, in our experiments, small particles play a role in epitaxy. Indeed, it is very difficult to detect particles smaller than 2 nm in diameter on the wafer or on the TEM grids. We believe that we were not able to detect 2 nm sized particles due to some factors:

- If such particles arrive on the carbon membrane, they would have melted into amorphous particles; we remind that epitaxial conditions lead to amorphous growth on an amorphous substrate. It is difficult then to distinguish such a small amorphous melted particle (smaller than 2.5 nm sized particles) from the amorphous membrane. The detection of plasma generated particles was possible in the study of Dornstetter [31] (Figure 49(a)) and Johnson et al. [96] (Figure 49(b)) since the particles were crystalline and bigger with a diameter of about 5 nm. Let us note also that the power densities used in our study for epitaxy ($0.17 - 0.056 \text{ W/cm}^2$) are much lower than that used by Dornstetter ($0.67-1.33 \text{ W/cm}^2$) to achieve microcrystalline Si films where crystallization has found to be mediated by plasma generated particles.
- The detection becomes more difficult for a complete coverage of the membrane, as in our case, where a continuous Si film is already present at 12 s and 90 s. Thus, further studies are needed for a shorter deposition time, 4 s for example.

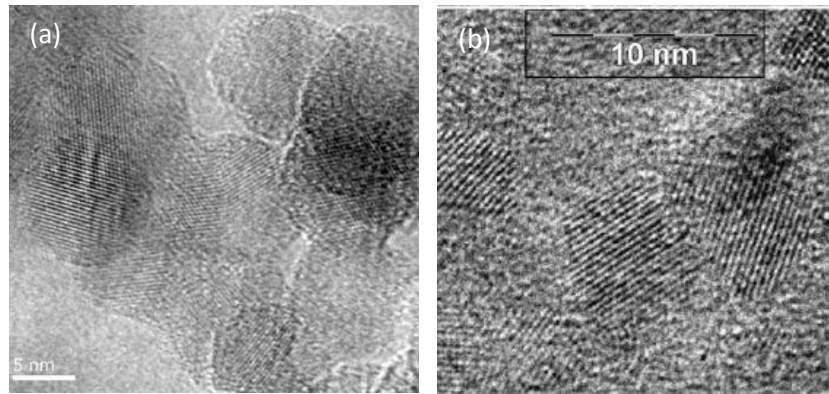


Figure 49. TEM images recorded on carbon membrane showing crystalline particles having a diameter of 5 to 10 nm, these images are taken from the study of (a) Dornstetter [31] and (b) Johnson et al. [96].

Inspired by the microcrystalline particles observed by Dornstetter [29] and obtained under microcrystalline growth conditions, we suggest for future work to slightly shift our epitaxial conditions (leading to amorphous deposition on the amorphous carbon membrane of the TEM grids) to microcrystalline conditions (mostly leading to microcrystalline deposition on the carbon membrane). In this case, if small particles (~ 2 nm) exist, a non-negligible fraction of particles would most probably be microcrystalline (as reported by Dornstetter). We can expect a difference of contrast in the TEM images between the amorphous membrane and those microcrystalline particles, and thus, their detection would be plausible, even for such small size. Taking images with defocusing (overfocusing or underfocusing) would also help their detection. So we propose to slightly tune our growth conditions to make microcrystalline deposition. This can be done by increasing the H_2 flow rate to crystallize the probable particles, but not by increasing the RF power which would modify the number, the size or the density of those particles (which would cause significant changes to nanoparticles).

Future work may include a statistical study of the particles collected on the TEM grids in which a correlation between particle size and particle density would be established for different deposition times in the transient regime. This would bring information on the time evolution of the detected particles in size and would give an idea of the evolution of the particle density within the plasma.

Finally, at this stage, we would conclude that the hillocks observed at the surface of samples deposited in CLUSTER reactor (CLUSTER-SiF₄) (Figure 33) are probably *not* the remnants of particles formed in the plasma, but one cannot exclude that they could be an assembly of smaller particles.

In contrast, etching appears as the best candidate to explain the initial roughness (Figure 33). Chemical etching can be caused by hydrogen atoms, fluorine atoms or HF molecules; chemo-mechanical etching could even be caused by plasma generated particles. For future work, we suggest to make simulations with molecular dynamics in order to check the possibility of sputtering by SiF_xH_yF_z aggregates. However,

we are sure that a deposition has taken place because TEM observations on the grids revealed a continuous Si film for 12 and 90 s (Figure 35). Thus, we cannot exclude a competition between deposition and etching.

Finally, with the absence of detection, with TEM, of particles smaller than 2 nm, we suggest that the traditional point of view and the relatively new approach can both contribute to deposition to some extent, we cannot exclude this hypothesis. We suggested a plan for future work that would offer a more precise view of the epitaxial growth by LT-PECVD.

3.4.4. Effect of the substrate

The depositions presented in the TEM images of Figure 37 and Figure 39 show that the epitaxial growth is more difficult on (111) than on (100)-oriented Si surfaces. Such an orientation sensitivity, especially at low temperature, might be explained by a geometrical argument: in the (100) case, each Si atom in the growing planes has to form two covalent bonds with the underneath plane, to be incorporated in the lattice, while Si atoms incorporated on (111) surfaces need to form only one bond with the underneath plane (and three with the upper planes), which gives more degrees of freedom for an amorphous growth. Both experimental results and molecular dynamics simulations [97-100] show that a temperature of few hundred degrees higher is needed to achieve good epitaxial growth on (111) compared to (100), on which it can occur close to room temperature. This explanation is coherent with our results: we observed for samples deposited at the same time and for the same conditions an epitaxial growth on Si (100) but an amorphous one on Si (111).

Moreover, the depositions on GaAs (100) (Figure 38) also revealed an epitaxial film but with a pronounced 3 dimensional growth quite typical of a Stranski-Krastanov growth mode. The layers nucleate as faceted 3D islands with a height around 4 nm. This type of growth is due to the presence of a tensile strain resulting from the lattice parameter mismatch between Si and GaAs ($\sim 4\%$, a_{GaAs} : 0.5653 nm, a_{Si} : 0.5430 nm). In other words, the microstructure of the epitaxial layer on GaAs is largely determined by relaxation of strain; this effect is notably used in the epitaxy of III-V semiconductors to make quantum dots [101].

3.5. Summary and perspectives

Takeaway message – Initial stages of epitaxial growth

- While silicon epitaxy by LT-PECVD is moving from a laboratory curiosity to an industrial perspective, the growth mechanisms are still a matter of debate. Here, we discuss two hypotheses: the traditional growth mediated by atoms, radicals and ions and the relatively new approach based on the melting of plasma generated clusters upon impact with the substrate.
- Concerning CLUSTER-SiF₄ depositions:
 - A transient regime in $\langle \epsilon \rangle$ was evidenced in the first 450 s of the growth. It occurred just after the plasma ignition and was correlated with particle formation in the plasma.
 - Short depositions were performed on Si wafers and on TEM grids in the transient regime for 12, 90 and 240 s. For depositions on the wafers, ellipsometry measurements and HRTEM images were in agreement: they showed a maximum surface roughness followed by smoothing effects until reaching a steady state regime. TEM observations on the grids revealed a continuous Si film as well as particles with a minimum size of 12 nm. We explained why these large particles cannot be the building blocks of the epitaxy.
 - If a growth mediated by particles occurs, these particles should be smaller than 2 nm. Such particles were not detected on the substrates, making it difficult to determine if the growth was done from the traditional or the relatively new view of growth.
- Concerning ARCAM-SiH₄ depositions:
 - Epitaxial short depositions showed very little specificities: a smooth surface, as revealed by the cross-sectional HRTEM images on the Si wafers, and some hydrogen platelets, as displayed by the plan-view TEM images on the TEM grids.
 - With TEM, we did not detect any particle smaller than 2 nm. The presence of such particle size would confirm the role of particles in the epitaxial growth.
- Since TEM observations seem not enough to check the presence of small particles (1-2 nm) even when using different types of substrates, the need for a more powerful method for the detection of such particles at the surface of the films emerges. Modelling is needed and other plasma characterization techniques should be used to figure out how plasmas behave.
- The growth mechanisms of epitaxy by LT-PECVD are still a hot topic for discussion. Deposition for shorter times would be interesting to check the hypothesis of the aggregation of small particles on the surface (to form a continuous film), before the full coverage of the surface substrate. Other strategies for future work were suggested to explore the growth mechanisms, like performing a statistical study of the particles collected on the TEM grids (size and density), and checking the detection of particles with slightly tuning the growth conditions into microcrystalline growth by increasing the H₂ flow rate.

Chapter 4. Epitaxy breakdown using SiF₄/H₂/Ar plasma

4.1. Introduction.....	67
4.2. Intentional epitaxy breakdown with increasing the RF power.....	69
4.2.1. RF power of 20 W on Si (100) substrate.....	69
4.2.2. RF Power of 25 W on Si (100) and Si (111) substrates.....	76
4.2.3. Summary of the results – epitaxy and breakdown by increasing the RF power.	82
4.3. Intentional epitaxy breakdown with increasing the H ₂ flow rate.....	84
4.3.1. Hydrogen flow rate of 2 sccm on Si (100) wafers	84
4.3.2. Hydrogen flux of 3 sccm on Si (100) wafers.....	90
4.3.3. Summary of results - epitaxy and breakdown by increasing the H ₂ flow rate....!	93
4.4. Discussion.....	95
4.4.1. Breakdown by power.....	96
4.4.2. Breakdown by hydrogen	100
4.5. Summary and perspectives.....	105

4.1. Introduction

Once epitaxial growth is established by LT-PECVD, it seems necessary to understand how it is sustained; for this it is obviously necessary to understand also how it is lost or how it breaks down. In general, when performing epitaxial growth, sudden breakdown occurs after a certain epitaxial thickness (limited-thickness epitaxy) which depends on the deposition conditions. As the SiF₄/H₂/Ar chemistry was studied for epitaxy by Ronan Léal in parallel to the present work, we focused on that chemistry to study epitaxy breakdown. The growth parameters in that case are the ratio of the flow rates of SiF₄, H₂ and Ar, the RF power density, the substrate and RF electrode temperatures, the pressure and the inter-electrode distance.

Epitaxy breakdown of Si thin films grown on (100) Si wafers was studied by Eaglesham et al. [102] using molecular beam epitaxy (MBE) at low temperature (LT) (< 500°C). They reported that layers grew epitaxially for a certain thickness before epitaxy began to fail. Similarly, Bratland et al. [103] investigated epitaxial breakdown of (001) oriented germanium layers deposited using LT-MBE over temperatures ranging from 95 to 190°C. Surface roughening reaching a critical value was reported to be the main reason for epitaxy breakdown at a certain thickness for both studies [103-107]. The breakdown of epitaxy has been also studied for other LT deposition methods like ion assisted deposition (IAD) [73] and hot-wire chemical vapor deposition (HWCVD) [108]. Some models were proposed to explain epitaxy breakdown and will be presented in the discussion part (section 4.4). However, the breakdown of epitaxy by PECVD at *low* substrate temperature has not been studied in the literature.

In this chapter, we are interested in making intentional Si epitaxy breakdown as a function of the hydrogen flow rate from one hand and the RF power from another hand by using LT-PECVD with a SiF₄/H₂/Ar plasma mixture. In the following, epitaxy breakdown is referred to the irreversible transition from a monocrystalline structure to another structure that leads to the complete loss of epitaxy. We aim at answering the following questions: how does the hydrogen influence/hinder the epitaxial growth? Or how does it play a role in breaking epitaxial growth into microcrystalline or amorphous growth? The same questions are raised for a high RF power. To answer these questions, an epitaxial Si film called “reference” (Figure 51) was deposited with optimized epitaxial conditions, namely 1 sccm of H₂ flow rate, 15 W and 3 Torr, and four samples were deposited at the same conditions but with changing one parameter at a time (Figure 50):

- either the RF power, namely at 20 and 25 W (section 4.2)
- or the H₂ flow rate, namely 2 and 3 sccm (section 4.3)

We chose to study the effect of the RF power and that of the H₂ flow rate on the epitaxial quality, inspired by the study of Dornstetter [31] where he pointed out two crystallization mechanisms in SiF₄/H₂/Ar chemistry: (i) surface (and subsurface) crystallization mediated by atomic hydrogen at high H₂ flow rate and (ii) plasma crystallization mediated by plasma generated particles at high power. The latter study was addressed to understand the amorphous to polycrystalline (or microcrystalline) transition in Si thin films deposited on an amorphous substrate (silicon nitride, SiN_x) by LT-PECVD.

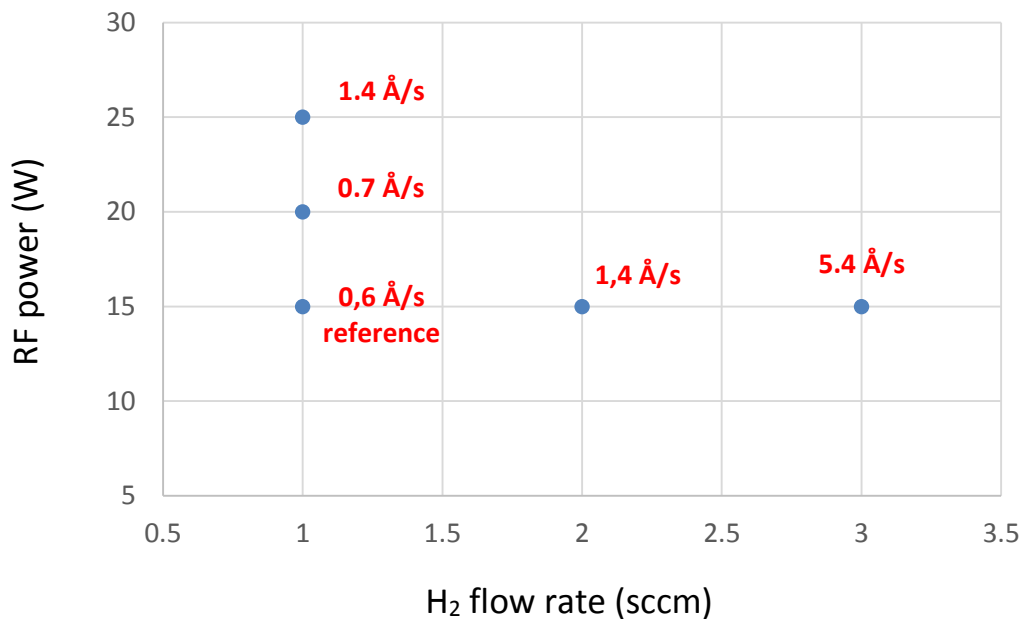


Figure 50. The growth conditions for the films presented in this chapter: two series of depositions were carried out starting from the reference film, by increasing either the RF power or the H₂ flow rate.

To understand the mechanisms of sudden epitaxy breakdown and subsequent growth of amorphous and microcrystalline Si phases, we present, in this chapter, cross-sectional TEM images for these samples; we highlight on the microstructural evolution of the layers with time before, during and after the breakdown. This is done thanks to electron diffraction patterns (EDPs) and Fast Fourier Transforms (FFT) of HRTEM images. Moreover, we present in-situ ellipsometry measurements and correlate them with TEM results.

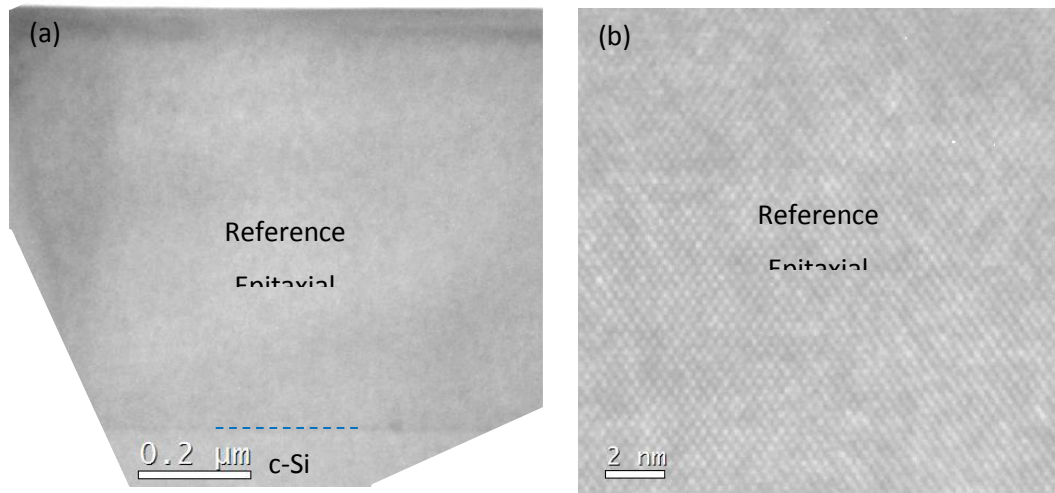


Figure 51. (a) Low magnification and (b) high resolution TEM images of the reference film obtained at a RF power of 15 W and a H_2 flow rate of 1 sccm. The microstructure reveals a thickness of 750 nm of high quality epitaxy that is almost free of defects.

4.2. Intentional epitaxy breakdown with increasing the RF power

In this section, we show the results of the films deposited using RF powers of 20 W and 25 W on (100) and (111) oriented Si wafers. We study how epitaxy is broken by increasing the RF power. We will extract information on the quality and/or roughness of the film as a function of the deposited thickness.

4.2.1. RF power of 20 W on Si (100) substrate

4.2.1.1. Crystalline structure evolution from TEM observations

Increasing the RF power from 15 to 20 W leads to significant changes in the structure of the film deposited on Si (100), as shown by the difference of contrast in Figure 52 which suggests an epitaxy breakdown.

We are interested here in studying the evolution of the film microstructure as a function of thickness in order to understand how epitaxy starts, sustains and breaks. For this, we performed a series of EDPs on different regions of the film using an aperture selecting a diameter of 330 nm, as shown in Figure 53. These regions are indicated by black dotted circles in Figure 52; they correspond to (i) the beginning of the film (region #1, Figure 53(a) and (d)), (ii) the film excluding the beginning (region #2, Figure 53(b) and (e)), and (iii) the top of the film (region #3, Figure 53(c))

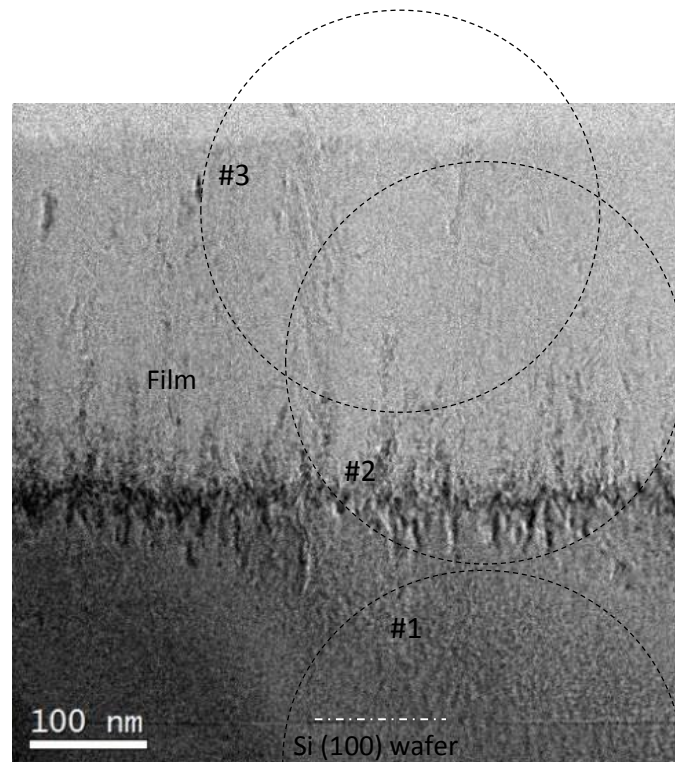


Figure 52. TEM image of the film deposited using a RF power of 20 W and a H_2 flow rate of 1 sccm. The black dotted circles indicate the areas selected for the EDPs shown in Figure 53.

Numbers are attributed to each area.

and (f)). From the EDP shown in Figure 53(d), it is clear that the first 120 nm of the film (region 1) have a perfect monocrystalline structure, indicating that epitaxial growth has occurred. The onset of epitaxy breakdown is visible in the EDP of Figure 53(e) with the apparition of some additional intense 111 spots and amorphous contribution. The latter is highlighted in Figure 54 displaying the profile of the blue rectangle in Figure 53(e); the small peak between 220 and 311 rings reflects the presence of a diffused part between these rings that is the typical contribution of amorphous Si. As a matter of fact, some of the additional 111 spots in Figure 54(e) are attributed to random microcrystalline growth and some of them are characteristic of twin orientations (yellow arrows, see chapter 5, section 5.1.2 for details). It appears therefore that the pathway taken by the film to break epitaxy is twin formation and amorphous growth. The whole chapter 5 is dedicated to twinning, it provides a description of twinning induced by epitaxy breakdown and some factors

that promote twin orientations. In this chapter, we focus on a parametric study of epitaxy breakdown.

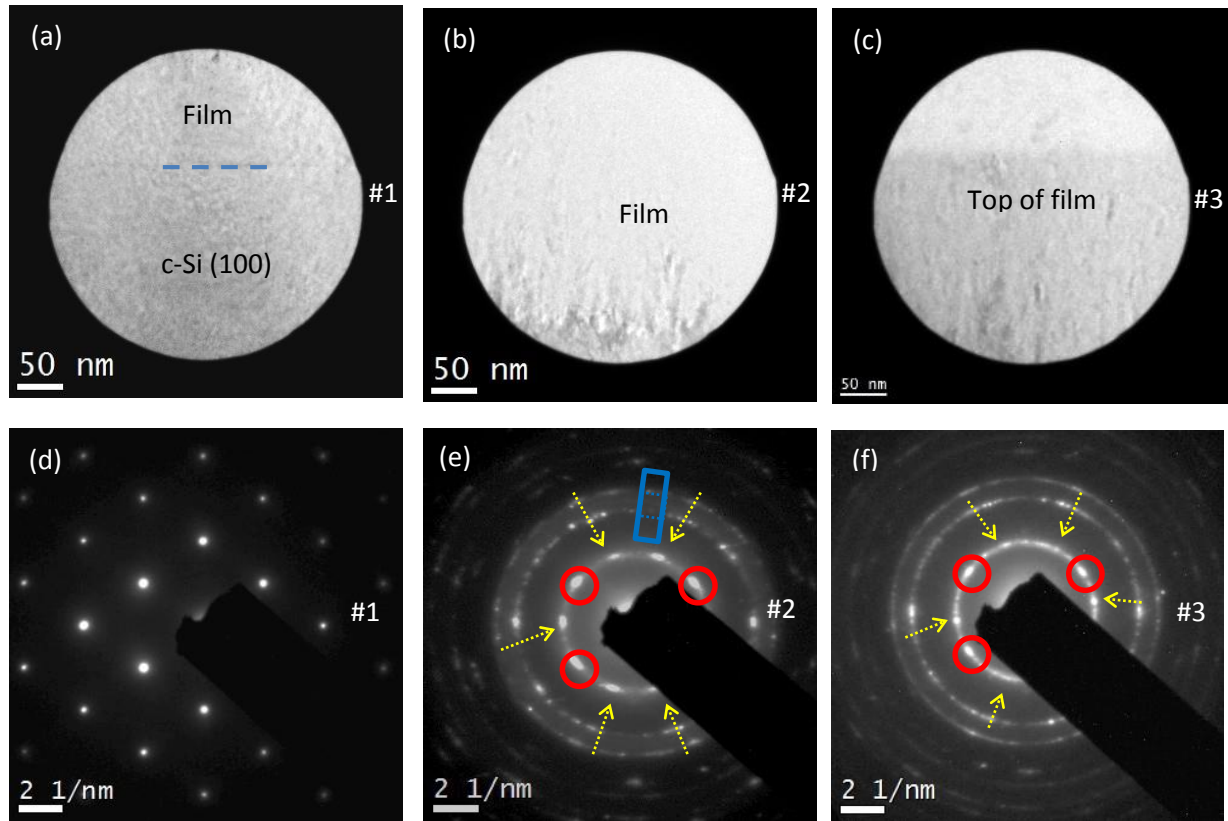


Figure 53. (a), (b) and (c) TEM images showing the areas selected for the EDPs shown in (d), (e) and (f), respectively. (d) shows a perfect monocrystalline structure in region #1, (e) shows the monocrystalline orientation of the wafer (circled in red), twin orientations (indicated by yellow arrows), random microcrystalline orientations and amorphous contribution, in region #2. (f) is somehow similar to (e) but with a larger contribution of random microcrystalline, in region #3.

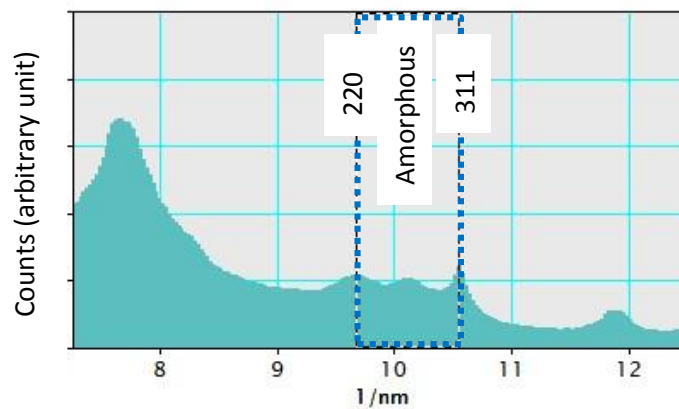


Figure 54. Profile of the blue rectangle in Figure 53(e) showing a small peak related to amorphous contribution in the film. It corresponds to the diffused part between 220 and 311 rings.

The top of the film is characterized in Figure 53(f). We can clearly observe a larger contribution of random microcrystalline in the detriment of twin contribution. Surprisingly, the substrate orientation (red circles) is still visible.

The HRTEM image of Figure 55 confirms the high quality epitaxy of the film in the first few tens of nm of growth. Despite that the film/ substrate interface is marked by a dark contrast in the low magnification image of Figure 52, it is hardly noticeable on the high resolution image of Figure 55. After a certain thickness of epitaxial growth, a dark contrast related to a high density of defects appears in a V-shape, as depicted in Figure 56.

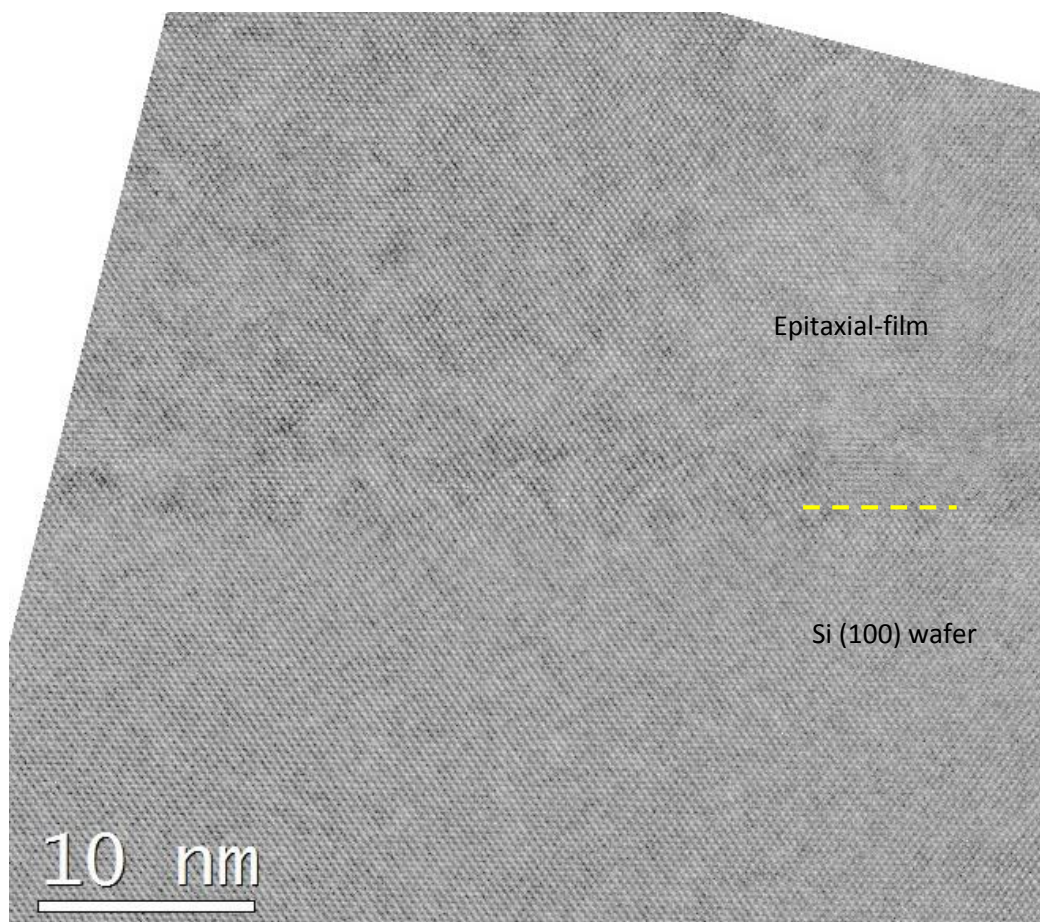


Figure 55. HRTEM image confirming epitaxial growth in the beginning of the film: $\{111\}$ planes are continuous from the wafer to the film across the interface.

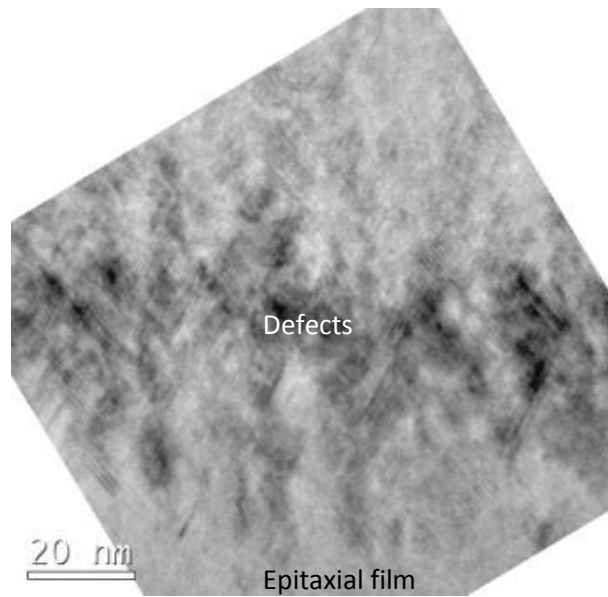


Figure 56. TEM image showing a high defect density after a certain thickness of epitaxial growth

4.2.1.2. Crystalline quality: correlating TEM and in-situ ellipsometry measurements

The growth of this layer was monitored by in-situ ellipsometry; the time evolution of the imaginary part of the pseudo dielectric function at 4.2 eV is shown in Figure 57. The signal of $\langle \epsilon_i \rangle$ can be classified into four regions as indicated in the same figure:

- Part 1 corresponding to a deposition time around 780 s ($t \sim 780$ s or a deposited thickness ~ 54 nm, given that the deposition rate is 0.7 \AA/S , see Figure 58), where $\langle \epsilon_i \rangle$ starts with a transient regime and stabilizes at around 35, it then decreases slowly to reach a value around 33.
- Part 2 corresponding to deposition time between $t \sim 780$ s and $t \sim 1620$ s (or a deposited thickness between ~ 54 nm and ~ 112 nm) where $\langle \epsilon_i \rangle$ undergoes a rapid drop and attains a value of 21. Since the TEM images (Figure 55) and EDPs (Figure 53) showed a good quality epitaxy for the first 120 nm (or $t < 1700$ s) of the film, the decrease in $\langle \epsilon_i \rangle$ in this part cannot be attributed to an epitaxy breakdown, it is rather attributed to an increasing surface roughness. We remind that $\langle \epsilon_i \rangle$ shown in Figure 57 is measured at 4.2 eV and so it has a penetration depth of 5 nm, which means that it is very sensitive to the surface state of the film.
- Part 3 corresponding to deposition time between $t \sim 1620$ s and $t \sim 3600$ s (or a deposited thickness between ~ 112 nm and ~ 248 nm) where $\langle \epsilon_i \rangle$ is stable at 21-20 (surface roughness is stable).

- Part 4 corresponding to deposition time $t > 3600$ s (or a deposited thickness > 248 nm) where a progressive drop of $\langle \epsilon_i \rangle$ is observed from 20 to 5, this is explained by an epitaxy breakdown. This part has a brighter contrast in TEM images indicating that amorphous growth occurred.

By correlating TEM observations and ellipsometry measurements, we can notice from Figure 58 that part 3, which initiates the transition to microcrystalline (part 4), displays a high density of defects (mainly twins) in the TEM image. In turn, part 3 is preceded by a roughening effect in part 2 which cannot be observed in our TEM images. Thus a correlation appears between twin formation and increased surface roughness.

Finally, to make sure that no plasma parameter has changed accidentally during the growth experiment (that could explain the sudden change in part 3), we monitored the time evolution of the plasma potential; it is shown in Figure 59. The plasma potential did not undergo an accidental change, it ranges between 52 and 58 V (with an average around 54 V), suggesting that the modification of the structure is most likely due to the growing material and not to an issue in the deposition chamber.

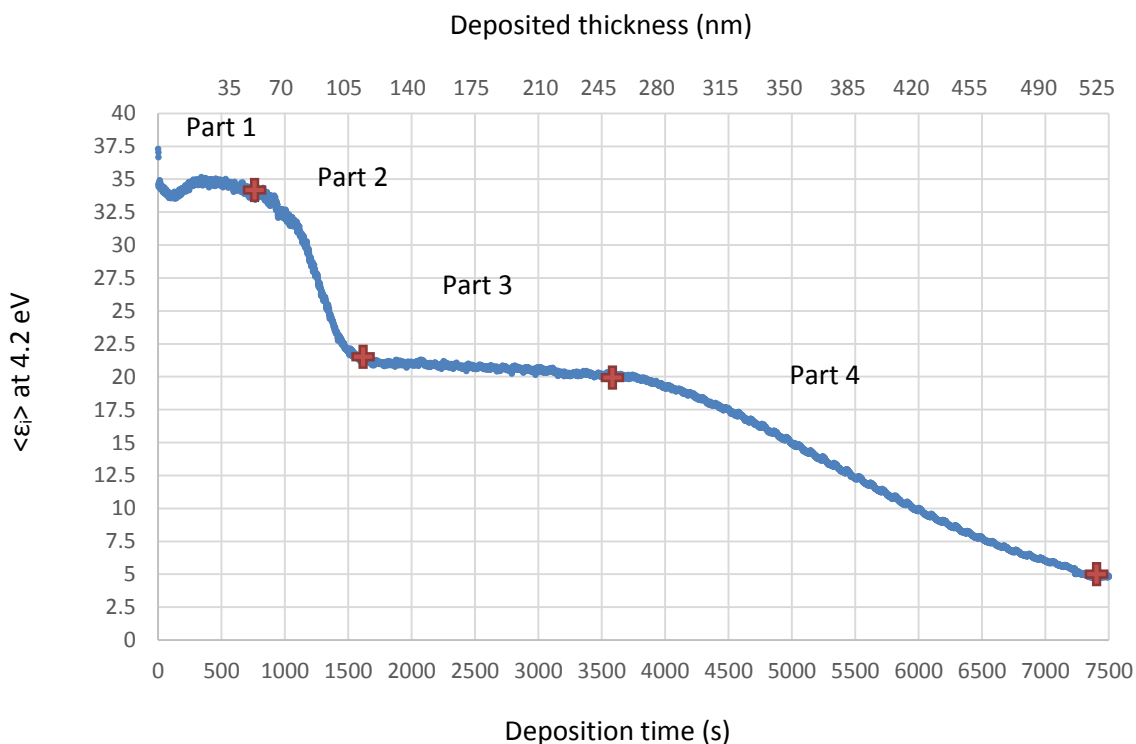


Figure 57. Time evolution of the imaginary part of the pseudo-dielectric function $\langle \epsilon_i \rangle$ measured at 4.2 eV, for the sample deposited using a RF power of 20 W and a H₂ flow rate of 1 sccm.

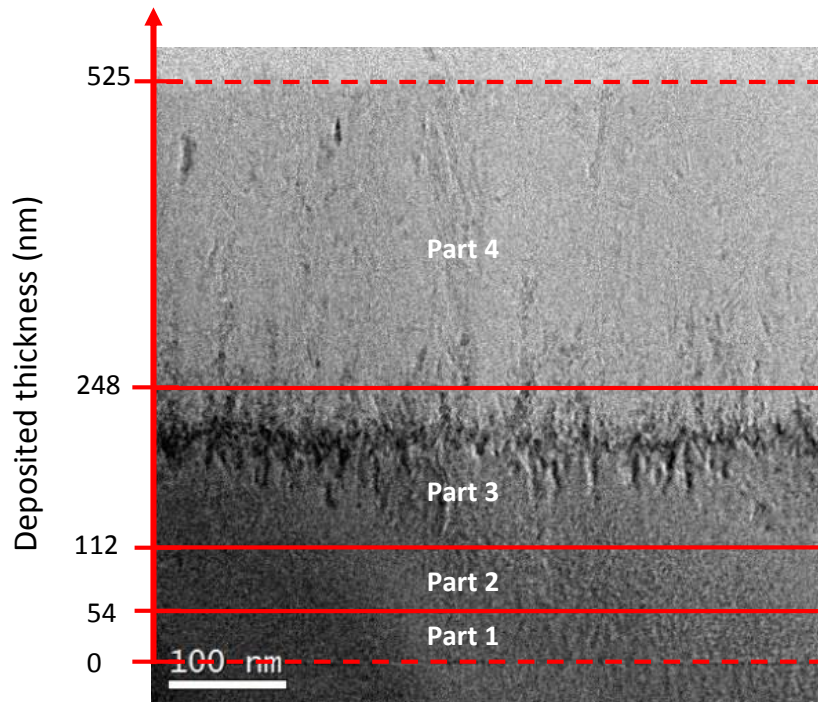


Figure 58. Decomposition of the film deposited at 20 W and 1 sccm of H_2 flow rate, into four parts in the light of the ellipsometry measurements of Figure 57.

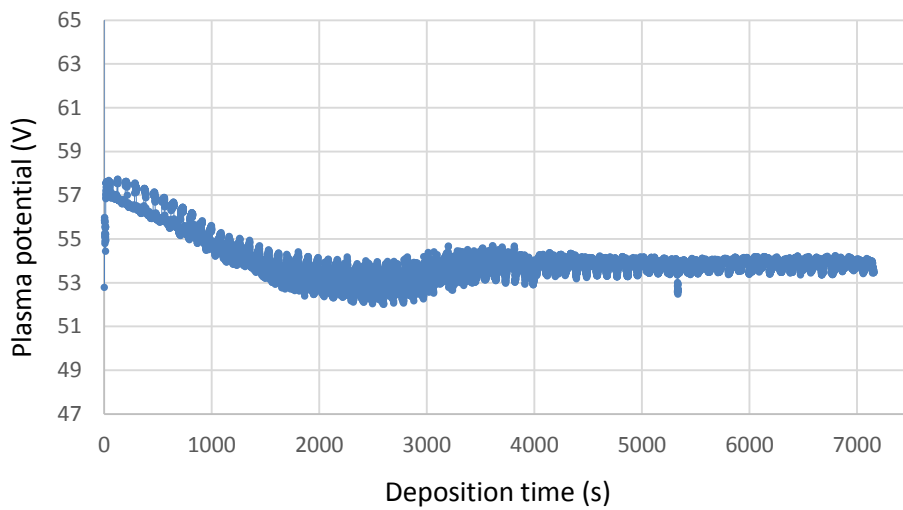


Figure 59. Plasma potential as a function of the deposition time for the film grown using a RF power of 20 W and a H_2 flow rate of 1 sccm.

4.2.2. RF Power of 25 W on Si (100) and Si (111) substrates

4.2.2.1. On Si (100)

4.2.2.1.1. Crystalline structure evolution from TEM observations

The structure of the films deposited with a RF power of 25 W, on Si (100), is shown in Figure 60. The entire film undergoes a complete change after a certain thickness (~ 870 nm in this case), it is similar, to some extent, to that deposited at 20 W. In the following, we present a detailed investigation on the evolution of the film structure with thickness by the means of TEM.

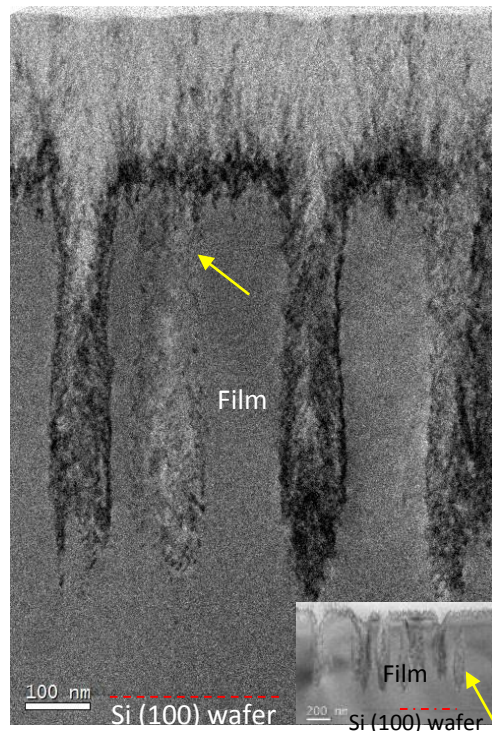


Figure 60. TEM image of the film deposited using a RF power of 25 W and a H₂ flow rate of 1 sccm.

Epitaxial growth can be clearly observed at the film/substrate interface, as shown in Figure 61. {111} planes continue from the substrate to the film across the dark interface and it is hard to notice a difference between the structure of the film and that of the wafer.

Within the monocrystalline matrix, defects appear as V-shapes starting from a distance about 110 nm from the interface, and continue in columnar structures (Figure 60). Figure 62 shows a HRTEM image corresponding to such defects and the FFTs of two regions outside and inside the columns (blue and red squares, respectively). The FFT of the blue square exhibits spots corresponding to the substrate orientation, whereas the FFT of the red square exhibits the signature of twinned orientations (in addition to substrate orientation). It is important to note that, sometimes, the twin

part can be healed or may disappear with thickness (see arrows in Figure 60), to the benefit of a monocrystalline structure.

The density of twin defects reaches a maximum at a distance of 780 nm from the interface. An EDP similar to that shown in Figure 54(b) characterizes this region.

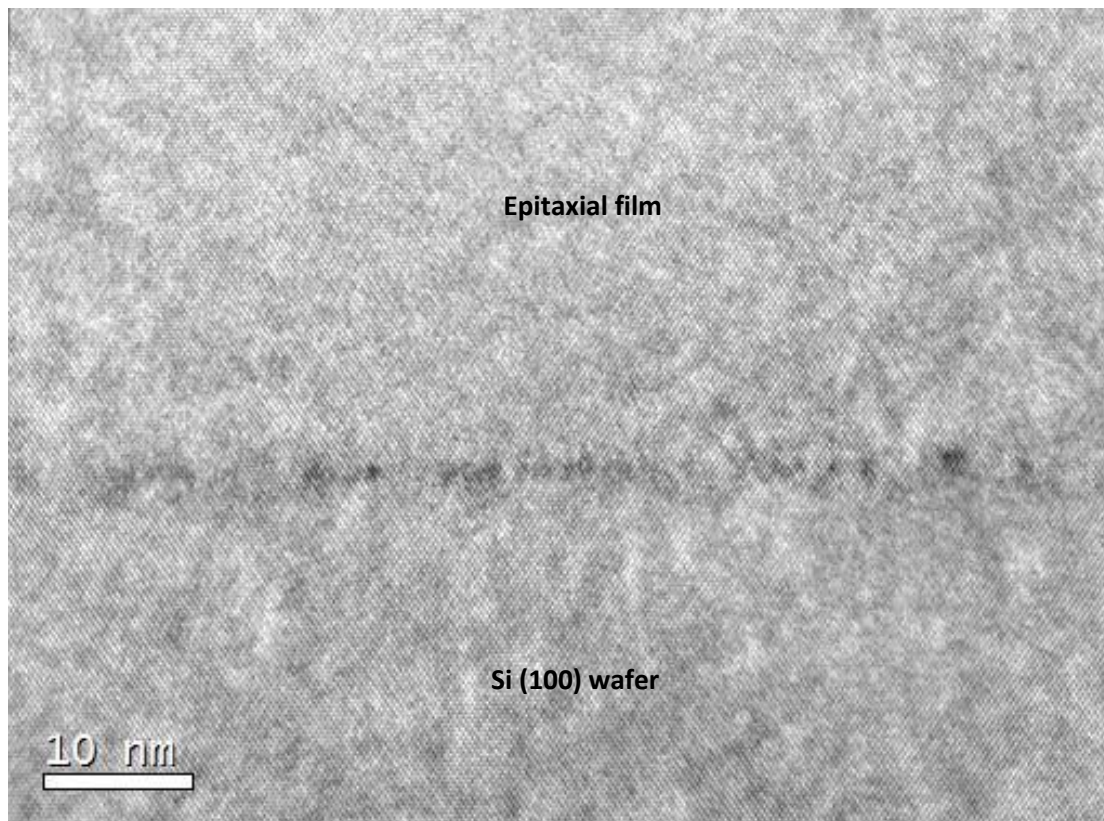


Figure 61. HRTEM image revealing epitaxy in the beginning of the film deposited using a RF power of 25 W and a H₂ flow rate of 1 sccm.

In order to study how epitaxy breaks down, we recorded an EDP (Figure 63(b))- using an aperture selecting a diameter of 210 nm on the top of the film - (Figure 63(a)). It shows a mixture of intense monocrystalline and twin spots, and less visible amorphous and microcrystalline contributions. An FFT (Figure 63(c)) selecting a square area of 40 × 40 nm² (red rectangle) allows us to better visualize the random microcrystalline and the amorphous contribution.

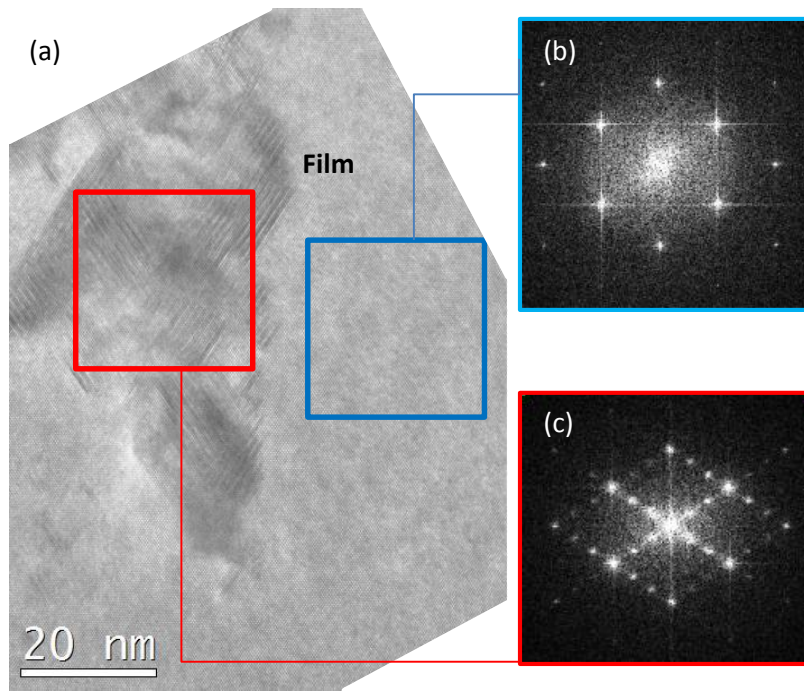


Figure 62. HRTEM image showing a V-shaped defect formed within the monocrystalline matrix in the film. (b) and (c) are FFTs performed on the matrix and on the defective region, respectively.

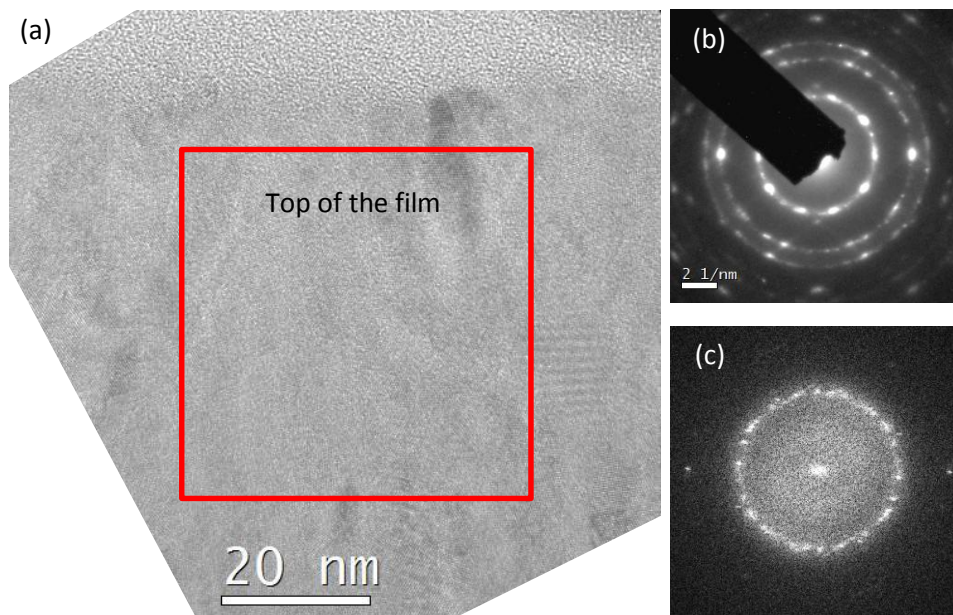


Figure 63. (a) HRTEM image taken from the top of the film, (b) EDP recorded on the top of the film including an area of 210 nm in diameter and dominated by monocrystalline and twin orientations (c) FFT corresponding to the red square showing microcrystalline and amorphous contributions.

4.2.2.1.2. Crystalline quality: correlating TEM and in-situ ellipsometry measurements

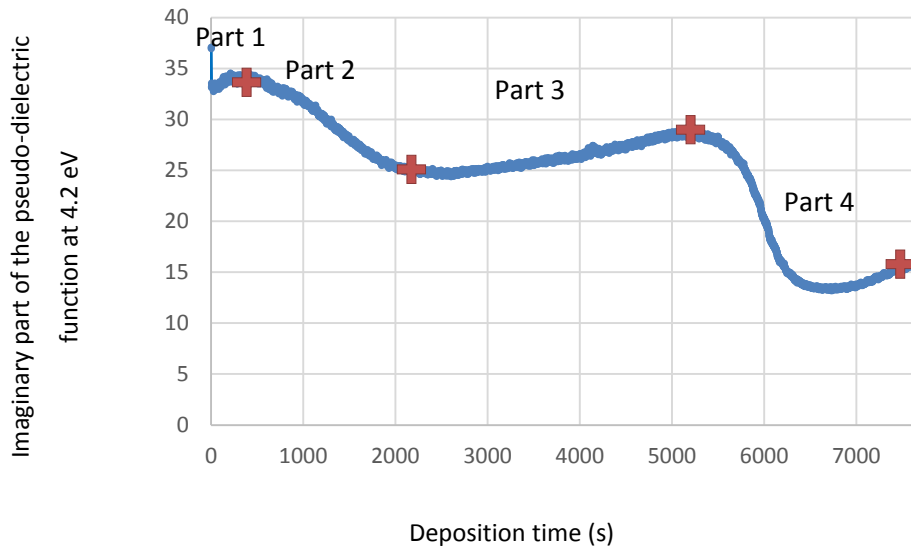


Figure 64. In-situ ellipsometry measurements monitoring the evolution of the film growth.

The signal of $\langle \epsilon_i \rangle$ is shown in Figure 64, it is complicated in this case but reveals a rapid decrease around $t= 500$ s and $t= 5400$ s. The first decrease might be related to the formation of the defective columnar structures within the monocrystalline matrix and the second one might be related to the onset of breakdown of epitaxy of the entire film. We can already distinguish four parts as indicated in this figure. The same analysis as that in section 4.2.1.2 applies here to some extent.

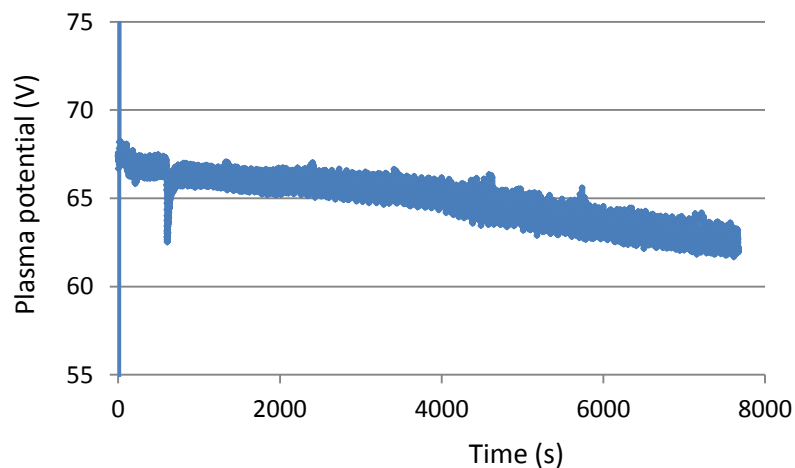


Figure 65. Plasma potential as a function of the deposition time for the film deposited using a RF power of 25 W and a H_2 flow rate of 1 sccm.

By checking the time evolution of the plasma potential (Figure 65), we have also verified, in this case, that no accidental change in the growth chamber has occurred during deposition. The plasma potential ranges between 62 and 68 V with no accidental change. The plasma potential here (for films deposited at 25 W) has a averaged value around 64 V, which is higher than that for films deposited using a RF power of 20 W (54 V).

4.2.2.2. On Si (111)

4.2.2.2.1. Crystalline structure evolution from TEM observations

TEM images of the films deposited on Si (111) at 25 W and 1 sccm of H₂ flow rate are presented in Figure 66. They show an epitaxy start (Figure 66(b)) then a breakdown evidenced by the bright part in Figure 66(a).

The evolution of the crystalline fraction is summarized in Figure 67. This figure shows that epitaxy occurred over ~ 25 nm, this result is quite interesting on Si (111) substrate. Epitaxy is broken down in this case also for the benefit of twin orientations, random microcrystalline orientations and amorphous growth; this is shown by the EDP in Figure 67(a), recorded on the white dotted circle in Figure 66(a). Twin orientations are indicated by arrows whereas substrate orientations are represented by red circles in the same figure. The subsequent growth is a mixture of microcrystalline and amorphous contributions as shown by the EDP of Figure 67(b) taken from the top of the film over a thickness of 750 nm. Note that the amorphous contribution is deduced from the diffused part between 220 and 311 rings in both patterns of Figure 67.

In order to better understand the crystalline structure around the dark regions appearing as “flames” in Figure 66(a), we performed FFTs inside one flame and outside it. The FFTs show that the dark parts (squares 1 and 2) are characterized by the presence of twinned orientations, besides monocrystalline orientations. The brighter regions outside flames (square 3) contain random microcrystalline and amorphous structure.

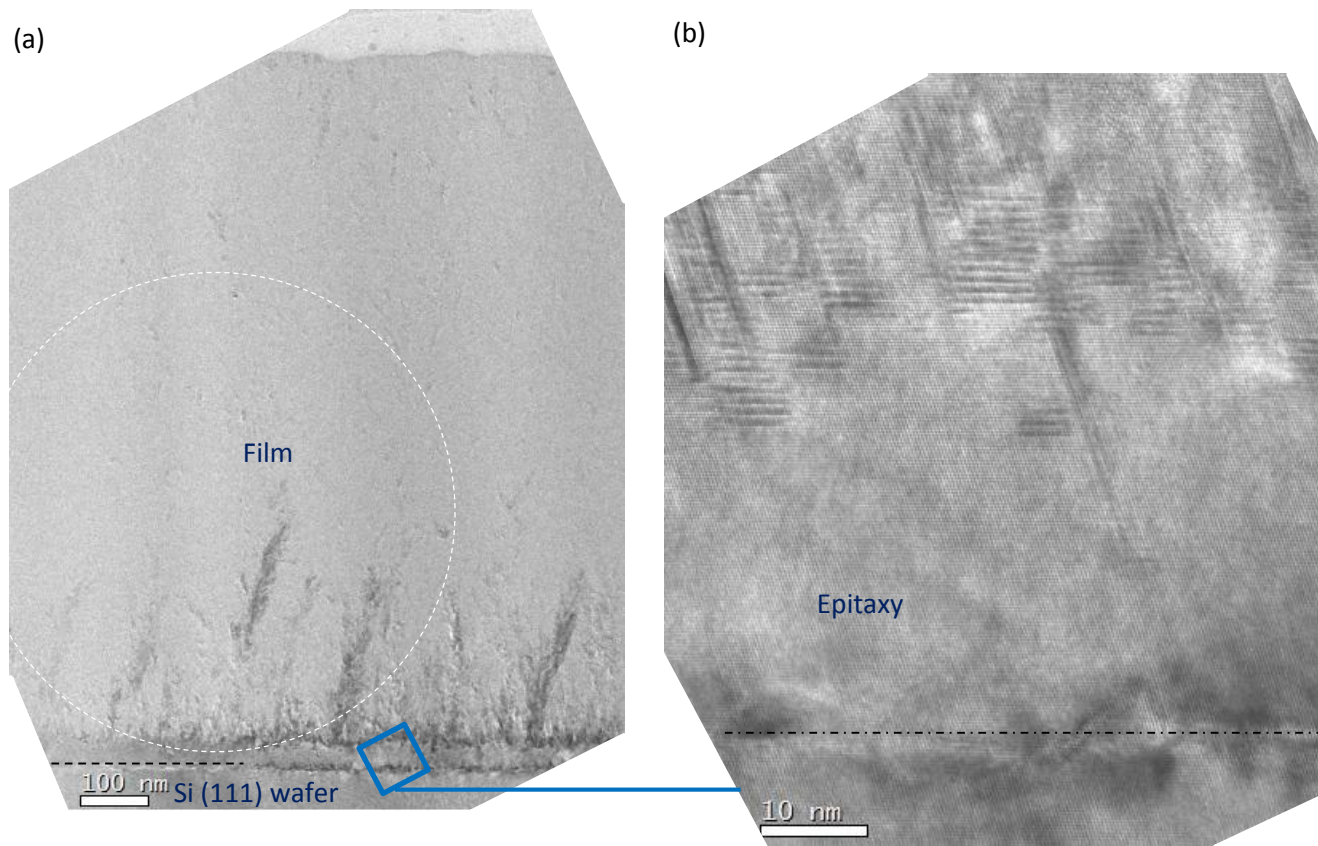


Figure 66. (a) TEM image of the sample deposited on Si (111) wafer using a RF power of 25 W and a H_2 flow rate of 1 sccm. The region of the film near the interface is enlarged in (b), it shows an epitaxial growth for the first 25 nm of the film growth.

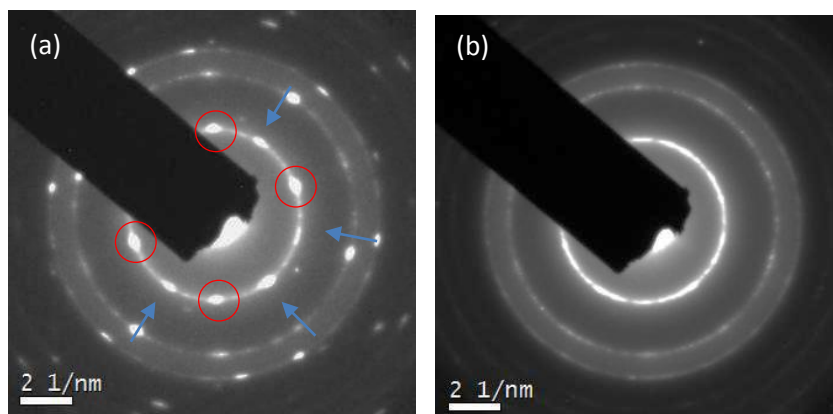


Figure 67. (a) EDP taken from the white dotted circle in Figure 66(a), it shows the presence of the monocrystalline wafer orientation (111 spots in red circles), twin orientations (indicated by arrows), random microcrystalline orientations and amorphous contribution. (c) EDP taken from the top of the film, it shows the presence of microcrystalline and amorphous phases.

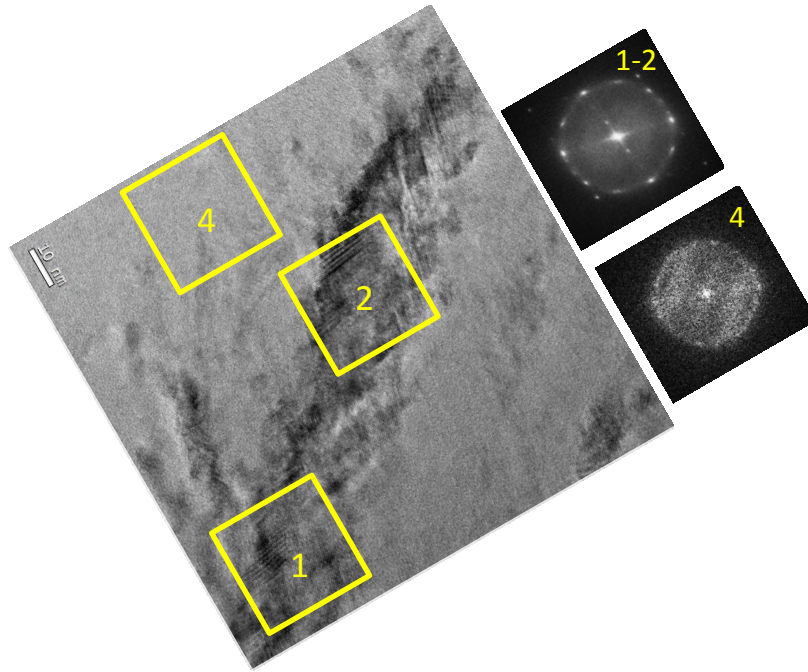


Figure 68. FFTs performed inside the flame and outside it. The dark region corresponds to monocrystalline and twin orientations, whereas the brighter is composed of amorphous and microcrystalline phases.

4.2.3. Summary of the results – epitaxy and breakdown by increasing the RF power

In this section, we give in Figure 69 a summary of the TEM observations concerning the effect of increasing the RF power from 15 W to 20 and 25 W on Si (100) substrates. The growth rate increased from 0.6 Å/s for 15 W, to 0.7 Å/s for 20 W and reached 1.4 Å/s for 25 W. The epitaxy breakdown is observed at 20 and 25 W, it was found to be related with surface roughening.

Epitaxy breakdown occurred by two steps: (i) formation of twin defects and stacking faults (onset of breakdown), and (ii) formation of a microcrystalline and amorphous phase (through secondary nucleation). Once the latter phase is established, epitaxy is completely lost and so the step (ii) is irreversible. Whereas, sometimes, the twin defects can be healed or may disappear with thickness (see the arrow in Figure 69), and so the step (i) can be reversible and this means that an “*epitaxy comeback*” is possible. This result is very interesting and may open new windows for research: when do we have an epitaxy comeback? and how is it possible? Finally, based on our results, Figure 70 would describe epitaxy breakdown and epitaxy comeback mechanisms.

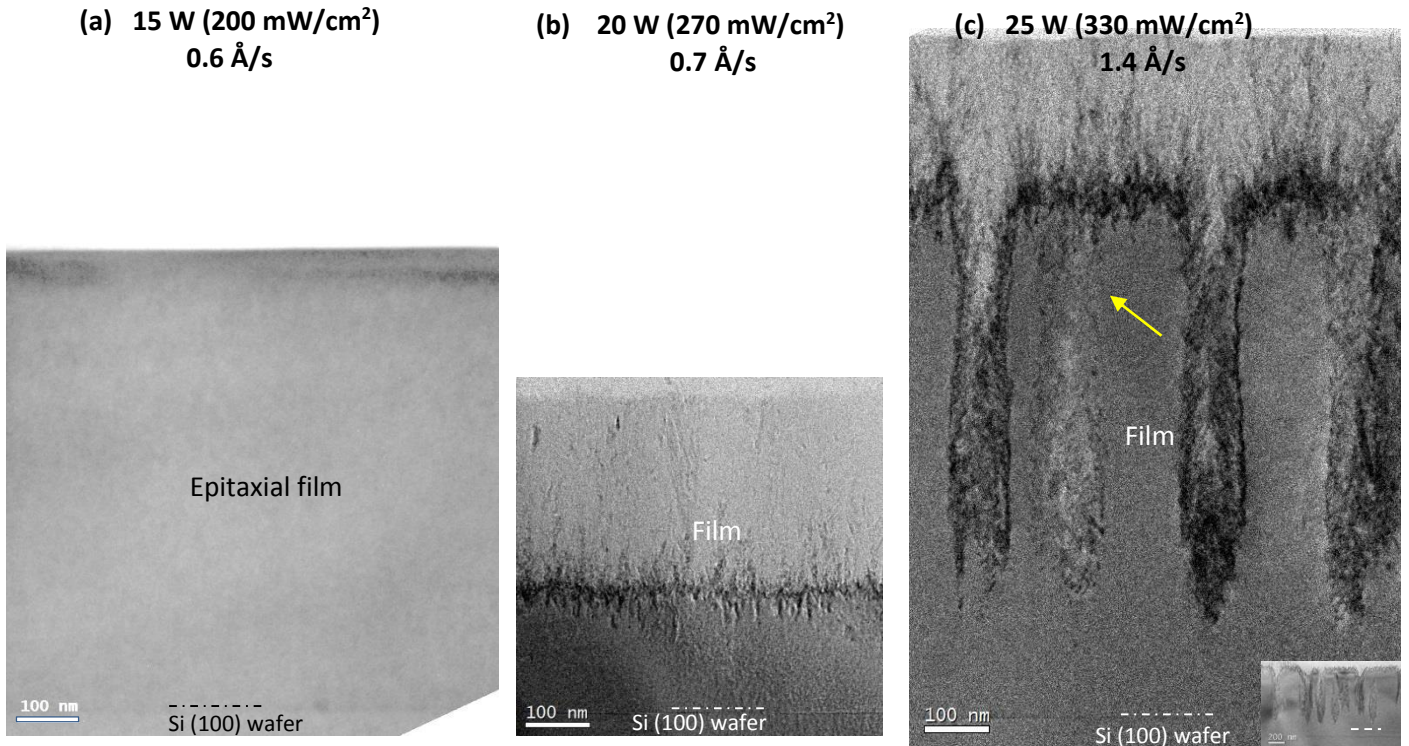


Figure 69. Summary of images corresponding to epitaxy (a) and epitaxy breakdown (b) and (c) for samples deposited on Si (100) using a H_2 flow rate of 1 sccm and different RF powers (15 W in (a), 20 W in (b) and 25 W in (c)).

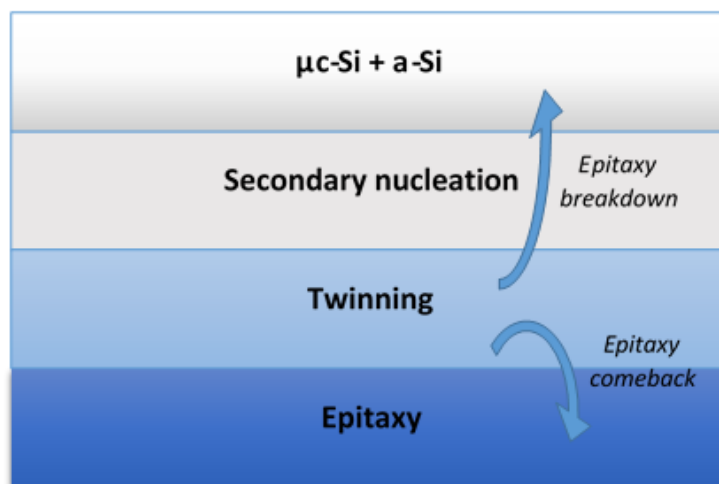


Figure 70. Description of epitaxy breakdown and *epitaxy comeback* mechanisms, on the basis of the TEM observations in this chapter. Epitaxy breakdown occurs by (i) twinning followed by (ii) formation of a microcrystalline and amorphous phase. Twinning can be reversible and so *epitaxy comeback* is sometimes possible.

4.3. Intentional epitaxy breakdown with increasing the H₂ flow rate

In this section, we study the epitaxy breakdown phenomena induced by increasing the flow rate of H₂. For this, we study the influence of using a H₂ flow rate of 2 and 3 sccm, knowing that perfect epitaxy was obtained using 1 sccm. Only (100) oriented Si was used here.

4.3.1. Hydrogen flow rate of 2 sccm on Si (100) wafers

4.3.1.1. Crystalline structure evolution from TEM observations

The layer deposited using a RF power of 15 W for a H₂ flow rate of 2 sccm includes a high density of planar defects, as shown in the conventional TEM image of Figure 71(a). A thinner cross-sectional TEM foil is presented in Figure 71(b) to better visualize these defects. At first sight, the film grew epitaxially over $\sim 2.46 \mu\text{m}$ since it presents the same contrast as the substrate; however it contains a high density of two types of defects: i) extended defects propagating from the interface to the film surface but also, ii) relatively small defects (250-500 nm). The interface is visible by a dark contrast between the film and the substrate.

The fact that the defect density is higher for the thicker TEM foil of Figure 71(a) can be attributed to the presence of a bigger quantity of matter in the thicker foil. The oblique defects seem to have a smaller length (250-500 nm) in the thinner foil, as the foil surfaces cut more of the defects in that case. These defects will be described in details after studying the evolution of the crystalline structure with the deposited thickness.

Diffraction patterns were recorded, on two zones of the film as depicted in Figure 71(b), to characterize the crystalline quality. One is recorded on a region including the wafer and the film, and the other one on the top of the film (and glue) as indicated by the white dotted circles in Figure 71(b). Both EDPs (Figure 72) reveal the signature of a monocrystalline film that follows the orientation of the substrate (epitaxy) without breakdown. It is clear and remarkable that the crystalline structure of the film is still monocrystalline despite the presence of a high density of defects.

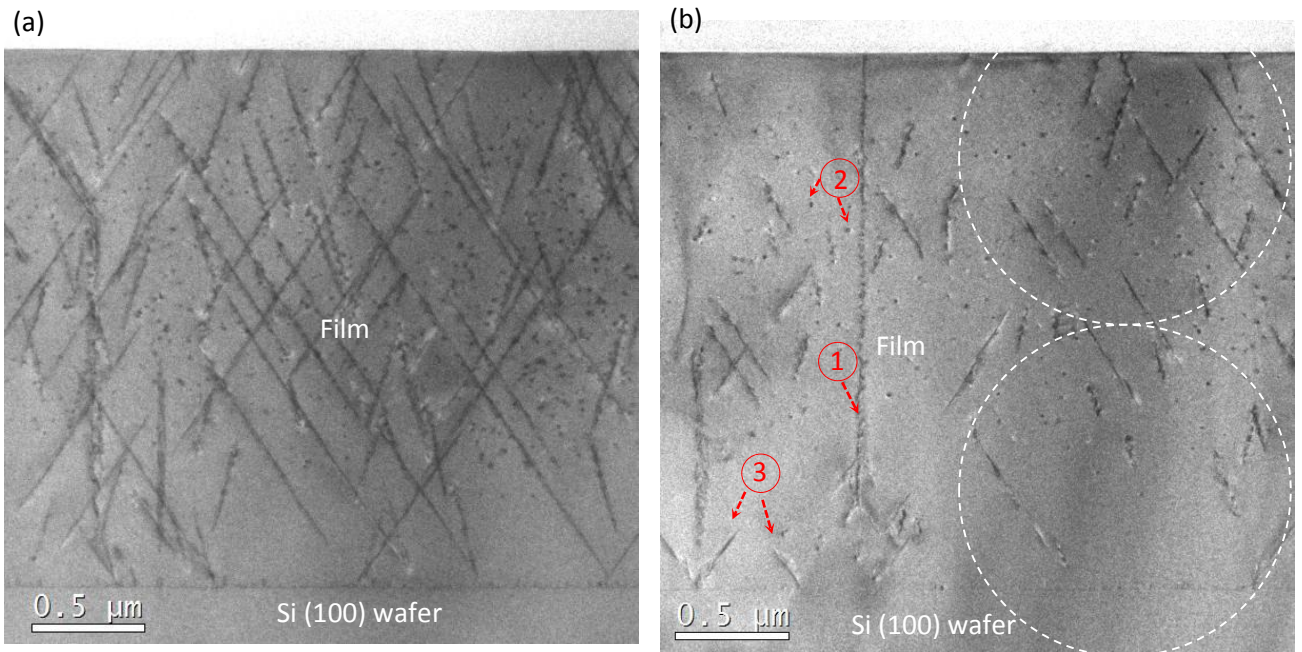


Figure 71. TEM images of the sample deposited on Si (100) using a RF power of 15 W and a H_2 flow rate of 2 sccm; (b) corresponds to a thinner region of the foil. White dotted circles in (b) indicate the areas selected for the EDPs shown in Figure 72. Numbers refer to defects discussed in the text.

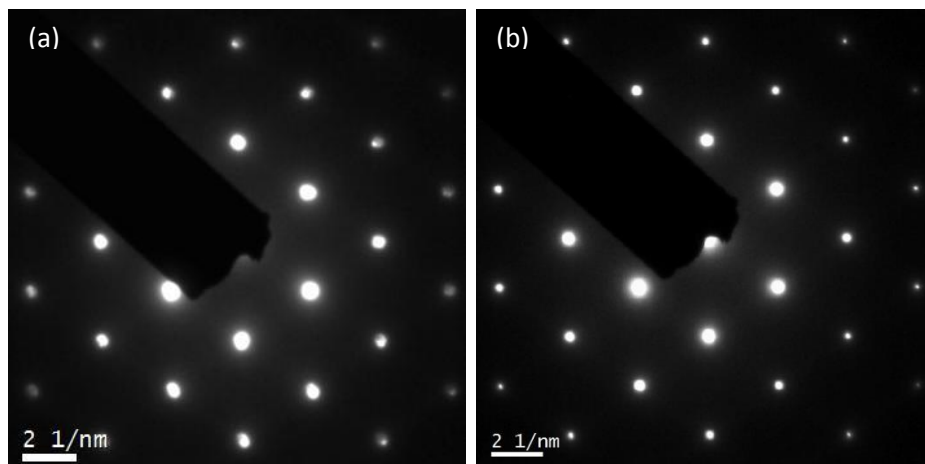


Figure 72. Diffraction patterns recorded on a region including (a) the wafer and the film and (b) the top of the film, as indicated by the white dotted circles of Figure 71.

From a zoom on the defects, we can extract the following points:

- The vertical line numbered 1 in Figure 71(b) presents a lot of Moiré fringes as shown by the HRTEM image of Figure 73, characteristic of twins having a boundary that does not follow $\{111\}$ mirror planes. Twin spots are indeed present in the FFT (see arrows in the inset of Figure 73) corresponding to the defective zone. Some of these defects propagate over 1 or 2 μm .

- The defects numbered 2 in Figure 71(b) are enlarged in Figure 74. These are about 10 nm sized platelets following $\{111\}$ planes. There are a lot of such platelets in the film starting from about 450 nm above the interface up to about 150 nm from the top of the film. They are surrounded by a dark contrast that has been reported in some studies [69] as a strain field due to a high concentration of hydrogen in the film (see Figure 47). Furthermore, the platelet in Figure 74 is not strictly limited to a single $\{111\}$ plane but migrates to adjacent $\{111\}$ planes.
- The defects numbered 3 in Figure 71(b) are stacking faults that follow $\{111\}$ planes. Interestingly, they display a white and black contrast from each side of the defects (Figure 75), we expect that this is due to some dislocations decorated by hydrogen as in reference [109].

It is important to notice that the stacking faults and the platelets following $\{111\}$ planes are the dominant features of these epitaxial layers, and this is expected since in general, in the case of epitaxial growth on (100) FCC crystals, most of the defects lie in the $\{111\}$ family planes and this is the case of these defects. A detailed discussion on these defects will be presented in section 4.4.2.

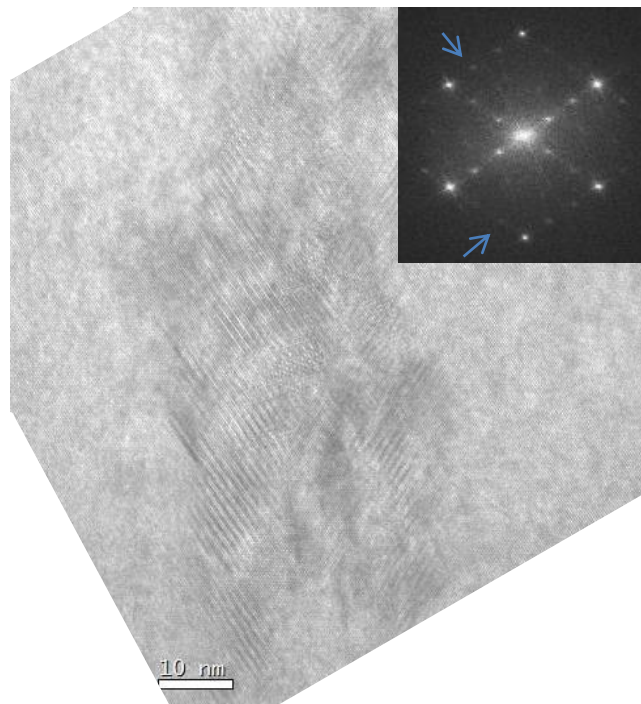


Figure 73. Defects numbered 1 in Figure 71(b) exhibiting Moiré fringes (due to stacking faults and twins). The inset corresponds to the FFT of this image, it shows monocrystalline and twin spots.

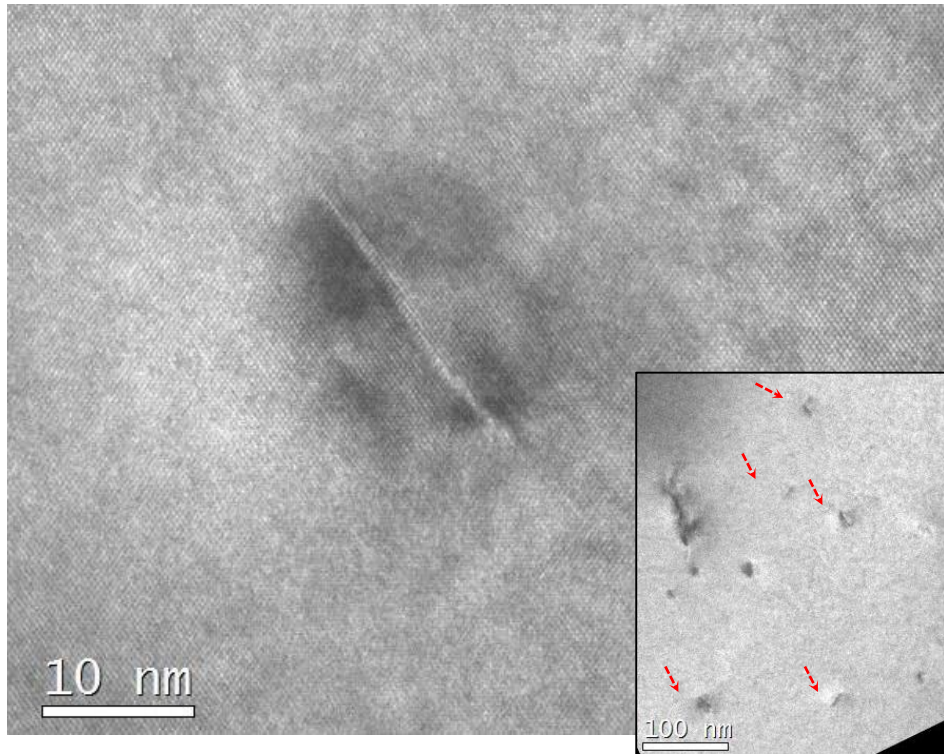


Figure 74. Defects numbered 2 are platelets following $\{111\}$ planes and having a size of the order of 10 nm. In the inset, arrows indicate the presence of a lot of platelets within the film

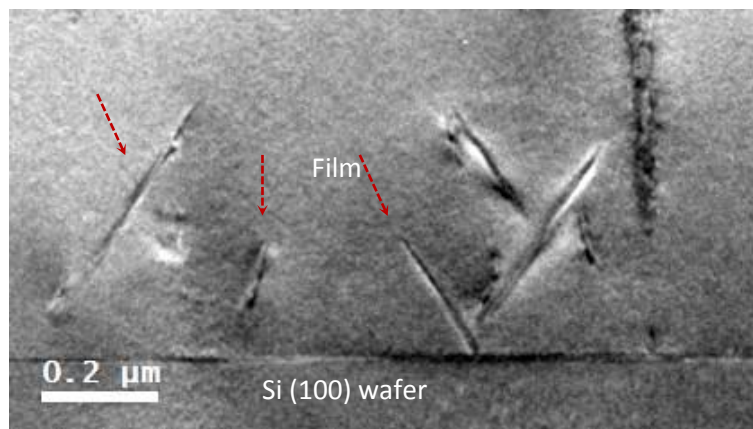


Figure 75. Defects numbered 3 are indicated by arrows, these are stacking faults following $\{111\}$ plane and displaying a strange contrast. They could correspond to dislocations decorated with hydrogen.

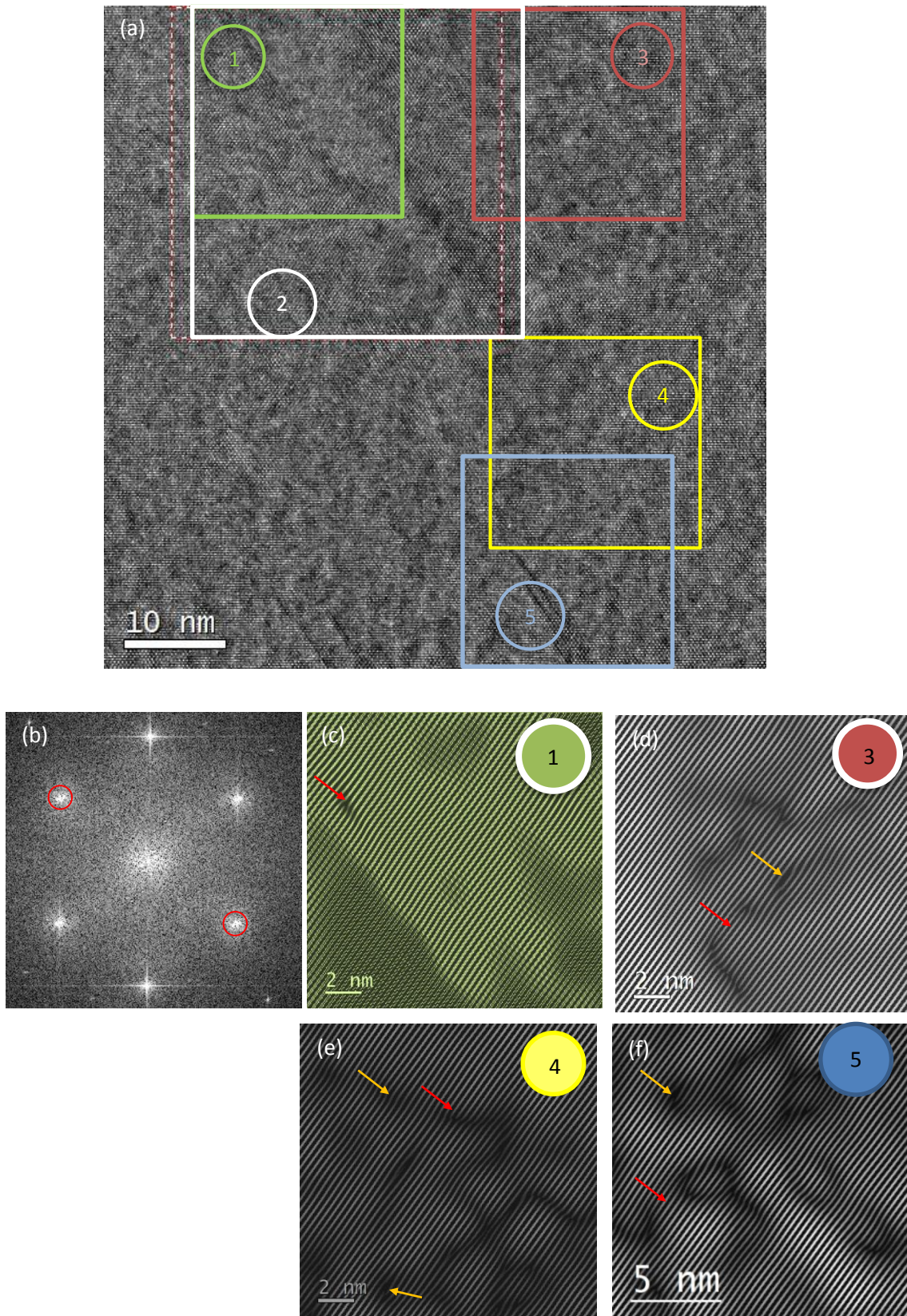


Figure 76. HRTEM image (a) and its associated diffractogram (b) where we selected (using masks of 0.7nm^{-1} in diameter) two 111 spots to obtain the filtered images in (c), (d), (e) and (f). Yellow arrows point at lattice distortions and the red ones at dislocations.

We now characterize some displacement field around defects (at a distance of ~ 50 nm from the interface) by using Fourier filters (Figure 76). We used masks on two 111 spots of the diffractogram (Figure 76(b)) associated with the HRTEM of Figure 76(a), to obtain filtered images as shown in Figure 76(c), (d), (e) and (f). The numbers in Figure 76(a) indicate the regions from where the filtered images are taken from. We can notice that the (-111) family of planes shows important distortions (yellow arrows), and several dislocations (red arrows). The loss of fringe contrast is the result of a high degree of disorder in the lattice and the phase shifts between fringes are associated with dislocations. We also found such defects on {200} planes as shown in Figure 77.

Thus, the presence of dislocations is confirmed. Moreover, the defects are found on adjacent {111} planes and not limited to a single plane, this would clarify why some fringes are curved or deformed.

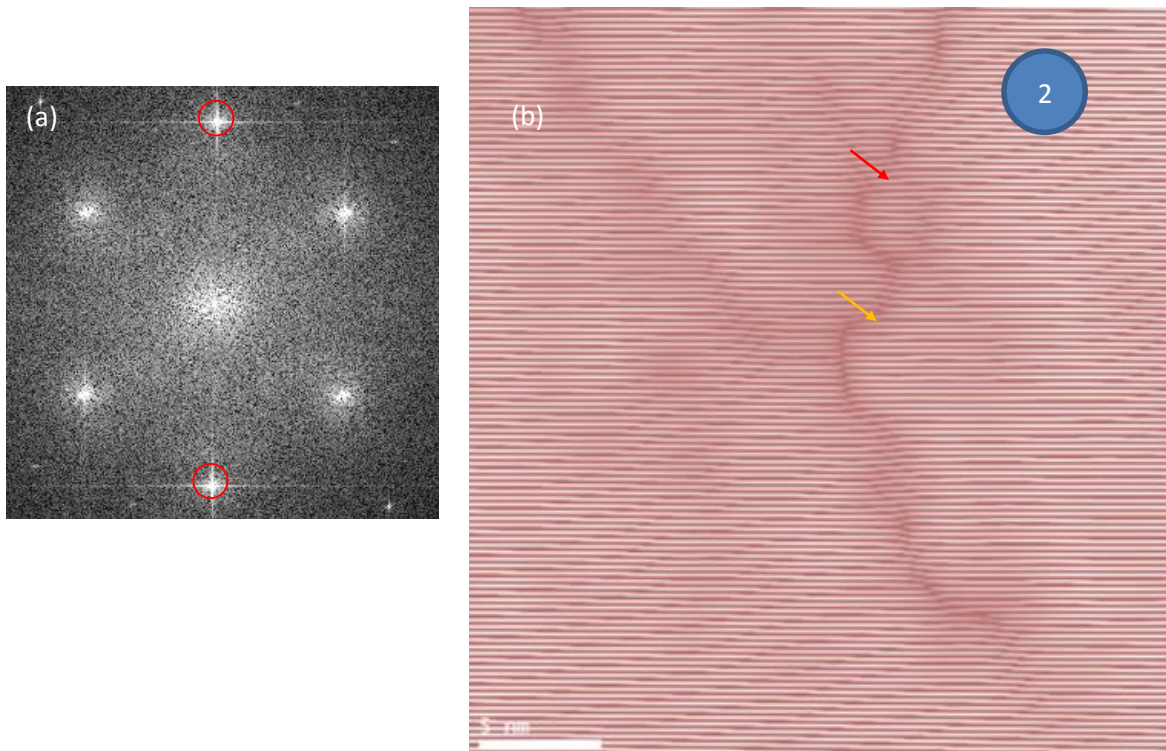


Figure 77. Selection of two 200 spots in the diffractogram (a) to form the filtered image (b).

4.3.1.2. Crystalline quality: correlating TEM and in-situ ellipsometry measurements

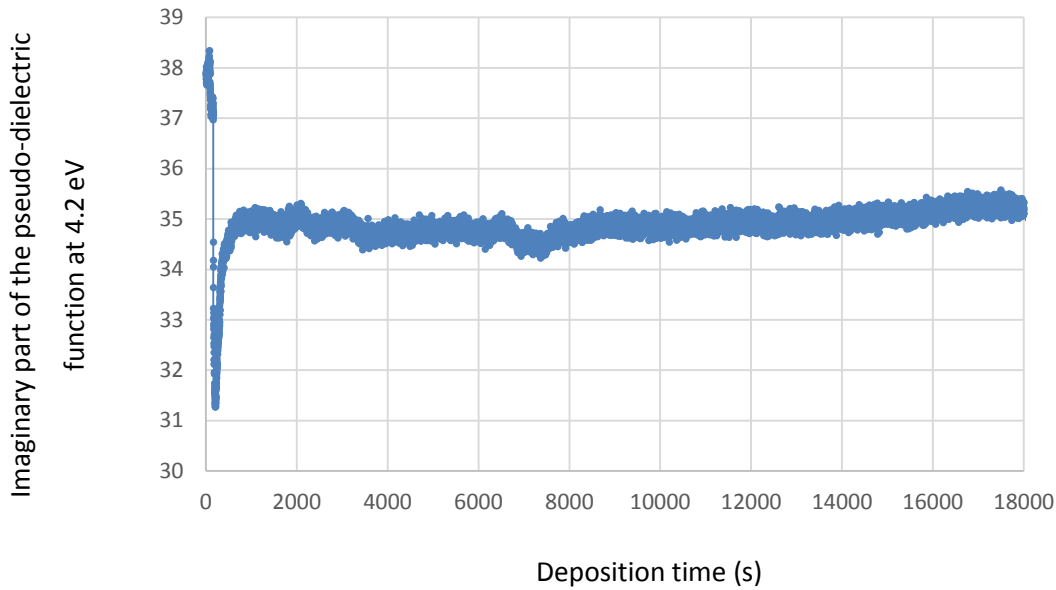


Figure 78. In-situ ellipsometry measurements monitoring the evolution of the film deposited using a RF power of 15 W and a H₂ flow rate of 2 sccm.

In-situ ellipsometry measurements indicate a stable signal at about 35 (in the steady-state regime), which means that epitaxial growth occurred (with an almost constant roughness). This result is in agreement with the EDPs of Figure 72.

4.3.2. Hydrogen flux of 3 sccm on Si (100) wafers

4.3.2.1. Crystalline structure evolution from TEM observations

The microstructure of the film deposited using a RF power of 15 W and a H₂ flow rate of 3 sccm is quite different from the previous sample (15 W and 2 sccm) as shown in Figure 79. The dark contrast in the film suggests that it is not monocrystalline anymore. In the following, we provide details on the evolution of the microstructure.

At the film/substrate interface, some defects are present like the {100} platelets visible in Figure 80; the other dark defects are most likely platelets that could be better visualized by tilting the sample under the electron beam during TEM experiments. The first 20 nm of the film appear to grow epitaxially (Figure 81(a)), then V-shaped defects are generated. They initiate a highly defective region of about 700 nm as in the case of the samples deposited at high power (Figure 56(a) and Figure 62). Figure 81(b) is taken from a very thin region of the TEM foil, it allows us to see {111} stacking faults like the defects numbered 3 in Figure 71. In addition, we can notice columnar structures growing through the film.

The defective region corresponds to a highly twinned structure, according to Figure 82 that shows a HRTEM image of this region and its corresponding EDP in the inset.

Finally, the white region near the top of the film is associated with amorphous and random microcrystalline growth, as confirmed by selected area EDPs (not shown here). The presence of an amorphous phase is the sign of an epitaxy breakdown occurring in the case of the sample due to a high flow rate of hydrogen.

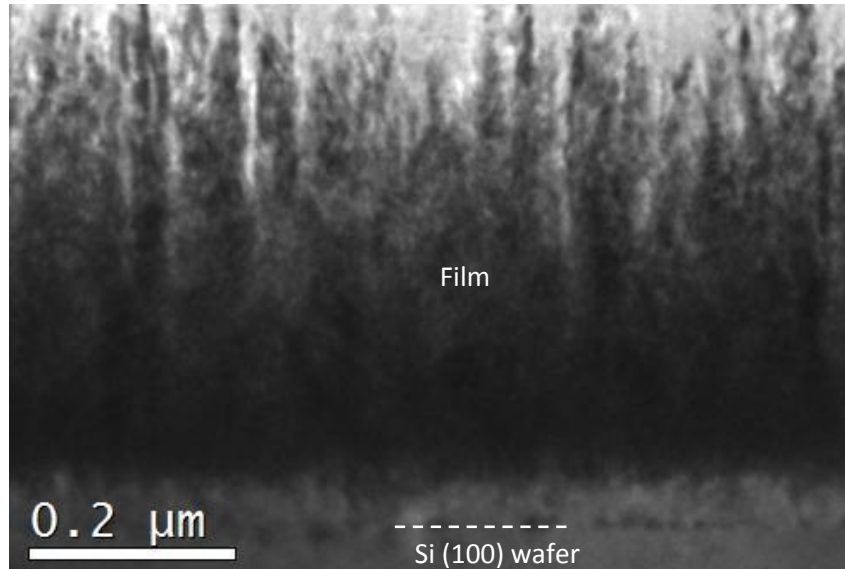


Figure 79. TEM image of the sample deposited on Si (100) using a RF power of 15 W and a H_2 flow rate of 3 sccm.

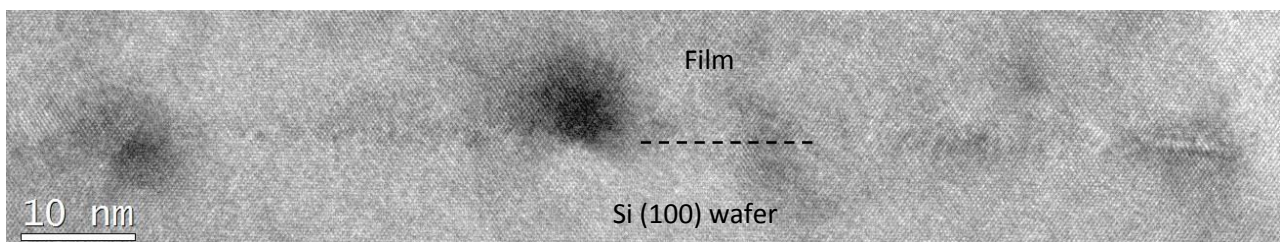


Figure 80. HRTEM image of the interface exhibiting some defects which are most likely hydrogen platelets.

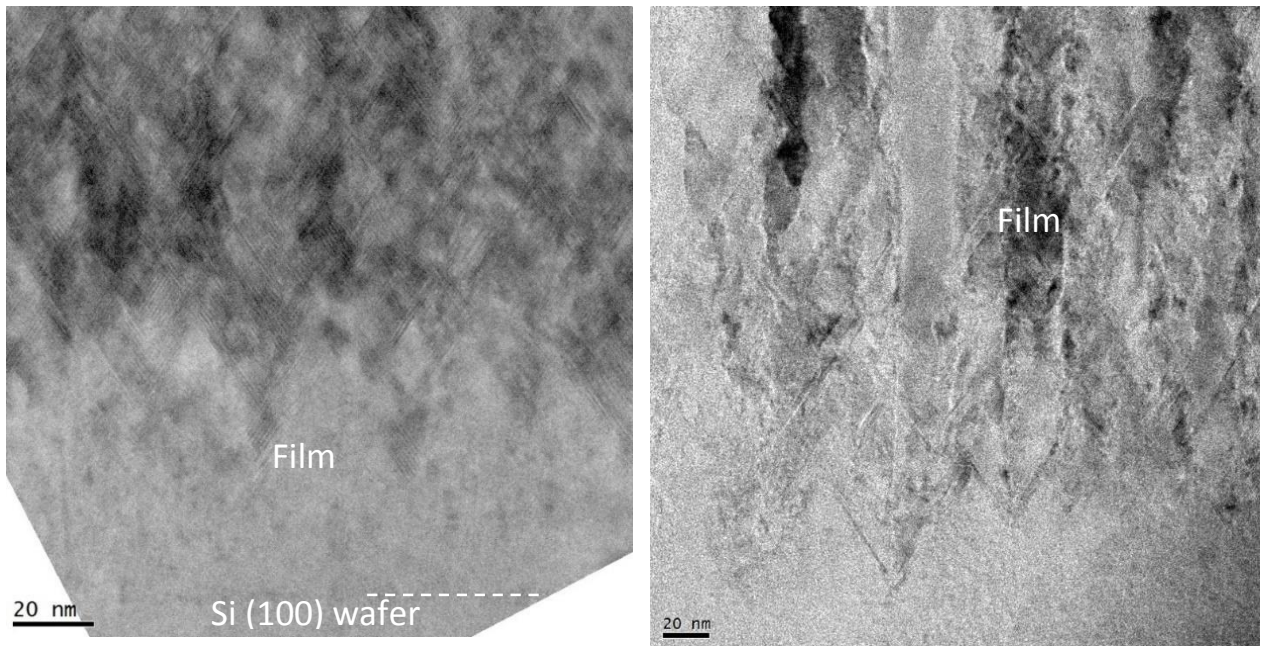


Figure 81. (a) TEM image showing the same crystalline structure in the first 20 nm of the film and in the wafer, then V-shaped defects appear initiating a highly defective region. (b) TEM image recorded on a thinner region of the TEM foil allowing us to better visualize the defects.

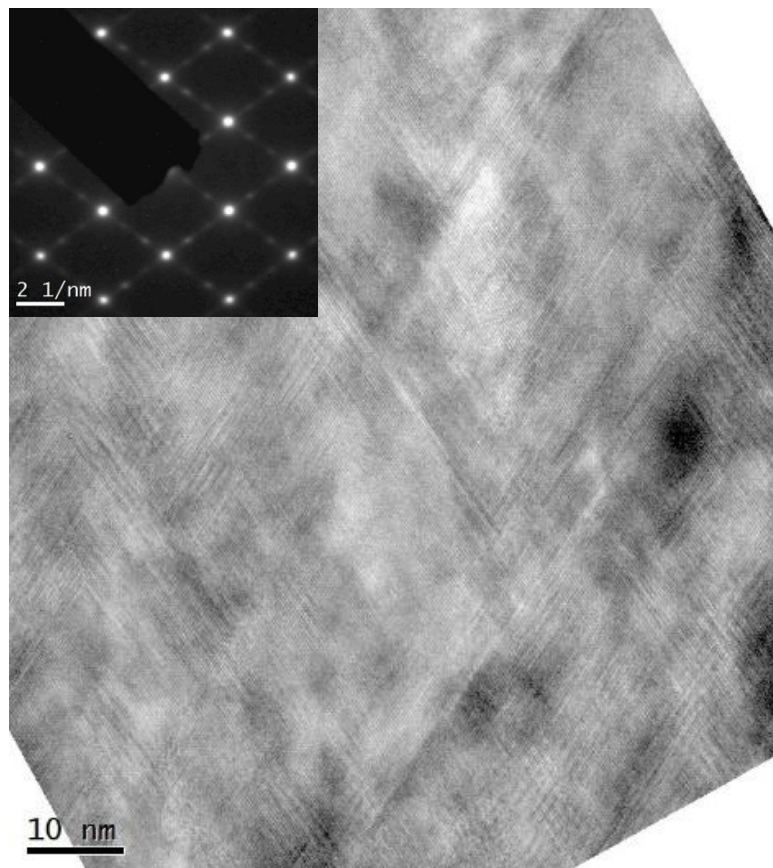


Figure 82. TEM image of the defective region, it corresponds to a highly twinned structure as shown by the EDP in the inset.

4.3.2.2. Crystalline quality: correlating TEM and in-situ ellipsometry measurements

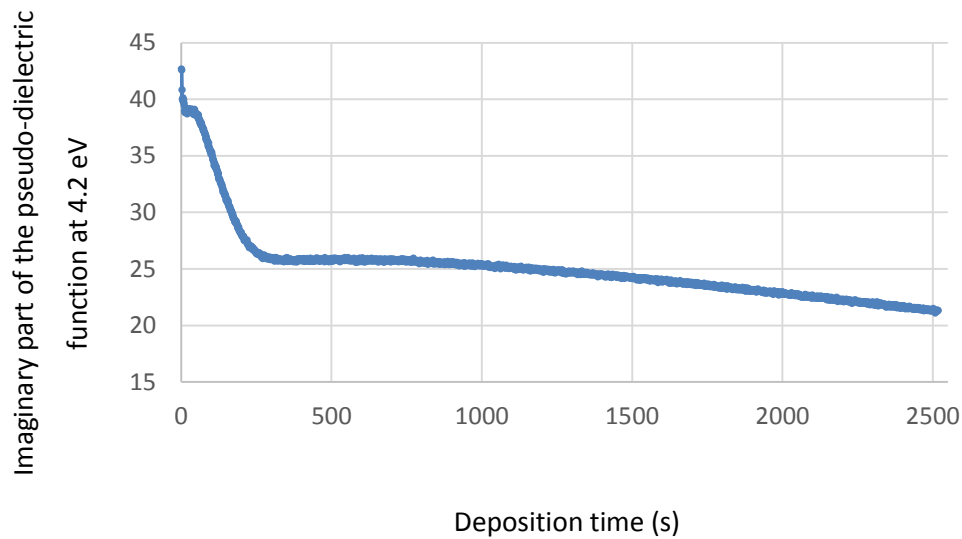


Figure 83. In-situ ellipsometry monitoring the evolution of the film structure deposited using a RF power of 15 W and a H₂ flow rate of 3 sccm.

In-situ ellipsometry measurements during the growth of this film are presented in Figure 83. The high value at about 38 reveals a high quality epitaxial growth for the first ~ 50 s. Then an abrupt decrease of $\langle \epsilon_i \rangle$ occurs (between $t \sim 45$ s and $t \sim 285$ s) till a value around 25 indicating either a roughening effect or a decrease of the crystalline quality. However, TEM images show that no amorphous or microcrystalline growth appears for deposition time $t < 500$ s (~ 270 nm). This suggests an abrupt increase of roughness between deposition times $t \sim 45$ s and $t \sim 285$ s. Then a stabilization of $\langle \epsilon_i \rangle$ is observed indicating a stable roughness. For deposition time $t > 850$ s, $\langle \epsilon_i \rangle$ decreases slowly revealing a degradation in the crystalline quality as shown by the TEM images in the upper part of the film.

4.3.3. Summary of results - epitaxy and breakdown by increasing the H₂ flow rate

We present here a summary of the influence of increasing the H₂ flow rate from 1 to 2 and 3 sccm. High quality epitaxy is achieved using 1 sccm, a defected epitaxy using 2 sccm and defective epitaxy followed by breakdown using 3 sccm (Figure 84). Hydrogen is mainly responsible for this change of the crystalline structure.

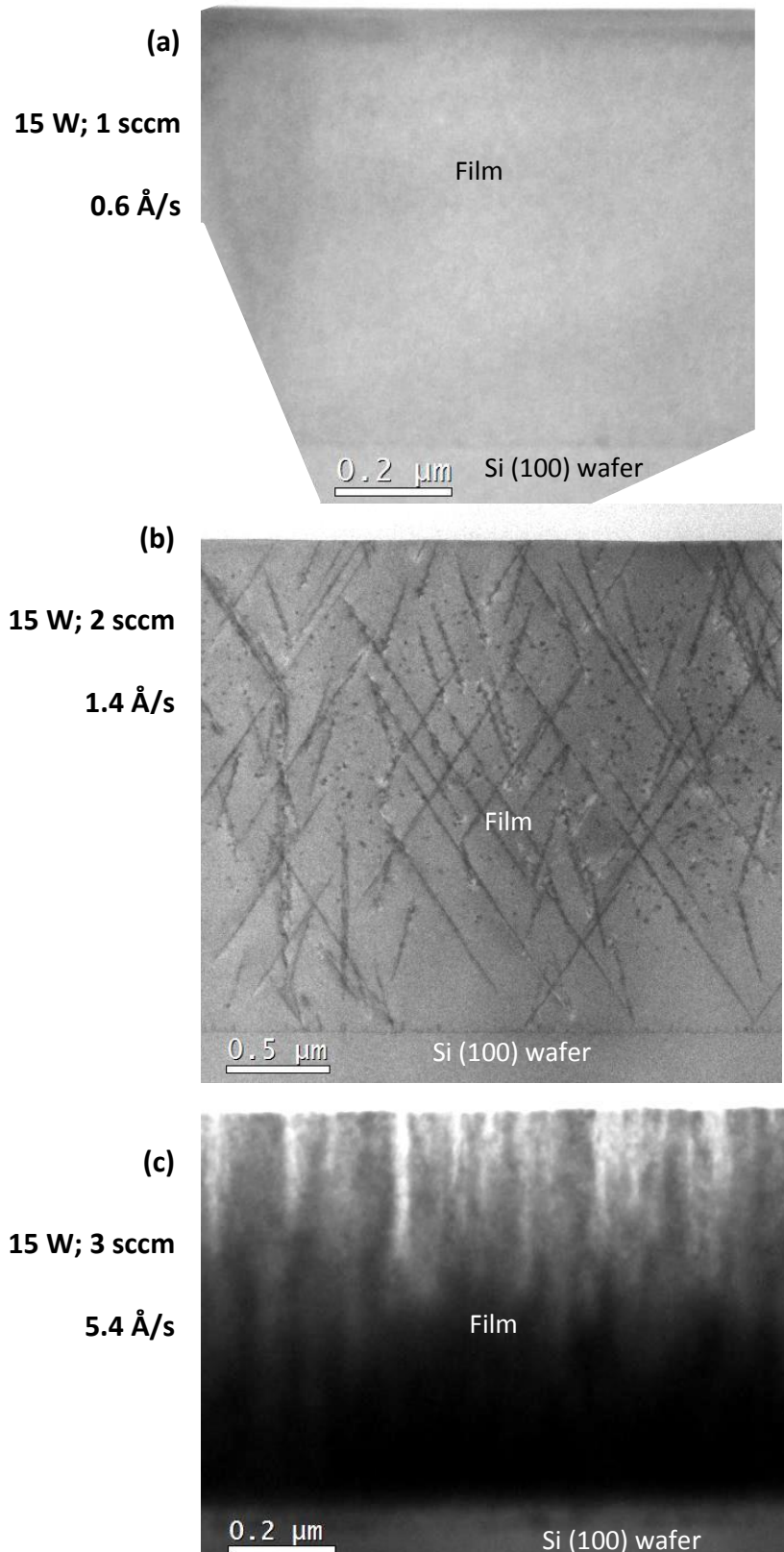


Figure 84. Summary of images corresponding to (a) epitaxy, (b) defective epitaxy and (c) epitaxy breakdown for films deposited using a RF power of 15 W and different H_2 flow rate: 1, 2 and 3 sccm respectively.

4.4. Discussion

For all the cases presented in this chapter, epitaxy breakdown can be noticed by an amorphous and microcrystalline growth, appearing at the end of a defective epitaxial growth characterized by a high density of twins and/or stacking faults. It is tempting to speculate that epitaxy breakdown occurs via a twinning phase.

In the following, we explore epitaxy breakdown and explain the TEM observations presented in this chapter within the framework of existing models or mechanisms leading to epitaxy breakdown. Such mechanisms have often been studied in the case of deposition by low-temperature molecular beam epitaxy (LT-MBE), but rarely for LT-PECVD. Defect accumulation [102] and continuous breakdown [102, 110] are some models that explained some cases of epitaxy breakdown, they can be summarized by a continuous increase in the concentration of lattice disorder. Moreover, impurity segregation models were reported to break epitaxy through segregation of background impurities like oxygen, carbon or hydrogen on the surface until reaching a certain coverage [102, 111]. Furthermore, kinetic roughening [21, 102, 103], due to limited adatom mobility, has been mentioned as responsible for breaking the epitaxy. New insights into epitaxy breakdown mechanisms are now presented and clarified for LT-PECVD and particularly for the SiF₄/H₂/Ar plasma chemistry.

Our discussion will be held in the light of the available models of epitaxy breakdown and the phenomenological model developed by Dornstetter et al. [39] for the particular SiF₄/H₂/Ar plasma chemistry. The main idea of the latter model is that the dissociation of SiF₄ produces atomic fluorine (F) which is scavenged by molecular hydrogen to form HF according to equation:



Based on the reactants of Equation 1, two regimes were identified: the first one was called “H₂-limited regime” where a low concentration of available hydrogen hindered the formation of HF (H₂ flow rate is highly depleted and atomic F is in excess); the second one was called “F-limited regime” where a low concentration of available atomic F hindered the formation of HF (H₂ is in excess).

4.4.1. Breakdown by power

4.4.1.1. Effect of increasing the RF power on epitaxy

4.4.1.1.1. Chemistry changes

Increasing the RF power has a strong influence on the SiF₄/H₂/Ar plasma chemistry. In fact, this results in further dissociation of SiF₄ molecules and consequently in a higher H₂ consumption to the benefit of HF formation, as predicted by the phenomenological model developed by Dornstetter et al. [39]. Increasing the RF power is equivalent to approaching to the H₂-limited regime which corresponds to a shortage of available H₂ in the plasma. Accordingly, we suggest that one of the factors limiting the epitaxial growth is the lack of atomic hydrogen (which is indeed one key parameter in Si epitaxy) in the high power regime described in section 4.2 (intentional breakdown by a high power). It is important to note that the increase of fluorine concentration has not been compensated by the addition of H₂ in our growth experiments.

4.4.1.1.2. Energetics of bombarding ions

From another point of view, one might think intuitively that when increasing the RF power, the ion bombardment energy increases and may cause damage to the film and so a probable epitaxy breakdown. In fact, it has been reported that when the ion bombardment energy increases above the level of binding energies, up to the threshold of atomic displacements, the positive effects of ion bombardment energies (like local atomic arrangements, enhanced mobility) are replaced by negative effects destroying epitaxy (like lattice damage and defect generation)[75].

When looking at the maximum kinetic energy a positive ion may acquire (given by the plasma potential), we note that it is around 54 and 64 eV for the films deposited at 20 and 25 W, respectively. We believe that an energy of 54 eV is not supposed to cause damage to the films deposited at 20 W, under a pressure of 3 Torr. In fact, according to the work of Bruneau et al. [65] (Figure 46), impinging ions exceeding a threshold energy induced atomic displacements in the Si lattice. The authors found a critical ion energy threshold near 52 eV for a pressure of 2.3 Torr but explained that an increase of the applied pressure would relax the threshold energy to much higher values (mainly due to the more collisional sheath and to the increasing mass of the incoming ions). All this to say that the epitaxy breakdown obtained when increasing the RF power could be affected by the ion bombardment energy (or equivalently the plasma potential).

4.4.1.2. Model of epitaxy breakdown due to increasing the RF power

The TEM images of the (100) Si films deposited using a power of 20 W are so far comparable to the TEM images obtained by Bratland et al. [103] (Figure 85 (a) and (b)) while reporting on epitaxial

breakdown of Ge (100) grown by LT-MBE. The authors demonstrated that epitaxy breakdown is driven by kinetic roughening due to low adatom mobility and the presence of barriers at step edges. This kinetic roughening was evidenced by the formation of a regular array

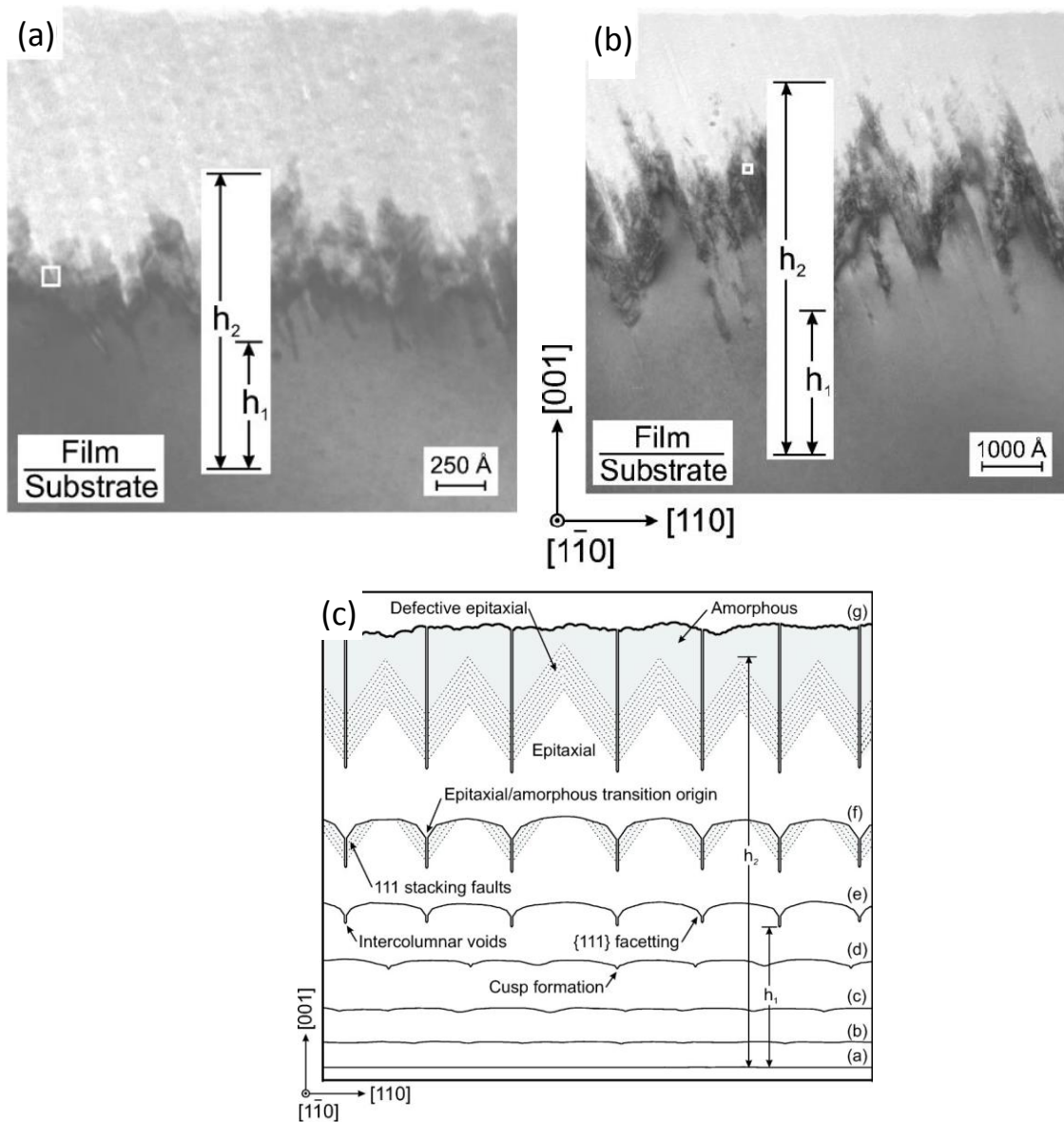


Figure 85. TEM images showing epitaxy breakdown for germanium Ge (100) layers deposited by LT-MBE for substrate temperatures of 95°C (a) and 135°C and (b) from the work of Bratland et al. [103]. They both show critical thicknesses h_1 and h_2 , where h_1 defines the onset of epitaxial breakdown and h_2 defines the entire film transformation from epitaxial to amorphous. (c) Schematic illustration revealing the evolution of the microstructure and surface morphology.

of round growth mounds that transformed into faceted pyramidal islands after certain temperature-dependent thickness, as shown by the schematic diagram of Figure 85(c) illustrating the evolution of the microstructure and surface morphology. The mounds were found to grow laterally and vertically with thickness, their surface width ω was thought to follow a power law dependence with layer thickness h : $\omega \propto h^\beta$, where β is called the roughening exponent. β describes how fast surface roughness develops; it is one key parameter to determine whether kinetic roughening mechanism occurs or not, therefore calculations of β were performed by some researchers [102, 103], but this is not in the scope of the present thesis. Bratland et al. showed that the onset of epitaxy breakdown occurred when the aspect ratio of the islands reaches a critical value (~ 0.02), independently of the temperature. At this critical moment, deep cusps bounded by $\{111\}$ facets⁴ appeared. Subsequent deposition on these faceted cusp leads to stacking faults and twin defects; this is how long-range order is lost and epitaxy breaks down.

Since our films are characterized by the presence of different sublayers, as judged by the cross-sectional TEM images, just like the TEM images of Bratland et al., it is most likely that epitaxy breakdown in the long time limit in our case is also caused by the kinetic roughening mechanism. This is consistent with the rapid roughening observed by the abrupt decrease of the in-situ ellipsometry signal (Figure 57) for deposition time between $t \sim 780$ s and $t \sim 1620$ s. This rapid roughening would be linked to a transformation from round islands to faceted pyramidal islands.

We suggest that the low adatom mobility is caused in our experiments by the shortage or lack of atomic hydrogen at the surface of the film with increasing the RF power, because it has been almost completely consumed in the plasma by the SiF₄ for the formation of HF. In fact, it is well known that in PECVD, the atomic hydrogen plays an important role in providing the film with additional energy through chemical annealing [74] at the surface, consisting of H atoms recombination on the surface and their re-emission as H₂⁵ (exothermic reactions releasing a considerable energy ~ 4.5 eV/at or 104 kcal/mol [112]). Thanks to this energy, atomic ordering in epitaxial sites at low substrate temperatures is possible through bond breaking (the binding energy of Si–Si are ~ 3.5 eV/at) and reforming reactions, according to molecular dynamics simulations [113]. However, when there is a lack in atomic hydrogen, it becomes more difficult for atoms to

⁴ low-energy faces in the diamond crystal structure

⁵ $H_{at} + -Si \rightarrow H - Si$: adsorption of atomic H on a Si surface dangling bond

$H_{at} + H - Si \rightarrow H_{2(g)} + -Si$: abstraction of the chemisorbed H by another incident atomic H and H₂ formation

rearrange in epitaxial conditions since their mobility is reduced. Briefly, a shortage of atomic hydrogen at the surface seems to lower adatom mobility causing a kinetic roughening.

Furthermore, our results show that epitaxy works better for the (100) surface than for the (111) one; similar results were obtained by Nerding et al. [73] on samples deposited in epitaxial conditions by ion-assisted deposition at LT. This is explained by the fact that for Si (100) and Si (111), the activation energies for adatom diffusion on Si (100) and Si (111) found in the literature are around 0.6 [73, 114] and 1.3 eV [73, 115], respectively.

The films deposited at 25 W resemble those deposited at 20 W, but two main differences can be clearly noticed (Figure 69):

- The entire film transformation from epitaxial to microcrystalline and amorphous occurred at a higher deposition thickness, namely ~ 700 nm for the film at 25 W compared to ~ 150 nm for that at 20 W.
- Defective columnar structures appear, for the sample deposited using 25 W, in the monocrystalline matrix. They present a high density of stacking faults and twin defects inducing the onset of local epitaxy breakdown in the film. The formation of such defects is mostly related to some ions with a high bombardment energy (high plasma potential), capable of inducing – locally – atomic displacements. The plasma potential in this case is above the critical potential (~ 61 V, for similar growth conditions, see Figure 86) that we have previously found by studying the effect of varying the plasma potential using in-situ ellipsometry [80]. In the latter studies, $\langle \epsilon_i \rangle$ was stable when the plasma potential is below 61 V but decreases abruptly above 61 V.

As the sample deposited at 25 W is found to be above the threshold plasma potential, it seems that the ions having the maximal ion bombardment energy (64 eV) mostly induce the onset of local epitaxy breakdown within the monocrystalline matrix, but some other ions having lower energy below the threshold for atomic displacements, mostly help sustaining epitaxy to higher thicknesses compared to that for the sample at 20 W, thanks to their higher average energy relatively.

To summarize, we suggest that when increasing the RF power from 200 to 330 mW/cm², kinetic roughening mechanism is the main factor causing epitaxy breakdown, this is mostly linked to reduced adatom mobility. Further investigations can be performed to monitor the evolution of topography and surface roughness with thickness in order to better characterize this kind of epitaxy breakdown.

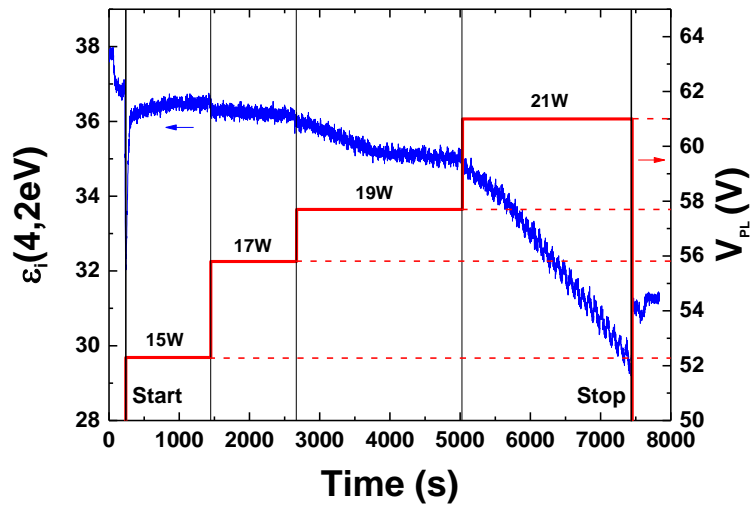


Figure 86. Time evolution of the pseudo-dielectric function at 4.2 eV and the plasma potential while increasing the RF power from 15 W to 21 W [80]. $\langle \epsilon_i \rangle$ is stable when the plasma potential is below 61 V but decreases abruptly above 61 V.

4.4.2. Breakdown by hydrogen

4.4.2.1. Effect of high H₂ flow rate on epitaxy

By looking at the microstructure of the films that are epitaxial at a H₂ flow rate of 1 sccm, defectively epitaxial at 2 sccm and turning into microcrystalline at 3 sccm – while keeping constant all other growth parameters –, it becomes clear that hydrogen plays a strong role in the monocrystalline-to-microcrystalline transition.

4.4.2.1.1. Dislocations

A large number of dislocations is observed, for the sample deposited using a H₂ flow rate of 2 sccm, in {111} and {200} planes (Figure 76 and Figure 77). Some dislocations in {111} planes resemble the dislocation loops that the reference [109] suggested to be the result of the accumulation of vacancies and interstitials and their condensations on {111} planes [116]. Since this kind of defect is characteristic of “hydrogenated” silicon, not silicon [109], it seems reasonable to associate the vacancies and interstitial defects to the diffusion of hydrogen atoms and their interaction with the Si lattice. In our opinion, the vacancies would be formed by a double role of in-diffusing hydrogen: breaking of Si–Si bonds by chemical annealing followed by the etching effect of the hydrogen atoms, occurring through the formation of volatile SiH₄ with a process involving atomic hydrogen and SiH_x species at the surface [117].

Dislocations decorated by hydrogen are most probably observed (defects numbered 3 in Figure 71) for the samples deposited at a H₂ flow rate of 2 sccm, and not for 1 sccm, indicating that the addition of H₂ induced the high density of defects in this sample. We suggest that the bonds breaking along {111} planes is induced by hydrogen atoms that easily diffuse inside the Si lattice and break Si–Si bonds by chemical annealing. According to the observations of Ghica et al. [109] on the same apparent type of defects (for a thinner TEM foil), these defects in {111} planes could correspond to a collection of hydrogen complexes defects (like H₂^{*}) (decorating some Si dangling bonds) aligned on a {111} plane. The reader is advised to read reference [118] for more information on the H₂^{*} defect.

4.4.2.1.2. Hydrogen platelets

Increasing the H₂ flow rate from 1 to 2 sccm causes the formation of hydrogen platelets, or hydrogen-decorated platelets, as exemplified in Figure 74. Such {111} defects were observed in the literature as a result of hydrogen implantation in Si [119]. Several atomic models of defects in {111} planes were described in the literature and summarized by Muto et al. [120]. They all consider that the Si–Si bonds break along {111} planes and are saturated with hydrogen atoms with some shifts of the Si lattice on each side of the defects. One of these models is described by Hochbauer [118] (Figure 87): hydrogen atoms reside at the bond centers of the [111] Si–Si bonds, then the formed Si–H–Si bonds are substituted by two Si–H bonds, changing the atomic arrangement from Si–H–Si to Si–H–H–Si [121]. Further in time, the diffusing H-atoms can finally agglomerate into a H₂-gas after splitting the two formed H-layers. With all these defects, the structure is still monocrystalline as indicated by the EDPs of Figure 72. One would ask, why do we still have a monocrystalline structure with all these defects? In fact, these defects are caused by the diffusion of hydrogen within the film. We propose that the same factor that causes the creation of such defects (hydrogen) also helps sustaining epitaxy so far: the etching⁶ effect of hydrogen might play a role in removing the weakly bonded Si atoms which are not in crystallographic configuration for epitaxial growth (etching of the unfavorable configurations, like

amorphous configuration [17, 122, 123]), this process will leave strong bonds allowing epitaxy to occur. We assume that the hydrogen decorating a large number of defects caused the weird contrast along them

⁶ $Si_{(solid)} + xH_{(plasma)} \rightarrow SiH_x_{(plasma)}$

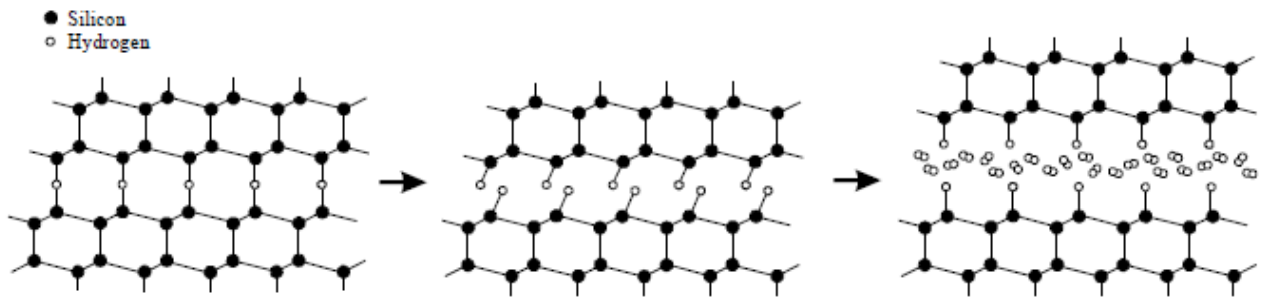


Figure 87. Schematic illustration of the hydrogen platelet generation and evolution according to Hochbauer [118].

Further increase of the H_2 flow rate to 3 sccm results in the apparition of a high concentration of twin defects besides the dislocations and the platelets (Figure 81 and Figure 82). It seems to us that the high energy communicated to the Si lattice by the insertion of atomic H could enable the formation of twin defects; more details on twinning and its possible origin are discussed in the next chapter.

4.4.2.2. Model of epitaxy breakdown due to increasing H_2 flow rate

The addition of the H_2 flow rate from 2 to 3 sccm dramatically increased the surface roughness, as revealed by the in-situ ellipsometry measurements (Figure 78 and Figure 83) and so significantly changed the surface morphology. Most importantly, this roughening effect is correlated with the reduction of the epitaxial thickness from $2.4 \mu\text{m}$ to few tens of nm for the samples deposited using 2 and 3 sccm, respectively, and with an epitaxy breakdown for the latter case. Since surface roughening and the decrease of the epitaxial thickness were consistently found when increasing the H_2 flow rate, it seems that epitaxy breakdown occurs as a consequence of roughening, as in the model of Bratland et al [103] (Figure 85).

Surface roughening induced by hydrogen was also reported by Adams et al. [104] to cause an epitaxy breakdown by MBE. Those authors found, when increasing the dose of hydrogen (deuterium), a rapid roughening of the films but, in contrary to our observations, a monocrystalline-to-amorphous transition. They suggested that the kinetic effect of hydrogen is responsible for the epitaxy breakdown, resulting from surface roughening and not from a critical hydrogen concentration at the surface.

Now the question on the origin of surface roughening in our LTE-PECVD growth is raised. We suggest that roughening can occur due to three reasons:

- Limited surface diffusion associated with higher deposition rates: The deposition rates increase by almost an order of magnitude when using the higher H₂ flow rate: 5.4 Å/s for 3 sccm vs 0.6 Å/s for 1 sccm. This increased deposition rate has also been reported in the work of Dornstetter et al. [39] for SiF₄/H₂/Ar plasma chemistry. As a consequence, the adatoms would not have enough time to find epitaxial sites, but instead they would set (in twinning configuration for example) once they are hit by upcoming atoms, acting as barriers to diffusion. This might explain the surface roughening for our growth conditions.
- Limited surface diffusion associated with hydrogen adsorption: as a consequence of increasing the hydrogen flow rate from 1 to 3 sccm while keeping the same substrate temperature, in the F-limited regime, a higher amount of adsorbed hydrogen remains at the surface of the Si film. In fact, it is well known in the literature that the adsorbed hydrogen can alter or lower the surface diffusion of Si and can thus lead to an accumulation of surface roughness [21, 102, 124]. In this context, Rosenblad et al. [21], while studying Si epitaxy by low-energy PECVD, observed the formation of stacking faults in a defect-free film and obtained similar TEM images (Figure 88) as the one in Figure 81; they showed that the adsorbed hydrogen causes an accumulation of surface roughness through hindering adatom migration, and that this facilitates the nucleation of the stacking faults. By mixing a small amount (4 %) of germane into silane, those authors were able to reduce hydrogen adsorption, and so the stacking faults which were observed without germane, disappeared completely. Accordingly, it is reasonable in our case to associate the roughening effects with the higher amount of hydrogen at the surface. Further work would be done to quantify the amount of incorporated hydrogen as a function of the H₂ flow rate and to give evidence of the discussed mechanism.

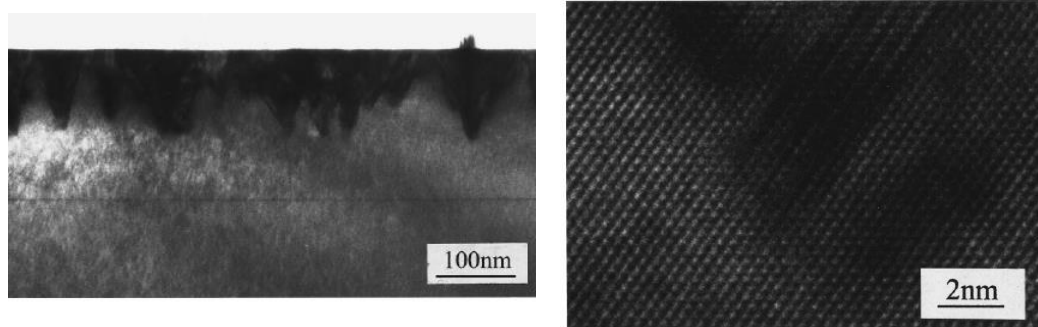


Figure 88. TEM images of Si films showing stacking faults appearing after a certain thickness of epitaxial growth, obtained in the work of Rosenblad et al. [21]. Such defects, also observed in our samples (Figure 81), were attributed to a buildup of roughness caused by the adsorbed hydrogen through reducing surface diffusion.

- Etching role of hydrogen: Surface roughening might be related to the etching role of hydrogen, inducing some roughness and crystalline defects, and initiating the formation of a microcrystalline phase. We recall that hydrogen plays an important role in achieving epitaxy: an optimized flow rate is capable to fulfill the balance between deposition⁷ and etching⁸ [17, 51]; when this balance is not respected, epitaxial growth cannot be sustained, a microcrystalline (or amorphous) phase can appear by increasing (or decreasing) the H₂ flow rate [31]. Further study will be necessary to precisely determine if etching occurs significantly at 3 sccm, by making a series of depositions around 3 sccm (for example 2.5, 3.5 and 4 sccm) and checking how the deposition rate changes.

Briefly, the loss of epitaxy is found to be linked to an increase of surface roughness during growth while increasing the H₂ flow rate. We suggest that hydrogen, by either limiting adatom surface diffusion, or etching, would most probably be indirectly responsible for the surface roughening and consequently the epitaxy breakdown.

⁷ $SiH_x(plasma) \rightarrow Si(solid) + xH(plasma)$

⁸ $Si(solid) + xH(plasma) \rightarrow SiH_x(plasma)$

4.5. Summary and perspectives

Takeaway message – Epitaxy breakdown using SiF₄/H₂/Ar

- Experiments of intentional breakdown of epitaxy were performed to get insight on the mechanisms responsible of epitaxy breakdown for LT-PECVD growth using SiF₄/H₂/Ar chemistry, by either increasing the RF power or the H₂ flow rate. Initially, the Si films form as a single-crystal material, but at a critical thickness, the epitaxial layers turn into microcrystalline and amorphous, via a twinning phase.
- The most likely mechanism for the breakdown of epitaxy is the accumulation of surface roughness sufficient to generate {111} facets. Twins and stacking faults may form on these facets disrupting thus epitaxial configuration.
- In the case of increasing the RF power (from 15 to 25 W), two types of breakdown were reported: global breakdown observed at a thickness above which epitaxy cannot be sustained anymore and onset of local breakdown observed as columnar defective structures embedded in a monocrystalline structure. The global breakdown (observed for samples deposited using 20 and 25 W) is likely due to a lack in atomic hydrogen on the surface, as it has been almost completely consumed in the plasma. This results in a reduction of the adatom mobility and consequently in a kinetic roughening effect. The onset of local breakdown (only for 25 W) is strongly correlated with a high ion bombardment energy exceeding a critical threshold, the latter mostly corresponds to atomic displacements and so to lattice damage.
- In the case of increasing the H₂ flow rate (from 1 to 3 sccm), we suggest that the excess of hydrogen would be responsible for the buildup of surface roughness and so for epitaxy breakdown (for the sample deposited at 3 sccm of H₂ flow rate) through limiting adatom diffusion (higher deposition rate, or higher hydrogen adsorption) or etching. The sample deposited at 2 sccm has a monocrystalline structure perturbed by defects induced by the addition of H₂ flow rate (stacking faults, platelets, dislocations). Further studies can be done to derive a structural model of such defects by performing quantitative image processing and simulation.
- Epitaxial breakdown of Si by LT-PECVD seems to result from kinetic roughening. But a complete understanding of the atomic mechanisms responsible for epitaxy breakdown has not emerged. Future experiments might be performed to study the topography of the film at different thicknesses before and after the breakdown.
- Now that the breakdown is attributed to the buildup of roughness, we can start working on strategies to eliminate such effects in order to extend the epitaxy window. For example, it is worth checking out if good epitaxy at high deposition rate could be achieved by increasing the H₂ flow rate and by adding small amount of germane [21] into our plasma mixture; this would reduce hydrogen adsorption with delaying breakdown to higher thicknesses.
- Most importantly, the study of epitaxy breakdown could help us extending the epitaxial window by suggesting to optimize some growth parameters such as H₂ flow rate or RF power, simply by checking the microstructure of the films.
- It seems interesting also to understand the occurrence of the epitaxy comeback for future work.

Chapter 5. Twinning in epitaxial films and fivefold symmetric diffraction patterns

5.1. Introduction.....	107
5.1.1. Overview of twinning and fivefold symmetry in literature.....	107
5.1.2. Fivefold symmetric diffraction patterns in Si thin films.....	108
5.2. Twinning in Si films promoted by epitaxy breakdown from SiF ₄ /H ₂ /Ar plasma.....	111
5.2.1. Epitaxy breakdown by increasing the RF power.....	112
5.2.2. Epitaxy breakdown caused by increasing the H ₂ flow rate	121
5.3. Twinning in Si films promoted by epitaxy breakdown from SiH ₄ /H ₂ /HMDSO/B ₂ H ₆ /Ar plasma....	126
5.3.1. Effect of the substrate.....	127
5.3.2. Effect of HMDSO flow rate.....	131
5.3.3. Number of twin operations.....	133
5.3.4. MT and microcrystalline contributions.....	133
5.3.5. Chemical analysis.....	136
5.4. Discussion.....	138
5.4.1. Growth twins and fivefold symmetry.....	138
5.4.2. Origin of twinning and multiple twinning	139
5.4.3. Twinning and epitaxy breakdown	143
5.4.4. Effect of the seed orientation on twinning - Si (100) vs Si (111)	148
5.5. Summary and perspectives	150

5.1. Introduction

5.1.1. Overview of twinning and fivefold symmetry in literature

During some nucleation and growth processes, such as crystal growth from the vapor or liquid phase, two or more intergrown crystals may form in a symmetrical fashion creating a complex crystalline edifice called a twin structure. Repeated twin formation or multiple twinning in crystalline solids was first observed in 1957 by Segall [125] in annealed copper. Since multiple twinning generally has a serious influence on the outward shape and symmetry of a crystal - and so on material properties - it has attracted scientific interest in various fields such as crystal growth, crystallography, surface science and thin films. It benefited from some publicity at the time of the discovery of quasicrystals, as the discoverers had to face skeptics who believed they were looking at multiple twinning [126-128]. The tendency of multiple twinning causing true fivefold symmetry has been widely found in materials of natural origin, like some viruses [129], protein supermolecules [130], minerals (sphalerite [131], marcasite [132]), as well as in synthetic materials and thin films, especially in small metal particles (like iron [133], silver [134] and gold [135]), and also in some elements of group IV (like diamond carbon [136], silicon [137] and germanium [137]). A review on fivefold symmetry was presented by Hofmeister [138], who listed a number of natural and synthetic occurrences with the associated references and some details on their characteristics. All these cases of fivefold symmetry induced by multiple twinning occur in small particles - usually few nanometers, sometimes up to few millimeters - that adopt a special morphology (decahedron, icosahedron, cuboctahedron), that is why the term "multiply twinned particles" or MTP is often used in the literature. For instance, Iijima [139] found decahedral MTP in small and spherical Si particles elaborated from a gas evaporation technique; he investigated structural details of these particles and described them as a packing of five tetrahedra leaving 7.5 degrees mismatch angle that causes plastic and elastic deformations. Maurice *et al.* [140] showed, while studying the effect of annealing amorphous Si layers, one small grain of Si with identifiable five twinned domains resulting in a nearly fivefold symmetry; these annealed layers contained a lot of stacking faults and a high density of twins, however no nanoparticle was observed in contrast to case of symmetry from MTP. In the present study, we shed light on primary, secondary and multiple twinning observed throughout Si thin layers. It leads in some cases to fivefold symmetric electron diffraction patterns (EDPs) originating from multiple twinning but not from the presence of multiply twinned nanostructures or nanoparticles. The observed symmetry is a *pseudo*-fivefold symmetry, occurring

over large areas, covering the whole surface investigated, as if it corresponded to a specific mode of crystal growth. This symmetry is observed in the reciprocal space only, not in the real space.

5.1.2. Fivefold symmetric diffraction patterns in Si thin films

In this chapter, we will present two cases of fivefold symmetric EDPs observed for the first time throughout several samples without the presence of MTP: the first one is observed on the Si layers deposited using $\text{SiF}_4/\text{H}_2/\text{Ar}$ plasma (as presented in the previous chapter) under epitaxy breakdown conditions, and the second one is observed on Si layers containing oxygen and carbon impurities (in the range of 0.3 - 5.5%) deposited using a plasma composed of silane (SiH_4), hexamethyldisiloxane (HMDSO, $\text{C}_6\text{H}_{18}\text{OSi}_2$), diborane (B_2H_6), H_2 and Ar. The growth in both cases was done by PECVD.

Before going into the details of each case, let us show how a fivefold symmetric EDP looks like, how can we recognize it and how can we build this symmetry from twinning.

5.1.2.1. Definition

A typical fivefold symmetric EDP recorded on one of our films in the $[0\bar{1}1]$ zone axis is shown in Figure 89.

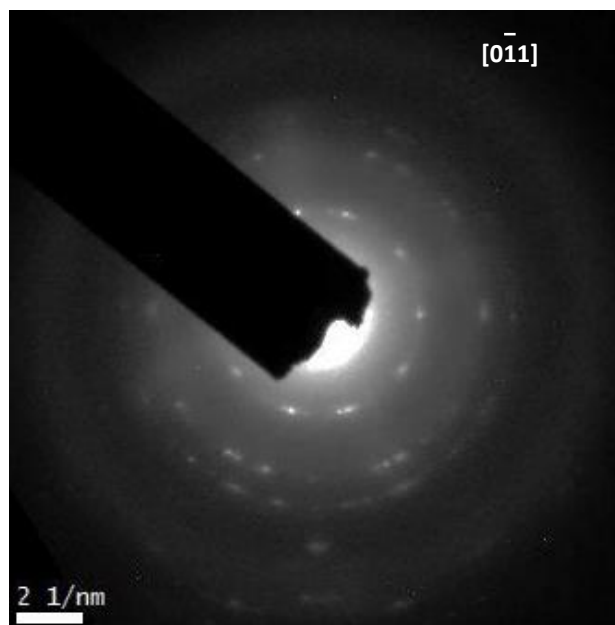


Figure 89. Electron diffraction pattern along the $[0\bar{1}1]$ zone axis displaying a fivefold symmetry (sample prepared with 0.45 sccm of HMDSO, see section 5.3)

This figure presents the characteristic 111, 220 and 311 Si rings, but these rings are discrete, not representing random microcrystalline structure, neither perfect monocrystalline one. Moreover, the ten spots of the smaller ring present a quasi-rotational symmetry. If we rotate the 111 spots - one time or five times - around the [0-11] axis with an angle near to $2\pi/5$, the pattern is transformed into a state that is hardly distinguishable from the initial one. Therefore, this EDP displays a very clear fivefold symmetry. In fact, this pattern appears to be characteristic of our layers and not associated with any specific area since it was observed on different regions of several samples. In addition, such patterns were systematically observed for samples with various growth conditions, the details are presented in the sections 5.2 and 5.3. Similar fivefold symmetric EDPs were reported in the literature, like the ones taken on MTPs with special morphologies [47, 141].

5.1.2.2. Double twinning

Let us now discuss the origin of the observed fivefold symmetry. For this, we will rebuild the EDP of Figure 89 using the HRTEM image of the area (Figure 90(a)) and its fast Fourier transform (FFT) (Figure 90 (b)) which has the same fivefold symmetry as the EDP.

We start from the monocrystalline substrate as a matrix: there, we find four 111 spots (Figure 90(c),1); by rotating these spots, in the anticlockwise direction, along the [0-11] axis with the angle between two families of {111} planes which is 70.53° ($\sim 2\pi/5$), we fall on diffraction spots corresponding to the primary twin (Figure 90(c),2). By repeating this operation a second time, we obtain the spots characteristic of second order twinning (Figure 90(c),3); this makes a total of eight spots. By doing one such operation in the clockwise direction (Figure 90 (c),4 and 5), we obtain the two additional 111 reflections that make ten. Further twinning just doubles or reinforces these spots. We thus need, at least, second order twinning in one direction and first order twinning in the other to obtain the ten spots. We will precisely analyze the number of twinning operations for different growth conditions for the two different plasma chemistries (see sections 5.2.1.1, 5.2.2.1 and 5.3.3).

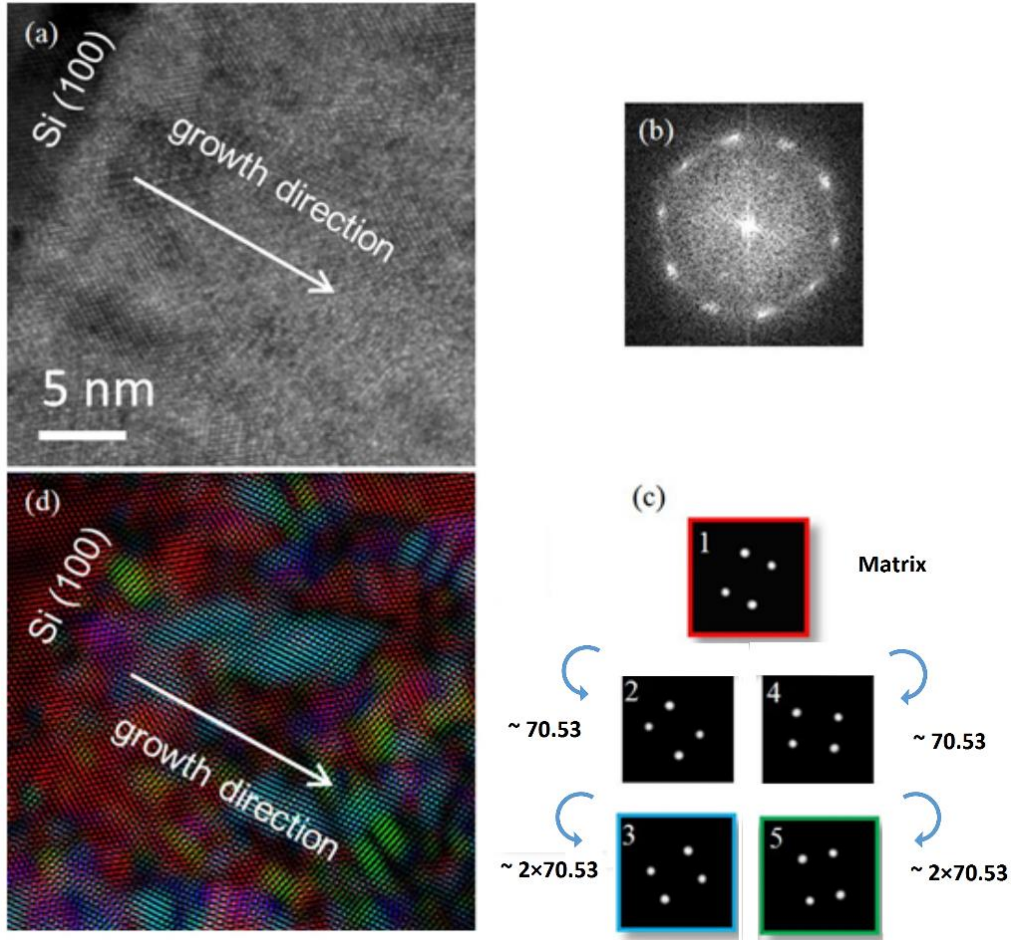


Figure 90. (a) HRTEM image, recorded in the [0-11] zone axis, of the same layer as that imaged in Figure 89(b) FFT of (a), (c) selection of five grain orientations and (d) colored image constructed from the IFFTs of orientations 1, 3 and 5.

The EDP of Figure 89 thus exhibits reflections characteristic of twinning and it becomes clear now that the fivefold symmetry (in the EDP and FFT) is obtained by a multiple twinning starting from a mother orientation which is that of the substrate. This suggests that epitaxial growth is one necessary condition for the formation of fivefold symmetric EDPs. Extra 220 and 311 spots in the EDP of Figure 89 also appear as a result of multiple twinning. It seems, therefore, that the associated layer is essentially composed of twinned monocrystalline domains. From this point on, we call this structure and the associated growth mode “multiply twinned” or MT. Thus the angle of rotation does not have the exact value of $2\pi/5$, but that of 70.53° , the angle between two families of $\{111\}$ planes, which is also the angle characteristic of twinning about a $\langle 110 \rangle$ axis.

In the HRTEM image of Figure 90(a), the five $\{111\}$ planes responsible for the ten 111 spots leading to the EDP symmetry are not clear. In the following, we make them visible with the application of

Fourier filters. We thus selected the five grain orientations described above, corresponding to the matrix and primary and double twinning in the two rotation directions. Then we performed inverse FFTs (IFFTs) in order to characterize the contribution of each orientation. Figure 90(d) shows an RGB image constructed by superimposing the IFFTs of orientations 1, 3 and 5 (one combination of orientations that includes all ten 111 spots), enabling us to distinguish three grains (red, blue and green) containing all five {111} plane families. One can clearly see that these grains of different orientations form no specific pattern, underlining that although the EDP displays a fivefold symmetry, the film does not. One may also note that, when going in the growth direction from the bottom to the top of the film, the first orientation (substrate orientation, in red) is progressively lost to the benefit of orientations 3 and 5, which correspond to double twinning in both of the rotation directions about the [0-11] axis.

Let us note at this stage that there is no reason why the same operations would not take place about the other, symmetrically equivalent, $\langle 110 \rangle$ axes. However, twinning around these would not give additional 111 reflections in the [0-11] EDP. For instance, first order twinning about the [011] axis would actually align a $\langle 411 \rangle$ axis with the beam direction, which would in turn reinforce the primary 220 reflections and add higher order reflections. This explains why the fivefold symmetry is clear only for the first 111 ring, but not so clear for higher index reflections.

5.2. Twinning in Si films promoted by epitaxy breakdown from SiF₄/H₂/Ar plasma

In this section, we investigate twinning phenomenon for Si thin layers deposited in epitaxy breakdown conditions by a SiF₄/H₂/Ar plasma. After a certain critical thickness is reached, the monocrystalline quality of these layers is degraded and a twinned structure (MT part) appeared, causing an epitaxy breakdown, as presented in the previous chapter. We study here, twinning in the epitaxial films and the possibility of developing fivefold symmetric EDPs, for two cases:

- Epitaxy breakdown caused by increasing the RF power (films at 20 and 25 W in Figure 91), starting from the reference film.
- Epitaxy breakdown (or onset of breakdown) caused by increasing the H₂ flow rate in the plasma mixture (films at 2 and 3 sccm in Figure 91), starting from the reference film.

In Figure 91, we remind the applied RF power, the H₂ flow rate and the seed orientation of the substrate, used during the deposition, for the different films presented in this chapter. The other growth conditions are the same for all these films and correspond to: SiF₄ and Ar flow rates of 3.6

and 88 sccm (respectively), pressure of 3 Torr, substrate and RF temperature of 200 and 100°C (respectively) and inter-electrode distance of 20 mm.

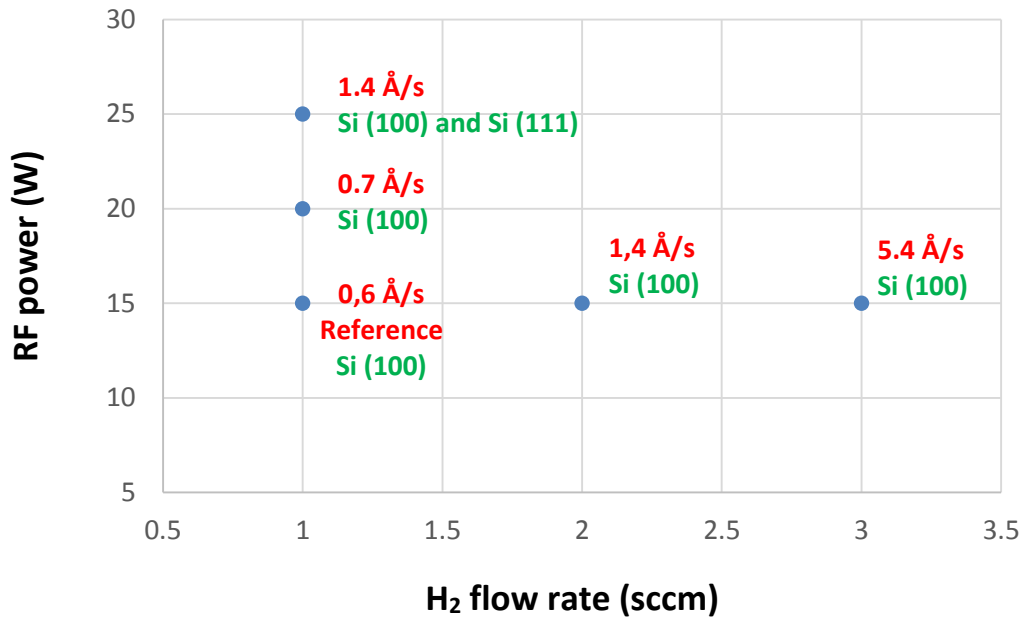


Figure 91. The growth conditions for the films presented in this chapter: two series of depositions were carried out starting from the reference film, by increasing either the RF power or the H₂ flow rate. The substrates used are Si (100) and Si (111), they are indicated for each film.

In each case, the number of twin operations will be evaluated using a quantitative analysis on the EDPs, and the MT part will be presented in details. Furthermore, the effect of the seed orientation on twinning will be investigated by showing results on (100) and (111) oriented Si substrates.

5.2.1. Epitaxy breakdown by increasing the RF power

Interestingly, all the samples deposited at a high RF power density (20 and 25 W) exhibit quasi-fivefold symmetric EDPs in their twinned part. These patterns (resulting from repeated twinning) will be studied in details in this section.

5.2.1.1. Number of twin operations in the MT part

We estimate here the number of twinning operations that is responsible for the establishment of fivefold symmetric EDPs. To do this, we perform a quantitative analysis on the 111 diffraction ring for the EDP of the film deposited on Si (100) at 20 W. To simplify this reasoning, we use 111 ring

since it has the minimum number of diffracted spots as compared with the other intense rings (220 and 311).

The idea is to look for diffracted intensities at angles away from the primary spots (substrate orientation) by $\pm n \times 70.53^\circ$ (and $\pi \pm n \times 70.53^\circ$), with n positive integer representing the order of twinning and 70.53° the twin angle about the [0-11] axis. Note that by “order of twinning” we describe the rotation of a domain with respect to the substrate orientation (“matrix”), not with its neighboring grain. Most of the grain boundaries in our system correspond to first order twinning. We take an extreme hypothesis, which is the presence of five orders of twinning ($n = 1, 2, 3, 4, 5$). These angles of rotation and their corresponding modulo π are presented in Figure 92 by red spots (anticlockwise) and blue spots (clockwise), only for $n = 1, 2, 3$ for visibility reasons. The primary spots (111 spots) are indicated by four black circles and the order of twinning is shown for each spot. We check in the following the validity of our hypothesis.

To correctly identify the diffracted peaks, we use the PASAD tool [142] and particularly the azimuthal projection of the EDP that transforms the spots situated on one diffraction ring into spots situated on one “diffraction line”. We performed this method on the EDP recorded on the MT part that displays quasi-fivefold symmetric EDP, as shown in Figure 93(a). Are presented in the same figure also, the azimuthal projection (Figure 93(b)) of the EDP as well as the profile of this projection for 111 reflection (Figure 93(c)).

For 111 ring, we find diffracted intensities at first and second order twinning ($n = 1, 2$), but we find no diffracted intensities at third and consequently fourth and fifth orders. We consider the spot marked by “M” (matrix) in Figure 93 as the reference (angle at 0 in Figure 92). The highly intense spot marked by M’ helped us to determine the rotation direction in Figure 93(c): M’ being away from M by $\sim 109^\circ$, it corresponds to the angle at 250.53° in Figure 92 (clockwise direction). Starting from M, there are no diffracted intensities forming 31° (angle at 328° in Figure 92) neither forming 77° (angle at 282°) associated with third order twinning. This means that the third, fourth and fifth orders do not have any sign in this EDP. The absence of the latter high order twinning is confirmed in other films and areas for samples deposited at 20 W and 25 W using (100) and (111) substrates. Thus, our hypothesis is valid only for two orders of twinning in either direction, and not five orders.

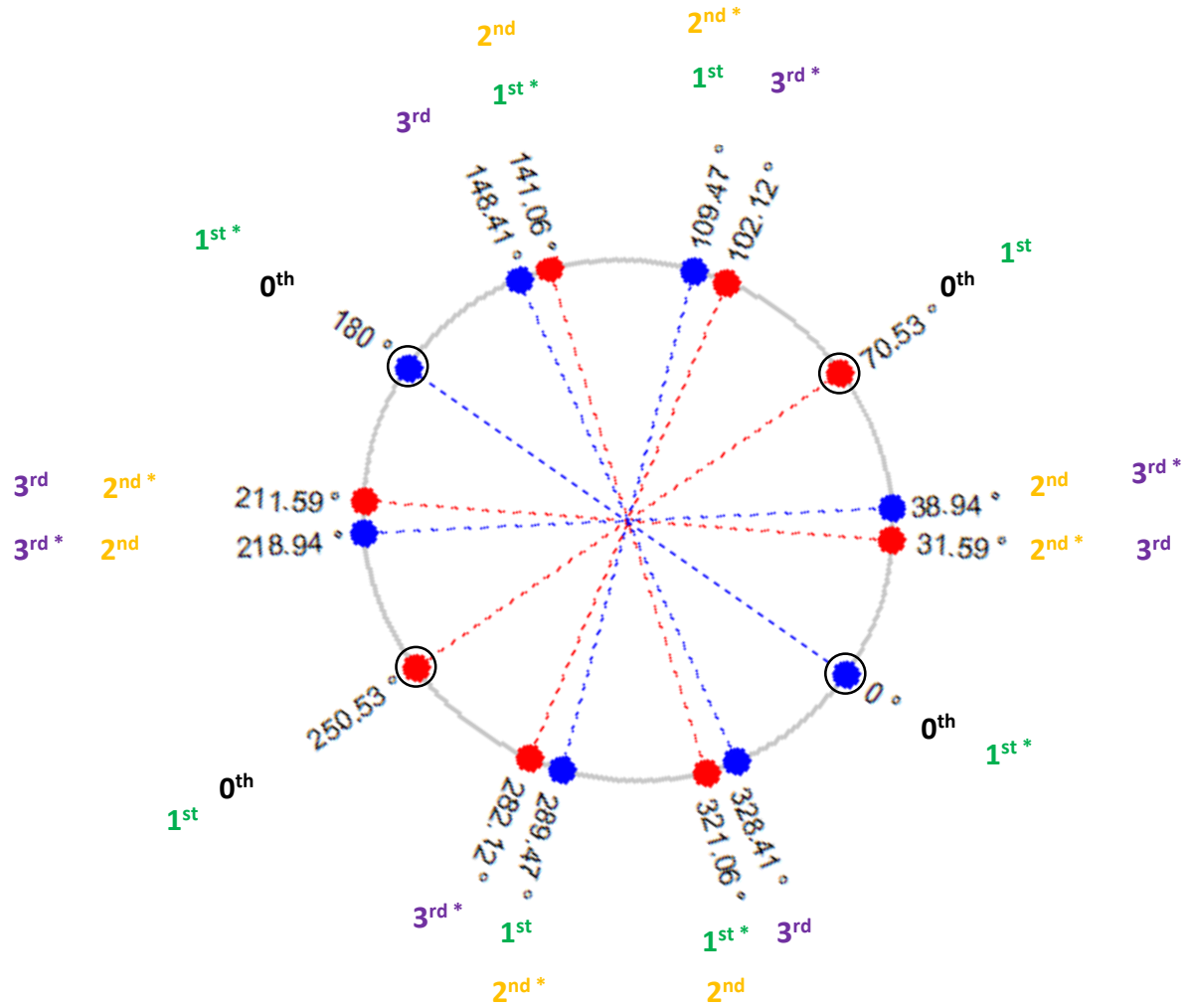


Figure 92. Schematic representation of the monocrystalline orientation of the substrate in black circles and the allowed twin positions in red (anticlockwise) and blue (clockwise) spots for 111 ring. The zone axis is [0-11] and the growth axis is vertical. The order of twinning is indicated for each spot. Orders marked by * refer to twinning of the plane family associated with the spots at 70.53° and 250.53°, the others refer to that associated with spots at 0 and 180°. Only three orders of twinning are illustrated for visibility.

Briefly, by analyzing the twinned part in the reciprocal space (EDP and FFT), we estimated the number of twin operations. In the next sections, we will characterize the twinned part in the real space by analyzing the TEM images. We will also highlight on some differences concerning the quasi-fivefold symmetric EDPs observed on Si (100) and Si (111) substrates.

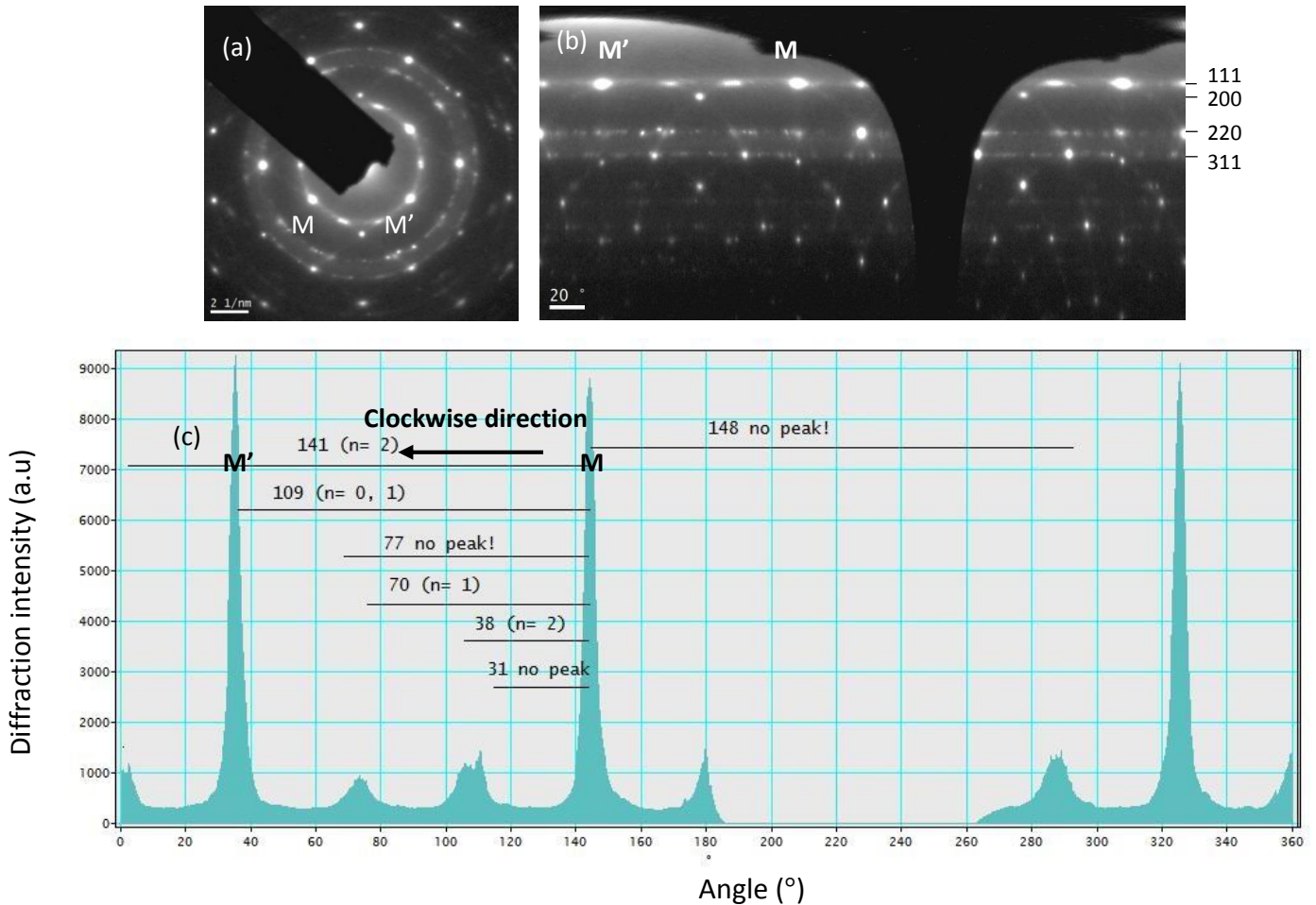


Figure 93. (a) EDP recorded on the MT part for the film deposited on Si (100) at 20 W, (b) azimuthal projection of (a), the black shape is caused by the beam-stopper used while recording the EDP. (c) Profile of 111 reflections deduced from (b). M and M' refer to spots of the monocrystalline grain (angles at 0 and 250.53° in Figure 92) and t refers to twin positions. The horizontal lines indicate the angles formed by the peak M and peaks attributed to a certain order of twinning about M situated at 0.

5.2.1.2. MT part structure

A characterization of the twinned part is provided in this section for the films deposited at 20 and 25 W. For that at 20 w, a bright contrast is visible in Figure 94(a) after the growth of the monocrystalline (or epitaxial) part, indicating a change in the crystalline quality. This suggests the formation of an amorphous phase in the bright part (as discussed in the previous chapter). Moreover, an intermediate “zigzag” line separates these two parts, with a very dark contrast, that is mostly due to the formation of defects (stacking faults, twins). The region around this zigzag line is presented in the TEM images of Figure 94(b). We can notice a lot of V-shaped defects. The two lines of the V form an angle around 70°, which is the angle between two families of {111} planes,

and also the angle characteristic of twinning about $\langle 110 \rangle$ axis. The MT part is referred to the region around the zigzag line.

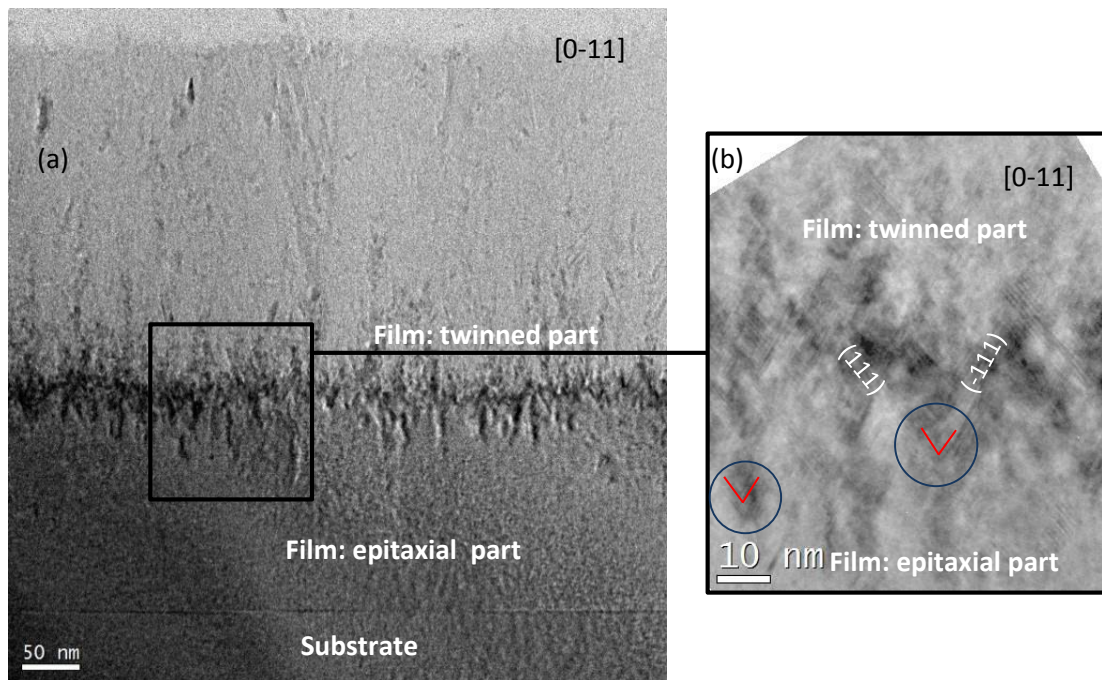


Figure 94. TEM images of the film deposited at 20 W: (a) shows the epitaxial and twinned parts of the film displaying different contrasts. A “zigzag” intermediate line separating these two parts is shown in (b) where V-shaped defects are noticeable.

A zigzag line was also observed for the films deposited at 25 W on Si (100) and Si (111) substrates, as depicted from Figure 95(a) and Figure 95(b), respectively. It is important to point out that there is a family of twin planes that is parallel to the interface in the case of Si (111) seed orientation. Whatever the favored growth direction (parallel or perpendicular to $\{111\}$ planes), this will have an influence on the growth geometry. A discussion will be presented about this point at the end of the chapter. This type of defects indicates that stacking errors exist at this stage of the growth; it initiates the multiply twinned part. In the next section, we highlight on the MT part and show that it composes of two different phases: the first one having a dark contrast with columnar structures and the second one having a brighter contrast.

Being initiated by stacking errors displaying V-shaped defects, the MT part is formed. Remarkably, this part is characterized by a dark phase exhibiting columnar structures propagating through the film.

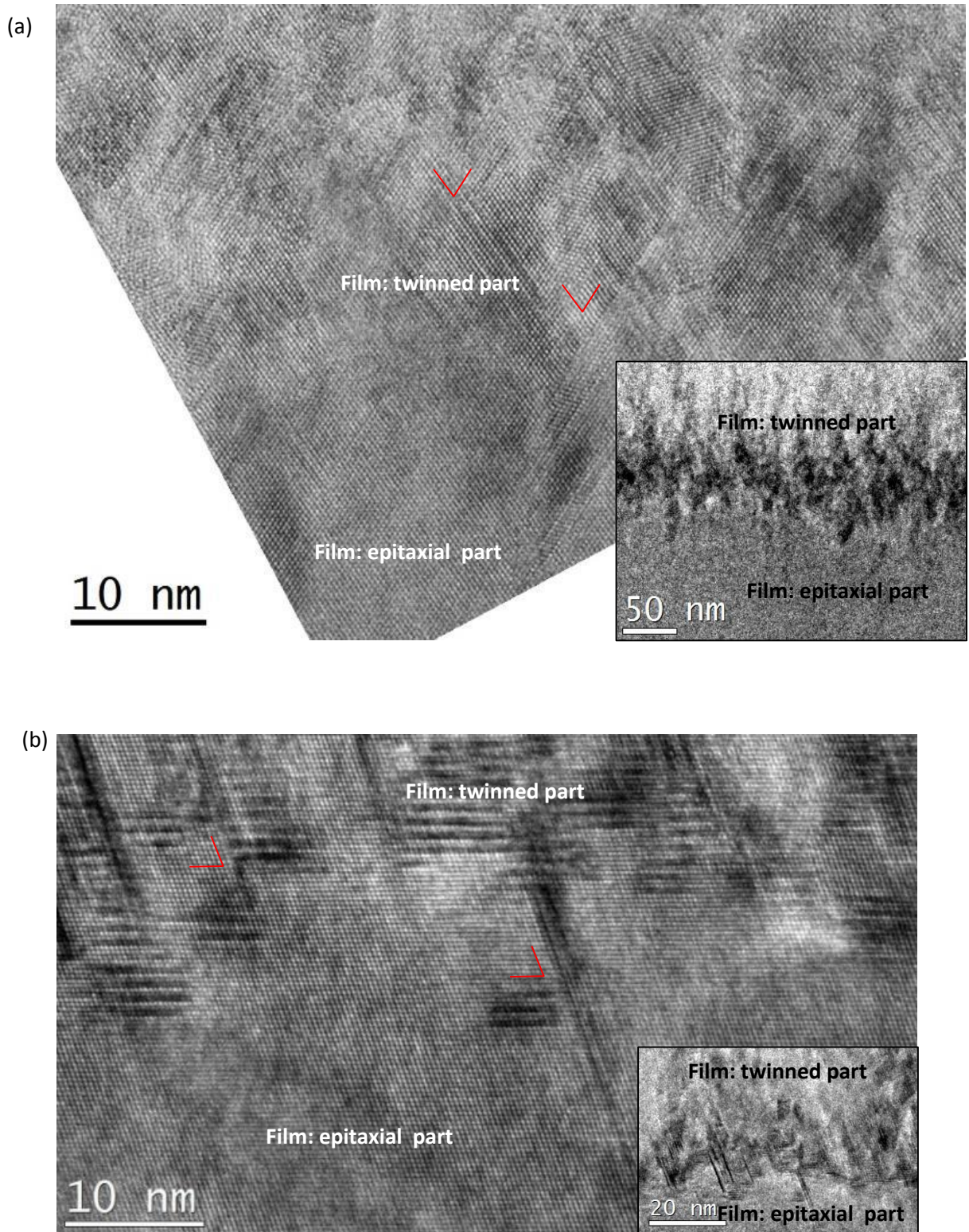


Figure 95. TEM images showing the twinned part (or MT part) around the zigzag line for the Si films deposited using a RF power of 25 W on (a) Si (100) and (b) Si (111) substrates. For both cases, V-shaped defects initiate the MT part.

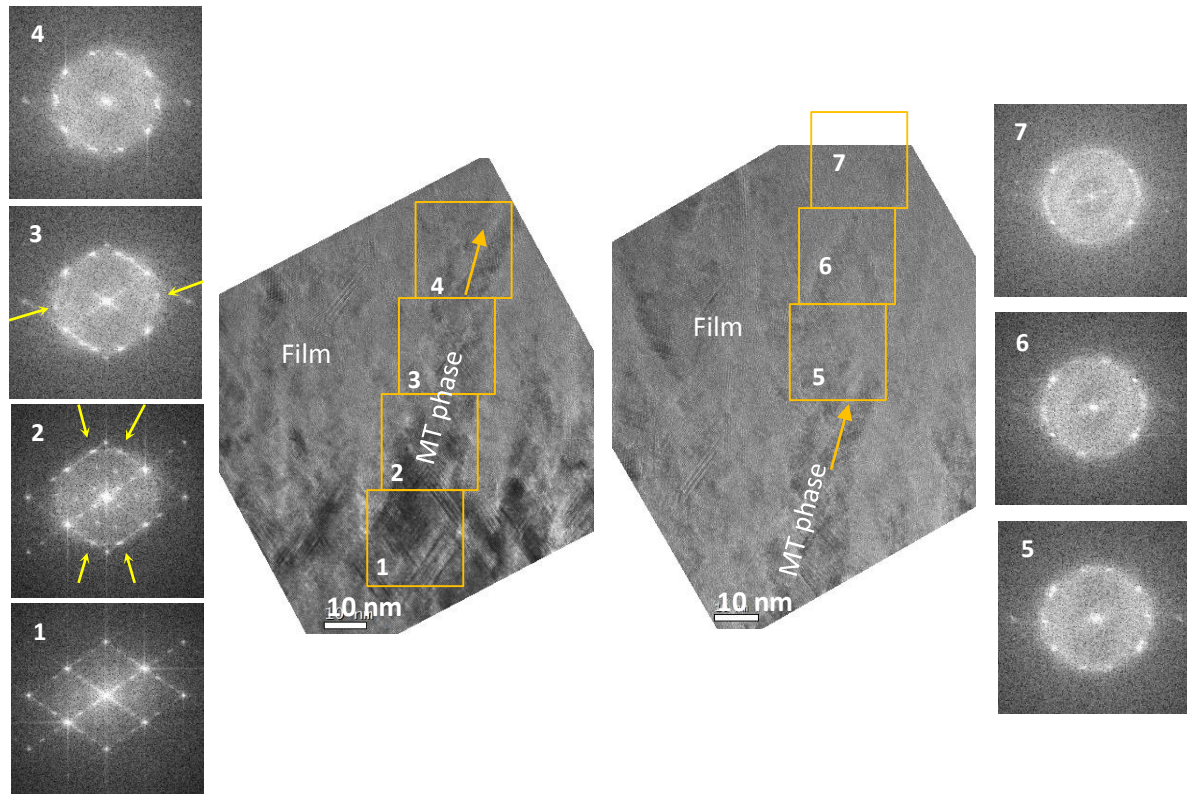


Figure 96. TEM images for the sample deposited on Si (100) at 20 W and a series of FFTs (1-7) performed on the squares drawn on the TEM images. These FFTs show the evolution of the MT phase crystallinity with thickness. The yellow arrows in the FFTs indicate the apparition of twin spots, the orange arrows in the TEM images indicate the growth direction of the darker phase

In order to characterize how this phase is developed with thickness, a series of FFTs has been performed on one columnar structure, as shown in Figure 96. These FFTs are labelled from (1) to (7), (1) being in the stacking error area from which the columnar structures start to form, and (7) being their end. These labels are also shown in the TEM images, illustrating the selected square regions ($23 \times 23 \text{ nm}^2$) for Fourier filtering. FFTs (1) and (2) show additional (111) spots that are the signature of twin formation, and also moiré spots indicating superimposition of twins in the beam direction. First order twinning in clockwise and anticlockwise directions manifests itself by intense spots in (2) (and less intense ones in (1)), while higher order twinning is formed in (3) (see arrows); the twin order was assigned for each spot as shown before in Figure 92. These twin orientations, together with the matrix orientation (orientation of the substrate), lead to the formation of a quasi-fivefold symmetry in (4). Starting from (5), the diffraction spots become extended and present distortions, until the symmetry disappears in (6) and (7). This is accompanied with a decrease of the crystalline contribution to the benefit of an amorphous contribution, as shown by the diffused part.

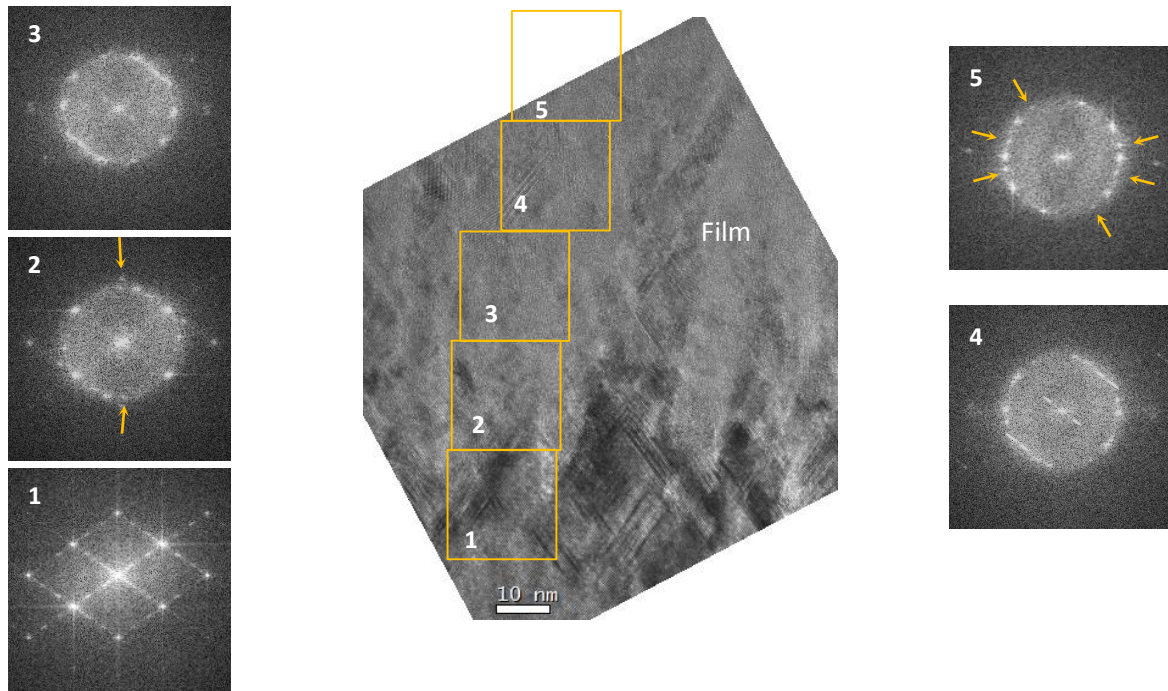


Figure 97. TEM image for the sample deposited on Si (100) at 20 W and a series of FFTs (1-5) performed on the squares drawn on the TEM images. These FFTs show the evolution of the crystalline structure of the bright phase with thickness. The blue arrows indicate spots associated with microcrystalline growth.

Let us now monitor the evolution - with thickness - of the brighter phase in the MT part. Similarly, a series of FFTs has been performed on this phase and is shown in Figure 97.

The most remarkable difference between the bright phase and the dark one is that FFTs of the former one present some intense spots corresponding to random microcrystalline growth, as shown in FFTs (2) and (5) (see arrows). A degradation of the crystalline quality is illustrated in FFTs (3) and (4) by the expansion of the spots associated with the matrix and twin orientations. None of these FFTs display a clear fivefold symmetry in contrast to those presented in the dark phase (Figure 96(4)). It is important to mention that an amorphous contribution also exists (diffused part).

From these observations done thanks to FFT mappings, we can deduce that there exist two phases in the MT part, with the following characteristics:

- A columnar structure with a dark contrast presenting MT phase with fivefold symmetric FFTs. The twin orientations in this phase are progressively lost to the benefit of the formation of an amorphous structure, without the apparition of a significant microcrystalline one.

- A brighter phase with no visible fivefold symmetry. Twin orientations exist in this phase and are quickly lost to the benefit of the formation of both an amorphous structure and a microcrystalline structure. This phase will be called microcrystalline phase (μc -phase).

5.2.1.3. Effect of the seed orientation on twinning - Si (100) vs Si (111)

To study the influence of the substrate orientation on twinning, a comparison between EDPs recorded on (100) and (111) oriented Si substrates is established and is shown in Figure 98 (a) and (b) respectively (samples deposited at 25 W). These EDPs were taken on regions associated with the beginning of twin formation, as shown in the insets. The most intense spots correspond to the matrix orientation and are shown by red circles; the less intense ones mainly correspond to twin positions. The diffused 111 ring in Figure 98(b) is the contribution of amorphous Si, this is confirmed by the diffused ring between 220 and 311 rings. Interestingly, if we look at the 111 ring, we can easily recognize one extended (or multiple) twin spot for (100) and (111) seeds, marked as A and F respectively, that displays less intensity than the other intense 111 diffraction spots.

The spot at A in Figure 98(a) is associated with second order twinning on a (100) seed (starting from spot B for an anticlockwise rotation); it is thus logic that its intensity appears lower than other twin spots which actually originate from the first order twinning. Surprisingly, the spot at F

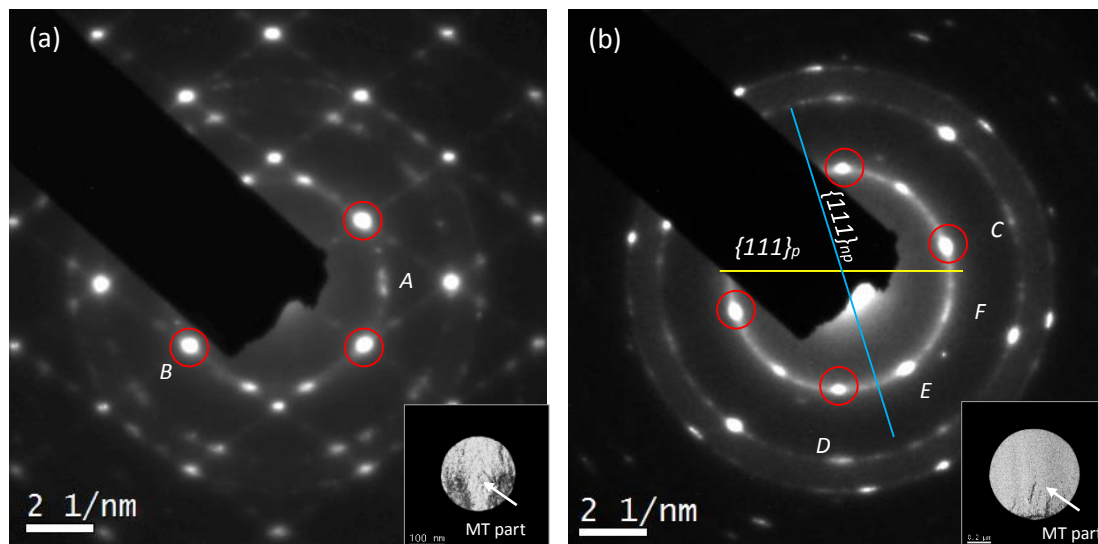


Figure 98. EDPs recorded on the films deposited from $\text{SiF}_4/\text{H}_2/\text{Ar}$ at 25 W on (a) Si (100) substrate and (b) Si (111) substrate. They are taken on regions associated with the beginning of twin formation, as shown in the insets.

in Figure 98(b) is an extended spot associated with first order twinning on a (111) seed (starting from spot D for an anticlockwise rotation) but displays a very low intensity. We next discuss one reason for this apparent low intensity at *F*; it is most probably related to the seed orientation

In fact, for Si (111) substrate, there exist two families of {111} planes in the matrix orientation: the first is parallel to the interface ($\{111\}_p$, *p* for parallel), and the second forms an angle of 70.53° with the former one ($\{111\}_{np}$, *np* for non-parallel), as indicated respectively by the yellow and blue lines in Figure 98(b). Let us consider first order twinning for both $\{111\}_p$ and $\{111\}_{np}$. This operation (mirror symmetry) on $\{111\}_{np}$ (respectively $\{111\}_p$) brings the spot marked by D (C) to the positions at E (F). The spots at *E* and *D* display comparable intensities. However, the spot at *F* displays a certain distortion and a much lower intensity than its parent C; this clearly means that the twinning is globally favored for $\{111\}_{np}$ but not favored for $\{111\}_p$ (the orientation of {111} planes parallel to the interface). In other words, we conclude from Figure 98(b) that $\{111\}_{np}$ is a more active twin plane than the $\{111\}_p$.

It seems therefore that twinning reveals an asymmetric aspect on Si (111). Twin formation and propagation is easier on a (100) seed than on (111). For a (100) seed orientation, the two families of {111} planes (the matrix) are symmetric about the [100] axis (growth direction), there is no reason to privilege twinning on one family over the other, so twinning occurs equivalently for both families. Whereas for a (111) seed orientation, one {111} family plane is parallel to the interface, so that twinning seems to be difficult, but the other {111} family does not exhibit any difficulty for twinning, suggesting a twinning asymmetry for geometrical considerations.

Briefly, twinning is efficient on Si (100) and occurs equivalently for the two {111} families of the matrix, in contrast to twinning on Si (111) that is not favored on $\{111\}_p$.

5.2.2. Epitaxy breakdown caused by increasing the H₂ flow rate

In this section, twin effect is studied for samples deposited under epitaxy breakdown conditions promoted by increasing the flow rate of H₂ in the plasma mixture (SiF₄/H₂/Ar). For deposition conditions corresponding to 1 sccm of H₂ and 15 W of RF power (sample “reference”), the films are completely monocrystalline without the presence of any defects (including twins). While increasing this flow rate to 2 sccm, the EDPs do not exhibit a clear effect of twinning (Figure 99(a)), but few local areas (Figure 99(b)) in the film present some twins as confirmed by their FFT (arrows indicate some twinned orientations in Figure 99(c), suggesting that twinning effects exist but remain negligible within the film. A further increase of this flow rate - up to 3 sccm- results in EDPs that

clearly display the presence of twins, but not the presence of fivefold symmetric EDPs (Figure 100). Thereafter, we investigate twinning in the latter films deposited using 3 sccm of H₂ flow rate and particularly the order of twinning and the structure of the twinned part.

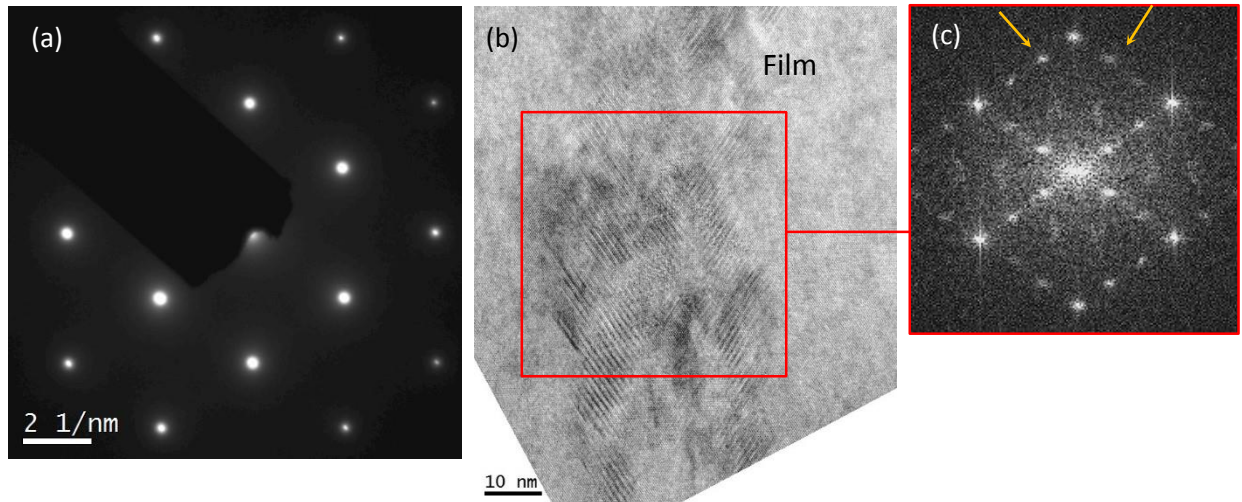


Figure 99. (a) Electron diffraction pattern for the sample deposited at 2 sccm of H₂ flow rate (10 W), showing a monocrystalline structure. (b) TEM image showing few regions (like the red rectangle) presenting a twinned region, which is confirmed in the FFT shown in (c).

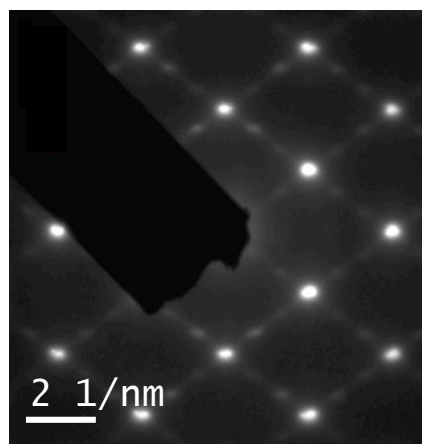


Figure 100. Electron diffraction pattern recorded on the sample deposited at a H₂ flow rate of 3 sccm. It exhibits twin spots associated with twinning.

5.2.2.1. Number of twin operations

We now analyze the number of twin operation in the films deposited using 3 sccm of H₂ flow rate. Given that the EDP of Figure 100 does not display a quasi-fivefold symmetry, we can conclude that there is no second order twinning in these films (because we have already shown in section 5.1.2.2 that such symmetry requires at least second order of twinning in one direction and first order of twinning in the other). The presence of first order twinning is confirmed using the method mentioned in 5.2.1.1, that consists in looking for diffracted intensities at angles away from the matrix orientation) by $\pm n \times 70.53^\circ$ (and $\pi \pm n \times 70.53^\circ$). A schematic representation of the matrix and the allowed twin positions (and their order) is presented for 220 ring in Figure 101(c). We take an extreme hypothesis which is the presence of five orders of twinning.

We perform this method on 220 reflections here instead of 111, because of the simpler geometry implying only two starting spots instead of four (see the black circles in Figure 101(c)), the number of 220 spots being smaller than for 111 ring here. We find 220 diffracted intensities at $\pm 70.5^\circ$ ($n=1$) and $\pm 109.5^\circ$ ($n=1$) but not at $\pm 7.4^\circ$ ($n=5$), $\pm 31.6^\circ$ ($n=3$), $\pm 38.9^\circ$ ($n=2$), neither at $\pm 77.9^\circ$ ($n=4$), as shown in the profile of the azimuthal projection of 220 ring in Figure 101(b) and Figure 101(d). This indicates that only first order twinning occurs in the film in clockwise and anticlockwise directions. It is important to mention that there exists a spot (spot number 3, or 5) between 31.6° and 38.9° (see Figure 101(d)) that is not attributed to a certain order of twinning, but is a double diffraction effect from the original matrix and first order twinning. This double diffraction effect (111 reflection in matrix followed by 220 reflection in twin (blue arrows in Figure 101(a)), or the opposite) can happen due to the fact that the TEM foil is thick enough so that it includes several orientations in the beam direction; the moiré fringes have the same origin.

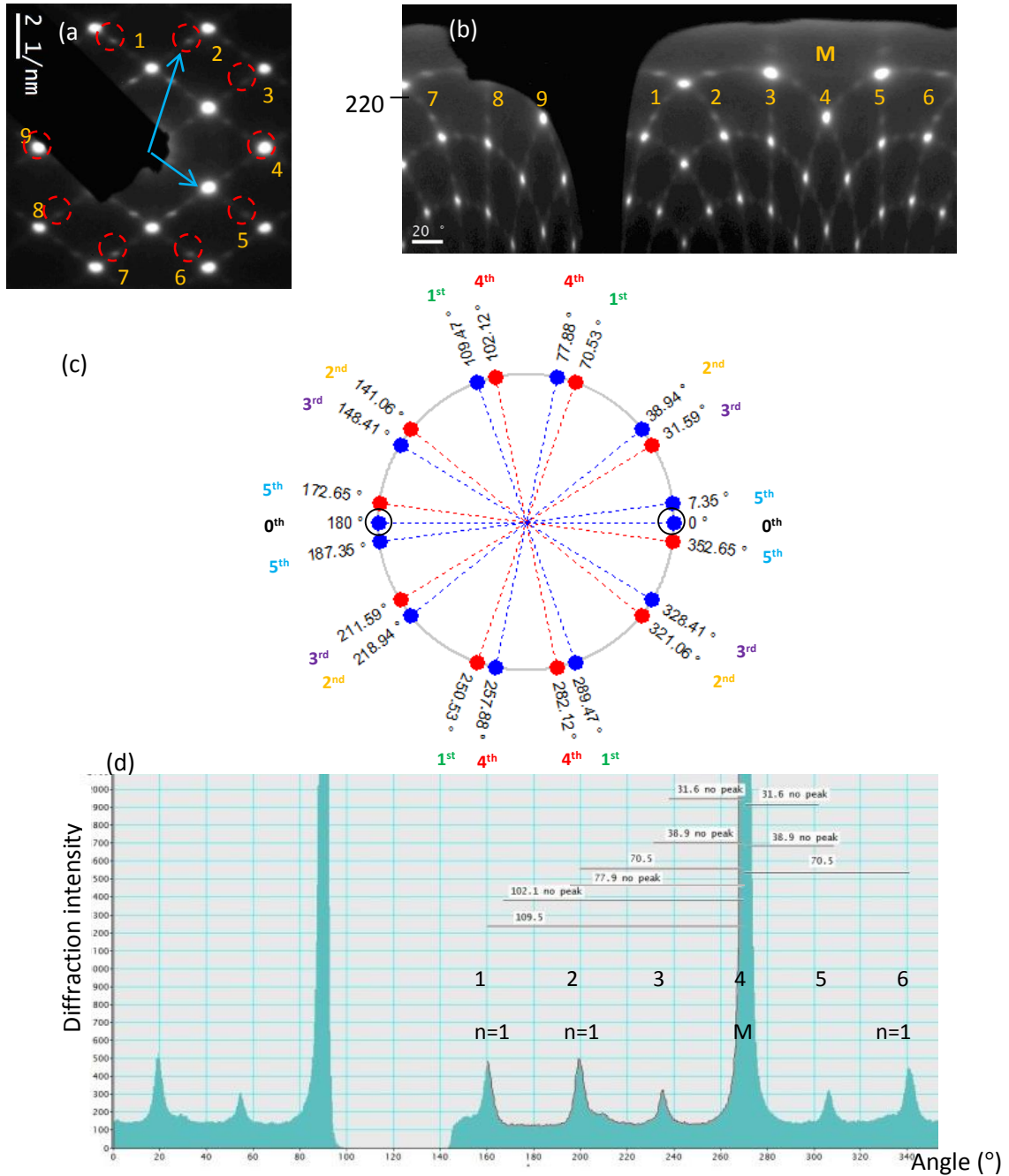


Figure 101. (a) EDP recorded on the sample deposited at a H_2 flow rate of 3 sccm. The profile of 220 ring is shown in (b) and its azimuthal projection in (d). (c) Schematic representation of the monocrystalline orientation of the substrate in black circles and the allowed twin positions in red (anticlockwise) and blue (clockwise) spots. M refers to one spot of the monocrystalline grain. The growth axis is vertical. The order of twinning is indicated for each spot.

5.2.2.2. Twinned structure

The structure of this film is presented in Figure 102. By looking at the thinnest part of the TEM foil, we observe columnar structures growing in a direction perpendicular to the interface (in contrast

to that oblique in Figure 96). There is a contrast in these columns related to defects, like twins and stacking faults and maybe related to strain. The presence of twins is confirmed in Figure 102.

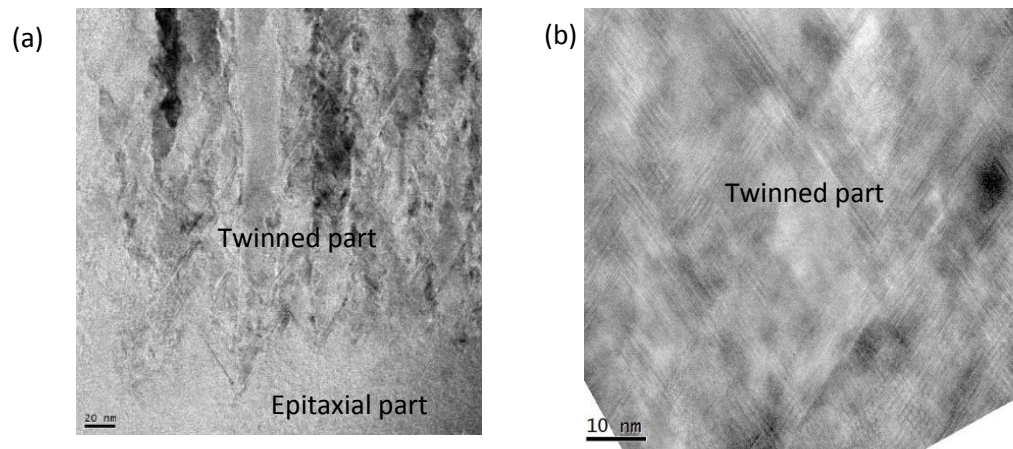


Figure 102. TEM images of the sample deposited at a H₂ flow rate of 3 sccm. (a) Thin part displaying columnar structures growing perpendicularly to the interface. (b) HRTEM image of the film revealing a high density of twins.

We previously showed (in section 5.2.1.2) that stacking errors initiate the multiply twinned part for samples deposited using high RF power of 20 and 25 W, on (100) and (111) seed orientations. Here also, by using a high flow rate of H₂, stacking errors do initiate as well the twinned part, this is clear from the V-shaped defects appearing after the growth of the monocrystalline part, as presented in Figure 102(a).

Briefly, twinning or repeated twinning was investigated on Si thin films grown using a SiF₄/H₂/Ar plasma. These samples were deposited in conditions of epitaxy breakdown associated with the use of a high RF power or a high H₂ flow rate. We concluded that:

- at high power (20 and 25 W at 1 sccm of H₂ flow rate), two orders of twinning in both direction create quasi-fivefold symmetric EDPs
- at high H₂ flow rate (2 and 3 sccm of H₂ flow rate at 10 W), only one order of twinning in both direction exists (no fivefold symmetry)

We also studied the structure of each sample and showed that the twinned part is preceded by stacking errors, exhibiting V-shapes.

In the following section, we investigate twinning effects using another plasma chemistry, which is SiH₄/H₂/HMDSO/B₂H₆/Ar. Repeated twinning was reported and was sufficient to develop fivefold symmetric EDPs.

5.3. Twinning in Si films promoted by epitaxy breakdown from SiH₄/H₂/HMDSO/B₂H₆/Ar plasma

These layers were deposited in the context of exploring the use of HMDSO to grow the p-type layer of amorphous silicon p-i-n solar cells. The importance of this precursor stems from it being a liquid source of oxygen and carbon that one may substitute for the conventional gaseous sources in photovoltaic industry. In a process where both liquid and gaseous precursors could be equivalently used, the former were proved to be six-times safer to handle than the latter [42]. In our previous study [46], we showed that HMDSO is an easy-to-handle precursor that enables us to control the crystalline fraction, the refractive index and dark conductivity of the films over a certain range, simply by changing the flow rate of this molecule. The aim of the present study is to investigate the microstructure of the layers deposited with HMDSO, which exhibit interesting fivefold symmetric EDPs observed throughout several samples without the presence of MTP.

The films were deposited on (100) Si wafers in a RF plasma-enhanced chemical vapor deposition (RF-PECVD) reactor. Prior to deposition, the substrates were treated *in situ* by a plasma composed of H₂ (2000 sccm) and SiH₄ (4 sccm). This treatment had been designed to form a thin seed layer to encourage microcrystalline growth (growth of nanocrystalline domains through random nucleation, resulting in little preferential crystalline orientation) on amorphous substrates. In the present case and when using Si (100) substrates, this treatment had the effect of partially etching the native oxide and promoting epitaxial growth. This was followed by the deposition of the Si films containing a non-negligible amount of carbon and oxygen, and which were deposited using SiH₄, H₂, HMDSO and B₂H₆ diluted to 1% in Ar. The latter layer will be called the “HMDSO layer” in this manuscript. To investigate the effect of HMDSO on the microstructure of our films, we varied only the flow rate of the HMDSO precursor from 0.05 to 2.4 sccm, while keeping all other growth parameters constant: the pressure was kept at 2.5 Torr, the RF power density at 0.17 W/cm², the substrate temperature at 150°C and gas flows in the ratio SiH₄/H₂/B₂H₆/Ar = 4/2000/0.02/1.58 sccm for the deposition of the HMDSO layer. More information about the growth conditions can be found in reference [46].

Given that the fivefold symmetric EDPs were observed under particular growth conditions related to epitaxy, we present these conditions, as a first step to highlight the role of epitaxy. Then we study the effect of HMDSO flow rate on the symmetry. Moreover, we used a quantitative analysis to estimate the number of twinning operations, the contribution of each order of twinning as well

as the fractions of microcrystalline and multiply twinned parts for different growth conditions. Finally, a chemical analysis is presented to establish carbon, oxygen and Si maps.

5.3.1. Effect of the substrate

We were surprised, at the beginning of the present study, to find that the EDPs (see Figure 89) of our HMDSO layers were very simple – displaying quasi-fivefold symmetry – while we were expecting powder patterns typical of microcrystalline growth. It seems therefore that the initial SiH_4/H_2 plasma mostly play an important role in promoting epitaxial growth through (partially) etching the native oxide from the wafer. In this section, the dependence of fivefold symmetric EPDs on epitaxy will be evidenced. To do so, three cases are presented illustrating different substrates:

- the first one enables epitaxial growth because its native oxide was partially etched,
- the second one has a thick native oxide, not sufficiently etched and so not allowing epitaxy and
- the third one is similar to the first but the growth was five times repeated on the same substrate (stack of six films)

Note that all the wafers used here did not have the native oxide removed before loading.

5.3.1.1. Si (100) wafer with epitaxial film/substrate interface

We analyze the microstructure of the films deposited on (100) single crystal Si substrates (at 0.45 sccm of HMDSO flow rate). The wafer we use here had a thin native oxide. Figure 103 shows that local epitaxy is established at the c-Si substrate/film interface where {111} planes are continuous across the interface, but we also find an amorphous phase at some zones. This clearly confirms that the SiH_4/H_2 plasma has partially etched the native oxide of the wafer.

In Figure 104 we show the relationship between the c-Si wafer orientation and the microstructure of the film grown at an HMDSO flow rate of 0.45 sccm. By comparing the EDPs recorded on the wafer, film and glue with the one recorded on the film and glue, we observe that the wafer and the film share four 111 diffraction spots as indicated by the red circles in Figure 104. This means that a part of the film has the orientation of the substrate, i.e., a relation of epitaxy.

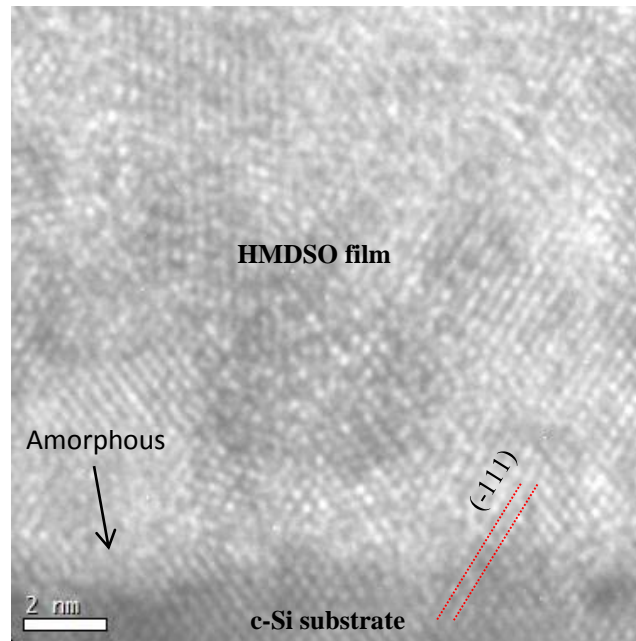


Figure 103. HRTEM image showing local epitaxy at the film/substrate interface and some amorphous regions

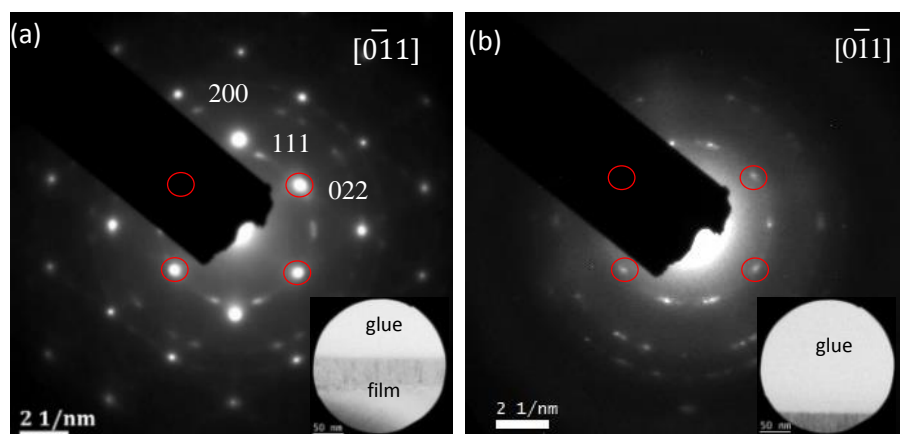


Figure 104. Electron diffraction patterns recorded on (a) the wafer, film and glue and (b) just the film and the glue.

Note that 200 reflections are forbidden by the extinction rules but are illuminated in the substrate by double diffraction due to dynamical considerations. Since the fivefold symmetry is very noticeable in the diffraction pattern of Figure 104(b), it seems that this HMDSO layer is essentially composed of twinned monocrystalline domains.

5.3.1.2. Si (100) without epitaxial film/substrate interface

We present here a layer deposited with an HMDSO flow rate of 0.24 sccm on a crystalline wafer Si (100) which has a thick native oxide. This oxide layer was ineffectively etched by the SiH₄/H₂ process, and remains mostly present on the wafer, thus preventing the establishment of local epitaxy at the interface (which is amorphous here) in contrast with the previous case.

The TEM image of Figure 105 shows the typical elongated microcrystalline grains of Si with an amorphous film/ substrate interface. The associated EDP recorded on the film reveals a powder pattern typical of microcrystalline Si (crystalline domains with random orientations) with additional diffused rings that suggest the presence of an amorphous phase. In fact, small {111} crystallites of a few nanometers have an extended signal in the reciprocal space and thus it is difficult to differentiate the amorphous contribution of Si from small crystalline domains in the EDP. In this case, the latter does not display any fivefold symmetry, the latter depending on whether or not local epitaxy occurs at the film/substrate interface.

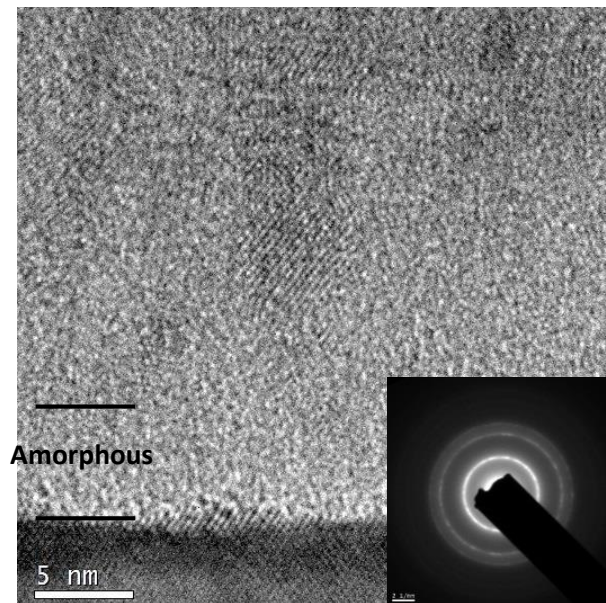


Figure 105. TEM image showing a layer deposited with an HMDSO flow rate of 0.24 sccm on Si (100) without epitaxial interface. The inset shows the EDP recorded on the film exhibiting no fivefold symmetry.

5.3.1.3. Si (100) wafer with epitaxial film/substrate interface – stacking of films with growth interruptions

In this section, we show the results of a stack of six films (Figure 106(a)) growing with different HMDSO flow rates. Two Si (100) oriented wafers were initially loaded into the reactor, and after the application of SiH₄/H₂ plasma and the growth of the film (0.45 sccm of HMDSO), the chamber

of the reactor was opened, the first wafer was left in place and the second wafer was replaced. This process was repeated five times for a total of six HMDSO flow rates (0.62, 0.72, 1.2, 2.1 and 2.4 sccm), resulting in the above mentioned stack of six films, as well as six individual films samples. The sample obtained with 0.45 sccm was the subject of section 5.3.1.1 and the comparison of the individual depositions will be the subject of section 5.3.2.

The stack on the first wafer thus included five interfaces, marked by five vacuum breaks. Such a vacuum break can enable the formation of a thin oxide layer at the surface of each HMDSO layer, which would presumably be etched by the SiH_4/H_2 plasma treatment.

The EDP recorded on the first film and wafer is that of Figure 104(a). However, a fivefold symmetry is hardly noticeable in the EDP recorded on the stack without the first film as shown in Figure 106(b), and instead it seems that there is a non-negligible component of random microcrystalline growth. While increasing the flow rate of HMDSO, the contrast of Figure 106(a) suggests that the films are becoming less crystalline, and this was confirmed by SAED on the top-most film which exhibited a completely amorphous structure.

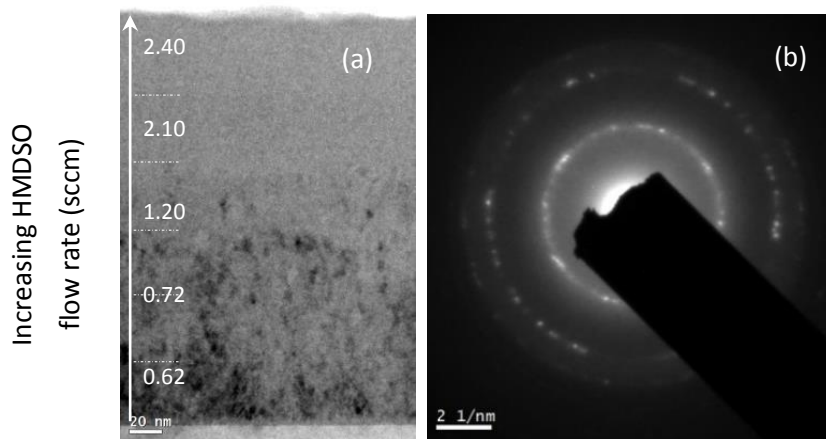


Figure 106. (a) Stack of films with different HMDSO flow rates and (b) EDP recorded on the stack without the first film.

Briefly, the fivefold symmetry was observed only in the case of epitaxial growth; it is obtained thanks to the SiH_4/H_2 plasma applied for surface preparation of the c-Si wafer that also resulted in the partial etching of the native oxide. This treatment (creating holes in the native oxide) would be sufficient for promoting epitaxial growth that is in turn one necessary condition for the apparition

of fivefold symmetric EDPs. The growth of the film stacking shows that this symmetry can be lost with the disorder of the layer underneath HMDSO layer.

5.3.2. Effect of HMDSO flow rate

In order to understand the role played by the presence of HMDSO in the precursor mix, we varied the HMDSO flow rate from 0.05 to 2.4 sccm while keeping constant all other growth parameters. A series of EDPs was recorded in the [0-11] zone axis, parallel to the substrate, in the same area for samples deposited at different HMDSO flow rates, as shown in Figure 107. The deposited films had a thickness around 40 nm, smaller than the diameter (around 215 nm) of the smallest selected area aperture back-projected to the specimen plane; we thus recorded these EDPs on zones which included the film and the glue, as shown in Figure 108, in such a way as to exclude any contribution from the crystalline substrate.

These EDPs show the characteristic 111, 220 and 311 Si rings, the diffused part corresponds to the glue and to amorphous carbon and Si present in the films. The film deposited at an HMDSO flow rate of 0.05 sccm has a quasi-monocrystalline structure but contains a high density of twins and stacking faults, which make characteristic V- shaped features most importantly at the film/substrate interface (Figure 109). This film has the highest crystalline fraction; with increasing the HMDSO flow rate, the crystalline fraction decreases and eventually becomes null at 2.4 sccm, where the EDP does not exhibit any crystalline signature. In other words, increasing the flow rate of HMDSO promotes the growth of an amorphous phase. This result is in agreement with the crystalline fraction evaluated from ellipsometric modeling of the films deposited on glass substrates [46]. What is more important is that the addition of HMDSO does not induce random microcrystalline growth; the films are a combination of multiply twinned oriented crystalline growth and amorphous growth. The details of this will be quantified in section 5.3.4.

It is also noteworthy that according to the Scherrer equation (relating the size of a diffracting domain to the full width at half maximum of a diffraction peak), the crystallite size measurement using 111 reflections is 5-6 nm for all the crystalline films represented in Figure 107(a-c). By the way, we very rarely observed 200 dynamical reflections from twinned grains: this is normal indeed if these grains are 5-6 nm thick in the beam direction.

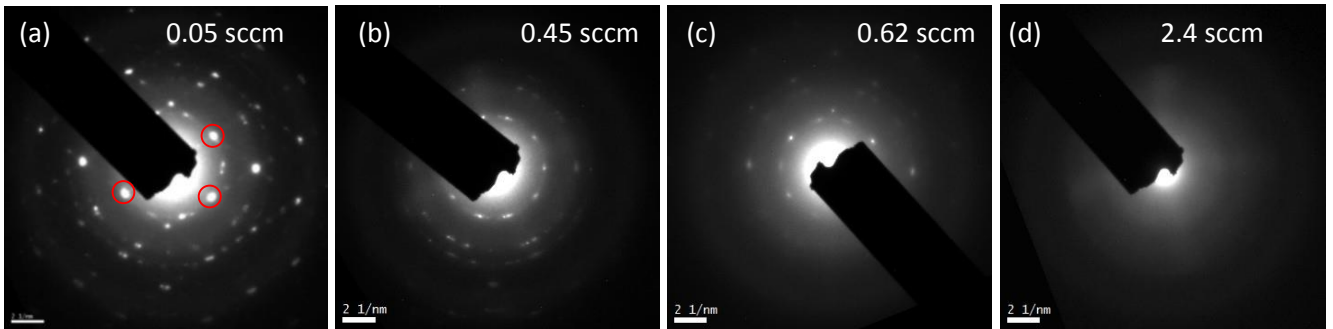


Figure 107. Electron diffraction patterns recorded on samples deposited with different HMDSO flow rates: (a) 0.05, (b) 0.45, (c) 0.62 and (d) 2.4 sccm, all except last showing multiple twinning.

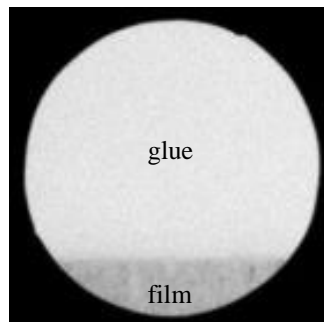


Figure 108. Electron diffraction pattern along the [0-11] zone axis recorded on the selected area shown in the inset including the film and the glue.

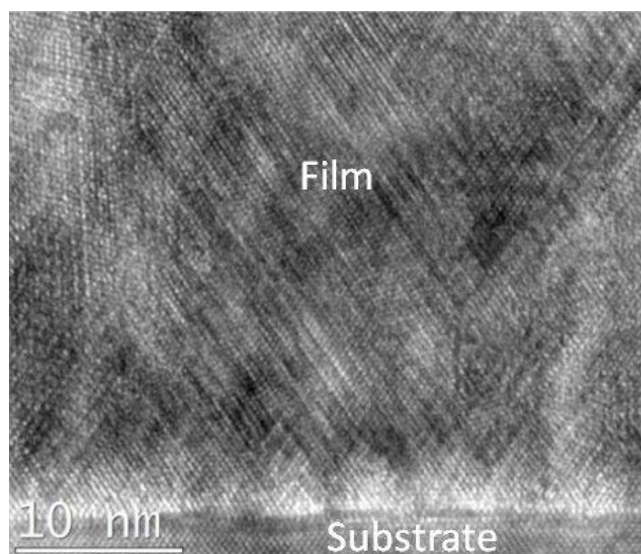


Figure 109. HRTEM image of the film deposited on Si (100) with 0.05 sccm of HMDSO.

5.3.3. Number of twin operations

It is interesting here to estimate the number of twinning operations (as we did in sections 5.2.1.1 and 5.2.2.1). For this, we look for diffracted intensities at angles away from the primary spots (substrate orientation) by $\pm n \times 70.53^\circ$ (and $\pi \pm n \times 70.53^\circ$). We perform this on the two 220 spots of the primary crystal orientation for the EDP shown in Figure 110(a). We use these reflections instead of the 111 because of the simpler geometry implying only two starting spots instead of four. We find 220 spots at first, second and third order twinning ($n = 1, 2, 3$), but we find no diffracted intensity at fourth and fifth orders. The absence of the latter higher order twinning is also confirmed in other films and areas. Thus, three orders of twinning are present in either direction.

It is important to note that after three rotations in one direction and two rotations in the other direction, the spots of the twinned grains do not superimpose, but occupy positions at $\pm 7.35^\circ$ from one to the other (spots at $\pm 31.59^\circ$ and $\pm 38.94^\circ$ for instance, see the discussion section). Another remarkable feature is that the spots corresponding to 31.59° , 38.94° , 211.59° , and 218.94° , indicate the presence of {111} planes almost parallel to the growth axis: they occur after second or third order twinning.

Moreover, we estimated the contribution of each twin order. For this, we calculated the occurrence of first, second and third order twinning in the whole film, by measuring the intensity of 220 spots at 70.53° , 141.06° and 211.59° (and their corresponding spots modulo π), clockwise and anti-clockwise; we chose 220 spots instead of 111 to avoid the ambiguity associated with 111 spots belonging to two orientations. Assuming the matrix intensity to be 100%, twinning intensity contributions came out at 16.7, 4.6 and 4.3 % for first, second and third order twinning, respectively.

5.3.4 MT and microcrystalline contributions

We here evaluate the fraction of MT crystal with respect to random microcrystalline, for the 111 diffraction ring. We did not include the evaluation on 220 diffraction spots since their intensities are small and comparable to the noise signal (especially for the samples deposited at 0.45 and 0.62 sccm of HMDSO flow rate). Our quantification method is based on discriminating diffraction spots occupying twin positions and those occupying non-twin positions, representing MT growth and microcrystalline growth, respectively. We consider the presence of three orders of twinning, in clockwise and anticlockwise directions, starting from the monocrystalline orientation of the

substrate. We define twin spots in the 111 ring in the same way as previously, by applying $\pm n \times 70.53^\circ$ rotations to the four spots of the matrix orientation. By taking one diffraction spot of the monocrystalline grain, that at 0° , for example, one may recognize that the allowed spots in twin position form angles of $\pm 31.59^\circ$, $\pm 38.94^\circ$, $\pm 70.53^\circ$ and $\pm 77.88^\circ$ or $\pm 102.12^\circ$. By applying this reasoning on the four monocrystalline spots (situated at 0° , 70.53° , 180° and 250.53°), one can cover all the allowed twin positions in an EDP (see the schematic representation of Figure 101(c)).

Figure 110(a) shows an example of the azimuthal projection, performed on the EDP of Figure 107(a); the black shape is caused by the beam-stopper used while recording the EDP. From the profile of 111 reflections (Figure 110 (b) and Figure 110(c)), the counting of the area under each peak was done after a background subtraction. According to the above-mentioned method for discriminating twin positions and non-twin positions, we assigned “M” for the spots of the monocrystalline grain, “t” for the allowed twin positions and “u” for unauthorized twin positions, as shown in Figure 110(b) and Figure 110(c). Finally, the fraction of MT material is calculated from the areas under “M” and “t” peaks, and the fraction of microcrystalline material is calculated from the areas under “u” peaks. These fractions represent only the crystalline part, since the amorphous part is included in the background signal and cannot be considered in our calculations.

For the sample deposited at 0.05 sccm of HMDSO flow rate, the proportion of additional spots, which cannot be attributed to twinning, and which would thus represent microcrystalline growth,

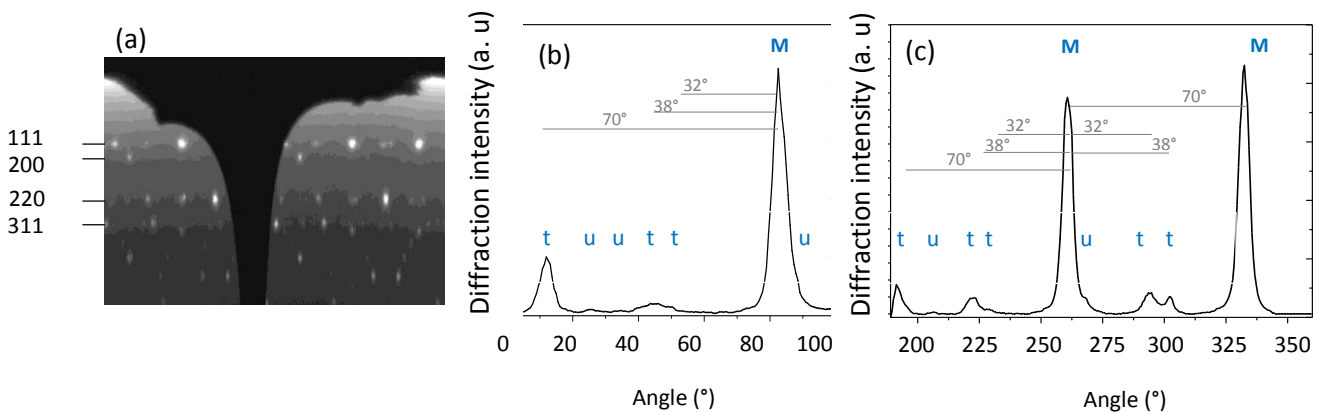


Figure 110. (a) Azimuthal projection of the EDP of Figure 107(a). (b) and (c) Profiles of 111 reflections deduced from (a) after background subtraction. M, t and u refer to the monocrystalline grain, allowed twin positions and unauthorized twin positions, respectively.

is 1.2 % (for 111 ring). In a similar way, the contributions of MT growth and microcrystalline growth were estimated for the three cases presented in section 5.3.1 concerning the effect of the substrate, and for the three crystalline samples presented in section 5.3.2 concerning the effect of the HMDSO flow rate. The results are summarized in Table 4 and Table 5, respectively.

It is clear from Table 4 that the fraction of MT part is strongly dependent on the film/substrate interface, as when it is epitaxial, the MT fraction has a very high value (98.2 %) and when it is not, this part is zero. In the case of the stack of films, this fraction has an intermediate value of 72.1 % which might be explained by the presence of a weakly epitaxial interface (presenting a certain disorder) between each of the five multiply twinned films. Thus, when the quality of the interface decreases, the fraction of the MT part decreases too, allowing microcrystalline growth to take place.

Table 5 shows that, when varying the flow rate of the HMDSO precursor, the proportions of the MT part and microcrystalline part do not change significantly. This means that the flow rate of HMDSO does not influence the structure of the crystalline phase; it essentially plays a role in encouraging the growth of an amorphous phase, as presented in Figure 107.

Table 4. Contribution of the MT part and the microcrystalline part among the crystalline reflections present in the EDPs for the three different states of the substrate mentioned in section 5.3.1: c-Si substrate with epitaxy where individual films and stacking of films were deposited and c-Si with the presence of the native oxide.

Case	HMDSO flow rate (sccm)	MT part (%)	Microcrystalline part (%)
Individual film with epitaxy	0.45	97.2	2.8
Stacking of films with epitaxy	0.62 → 2.4 (stack)	70.1	29.9
Individual film without epitaxy	0.24	0	100

Table 5. Contribution of the MT part and the microcrystalline part among the crystalline reflections present in the EDPs for the three crystalline samples deposited under different HMDSO flow rates (section 5.3.2) in epitaxial relation with the substrate.

HMDSO flow rate (sccm)	MT part (%)	Microcrystalline part (%)
0.05	98.8	1.2
0.45	97.2	2.8
0.62	96.7	3.3

5.3.5. Chemical analysis

As impurities may play a role in crystalline defect formation, it is important to know where they are in the sample: if any segregation or precipitation has taken place. Thus, we recorded elemental maps of silicon, carbon and oxygen, using energy-filtered TEM (EFTEM), on samples deposited with an HMDSO flow rate of 0.45 sccm on Si (100) with epitaxial film/substrate interface. The concentrations of these elements were quantified by correlating EFTEM and secondary ion mass spectrometry (SIMS) measurements expressed as arbitrary units and atoms/cm³, respectively. Given that the bulk of the substrate does not contain oxygen and carbon before TEM sample preparation, and that its oxidation (or contamination) occurs on the TEM foil surfaces after sample preparation, we considered the bulk of the substrate as the level of contamination with carbon and oxygen. In order to have accurate elemental concentrations in the film, we first subtracted this contamination level, assuming that it is happening identically in the bulk of the film and in that of the substrate, and then we set the average value of the elemental profile in the bulk of the film as the average value of SIMS measurement in the same region.

A lack of Si atoms at the interface manifests itself as a dark contrast in the Si map (Figure 111(a)), and a smaller concentration of Si in HMDSO layer with respect to that of the wafer is also observed. In the oxygen map ((Figure 111(b)), the presence of a white thin oxygen-rich layer at the interface shows that the native oxide of the wafer was not completely etched. This interfacial oxide layer is presented by a peak in the profile of oxygen ((Figure 111(d)) having a concentration of $\sim 8.4 \times 10^{21}$ oxygen atoms/cm³. A non-negligible amount of oxygen is found in the film and is estimated at $\sim 2 \times 10^{21}$ at/cm³. In the carbon map (Figure 111(c)), we see no obvious contrast between the wafer and the film, but the profile of carbon ((Figure 111 (e)) shows the existence of $\sim 2 \times 10^{21}$ carbon

at/cm³ in the film. A small peak in this profile is present at the interface, which might be caused by carbon contamination of the surface of the wafer before deposition. At this point, we can explain the lack of Si at the interface by a higher concentration of carbon and oxygen (impurities) atoms at this interface compared to these concentrations in the bulk of the wafer. It should be noted that the thickness map of the film, deduced from the ratio of the total beam intensity over that of elastically scattered electrons, indeed appeared constant with no fluctuations, suggesting that the missing Si atoms had been replaced by other elements.

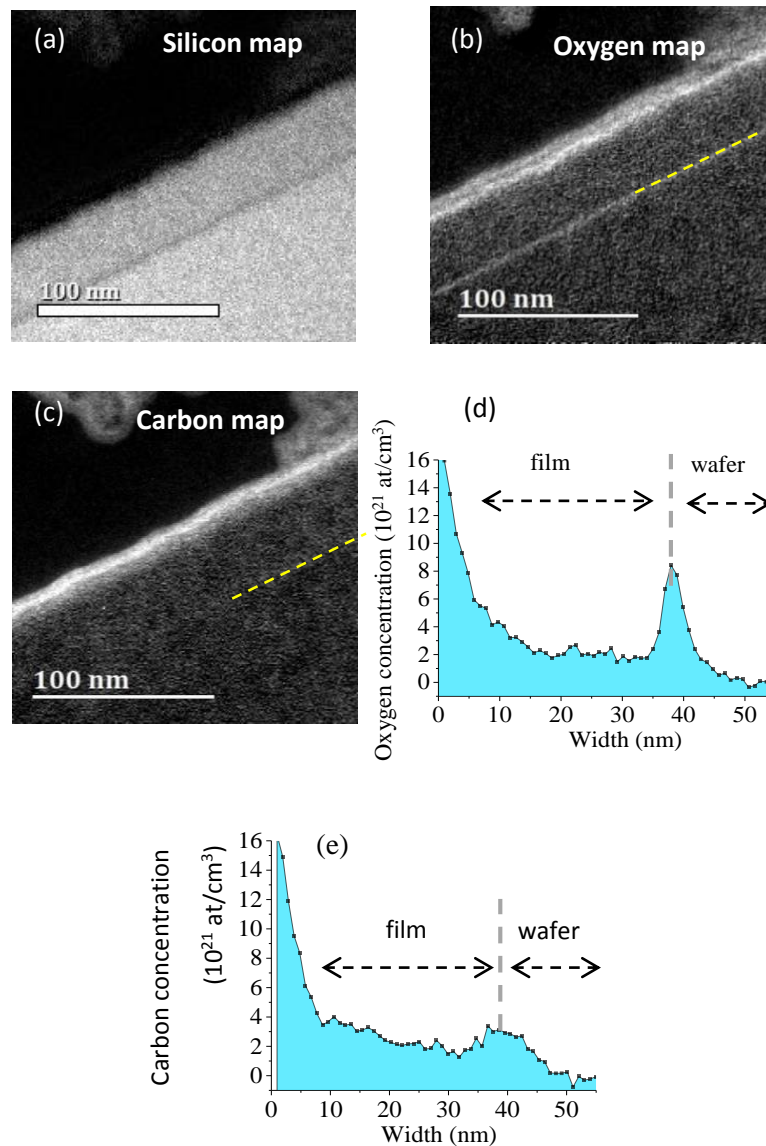


Figure 111. Elemental maps of silicon (a), oxygen (b) and carbon (c). (d) and (e) represent the profiles of oxygen and carbon, respectively.

It is important to note that the presence of oxygen and carbon in the film comes from the use of the HMDSO precursor which contains one oxygen atom and six carbon atoms per HMDSO molecule. We showed in previous work [46] that when increasing the flow rate of HMDSO, there is more carbon and oxygen incorporation in the film, which causes a decrease in the crystalline fraction and explains the trend of Figure 107. However and quite remarkably, whatever the flow rate of HMDSO precursor, carbon and oxygen are incorporated in about equal concentrations [46] and the ratio of the multiply twinned part to microcrystalline part is kept unchanged as we have showed in section 5.3.4.

5.4. Discussion

5.4.1. Growth twins and fivefold symmetry

On the basis of the results presented above, it is clear that the fivefold symmetry observed in the [0-11] diffraction patterns of our films is associated with secondary or multiple twinning. Primary twinning is also observed for some samples without higher orders of twinning. In fact, the formation of growth twins is not surprising, as the misplacement of atoms happens naturally during crystal growth, and the occurrence of multiple twinning is also not surprising since it was frequently reported in the literature. For instance, multiple twinning was observed on homoepitaxial Si layers [143] and on gallium arsenide grown on germanium [144], appearing as tripyramids and hillocks, respectively. But, the occurrence of repeated twinning giving rise to fivefold symmetric EDPs without the formation of multiply twinned nanoparticles is unexpected. Symmetry five is frequently found in the literature on decahedral particles [47, 139, 145, 146] composed of five crystalline domains with well-defined twin boundaries and sharing one common axis, in contrast to the case of the films presented in this chapter deposited using $\text{SiF}_4/\text{H}_2/\text{Ar}$ or $\text{SiH}_4/\text{H}_2/\text{HMDSO}/\text{B}_2\text{H}_6/\text{Ar}$. In other words, the boundaries between domains most of the time do not contain, specifically, the [0-11] common axis which is also the zone axis of the micrographs and EDPs. Actually, symmetry five starts to be seen in the EDPs of these films when three twinned crystal orientations (including five different {111} orientations) are present in the area selected for diffraction and not necessarily five. Moreover, our twin boundaries do not share one common axis and are incoherent (not following {111} planes) for the samples deposited from both plasma chemistries.

In addition, epitaxial growth is one necessary factor for the formation of this symmetry, unlike the case of MTPs where the occurrence of this symmetry is not directly linked to epitaxial growth [141].

However, the most remarkable difference between the present case and that of MTPs regards the closure defect. Generally, in MTPs, this type of defects is due to the fact that the twinning operation corresponds to a 70.53° rotation about $\langle 110 \rangle$, so that there remains a gap or a mismatch of 7.35° ($360^\circ - 5 \times 70.53^\circ$) between the fifth twinned grain and the original matrix. In some MTPs, this closure defect is healed by the generation of strain and deformations, like the elastic and plastic deformations occurring, respectively, in the internal and external regions of the particle [139]. This, in turn, may give in certain cases a perfect fivefold symmetry. However, such healing clearly implies severe deformation and a freedom of displacement for the atoms that may be possible in nm-scale particles where surfaces are never far away, but is unimaginable in the bulk of a thin film. Whereas in our study, no closure defects are observed in the EDPs: the multiplicity of some reflections (e.g. 31.59° and 38.94° in Fig. 5) occurring after two or three orders of twinning, indicate that our twin angles are perfect and not modified for closure.

5.4.2. Origin of twinning and multiple twinning

A question still remains unanswered concerning the origin of twins. In fact, it is well-known that when a collection of atoms assembles itself as a stable crystal, it takes a configuration of lowest free energy state; any departure from this configuration requires a higher energy [147]. Since twinning (or twin boundaries) configuration is one possible departure from the rest of the crystal configuration, the question of what permits these atoms to assume this higher energy state is raised. While the mechanisms of twinning have been investigated since the early days of the growth of diamond semiconductor materials, a complete explanation of twin formation is still missing and the literature on this subject is quite confusing [148]. Indeed, many factors contributing to the formation of twins have been mentioned. In an attempt to understand the occurrence of twin features in our samples, we will try to relate our observations to other studies exhibiting twinning effects.

- Nucleation errors:

Smith [148] envisaged three mechanisms for twin formation in crystal growth: nucleation error, epitaxial inheritance and synneusis. Here, we obviously have the first one (nucleation error), which happens when faulty positions are taken by atoms in the nucleus leading to the formation of two parts with a common surface. During the nucleation of our HMDSO films, a lot of V-shaped areas originating at the interface indicate that the presence of nucleation errors start at the substrate surface. The other mechanisms do not apply here as the second one (epitaxial inheritance) needs

a twinned substrate and the third one (synneusis, also called combination twins [149], agglutination twinning [150, 151] or oriented attachment [152]) takes place in a liquid.

- Preferential growth direction:

Interface and seed orientation was reported by Billig [153] to be an important reason that helps the occurrence of twins. He stated that the probability of twinning increases with the alignment of the resulting {111} planes to the growth axis. According to him, the seed that mostly gave rise to twins had a (100) orientation. In other words, a deviation of the actual growth direction from the preferred growth direction is a major reason for the occurrence of twinning. Similar considerations were taken by Bulling *et al.* [154] and discussed by Carstens [155]. In the present work, a geometrical analysis shows that two or three successive twin operations, occurring either in clockwise or anticlockwise directions, bring a family of {111} planes at $\pm 3.7^\circ$ of the growth direction, which in that case, becomes close to a $\langle 211 \rangle$ axis. This is illustrated by the shift of color, when looking to the crystal orientation in Figure 90(d), from red close to the substrate to blue and green away from it. Thus, after such clockwise and anticlockwise rotations, one obtains the five orientations that we observe indeed. It seems, therefore, that the [100] axis is not the axis dynamically preferred for the growth, and that changing it for an axis parallel to a twinned {111} plane would be more efficient for the growth. Such geometry occurs after double or triple twinning, which are indeed the orders of twinning we observed in the films exhibiting quasi-fivefold symmetric EDPs in this chapter.

- Presence of impurity defects:

Holloway and Bobb [144] attributed the formation of twins in epitaxial growth of gallium arsenide to the incorporation of impurities, such as oxygen and water vapor. Similar considerations were supported by Pizzarello [156] while describing his experimental procedure. Bulling *et al.* [154] found an increased twin density in germanium with the concentration of gallium contaminant, and Billig [157] speculated that the presence of impurities may explain twinning in dendrites. Thus, twin formation in layers deposited with HMDSO precursor may also correlate with the presence of carbon and oxygen impurities. The specificity of these impurities stems from being incorporated in Si lattice in about equal amounts. It is known that carbon atoms occupy substitutional sites [158-160] and so contribute to a reduction in the lattice parameter of silicon, whereas oxygen atoms occupy interstitial sites [160, 161] and so contribute to an increase in the lattice parameter of Si. These two effects most probably interfere in some way. Increasing the concentrations of both impurities obviously promotes the generation of amorphous Si (section 5.3.2); it remains unclear whether it also helps or not the formation of twinning.

- High flow rate of H₂ in the plasma mixture:

From another point of view, the plasma conditions applied for the deposition of Si films from SiF₄/H₂/Ar plasma (2 and 3 sccm of H₂ flow rate) as well as for the deposition of the HMDSO layers (SiH₄/H₂= 4/2000) correspond to an excess of hydrogen. In fact, in order to compensate the amorphization effects due to the presence of carbon and oxygen in the case of HMDSO layers, a high ratio of SiH₄/H₂ has been used to promote the crystallization [52]. Several references showed the effect of hydrogen on the crystallization of Si thin films. For instance Dornstetter et al. [39] showed that crystallization mediated by atomic hydrogen happens when using a high hydrogen flow rate. It seems therefore that this excess of hydrogen atoms in both plasma chemistries provides the Si lattice with an excess of energy to crystallize, and contributes in the creation of some defects in the form of twins (by reaching a higher energy state). Such an extra energy provided by a highly diluted H₂ plasma has been reported by Cuony et al [162], in the case of a mixed Si/SiO₂ phase, where it allowed phase separation by increasing adatom mobility. The fact that the twin boundaries are mostly incoherent (not following {111} mirror planes) in our samples could also be related to this extra energy. However, for the HMDSO layers only, this incoherence might also be linked to the probable presence of segregated carbon and oxygen impurities.

- High RF power:

A major change caused by increasing the applied power concerns the species impinging at the surface of the substrate or film. Generally in standard PECVD reactors, increasing the RF power is equivalent to increasing the flux and energy of positive ions at the same time. This appears as a source of supplemental energy provided to the growing system, which could enable the system to reach higher energy states and so to form twins. Several references are consistent with this and showed that an excess of ion bombardment energy produced damages in the film and a degradation of the crystalline quality [19, 65]. The formation of twin defects due to an increasing RF power was previously discussed in the chapter 4 (section 4.4.1.2).

- High growth rate:

The occurrence of stacking errors like twins, during the nucleation stage or during further growth, may classically be attributed to a high growth rate, as then, atoms do not have time to find the lowest energy sites before they receive neighbors that fix them. In the particular case of the film deposition at (1 sccm, 25 W) or (3 sccm, 15 W) from SiF₄/H₂/Ar chemistry, the growth rate has increased significantly from 0.6 Å/s for the reference film (perfect epitaxy) to 1.4 or 5.4 Å/s, respectively. However, the growth rate does not seem to play a role in the occurrence of twins in the case of the HMDSO layers since they were deposited at relatively low growth rate (0.5 Å/s).

Table 6. Potential reasons for the occurrence of twinning for three cases categorized by the order of their twins: twinning in HMDSO layers, twinning in samples deposited using SiF₄/H₂/Ar at 20 and 25 W of RF power (1 sccm), and twinning in samples deposited at 3 sccm of H₂ flow rate (15 W).

Possible causes of twinning	HMDSO layers (n= 3)	Samples at high RF power (SiF ₄ /H ₂ /Ar) (n= 2)		Samples at high H ₂ flow rate (3 sccm) (SiF ₄ /H ₂ /Ar) (n= 1)
		20 W	25 W	
Pref. growth direction	✓	✓	✓	✗
Presence of impurity defects	✓	✗	✗	✗
High growth rate (> 1 Å/s)	✗	✗	✓	✓
High flow rate of H ₂	✓	✗	✗	✓
High RF power	-	✓	✓	✗

In Table 6, the potential reasons for the occurrence of twinning are shown for three cases categorized by the order of their twins: twinning in HMDSO layers (twin order= 3), twinning in films deposited with SiF₄/H₂/Ar at high RF power 20 and 25 W (twin order= 2), and at high H₂ flow rate at 3 sccm (twin order= 1). From this table, we can extract the following points:

- The choice of a preferential growth direction other than [100] axis could well be the driving force for the multiple twinning - and for the observation of quasi-fivefold symmetric EDPs- which occurs in the case of HMDSO layers and films deposited at 20 and 25 W (presence of triple and double twinning respectively).
- The presence of impurity defects can be considered as an additional reason for twinning but not a necessary condition, since no significant amount of defects was detected in films deposited from SiF₄/H₂/Ar.
- Considering the growth parameters, namely the use of a high flow rate of H₂ or the application of a high RF power, they provide the lattice with supplementary energy to reach a higher energy state, and might be the first reason for allowing wrong stacking in all the films.
- High growth rate may also play a role in the formation of twinning for the films deposited at 3 sccm of H₂ flow rate or at 25 W of RF power. The increased growth rate is mostly due to the increase of the H₂ flow rate or the RF power, as shown by Dornstetter [31].

5.4.3. Twinning and epitaxy breakdown

From the observations of all the samples presented in this chapter, it becomes clear now that the monocrystalline orientation in the film is lost by the formation of twinning or repeated twinning, triggered by stacking errors. In other words, twinning manifests itself to be the most important feature of epitaxy breakdown, the latter being caused by the application of a high RF power or a high H₂ flow rate. Twinning in our case is mainly due to the growth parameters that enable the system to reach higher energy states and thus develop twins.

The twinned part in these films appears after a monocrystalline growth and disappears in some cases after a certain thickness. We showed that this part is initiated by stacking errors, but we did not highlight on twinning growth modes, neither on the path used by the system to lose the twinned orientations (twinning breakdown). Are they lost to the benefit of a microcrystalline or an amorphous growth? In the following, we discuss twinning breakdown, based on our observations for the two plasma chemistries used for the growth.

5.4.3.1. Discussion on twinning in HMDSO layers

5.4.3.1.1. Growth modes

According to measurements made on samples obtained under several growth conditions, the proportions of multiply twinned growth and microcrystalline growth in HMDSO layers (displayed in Table 4 and Table 5) depend on the effective removal of the native oxide from the c-Si substrate and not on HMDSO flow rate.

In fact, around 98.2 % of the crystalline phase is in an orientation consistent with MT when the native oxide has been efficiently removed from the substrate. There remains ~1.8 % of random microcrystalline growth that might come from some small amorphous regions (residual native oxide). The fraction of the MT growth decreases to 72.1 % when the HMDSO layer (e.g. the last of the five films in the stack) grows on a previous layer that has a MT structure (much less ordered than a monocrystalline structure). This fraction becomes null when the surface state beneath HMDSO layer is amorphous, and instead, microcrystalline growth is established, and appears as the typical conical growth [163, 164] where crystalline domains with random orientations appear. Therefore, depending on how efficient was the surface cleaning of the substrate, microcrystalline growth (random orientation) can be suppressed in favor of a MT growth (with memory of the orientation of the substrate). This competition between twinned epitaxial and microcrystalline

growth modes is expected since our layers are near the amorphous-to-microcrystalline transition when deposited on glass substrates [46].

The phenomenon of epitaxy breakdown starts from the very beginning of growth, progressively as a function of the deposited thickness. Its most remarkable feature is the fact that it generates a structure made of twins. The fact that second and third order twinning appear in equivalent ratios (4.6 and 4.3 % respectively) seems to be consistent with a scenario where these two orders finally dominate and exchange between each other.

5.4.3.1.2. Twinning breakdown

For HMDSO layers, with the addition of a higher flow rate of HMDSO in the precursor mixture, the twinned orientations are lost to the benefit of an amorphous growth, without the apparition of any microcrystalline signature in the EDPs (see Figure 107). This amorphous growth is associated with the incorporation of higher amounts of carbon and oxygen into the films.

In the case of the stacking of films (Figure 106 and Table 4), the twinned orientations are lost progressively, to the benefit of the formation of a random microcrystalline growth that hinders the apparition of fivefold symmetric EDPs. This is mostly related to the fact that a new HMDSO layer is being deposited on an already grown MT structure (that presents some disorder) and not on a perfect monocrystalline one.

5.4.3.2. Discussion on twinning in Si films (SiF₄/H₂/Ar)

5.4.3.2.1. Growth modes

The previous plasma chemistry was very specific because it uses HMDSO precursor that contains at the same time Si, O and C elements, and the dissociation of this precursor makes the plasma more complex. Thus, the observed twinning in that specific plasma chemistry remains very particular, and its discussion is limited as that the available literature is scarce. However, in the case of SiF₄/H₂/Ar, which is a more known plasma (that was achieved to replace SiH₄/H₂ plasma), twinning can benefit from a relatively wider vision. In the following, we check if the breakdown of epitaxy is always mediated or accompanied by twin formation. To do this, we discuss our observations on samples grown in epitaxy breakdown conditions using this plasma chemistry at first, and then we compare these observations with the ones corresponding to a SiH₄/H₂ plasma.

Let us start with SiF₄/H₂/Ar plasma. We showed in this chapter that epitaxy breakdown for all samples deposited at high RF power (20 and 25 W) or at high H₂ flow rate (3 sccm) was mediated by twinning or repeated twinning. We have made similar observations on samples grown on Si

(100) using the same growth conditions, except for the flow rate of H₂ and the power that corresponded to 2 sccm and 20 W respectively. The epitaxial structure in the latter samples was sustained for 70 nm, then degraded into a twinned structure in this case also, as shown by the EDP recorded on regions marked by 1 and 2 (Figure 112 (a) and Figure 112 (c)), and by the TEM image shown in (d) recorded on region 2. The twinning breakdown here corresponded to a transition into microcrystalline and amorphous phase as presented by the random microcrystalline spots and the diffused ring in the EDP recorded on region 3 (b).

Moreover, epitaxy breakdown induced by twinning was observed on another sample deposited on a (111) oriented substrate, with similar growth parameters but for a H₂ flow rate of 1.5 sccm and an applied power of 15 W. Figure 113 shows a TEM image of this sample and an EDP recorded on a zone of the film near to the interface, as shown by the circle in Figure 113(a); the latter displays spots characteristic of repeated twinning; it resembles that shown in Figure 98(b).

A similar observation using the same chemistry but in another PECVD reactor (CLUSTER) was done on samples grown on Si (100) by Dornstetter and characterized by Florea [165]. It shows that the breakdown of epitaxy occurs with the formation of defects oriented along {111} planes and identified as twins, as presented in Figure 114. Note that this breakdown was induced by the variation of the hydrogen flow rate from 4 to 6 sccm; the growth conditions are: SiF₄/H₂/Ar = 10/2/88, power = 40 W (or 0.53 W/cm²), pressure = 3.8 Torr.

Briefly, all these cases presented using SiF₄/H₂/Ar chemistry have a common feature: epitaxy breakdown is characterized by twin or repeated twin formation. Nevertheless, can we decide that twinning is the first step and only way to break Si epitaxy? To answer this question, we will check if the epitaxy breakdown of Si also occurs by twinning using another PECVD chemistry, which is the famous SiH₄/H₂ chemistry.

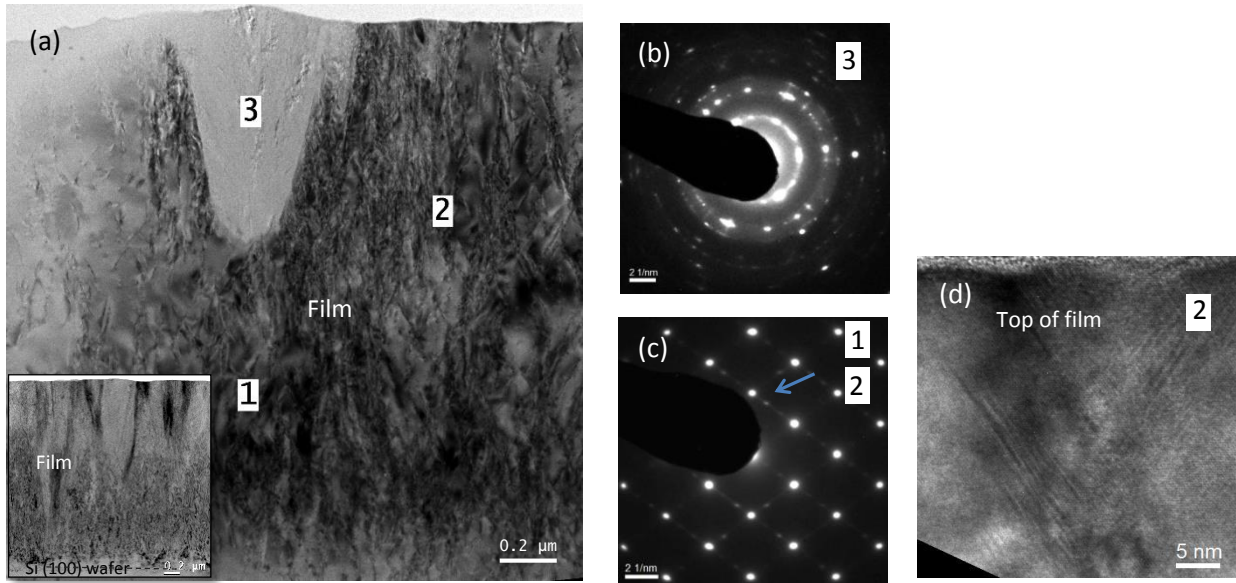


Figure 112. (a) TEM image showing epitaxy breakdown, on Si (100) wafer, mediated by twin formation for a sample deposited in the same growth conditions as our samples deposited in $\text{SiF}_4/\text{H}_2/\text{Ar}$ plasma except for the flow rate of H_2 and the power that corresponded to 2 sccm and 20 W respectively. (b) EDP corresponding to region 3, (c) EDP corresponding to region 1 and 2 (the arrow indicate a twin spot) and (d) TEM image showing the twinned structure of region 2.

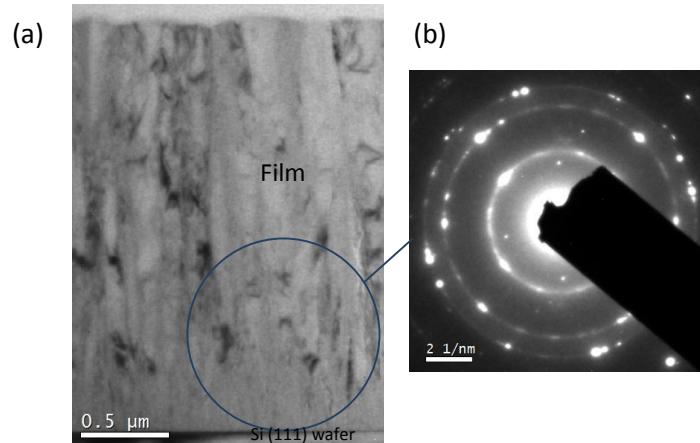


Figure 113. (a) TEM image showing epitaxy breakdown, on Si (111) wafer, occurring by the means of twin formation for another sample deposited in the same growth conditions as our samples deposited in $\text{SiF}_4/\text{H}_2/\text{Ar}$ plasma except for the flow rate of H_2 and the power that corresponded to 1.5 sccm and 15 W respectively. (b) EDP recorded on the circled region of (a) exhibiting spots characteristic of repeated twinning



Figure 114. Onset of epitaxy breakdown occurring with the formation of defects oriented along $\{111\}$ planes and identified as twins (V-shaped defects). This sample was deposited on a Si (100) wafer in CLUSTER reactor [165].

In PICM, Bruneau et al. [65] reported on epitaxy breakdown while studying the effect of ion energy at high and low pressure. They used a specific type of power source which is the tailored voltage waveform (TVW) to vary the ion energy, for low pressure regime, namely for pressure below 1 Torr. In these particular conditions, when increasing the plasma potential from 9 V to 47 V, the structure quality changes from an epitaxial phase to an epitaxial and amorphous phase. Interestingly, the epitaxy breakdown is characterized by large and distorted diffraction spots, without twin formation.

However, for the high pressure regime, namely above 2 Torr, and for the particular conditions where plasma potential ~ 77 V, our results revealed that the onset of epitaxy breakdown is characterized by twinning- primary and secondary- as shown by the EDP recorded on the beginning of the grain formation (see Figure 115).

All this motivates us to state that twinning is not a universal phenomenon for epitaxy breakdown: it appears in some special PECVD growth conditions of Si thin films. Further investigations are needed to better understand the correlation between the growth conditions and that the occurrence of twinning in epitaxy breakdown by PECVD.

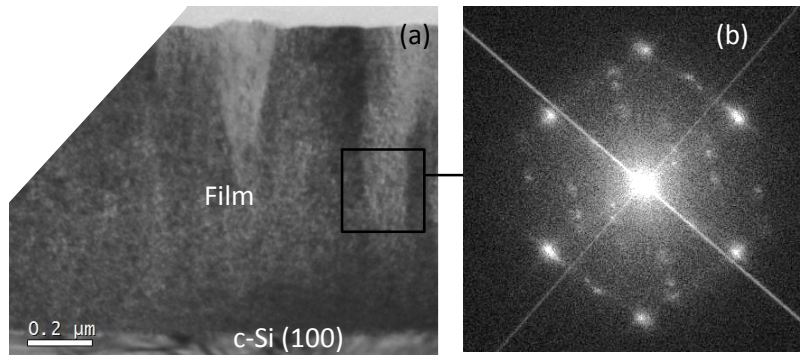


Figure 115. (a) Film deposited on Si (100) wafer, using SiH_4/H_2 plasma chemistry. The epitaxy breakdown occurs by the means of primary and secondary twin formation as shown by (b) the FFT performed on the rectangular area in (a).

5.4.3.2.2. Twinning breakdown

Concerning the twinned part for samples deposited at high RF power (20 and 25 W for 1 sccm of H_2 flow rate), we showed that it composes of two phases: MT phase displaying columnar structures with a dark contrast grown within a bright phase (μc phase). With the evolution of thickness, the twinned orientations of the MT phase are progressively lost through secondary nucleation and finally to the benefit of an amorphous growth (see section 5.2.1.2), whereas the other phase exhibits amorphous and random microcrystalline growth with thickness. It is important at this stage to remind that these films were deposited near the amorphous-to-microcrystalline transition, and this justifies the twinning breakdown into a microcrystalline or amorphous phase.

5.4.4. Effect of the seed orientation on twinning - Si (100) vs Si (111)

We study here the influence of (100) and (111) seed orientations on twinning in Si thin films. To do this, we consider the films deposited on Si (100) and on Si (111) at the same time in the same growth conditions, corresponding to a RF power of 25 W and to a hydrogen flow rate of 1 sccm.

We already mentioned that, due to dynamical considerations, second order twinning tends to align $\{111\}$ planes with the growth axis in the case of using a (100) oriented Si substrate. This of course is no longer valid for a (111) substrate. In this case, twinning with respect to the family of planes parallel to the interface does not change the growth axis. Second order twinning with respect to the three other families does not bring a $\{111\}$ family parallel to the growth axis.

These observations seem to be consistent with the considerations taken by Billig [153] who mentioned that the probability of twinning increases with the alignment of the resulting or twinned $\{111\}$ planes to the growth axis. In addition, we already showed in section 5.2.1.3 that $\{111\}_{\text{np}}$

planes are mostly active for twinning (active mirror planes), in contrast to the $\{111\}_p$. This, consequently, explains the non-symmetrical aspect of twinning on a (111) seed orientation. All this could also fit with the conclusions of Billig, Bulling et al. [154] and Carstens [155], stating that a (100) seed orientation is more likely to generate twins than a (111) orientation. Furthermore, this seems also to fit with the descending hierarchy of seed orientations versus twin effectiveness given by Faust and John [137].

5.5. Summary and perspectives

Takeaway message – Twinning in epitaxial films and fivefold symmetric EDPs

- Epitaxy breakdown occurs by twinning, in the cases studied, a mechanism which is traced back to stacking errors. The path used by the films (presented in this chapter) to lose their epitaxial orientation is through twin (or repeated twin) formation, inducing in some cases the formation of fivefold symmetric electron diffraction patterns. Generally, the twinned orientations are found to be lost, with thickness, to the benefit of an amorphous and microcrystalline phase.
- For the first time to our knowledge, this symmetry is found without the presence of the multiply twinned particles frequently reported in the literature. This symmetry is explained by the presence of at least two orders of twinning occurring in clockwise and anticlockwise directions, and this was proved by reconstructing the twin images in HRTEM pictures with the use of Fourier filters.
- A clear fivefold symmetry is observed in EDPs recorded for HMDSO layers ($\text{SiH}_4/\text{H}_2/\text{HMDSO}/\text{B}_2\text{H}_6/\text{Ar}$ plasma) and for samples deposited by $\text{SiF}_4/\text{H}_2/\text{Ar}$ plasma at high power (20 and 25 W, Figure 91) or at high H_2 flow rate (3 sccm), having an epitaxial connection with an underlying c-Si wafer.
- For samples deposited using $\text{SiF}_4/\text{H}_2/\text{Ar}$ plasma, this symmetry is the result of a second order twinning occurring in either direction. For HMDSO layers, the symmetry is attributed to third order twinning, observed for a range of HMDSO flow rates (from 0.05 up to 0.62 sccm).
- A quantitative analysis is developed to estimate the order of twinning in these films and the contribution of each twin order, as well as to discriminate twin positions from random microcrystalline ones in the EDPs.
- The occurrence of twinning and consequently the breakdown of epitaxy could be attributed to several factors that maintained the stacking errors: preferential growth direction (or dynamical considerations), presence of impurity defects, high growth rate, high flow rate of H_2 or high RF power. However, dynamical considerations where the system tends to align $\{111\}$ planes with the growth direction would explain repeated twinning and the fivefold symmetric EDPs.
- A comparison of twinning using (100) and (111) seed orientations was established. It suggested that a (100) seed is more likely to cause twinning than a (111).
- Nevertheless, twinning was proved not to be a universal phenomenon for epitaxy breakdown of Si during PECVD growth. Further investigations are needed to better understand the propensity of twinning in epitaxial growth.

Chapter 6. Conclusion and perspectives

6.1. Contribution to the research field.....	152
6.2. Perspectives for future work.....	153

In this thesis, we have studied Si epitaxial growth by low-temperature ($\sim 200^\circ\text{C}$) plasma enhanced chemical vapor deposition (LT-PECVD). This technique mainly relies on a plasma to dissociate the gas precursors, in contrast to the standard techniques that use the thermal energy of the substrate to ensure this dissociation. Our starting goal was to give insight into Si epitaxial growth by LT-PECVD for a fundamental knowledge, with the use of transmission electron microscopy (TEM) as the main experimental tool.

6.1. Contribution to the research field

We were interested in determining how epitaxy is triggered. For this, we studied the initial stages of Si epitaxial growth by performing a series of very short depositions (from few tens to few hundreds of seconds), on different types of substrates, using $\text{SiF}_4/\text{H}_2/\text{Ar}$ plasmas. A transient regime was observed in the plasma potential, as well as in the imaginary part of the pseudo-dielectric function $\langle \epsilon_i \rangle$. This occurred just after the plasma ignition and is correlated with particle formation in the plasma. In some cases, HRTEM images revealed islands formed on top of the wafer in the transient regime with a higher growth rate than that of the rest of the film. A maximum surface roughness is observed at a critical deposition time, followed by smoothing effects before reaching the steady-state regime. These results reminded us of thin film growth mediated by the plasma generated particles, which is a relatively new approach based on nanoparticles melting upon impact with the substrate. We presented a discussion on the growth mechanisms of our epitaxial films based on the traditional growth mediated by radicals and on the approach with nanoparticles. However, more work is required to be able to assess the role of particles in such growth.

Once epitaxy by LT-PECVD is established, it is highly desirable to sustain it to high thicknesses. Getting insight into the factors maintaining epitaxy, or exploring the pathway to epitaxy breakdown was rarely discussed in literature. It has been studied in this thesis by making experiments of intentional epitaxy breakdown with $\text{SiF}_4/\text{H}_2/\text{Ar}$ chemistry, by either increasing the RF power or the H_2 flow rate. Initially, the Si films grew as a single-crystal material, but at a critical thickness, the epitaxial layers turned into microcrystalline and amorphous, via a twinning phase. Such breakdown occurred globally where the entire film has lost epitaxial configuration, and sometimes the onset of epitaxy breakdown occurred locally (partially) where columnar structures of defective monocrystalline have been formed in a monocrystalline structure. We discussed the probable reasons for the breakdown of epitaxy in such parametric study. The hydrogen depletion (or the flow rate ratio of H_2 and SiF_4) and the ion bombardment energy (linked to the applied RF power) are the key parameters that affect epitaxial growth. We found that twinning is the general trend of epitaxy breakdown in our films. With those results, it is tempting to speculate that the breakdown of epitaxy by LT-PECVD occurs most likely by

surface roughening that generates {111} facets. Twins and stacking faults would form on these facets thus disrupting epitaxial configuration. Now that the breakdown of epitaxy is linked to a twin formation that probably stems from surface roughening, we can start working on strategies to eliminate such effects in order to extend the epitaxial window.

Twinning was studied in details for samples deposited in epitaxial conditions using the $\text{SiF}_4/\text{H}_2/\text{Ar}$ and the $\text{SiH}_4/\text{H}_2/\text{HMDSO}/\text{B}_2\text{H}_6/\text{Ar}$ (hexamethyldisiloxane for HMDSO) plasma chemistries. We observed fascinating quasi-fivefold symmetric EDP on some of these samples. This original quasi-symmetry is due to multiple twinning, it has often been observed on decahedral particles, but very seldom on bulk materials. By rebuilding the electron diffraction patterns of these films using HRTEM images and their fast Fourier transforms (FFTs), we explained how multiple twinning can generate such a symmetry. We developed a quantitative analysis method to discriminate twin positions from random microcrystalline ones in the EDPs, to estimate the number of twin operations and to evaluate the contribution of each twin order. Interestingly, increasing the flow rate of HMDSO lead to increasing the contribution of the amorphous phase at the expenses of the multiple twinned phase but without the apparition of significant microcrystalline phase. Numerous reasons for the observed twinning were discussed, they could be related to nucleation error, interface and seed orientation (or dynamical considerations), presence of impurities, and excess or shortage of hydrogen atoms. However, the main cause for multiple twinning – and fivefold symmetry – in our films would be the dynamical tendency to form {111} planes parallel to the growth axis.

During this doctoral work, we optimized the traditional mechanical polishing for TEM sample preparation, in such a way to transform it into a fast preparation method. The key parameter for this achievement is polishing the first face of several sandwiches (two to four sandwiches) simultaneously, each sandwich being composed of few films (two to four films). This is followed by polishing the second face of each sandwich individually since this is the most critical step in the thinning procedure. The latter is finalized by ion milling using PIPS (precision ion polishing system) for few minutes. Thanks to this achievement, the cheap tripod polishing method becomes competitive with the relatively expensive focus ion beam (FIB) technique.

6.2. Perspectives for future work

It is clear that a complete understanding of epitaxial growth by LT-PECVD is still missing. Now that we understood some factors limiting the detection (by TEM) of particles that would contribute to epitaxy, we suggest, for future work, some experiments concerning the initial stages of epitaxial growth. For example, it would be interesting to perform very short depositions, from 2 to 5 seconds, on Si and GaAs

wafers and on TEM grids simultaneously. The advantage of these experiments is to avoid the full coverage of the surface of the substrate, making possible the detection of the nanometric particles. Moreover, a slight tune of the growth parameters to make microcrystalline deposition (by changing only the H₂ flow rate) would be interesting to crystallize the particles: the crystallized particles could be clearly distinguished from the amorphous TEM grids.

Future work may also include a better understanding of how does exactly the hydrogen incorporate into the crystalline Si lattice. Thanks to a quantitative image processing of some defects, we could establish a structural model that would explain the formation of such defects. An alternating solution to answer this question would be to grow a thin epitaxial layer of few nanometers and expose it to hydrogen radicals inside the environmental TEM that arrived recently at LPICM (NanoMAX part of "Equipex" TEMPOS) to characterize the effect of hydrogen on the Si lattice.

In the light of the results of intentional epitaxy breakdown experiments, we can suggest new ways to sustain epitaxy for thicker layers produced at a high deposition rate. For example, as a starting point, we can begin by growing epitaxial layers with an excess of H₂ flow rate (like the conditions of 3 sccm, 15 W in chapter 4), the film will grow epitaxially at a high growth rate ($\sim 5 \text{ \AA/s}$); when roughening effects start to be observed with in-situ ellipsometry, we can tune the growth parameters in such a way as to heal the surface roughening. We can work on strategies to achieve the healing, like increasing the SiF₄ flow rate (to compensate the effect of excess hydrogen), for example. This method could allow the film to benefit from an acceptably high growth rate without breaking epitaxy. Another suggestion is the addition of germane in the plasma mixture to compensate the negative effect of the adsorption of hydrogen on the surface. Other multi-step processes can be tested in this context in order to heal the surface roughening. Regarding twin defects, it seems interesting to study the occurrence of their healing that would make possible an *epitaxy comeback*. Such reasoning could open the door to new growth processes allowing to break the records of the maximum epitaxial thickness deposited with LT-PECVD.

References

- [1] J. D. Newton, *Uncommon Friends: Life with Thomas Edison, Henry Ford, Harvey Firestone, Alexis Carrel, and Charles Lindbergh*: Harcourt Brace Jovanovich, 1987.
- [2] REN21, "Renewables 2016 global status report," Paris2016.
- [3] "PHOTOVOLTAICS REPORT," Fraunhofer ISE and PSE AG, Freiburg 6 June 2016.
- [4] M. A. Green, K. Emery, Y. Hishikawa, W. Warta, and E. D. Dunlop, "Solar cell efficiency tables (version 43)," *Progress in Photovoltaics: Research and Applications*, vol. 22, pp. 1-9, 2014.
- [5] P. Kapur, M. Moslehi, A. Deshpande, V. Rana, J. Kramer, S. Seutter, *et al.*, "Manufacturable, Non-plated, Non-Ag Metallization based 20.44% Efficient, 243 cm² Area, Back Contacted Solar Cell on 40 μ m Thick Mono-Crystalline Silicon," in *28th EUPVSEC Proceedings*, 2013.
- [6] T. Höchbauer, A. Misra, M. Nastasi, and J. W. Mayer, "Physical mechanisms behind the ion-cut in hydrogen implanted silicon," *Journal of Applied Physics*, vol. 92, pp. 2335-2342, 2002.
- [7] M. Bruel, B. Aspar, and A.-J. Auberton-Hervé, "Smart-Cut: A New Silicon On Insulator Material Technology Based on Hydrogen Implantation and Wafer Bonding*," *Japanese Journal of Applied Physics*, vol. 36, p. 1636, 1997.
- [8] L. Royer, "Recherches expérimentales sur l'épitaxie ou orientation mutuelle de cristaux d'espèces différentes," *Société française de minéralogie et de cristallographie*, vol. 51, pp. 7-159, 1928.
- [9] E. K. Schmich, "High-temperature CVD processes for crystalline silicon thin-film and wafer solar cells," Dissertation, University of Konstanz, 2008.
- [10] B. S. Meyerson, F. K. LeGoues, T. N. Nguyen, and D. L. Harnage, "Nonequilibrium boron doping effects in low - temperature epitaxial silicon films," *Applied Physics Letters*, vol. 50, pp. 113-115, 1987.
- [11] R. Cariou, M. Labrune, and P. Roca i Cabarrocas, "Thin crystalline silicon solar cells based on epitaxial films grown at 165 °C by RF-PECVD," *Solar Energy Materials and Solar Cells*, vol. 95, pp. 2260-2263, 2011.
- [12] R. Léal, J.-C. Dornstetter, F. Haddad, G. Poulain, J.-L. Maurice, and P. Roca i Cabarrocas, "Silicon epitaxy by low-temperature RF-PECVD using SiF₄/H₂/Ar gas mixtures for emitter formation in crystalline solar cells," in *Photovoltaic Specialist Conference (PVSC), IEEE 42nd*, 2015, pp. 1-5.
- [13] K. Nagamine, A. Yamada, M. Konagai, and K. Takahashi, "Epitaxial Growth of Silicon by Plasma Chemical Vapor Deposition at a Very Low Temperature of 250°C," *Japanese Journal of Applied Physics*, vol. 26, p. L951, 1987.
- [14] N. Shibata, K. Fukuda, H. Ohtoshi, J.-i. Hanna, S. Oda, and I. Shimizu, "Preparation of Polycrystalline Silicon by Hydrogen-Radical-Enhanced Chemical Vapor Deposition," *Japanese Journal of Applied Physics*, vol. 26, p. L10, 1987.
- [15] S. Suzuki and T. Itoh, "Effect of Si - Ge buffer layer for low - temperature Si epitaxial growth on Si substrate by rf plasma chemical vapor deposition," *Journal of Applied Physics*, vol. 54, pp. 1466-1470, 1983.
- [16] T. J. Donahue, W. R. Burger, and R. Reif, "Low - temperature silicon epitaxy using low pressure chemical vapor deposition with and without plasma enhancement," *Applied Physics Letters*, vol. 44, pp. 346-348, 1984.
- [17] C. C. Tsai, G. B. Anderson, R. Thompson, and B. Wacker, "Control of silicon network structure in plasma deposition," *Journal of Non-Crystalline Solids*, vol. 114, pp. 151-153, 1989.
- [18] C. C. Tsai, G. B. Anderson, and R. Thompson, "Low temperature growth of epitaxial and amorphous silicon in a hydrogen-diluted silane plasma," *Journal of Non-Crystalline Solids*, vol. 137-138, Part 2, pp. 673-676, 1991.

- [19] T. Ohmi, K. Hashimoto, M. Morita, and T. Shibata, "Study on further reducing the epitaxial silicon temperature down to 250 °C in low - energy bias sputtering," *Journal of Applied Physics*, vol. 69, pp. 2062-2071, 1991.
- [20] C.-H. Chen and T.-R. Yew, "Silicon epitaxial growth by plasma enhanced chemical vapor deposition from SiH₄/H₂ at 165–350°C," *Journal of Crystal Growth*, vol. 147, pp. 305-312, 1995.
- [21] C. Rosenblad, H. R. Deller, A. Dommann, T. Meyer, P. Schroeter, and H. von Känel, "Silicon epitaxy by low-energy plasma enhanced chemical vapor deposition," *Journal of Vacuum Science & Technology A*, vol. 16, pp. 2785-2790, 1998.
- [22] S. De Wolf and M. Kondo, "Abruptness of a-Si:H/c-Si interface revealed by carrier lifetime measurements," *Applied Physics Letters*, vol. 90, p. 042111, 2007.
- [23] H. G. E. Gohary and S. Sivoththaman, "Influence of different RTP temperature profiles on low temperature epitaxially grown PECVD Si emitters," in *Photovoltaic Specialists Conference (PVSC), 2009 34th IEEE*, 2009, pp. 001331-001334.
- [24] A. Mosleh, S. A. Ghetmiri, B. R. Conley, H. Abu-Safe, Z. Waqar, M. Benamara, *et al.*, "Nucleation-step study of silicon homoepitaxy for low-temperature fabrication of Si solar cells," in *2013 IEEE 39th Photovoltaic Specialists Conference (PVSC)*, 2013, pp. 2646-2650.
- [25] D. Shahrjerdi, B. Hekmatshoar, S. W. Bedell, M. Hopstaken, and D. K. Sadana, "Low-Temperature Epitaxy of Compressively Strained Silicon Directly on Silicon Substrates," *Journal of Electronic Materials*, vol. 41, pp. 494-497, 2012.
- [26] M. Moreno and P. R. i. Cabarrocas, "Ultra-thin crystalline silicon films produced by plasma assisted epitaxial growth on silicon wafers and their transfer to foreign substrates*," *EPJ Photovolt.*, vol. 1, p. 10301, 2010.
- [27] M. Labrune, M. Moreno, and P. Roca i Cabarrocas, "Ultra-shallow junctions formed by quasi-epitaxial growth of boron and phosphorous-doped silicon films at 175 °C by rf-PECVD," *Thin Solid Films*, vol. 518, pp. 2528-2530, 2010.
- [28] R. Cariou, W. Chen, J.-L. Maurice, J. Yu, G. Patriarche, O. Mauguin, *et al.*, "Low temperature plasma enhanced CVD epitaxial growth of silicon on GaAs: a new paradigm for III-V/Si integration," *Scientific Reports*, vol. 6, p. 25674, 2016.
- [29] P. Roca i Cabarrocas, A. Fontcuberta i Morral, and Y. Poissant, "Growth and optoelectronic properties of polymorphous silicon thin films," *Thin Solid Films*, vol. 403–404, pp. 39-46, 2002.
- [30] T. Nguyen-Tran, P. Roca i Cabarrocas, and G. Patriarche, "Study of radial growth rate and size control of silicon nanocrystals in square-wave-modulated silane plasmas," *Applied Physics Letters*, vol. 91, p. 111501, 2007.
- [31] J.-C. Dornstetter, "Microcrystalline silicon deposited from SiF₄/H₂/Ar plasmas and its application to photovoltaics," PhD thesis, Ecole Polytechnique, 2014.
- [32] J.-C. Dornstetter, J. Wang, B. Bruneau, E. V. Johnson, and P. Roca i Cabarrocas, "Material and growth mechanism studies of microcrystalline silicon deposited from SiF₄/H₂/Ar gas mixtures," *Canadian Journal of Physics*, vol. 92, pp. 740-743, 2014.
- [33] Y. Djeridane, A. Abramov, and P. Roca i Cabarrocas, "Silane versus silicon tetrafluoride in the growth of microcrystalline silicon films by standard radio frequency glow discharge," *Thin Solid Films*, vol. 515, pp. 7451-7454, 2007.
- [34] A. Abramov and P. R. i. Cabarrocas, "Addition of SiF₄ to standard SiH₄+H₂ plasma: an effective way to reduce oxygen contamination in μc-Si:H films," *physica status solidi (c)*, vol. 7, pp. 529-532, 2010.
- [35] S. Kasouit, S. Kumar, R. Vanderhaghen, P. Roca i Cabarrocas, and I. French, "Fluorine and hydrogen effects on the growth and transport properties of microcrystalline silicon from SiF₄ precursor," *Journal of Non-Crystalline Solids*, vol. 299–302, Part 1, pp. 113-117, 2002.
- [36] R. Brenot, "Corrélation entre mode de croissance et propriétés de transport du silicium microcristallin, établie par rélectométrie micro-onde et ellipsométrie," PhD thesis, Ecole Polytechnique, France, 2000.

- [37] S. Kasouit, "Mécanismes de croissance et transport dans le silicium microcristallin fluoré. Application aux transistors en couches minces et transfert technologique," PhD thesis, Ecole Polytechnique, France, 2003.
- [38] A. Torres Rios, Y. Djeridane, P. L. Reydet, J. P. Reyal, and P. Roca i Cabarrocas, "Epitaxial Growth of Crystalline Silicon on N42 Alloys by PECVD at 175 °C for Low Cost and High Efficiency Solar Cells," in *26th EUPVSEC 2011*, pp. 2435 - 2438.
- [39] J.-C. Dornstetter, B. Bruneau, P. Bulkin, E. V. Johnson, and P. Roca i Cabarrocas, "Understanding the amorphous-to-microcrystalline silicon transition in SiF₄/H₂/Ar gas mixtures," *The Journal of Chemical Physics*, vol. 140, p. 234706, 2014.
- [40] P. Sichanugrist, T. Sasaki, A. Asano, Y. Ichikawa, and H. Sakai, "Amorphous silicon oxide and its application to metal/n-i-p/ITO type a-Si solar cells," *Solar Energy Materials and Solar Cells*, vol. 34, pp. 415-422, 1994.
- [41] F. Demichelis, C. F. Pirri, and E. Tresso, "Microcrystallization formation in silicon carbide thin films," *Philosophical Magazine Part B*, vol. 66, pp. 135-146, 1992.
- [42] P. Goyal and V. Fthenakis, "Comparison of Risks Related to Liquid and Gaseous Precursors for Doping Silicon Thin Films in the Photovoltaic Industry," presented at the 29th European Photovoltaic Solar Energy Conference and Exhibition, Amsterdam, 2014.
- [43] V. M. Fthenakis and P. D. Moskowitz, "Characterization and control of phosphine hazards in photovoltaic cell manufacture," *Solar Cells*, vol. 22, pp. 303-317, 1987.
- [44] D. S. Kim, Y. H. Lee, and N. H. Park, "Deposition of thermally stable, low dielectric constant fluorocarbon/SiO₂ composite thin film," *Applied Physics Letters*, vol. 69, pp. 2776-2778, 1996.
- [45] D. Trunec, L. Zajíčková, V. Buršíková, F. Studnička, P. Sťahel, V. Prysiazny, *et al.*, "Deposition of hard thin films from HMDSO in atmospheric pressure dielectric barrier discharge," *Journal of Physics D: Applied Physics*, vol. 43, p. 225403, 2010.
- [46] P. Goyal, J. Hong, F. Haddad, J.-L. Maurice, P. Roca i Cabarrocas, and E. Johnson, "Use of hexamethyldisiloxane for p-type microcrystalline silicon oxycarbide layers," *EPJ Photovolt.*, vol. 7, pp. 1-8, 2016 2016.
- [47] R. Esparza, G. Rosas, E. Valenzuela, S. A. Gamboa, U. Pal, and R. Pérez, "Structural analysis and shape-dependent catalytic activity of Au, Pt and Au/Pt nanoparticles," *Revista Matéria*, vol. 13, pp. 579-586, 2008.
- [48] M. A. Lieberman and A. J. Lichtenberg, in *Principles of Plasma Discharges and Materials Processing*, ed: John Wiley & Sons, Inc., 2005, pp. i-xxxv.
- [49] P. Roca i Cabarrocas, J. B. Chévrier, J. Huc, A. Lloret, J. Y. Parey, and J. P. M. Schmitt, "A fully automated hot - wall multiplasma - monochamber reactor for thin film deposition," *Journal of Vacuum Science & Technology A*, vol. 9, pp. 2331-2341, 1991.
- [50] P. Roca i Cabarrocas, "Science des matériaux et techniques du reacteur dans le depot par procede plasma rf de photopiles et d'autres dispositifs en silicium amorphe hydrogene," PhD thesis, Paris 7, 1988.
- [51] R. Cariou, "Epitaxial growth of Si(Ge) materials on Si and GaAs by low temperature PECVD: towards tandem devices," PhD thesis, Ecole Polytechnique, 2014.
- [52] P. Goyal, "Use of liquid precursors for plasma deposition of p-type doped layers for silicon photovoltaics," PhD thesis, Ecole Polytechnique, 2015.
- [53] D. B. Williams and C. B. Carter, *Transmission Electron Microscopy: A Textbook for Materials Science*: Springer, 2009.
- [54] L. Reimer and H. Kohl, *Transmission Electron Microscopy*, 5 ed. vol. 3, 2008.
- [55] J. P. Eberhart, *Analyse structurale et chimique des matériaux*: Dunod, 1997.
- [56] J. P. Benedict, R. Anderson, S. J. Klepeis, and M. Chaker, "A Procedure for Cross Sectioning Specific Semiconductor Devices for Both SEM and TEM Analysis," *MRS Online Proceedings Library Archive*, vol. 199, p. 189 1990.
- [57] H. G. Tompkins and E. A. Irene, *Handbook of Ellipsometry*: Springer Berlin Heidelberg, 2005.
- [58] R. M. A. Azzam and N. M. Bashara, *Ellipsometry and Polarized Light*: North-Holland, 1999.

- [59] K. Vedam, "Spectroscopic ellipsometry: a historical overview," *Thin Solid Films*, vol. 313–314, pp. 1-9, 1998.
- [60] D. A. G. Bruggeman, "Berechnung verschiedener physikalischer Konstanten von heterogenen Substanzen. I. Dielektrizitätskonstanten und Leitfähigkeiten der Mischkörper aus isotropen Substanzen," *Annalen der Physik*, vol. 416, pp. 636-664, 1935.
- [61] P. Roca i Cabarrocas, R. Cariou, and M. Labrune, "Low temperature plasma deposition of silicon thin films: From amorphous to crystalline," *Journal of Non-Crystalline Solids*, vol. 358, pp. 2000-2003, 2012.
- [62] A. Matsuda, "Thin-Film Silicon –Growth Process and Solar Cell Application–," *Japanese Journal of Applied Physics*, vol. 43, p. 7909, 2004.
- [63] C. C. Tsai, G. B. Anderson, R. Thompson, and B. Wacker, "Proceedings of the Thirteenth International Conference on Amorphous and Liquid Semiconductors Control of silicon network structure in plasma deposition," *Journal of Non-Crystalline Solids*, vol. 114, pp. 151-153, 1989/12/01 1989.
- [64] S. Sriraman, S. Agarwal, E. S. Aydil, and D. Maroudas, "Mechanism of hydrogen-induced crystallization of amorphous silicon," *Nature*, vol. 418, pp. 62-65, 2002.
- [65] B. Bruneau, R. Cariou, J.-C. Dornstetter, M. Lepecq, J.-L. Maurice, P. Roca i Cabarrocas, *et al.*, "Ion Energy Threshold in Low-Temperature Silicon Epitaxy for Thin-Film Crystalline Photovoltaics," *IEEE Journal of Photovoltaics*, vol. 4, pp. 1361-1367, 2014.
- [66] L. W. Chen, Y. Shibuta, M. Kambara, and T. Yoshida, "Molecular dynamics simulation of Si nanoclusters in high rate and low temperature epitaxy," *Journal of Applied Physics*, vol. 111, p. 123301, 2012.
- [67] H.-L. T. Le, "Molecular dynamics simulations of H-induced plasma processes and cluster-catalyzed epitaxial growth of thin silicon films," PhD thesis, Ecole Polytechnique, 2014.
- [68] P. Roca i Cabarrocas, K. H. Kim, R. Cariou, M. Labrune, E. V. Johnson, M. Moreno, *et al.*, "Low Temperature Plasma Synthesis of Nanocrystals and their Application to the Growth of Crystalline Silicon and Germanium Thin Films," *MRS Online Proceedings Library Archive*, vol. 1426, pp. 319-329, 2012.
- [69] G. Moras, L. C. Ciacchi, C. Elsässer, P. Gumbsch, and A. De Vita, "Atomically Smooth Stress-Corrosion Cleavage of a Hydrogen-Implanted Crystal," *Physical Review Letters*, vol. 105, p. 075502, 2010.
- [70] T. A. Witten and L. M. Sander, "Diffusion-Limited Aggregation, a Kinetic Critical Phenomenon," *Physical Review Letters*, vol. 47, pp. 1400-1403, 1981.
- [71] S. Oda, S. i. Ishihara, N. Shibata, H. Shirai, A. Miyauchi, K. Fukuda, *et al.*, "The Role of Hydrogen Radicals in the Growth of a-Si and Related Alloys," *Japanese Journal of Applied Physics*, vol. 25, p. L188, 1986.
- [72] G. Cicala, P. Capezzuto, and G. Bruno, "Microcrystalline silicon by plasma enhanced chemical vapor deposition from silicon tetrafluoride," *Journal of Vacuum Science & Technology A*, vol. 19, pp. 515-523, 2001.
- [73] M. Nerding, L. Oberbeck, T. A. Wagner, R. B. Bergmann, and H. P. Strunk, "Single to polycrystalline transition in silicon growth by ion-assisted deposition at low temperatures," *Journal of Applied Physics*, vol. 93, pp. 2570-2574, 2003.
- [74] K. Nakamura, K. Yoshino, S. Takeoka, and I. Shimizu, "Roles of Atomic Hydrogen in Chemical Annealing," *Japanese Journal of Applied Physics*, vol. 34, p. 442, 1995.
- [75] J. W. Rabalais, A. H. Al-Bayati, K. J. Boyd, D. Marton, J. Kulik, Z. Zhang, *et al.*, "Ion-energy effects in silicon ion-beam epitaxy," *Physical Review B*, vol. 53, pp. 10781-10792, 1996.
- [76] C. Schelling, "Growth and characterization of self-organized and "organized" Si and Si_{1-x}Ge_x nanostructures," PhD thesis, Johannes-kepler-University, 2000.
- [77] R. L. Schwoebel and E. J. Shipsey, "Step Motion on Crystal Surfaces," *Journal of Applied Physics*, vol. 37, pp. 3682-3686, 1966.
- [78] S. Heun, J. Falta, and M. Henzler, "The initial stages of epitaxial growth of silicon on Si(100)–2 × 1," *Surface Science*, vol. 243, pp. 132-140, 1991.

- [79] P. E. Acosta-Alba, O. Kononchuk, C. Gourdel, and A. Claverie, "Surface self-diffusion of silicon during high temperature annealing," *Journal of Applied Physics*, vol. 115, p. 134903, 2014.
- [80] R. Léal, J.-C. Dornstetter, F. Haddad, B. Bruneau, R. Cariou, W. Chen, *et al.*, "Epitaxial Growth of Silicon Thin Films by Low Temperature RF-PECVD from SiF₄/H₂/Ar," presented at the EU PVSEC Proceedings, 2014.
- [81] D. B. Graves and D. Humbird, "Surface chemistry associated with plasma etching processes," *Applied Surface Science*, vol. 192, pp. 72-87, 2002.
- [82] C. G. V. d. Walle and J. Neugebauer, "HYDROGEN IN SEMICONDUCTORS," *Annual Review of Materials Research*, vol. 36, pp. 179-198, 2006.
- [83] C. G. Van de Walle and J. Neugebauer, "Hydrogen interactions with self-interstitials in silicon," *Physical Review B*, vol. 52, pp. R14320-R14323, 1995.
- [84] U. I. Schmidt, B. Schröder, and H. Oechsner, "Influence of powder formation in a silane discharge on a-Si:H film growth monitored by in situ ellipsometry," *Journal of Non-Crystalline Solids*, vol. 164, pp. 127-130, 1993.
- [85] M. Meaudre, R. Meaudre, R. Butté, S. Vignoli, C. Longeaud, J. P. Kleider, *et al.*, "Midgap density of states in hydrogenated polymorphous silicon," *Journal of Applied Physics*, vol. 86, pp. 946-950, 1999.
- [86] M. Brinza, G. J. Adriaenssens, and P. Roca i Cabarrocas, "Time-of-flight measurements of carrier drift mobilities in polymorphous silicon," *Thin Solid Films*, vol. 427, pp. 123-126, 2003.
- [87] P. Roca i Cabarrocas, T. Nguyen-Tran, Y. Djeridane, A. Abramov, E. Johnson, and G. Patriarche, "Synthesis of silicon nanocrystals in silane plasmas for nanoelectronics and large area electronic devices," *Journal of Physics D: Applied Physics*, vol. 40, p. 2258, 2007.
- [88] T. Matsoukas and M. Russell, "Particle charging in low - pressure plasmas," *Journal of Applied Physics*, vol. 77, pp. 4285-4292, 1995.
- [89] C. Cui and J. Goree, "Fluctuations of the charge on a dust grain in a plasma," *IEEE Transactions on Plasma Science*, vol. 22, pp. 151-158, 1994.
- [90] P. Roca i Cabarrocas, P. Gay, and A. Hadjadj, "Experimental evidence for nanoparticle deposition in continuous argon-silane plasmas: Effects of silicon nanoparticles on film properties," *Journal of Vacuum Science & Technology A*, vol. 14, pp. 655-659, 1996.
- [91] C. Hollenstein, "The physics and chemistry of dusty plasmas," *Plasma Physics and Controlled Fusion*, vol. 42, p. R93, 2000.
- [92] U. I. Schmidt and D. B. Graves, "In situ characterization of the transient behavior of particles in low pressure plasmas," *Journal of Vacuum Science & Technology A*, vol. 14, pp. 595-602, 1996.
- [93] P. Roca i Cabarrocas, "Towards high deposition rates of a-Si:H: The limiting factors," *Journal of Non-Crystalline Solids*, vol. 164-166, Part 1, pp. 37-42, 1993.
- [94] A. A. Fridman, L. Boufendi, T. Hbid, B. V. Potapkin, and A. Bouchoule, "Dusty plasma formation: Physics and critical phenomena. Theoretical approach," *Journal of Applied Physics*, vol. 79, pp. 1303-1314, 1996.
- [95] N. Ning and H. Vach, "Deposition Dynamics of Hydrogenated Silicon Clusters on a Crystalline Silicon Substrate under Typical Plasma Conditions," *The Journal of Physical Chemistry A*, vol. 114, pp. 3297-3305, 2010.
- [96] E. V. Johnson, G. Patriarche, and P. Roca i Cabarrocas, "Directional growth of Ge on GaAs at 175°C using plasma-generated nanocrystals," *Applied Physics Letters*, vol. 92, p. 103108, 2008.
- [97] M. Labrune, "Silicon surface passivation and epitaxial growth on c-Si by low temperature plasma processes for high efficiency solar cells," PhD thesis, Ecole Polytechnique, 2011.
- [98] L. Csepregi, E. F. Kennedy, J. W. Mayer, and T. W. Sigmon, "Substrate - orientation dependence of the epitaxial regrowth rate from Si - implanted amorphous Si," *Journal of Applied Physics*, vol. 49, pp. 3906-3911, 1978.
- [99] B. E. Weir, B. S. Freer, R. L. Headrick, D. J. Eaglesham, G. H. Gilmer, J. Bevk, *et al.*, "Low - temperature homoepitaxy on Si(111)," *Applied Physics Letters*, vol. 59, pp. 204-206, 1991.

- [100] U. K. Das, M. Z. Burrows, M. Lu, S. Bowden, and R. W. Birkmire, "Surface passivation and heterojunction cells on Si (100) and (111) wafers using dc and rf plasma deposited Si:H thin films," *Applied Physics Letters*, vol. 92, p. 063504, 2008.
- [101] N. Gogneau, D. Jalabert, E. Monroy, T. Shibata, M. Tanaka, and B. Daudin, "Structure of GaN quantum dots grown under "modified Stranski-Krastanow" conditions on AlN," *Journal of Applied Physics*, vol. 94, pp. 2254-2261, 2003.
- [102] D. J. Eaglesham, "Semiconductor Molecular-Beam Epitaxy at Low-Temperatures," *Journal of Applied Physics*, vol. 77, pp. 3597-3617, 1995.
- [103] K. A. Bratland, Y. L. Foo, J. A. N. T. Soares, T. Spila, P. Desjardins, and J. E. Greene, "Mechanism for epitaxial breakdown during low-temperature Ge(001) molecular beam epitaxy," *Physical Review B*, vol. 67, p. 125322, 2003.
- [104] D. P. Adams, S. M. Yalisove, and D. J. Eaglesham, "Effect of Hydrogen on Surface Roughening during Si Homoepitaxial Growth," *Applied Physics Letters*, vol. 63, pp. 3571-3573, 1993.
- [105] O. P. Karpenko, S. M. Yalisove, and D. J. Eaglesham, "Surface roughening during low temperature Si(100) epitaxy," *Journal of Applied Physics*, vol. 82, pp. 1157-1165, 1997.
- [106] M. V. Ramana Murty and H. A. Atwater, "Crystal-state - amorphous-state transition in low-temperature silicon homoepitaxy," *Physical Review B*, vol. 49, pp. 8483-8486, 1994.
- [107] M. Copel and R. M. Tromp, "H coverage dependence of Si(001) homoepitaxy," *Physical Review Letters*, vol. 72, pp. 1236-1239, 1994.
- [108] C. W. Teplin, E. Iwaniczko, B. To, H. Moutinho, P. Stradins, and H. M. Branz, "Breakdown physics of low-temperature silicon epitaxy grown from silane radicals," *Physical Review B*, vol. 74, p. 235428, 2006.
- [109] C. Ghica, L. C. Nistor, M. Stefan, D. Ghica, B. Mironov, S. Vizireanu, *et al.*, "Specificity of defects induced in silicon by RF-plasma hydrogenation," *Applied Physics A*, vol. 98, pp. 777-785, 2009.
- [110] H. Jorke, H. J. Herzog, and H. Kibbel, "Kinetics of Ordered Growth of Si on Si(100) at Low-Temperatures," *Physical Review B*, vol. 40, pp. 2005-2008, 1989.
- [111] J. Thiesen, H. M. Branz, and R. S. Crandall, "Explanation of the limiting thickness observed in low-temperature silicon epitaxy," *Applied Physics Letters*, vol. 77, pp. 3589-3591, 2000.
- [112] D. D. Koleske, S. M. Gates, and J. A. Schultz, "Facile abstraction of chemisorbed D on Si(100) by atomic H," *The Journal of Chemical Physics*, vol. 99, pp. 5619-5622, 1993.
- [113] H.-L. T. Le, N. C. Forero-Martinez, and H. Vach, "Hydrogen-induced healing of cluster-damaged silicon surfaces," *Chemical Physics Letters*, vol. 610-611, pp. 223-227, 2014.
- [114] G. Brocks, P. J. Kelly, and R. Car, "Binding and diffusion of a Si adatom on the Si(100) surface," *Physical Review Letters*, vol. 66, pp. 1729-1732, 1991.
- [115] A. V. Latyshev, A. B. Krasilnikov, and A. L. Aseev, "Self-diffusion on Si(111) surfaces," *Physical Review B*, vol. 54, pp. 2586-2589, 1996.
- [116] C. Ghica, L. C. Nistor, H. Bender, O. Richard, G. V. Tendeloo, and A. Ulyashin, "TEM characterization of extended defects induced in Si wafers by H-plasma treatment," *Journal of Physics D: Applied Physics*, vol. 40, p. 395, 2007.
- [117] J. Abrefah and D. R. Olander, "Reaction of atomic hydrogen with crystalline silicon," *Surface Science*, vol. 209, pp. 291-313, 1989.
- [118] T. Höchbauer, "On the mechanisms of hydrogen implantation induced silicon surface layer cleavage," Dissertation, Philipps-Universität Marburg, 2001.
- [119] C. Ghica, L. C. Nistor, H. Bender, O. Richard, G. Van Tendeloo, and A. Ulyashyn, "Characterization of {111} planar defects induced in silicon by hydrogen plasma treatments," *Philosophical Magazine*, vol. 86, pp. 5137-5151, 2006.
- [120] S. Muto, S. Takeda, and M. Hirata, "Hydrogen-induced platelets in silicon studied by transmission electron microscopy," *Philosophical Magazine A*, vol. 72, pp. 1057-1074, 1995.
- [121] C. M. Varma, "Hydrogen-implant induced exfoliation of silicon and other crystals," *Applied Physics Letters*, vol. 71, pp. 3519-3521, 1997.
- [122] H. N. Wanka and M. B. Schubert, "High silicon etch rates by hot filament generated atomic hydrogen," *Journal of Physics D: Applied Physics*, vol. 30, p. L28, 1997.

- [123] I. Solomon, B. Drévilion, H. Shirai, and N. Layadi, "Plasma deposition of microcrystalline silicon: the selective etching model," *Journal of Non-Crystalline Solids*, vol. 164, pp. 989-992, 1993.
- [124] J. E. Vasek, Z. Zhang, C. T. Salling, and M. G. Lagally, "Effects of hydrogen impurities on the diffusion, nucleation, and growth of Si on Si(001)," *Physical Review B*, vol. 51, pp. 17207-17210, 1995.
- [125] R. L. Segall, "Unusual Twinning in Annealed Copper," *Transactions of the American Institute of Mining and Metallurgical Engineers*, vol. 209, pp. 50-50, 1957.
- [126] D. Shechtman, I. Blech, D. Gratias, and J. W. Cahn, "Metallic Phase with Long-Range Orientational Order and No Translational Symmetry," *Physical Review Letters*, vol. 53, pp. 1951-1953, 1984.
- [127] L. Pauling, "Apparent Icosahedral Symmetry Is Due to Directed Multiple Twinning of Cubic-Crystals," *Nature*, vol. 317, pp. 512-514, 1985.
- [128] L. Pauling, "Unified Structure-Theory of Icosahedral Quasicrystals - Evidence from Neutron Powder Diffraction Patterns That Alcrfemnsi, Alculimg, and Tinifesi Icosahedral Quasicrystals Are Twins of Cubic-Crystals Containing About 820 or 1012 Atoms in a Primitive Unit Cube," *Proceedings of the National Academy of Sciences of the United States of America*, vol. 85, pp. 8376-8380, 1988.
- [129] R. C. Williams and K. M. Smith, "The Polyhedral Form of the Tipula Iridescent Virus," *Biochimica Et Biophysica Acta*, vol. 28, pp. 464-469, 1958.
- [130] J. Walz, T. Tamura, N. Tamura, R. Grimm, W. Baumeister, and A. J. Koster, "Tricorn protease exists as an icosahedral supermolecule in vivo," *Molecular Cell*, vol. 1, pp. 59-65, 1997.
- [131] C. Palache, "Multiple twins of diamond and sphalerite," *Amer. Mineral.*, vol. 17, pp. 360-361, 1932.
- [132] J. Kourimsky and F. Tvrz, in *Bunte Welt der Minerale*, Prague, 1977, p. 59.
- [133] A. J. Melmed and D. O. Hayward, "On the Occurrence of Fivefold Rotational Symmetry in Metal Whiskers," *The Journal of Chemical Physics*, vol. 31, pp. 545-546, 1959.
- [134] G. Bögels, J. G. Buijnsters, S. A. C. Verhaegen, H. Meekes, P. Bennema, and D. Bollen, "Morphology and growth mechanism of multiply twinned AgBr and AgCl needle crystals," *Journal of Crystal Growth*, vol. 203, pp. 554-563, 1999.
- [135] Z. L. Wang, "Structural Analysis of Self-Assembling Nanocrystal Superlattices," *Advanced Materials*, vol. 10, pp. 13-30, 1998.
- [136] J. Bühler and Y. Prior, "Study of morphological behavior of single diamond crystals," *Journal of Crystal Growth*, vol. 209, pp. 779-788, 2000.
- [137] J. W. Faust and H. F. John, "The growth of semiconductor crystals from solution using the twin-plane reentrant-edge mechanism," *Journal of Physics and Chemistry of Solids*, vol. 25, pp. 1407-1415, 1964.
- [138] H. Hofmeister, "Fivefold twinned nanoparticles," in *Encyclopedia of Nanoscience and Nanotechnology* vol. 3, H. S. Nalwa, Ed., ed: American Scientific Publishers, 2004, pp. 431-452.
- [139] S. Iijima, "Fine Particles of Silicon. II. Decahedral Multiply-Twinned Particles," *Japanese Journal of Applied Physics*, vol. 26, pp. 365-372, 1987.
- [140] J. L. Maurice, J. Dixmier, T. Kretz, P. Legagneux, F. Plais, and D. Pribat, "Microstructure and Transistor Properties of Solid-State-Crystallised Polysilicon: Effect of a Prolonged 600°C Anneal," *Solid State Phenomena*, vol. 37-38, pp. 335-342, 1994.
- [141] S. Iijima, "Fine Particles of Silicon. I. Crystal Growth of Spherical Particles of Si," *Japanese Journal of Applied Physics*, vol. 26, pp. 357-364, 1987.
- [142] C. Gammer, C. Mangler, C. Rentenberger, and H. P. Karnthaler, "Quantitative local profile analysis of nanomaterials by electron diffraction," *Scripta Materialia*, vol. 63, pp. 312-315, 2010.
- [143] G. R. Booker, "Tripyramids and Associated Defects in Epitaxial Silicon Layers," *Philosophical Magazine*, vol. 11, pp. 1007-1020, 1965.
- [144] H. Holloway and L. C. Bobb, "Oriented Growth of Semiconductors .V. Surface Features and Twins in Epitaxial Gallium Arsenide," *Journal of Applied Physics*, vol. 38, pp. 2893-2896, 1967.
- [145] L. D. Marks and D. J. Smith, "High resolution studies of small particles of gold and silver: I. Multiply-twinned particles," *Journal of Crystal Growth*, vol. 54, pp. 425-432, 1981.

- [146] C. Y. Yang, "Crystallography of decahedral and icosahedral particles: I. Geometry of twinning," *Journal of Crystal Growth*, vol. 47, pp. 274-282, 1979.
- [147] M. J. Buerger, "The genesis of twin crystals," *American Mineralogist*, vol. 30, pp. 469-482, 1945.
- [148] J. V. Smith, "Twins and Related Structures," in *Feldspar Minerals: 2 Chemical and Textural Properties*, ed Berlin, Heidelberg: Springer Berlin Heidelberg, 1974, pp. 303-398.
- [149] J. V. Ross, "Combination twinning in plagioclase feldspars," *American Journal of Science*, vol. 255, pp. 650-655, 1957.
- [150] P. Hartman, "On the Morphology of Growth Twins," in *Zeitschrift für Kristallographie - Crystalline Materials* vol. 107, ed, 1956, pp. 225-237.
- [151] K. E. Seifert, "The genesis of plagioclase twinning in the Nonewaig granite," *American Mineralogist*, vol. 49, pp. 297-320, 1964.
- [152] M. Nespolo and G. Ferraris, "The oriented attachment mechanism in the formation of twins - a survey," *European Journal of Mineralogy*, vol. 16, pp. 401-406, 2004.
- [153] E. Billig, "Growth twins in crystals of low co-ordination number," *Journal of the Institute of Metals*, vol. 83, pp. 53-56, 1954.
- [154] G. F. Bulling, J. W. Rutter, and W. A. Tiller, "Growth twins in germanium," *Canadian Journal of Physics*, vol. 34, pp. 234-240, 1956.
- [155] H. Carstens, "Kinetic considerations in the genesis of growth twinning: a discussion," *American Mineralogist*, vol. 53, pp. 342-344, 1968.
- [156] F. A. Pizzarello, "Chemical transport and epitaxial deposition of gallium arsenide " *Journal of the Electrochemical Society*, vol. 110, pp. 1059-1065, 1963.
- [157] E. Billig, "Some speculations on the growth mechanism of dendrites " *Acta Metallurgica*, vol. 5, pp. 54-55, 1957.
- [158] J. A. Baker, T. N. Tucker, N. E. Moyer, and R. C. Buschert, "Effect of Carbon on the Lattice Parameter of Silicon," *Journal of Applied Physics*, vol. 39, pp. 4365-4368, 1968.
- [159] R. C. Newman and J. B. Willis, "Vibrational absorption of carbon in silicon," *Journal of Physics and Chemistry of Solids*, vol. 26, pp. 373-379, 1965.
- [160] R. C. Newman, "Defects in silicon," *Reports on Progress in Physics*, vol. 45, pp. 1163-1210, 1982.
- [161] W. L. Bond and W. Kaiser, "Interstitial versus substitutional oxygen in silicon," *Journal of Physics and Chemistry of Solids*, vol. 16, pp. 44-45, 1960.
- [162] P. Cuony, D. T. L. Alexander, I. Perez-Wurfl, M. Despeisse, G. Bugnon, M. Boccard, *et al.*, "Silicon Filaments in Silicon Oxide for Next-Generation Photovoltaics," *Advanced Materials*, vol. 24, pp. 1182-1186, 2012.
- [163] R. W. Collins, A. S. Ferlauto, G. M. Ferreira, C. Chen, J. Koh, R. J. Koval, *et al.*, "Evolution of microstructure and phase in amorphous, protocrystalline, and microcrystalline silicon studied by real time spectroscopic ellipsometry," *Solar Energy Materials and Solar Cells*, vol. 78, pp. 143-180, 2003.
- [164] R. Krankenhagen, M. Schmidt, S. Grebner, M. Poschenrieder, W. Henrion, I. Sieber, *et al.*, "Correlation between structural, optical and electrical properties of $\mu\text{-Si}$ films," *Journal of Non-Crystalline Solids*, vol. 198-200, Part 2, pp. 923-926, 1996.
- [165] J.-C. Dornstetter, L. I. Florea, and P. Roca i Cabarrocas, "Epitaxie sur silicium en $\text{SiF}_4/\text{H}_2/\text{Ar}$," Unpublished, 2014.

List of publications

Peer reviewed journals

- **F. Haddad**, P. Goyal, E. Johnson, J. Hong, P. Roca i Cabarrocas, J.-L. Maurice, “Quasi-fivefold symmetric electron diffraction patterns due to multiple twinning in silicon thin films grown from hexamethyldisiloxane”, *Journal of Applied Crystallography*, 49 (2016) part 6, 2226-2234
- R. Léal, **F. Haddad**, G. Poulain, J.-L. Maurice, P. Roca i Cabarrocas, « High quality boron-doped epitaxial layers grown at 200°C from SiF₄/H₂/Ar gas mixtures for emitter formation in crystalline silicon solar cells», *submitted to Journal of Applied Physics*.
- W. Chen, V. Depauw, **F. Haddad**, J.-L. Maurice, P. Roca i Cabarrocas, “Influence of anodic bonding on the surface passivation quality of crystalline silicon”, *Solar Energy Materials and Solar Cells*, 157 (2016) 154-160.
- P. Goyal, J. Hong, **F. Haddad**, J.-L. Maurice, P. Roca i Cabarrocas, E. Johnson, “Use of hexamethyldisiloxane for p-type microcrystalline silicon oxycarbide layers”, *EPJ Photovolt.*, 7 (2016) 70301.

Conference proceedings

- R. Léal, J.-C. Dornstetter, **F. Haddad**, G. Poulain, J.-L. Maurice, P. Roca i Cabarrocas, “Silicon epitaxy by low-temperature RF-PECVD using SiF₄/H₂/Ar gas mixtures for emitter formation in crystalline solar cells”, in: Photovoltaic Specialist Conference (PVSC), 2015 IEEE 42nd, 2015, pp. 1-5.
- R. Léal, J.C. Dornstetter, **F. Haddad**, B. Bruneau, R. Cariou, W. Chen, I. Cosme, G. Poulain, J.L. Maurice, P. Roca i Cabarrocas, “Epitaxial Growth of Silicon Thin Films by Low Temperature RF-PECVD from SiF₄/H₂/Ar”, in: EU PVSEC Proceedings, 2014, pp. 1-4.

Oral and poster presentations

- **F. Haddad**, P. Goyal, R. Léal, J. Hong, E. Johnson, P. Roca i Cabarrocas, J.-L. Maurice, “Fivefold symmetric diffraction patterns in silicon thin films induced by multiple twinning”, *Poster*, EMC, Lyon 2016.
- **F. Haddad**, P. Goyal, E. Johnson, J. Hong, P. Roca i Cabarrocas, J.-L. Maurice, “Fivefold symmetries in the multiple twinning found in p-type microcrystalline silicon alloys grown from hexamethyldisiloxane”, *Oral Presentation*, ICANS, Aachen 2015.

- **F. Haddad**, R. Léal, J.-C. Dornstetter, P. Narchi, J.-L. Maurice, P. Roca i Cabarrocas, “Low temperature epitaxial growth of silicon thin films from SiF₄/H₂/Ar plasma chemistry”, *Poster*, EMRS, Lille 2015.
- **F. Haddad**, R. Léal, J.-C. Dornstetter, J.-L. Maurice and P. Roca i Cabarrocas, “Thin-film silicon solar cells: structure as a function of elaboration conditions”, *Poster*, JNPV, Dourdan 2014.

Title: Transmission electron microscopy study of low-temperature silicon epitaxy by plasma enhanced chemical vapor deposition

Abstract : This thesis focuses on low temperature (LT, $\sim 200^\circ\text{C}$) epitaxial growth of silicon thin films by plasma enhanced chemical vapor deposition (PECVD) for solar cell applications. Our starting goal was to acquire a better understanding of epitaxial growth, by using transmission electron microscopy (TEM) as the main experimental tool. First, we investigated the initial stages of epitaxial growth using $\text{SiF}_4/\text{H}_2/\text{Ar}$ chemistry by performing a series of short depositions – from few tens to few hundred of seconds – on different types of substrates. We made a correlation between TEM images and in-situ ellipsometry measurements. We discussed the growth mechanisms under the hypotheses of the traditional growth mediated by atoms, radicals and ions and the relatively new approach based on the melting of plasma generated nanoparticles upon impact with the substrate. Additionally, in order to understand how epitaxy by LT-PECVD is sustained, we studied how it breaks down. For that, experiments of intentional breakdown of epitaxy were performed by either increasing the RF power or the hydrogen flow rate using the same $\text{SiF}_4/\text{H}_2/\text{Ar}$ chemistry. In both cases, the breakdown mechanism was based on the development of twins and stacking faults thus disrupting epitaxial configuration; this was accommodated with surface roughening. Thanks to this new understanding of epitaxy breakdown, we proposed some ways to sustain epitaxy for higher thicknesses. Moreover, we fascinatingly observed a quasi-fivefold symmetry in the diffraction patterns for these layers and for layers deposited using $\text{SiH}_4/\text{H}_2/\text{HMDSO}/\text{B}_2\text{H}_6/\text{Ar}$ plasma chemistry as well. We attributed such symmetry to the breakdown of epitaxy through multiple twinning. We developed a quantitative analysis method to discriminate twin positions from random microcrystalline ones in the diffraction patterns and to estimate the order of twinning. We also discussed some probable reasons for the occurrence of twinning and multiple twinning in a fivefold symmetry fashion. Finally, one important achievement to the TEM world is the optimization, during this thesis, of the traditional TEM sample preparation (tripod polishing), transforming it from a long and boring method to a fast method that is competitive with the relatively expensive focus ion beam (FIB) technique.

Keywords : TEM, electron diffraction, PECVD epitaxy, low temperature, silicon, twinning, epitaxy breakdown.

Titre : Etude par microscopie électronique en transmission de l'épitaxie du silicium à basse température par dépôt chimique en phase vapeur assisté par plasma

Résumé : Cette thèse s'intéresse à la croissance épitaxiale à basse température ($\sim 200^\circ\text{C}$) des couches minces de silicium par dépôt chimique en phase vapeur assisté par plasma (PECVD), pour des applications aux cellules solaires. L'objectif de départ était de mieux comprendre cette croissance épitaxiale, en utilisant la microscopie électronique en transmission (MET) comme principal outil expérimental. D'abord, nous avons étudié les premiers stades de cette croissance épitaxiale en chimie $\text{SiF}_4/\text{H}_2/\text{Ar}$, en menant une série de dépôts courts – quelques dizaines jusqu'à quelques centaines de secondes – sur différents types de substrats. Nous avons établi une corrélation entre les images MET et les mesures d'ellipsométrie in-situ. Nous avons discuté les mécanismes de croissance en nous basant sur l'hypothèse de la croissance traditionnelle à base d'atomes, radicaux et ions et l'hypothèse reposant sur la fonte des nanoparticules générées par le plasma au moment de l'impact avec le substrat. De plus, pour comprendre comment l'épitaxie par PECVD à basse température se maintient, nous avons étudié comment elle se brise. Pour cela, des expériences de perte d'épitaxie ont été visées en augmentant soit la puissance de la source RF, soit le flux d'hydrogène, toujours pour une chimie $\text{SiF}_4/\text{H}_2/\text{Ar}$. Dans les deux cas, le mécanisme de brisure d'épitaxie fait intervenir des macles et des fautes d'empilement qui interrompent la configuration épitaxiale ; ceci est accompagné par une rugosification de surface. Grâce à cette nouvelle compréhension de la brisure d'épitaxie, nous proposons quelques moyens pour maintenir l'épitaxie pour de plus grandes épaisseurs. En outre, nous avons observé une fascinante quasi-symétrie cinq dans les diagrammes de diffraction pour ces couches et aussi pour d'autres élaborées par un plasma de chimie $\text{SiH}_4/\text{H}_2/\text{HMDSO}/\text{B}_2\text{H}_6/\text{Ar}$. Nous avons attribué une telle symétrie à une brisure d'épitaxie par l'intermédiaire d'un maillage multiple. Nous avons développé une méthode quantitative qui permet de discriminer les positions de maillage de celles du microcristal aléatoire dans les diagrammes de diffraction et d'estimer l'ordre du maillage. Nous avons aussi discuté quelques raisons probables pour l'incidence du maillage et du maillage multiple sous forme de symétrie cinq. Finalement, une importante réalisation pour le monde de la MET, durant cette thèse, est l'optimisation de la préparation traditionnelle d'échantillon (polissage par tripode). Nous l'avons transformée d'une méthode longue et ennuyeuse en une méthode rapide qui devient compétitive par rapport à la technique du FIB relativement chère.

Mots clés : MET, diffraction électronique, épitaxie par PECVD, basse température, silicium, maillage, brisure d'épitaxie.

